Measurement of Arctic sea ice from satellite altimetry: the potential and limitations of CryoSat-2 SARIn mode

PhD Thesis

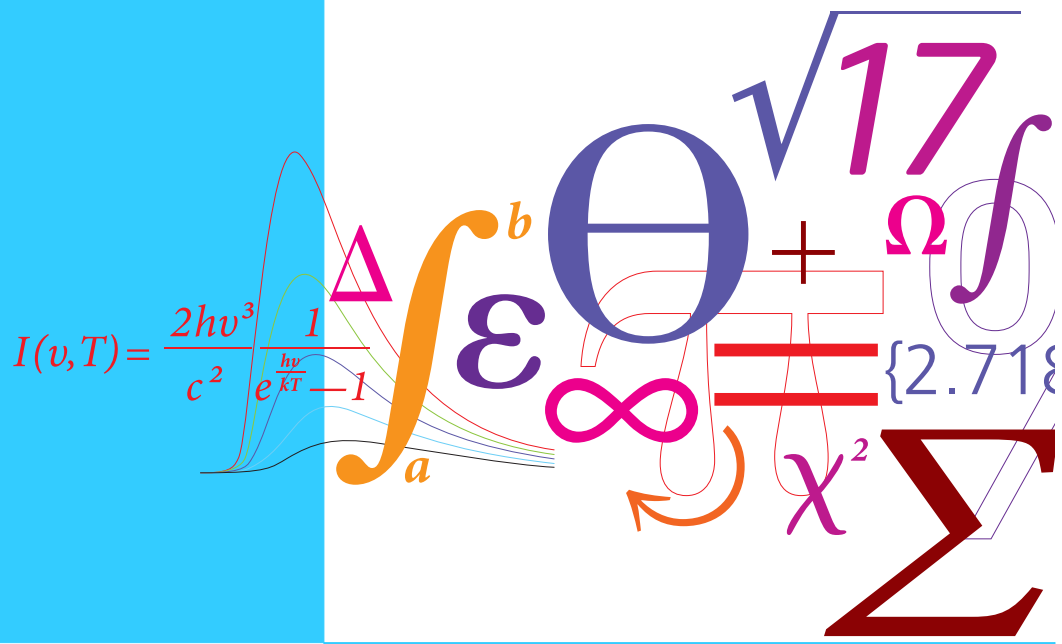

Candidate: **Alessandro Di Bella**

Supervisor: Prof. René Forsberg, DTU Space

Co-supervisor: Dr. Henriette Skourup, DTU Space

Date: February 2019

DTU Space
National Space Institute

Jet Propulsion Laboratory
California Institute of Technology

To my dad

No matter what, I will always keep loving and smiling

Preface

This PhD thesis is submitted to DTU Space, National Space Institute at the Technical University of Denmark (DTU) in partial fulfilment of the requirements to obtain the PhD degree. The research presented in this thesis has been conducted between December 15, 2015 and February 28, 2019 at the Division of Geodynamics, DTU Space. The project has been supervised by Prof. René Forsberg and Senior Scientist Henriette Skourup, both from DTU Space. Part of the PhD project was financially supported by the project *Space-borne observations for detecting and forecasting sea ice cover extremes* (SPICES), funded mainly by the European Union's Horizon 2020 Programme.

During the three years, I had the opportunity to attend the ESA Living Planet Symposium 2016 in Prague, Czech Republic, the American Geophysical Union (AGU) Fall Meeting 2016 in San Francisco, CA, USA, the AGU Fall Meeting 2017 in New Orleans, LA, USA and the ESA 25 Years of Progress in Radar Altimetry meeting in Ponta Delgada, Azores, Portugal. In addition, I had the privilege to participate in the international Sea Ice Workshop in Hamburg, Germany and the CryoSat-2 Quality Working Group #7 meeting in Frascati, Italy as well as several other international workshops. During the PhD project, I also took part in the 8^{th} International Summer School on Radar/SAR at the Fraunhofer Institute for High Frequency Physics and Radar Techniques (FHR), in Bonn, Germany and the 3^{rd} Snow Science Winter School organised by the Finnish Meteorological Institute (FMI) in Sodankylä, Finland. In the spring of 2017, I was part of the ESA CryoVEx ground team collecting in-situ measurements in Greenland. All these experiences gave me the opportunity to broaden my knowledge in fields strictly related to the topic of this PhD project and to meet an incredible number of valuable fellow researchers with whom I had the pleasure to share a great deal of interesting discussions.

Part of the work presented in this thesis has been carried out during a 7-month stay at the NASA Jet Propulsion Laboratory (JPL), Pasadena, CA, USA, where I worked closely with Dr. Kwok and Dr. Armitage to deepen my knowledge in the processing of CryoSat-2 data. This external research stay and the aforementioned conferences were partly funded by the Idella Foundation, the Ostenfelds Fond and the Otto Mønsteds Fond.

Summary

Sea ice plays a fundamental role in the global climate system, influencing directly the albedo of our planet and regulating the exchange of heat between the atmosphere and the ocean. Observations from satellites and submarine data have shown a rapid reduction of the ice-covered area and a general thinning of Arctic sea ice in the last three decades. Satellite altimetry can be used to infer sea ice thickness from the direct measurement of the sea ice freeboard, i.e. the height of the ice surface above the local sea level. However, in the freeboard-to-thickness conversion the freeboard and the associated errors are typically multiplied by a factor of $\sim$10, thus, it is fundamental to both improve the accuracy of freeboard estimates as well as to minimise their uncertainty.

The largest source of freeboard uncertainty, after the contribution due to the lack of knowledge of the Arctic snow cover, originates from the poor knowledge of the sea surface height (SSH) in ice-covered regions. CryoSat-2's (CS) interferometric mode (SARIn) enables to process waveforms whose power echo is dominated by the strong reflection from off-nadir leads, referred to as "snagged" waveforms, which are usually discarded in common SAR altimetry data processing. In fact, the available phase information can be used to correct for the associated range error and to retrieve a larger number of valid SSH measurements which, ultimately, increases the accuracy as well as reduces the uncertainty of the area-averaged SSH. The SARIn phase information is currently not used by the scientific community in the estimation of sea ice freeboard and thickness, probably because of the scarce SARIn coverage of the Arctic Ocean. However, despite changes in the SARIn acquisition mask throughout the years, CS still operates in SARIn mode along the entire coastline of the Arctic Ocean. In this work, an assessment of the potential and limitations of the CS SARIn mode with respect to the estimation of the sea ice freeboard and thickness in the Arctic is performed. Besides being of interest to the sea ice community, such an assessment could inform the proposal and design of future SARIn-only satellite altimetry missions.

The first part of this project investigates how the phase information provided by the CS SARIn acquisition mode affects Arctic sea ice freeboard and thickness retrievals as well as their corresponding random uncertainties. An Arctic sea ice processor (ASIP) is developed at DTU to process CS SAR and SARIn L1b waveforms according to both a regular SAR processing scheme, where only the power echoes are used, as well as by using the SARIn phase information. It is shown that CS SARIn mode can accurately detect off-nadir leads up to $\sim$2 km from the satellite nadir and correct for the associated range overestimation using the interferometric information. The comparison of along-track sea ice freeboard estimates from ASIP with airborne measurements from the ESA CryoVEx and NASA Operation IceBridge (OIB) campaigns indicates that, by using the phase information, the average random freeboard uncertainty of single CS freeboard estimates can potentially be reduced without introducing a bias on the average freeboard heights. Differences between SAR and SARIn freeboard heights at the boundaries of the SARIn mask, due to the larger noise of SARIn waveforms compared to SAR, are analysed and it is shown that continuity between SAR and SARIn regions can be achieved. By correcting for the overestimated

range due to the snagging effect, it is possible to process more waveforms than in a regular SAR processing scheme. The larger amount of both the processed waveforms and the detected leads is then increased significantly. In SARIn areas, this results in a 14% and 13% average reduction of the gridded random uncertainty of freeboard and thickness estimates, respectively, when compared to the results from the regular SAR reference case. During the analysis performed in this part of the study, an issue in the ESA Baseline C IPF1, the processor responsible of computing SAR and SARIn L1b waveforms, is detected. This issue, causing inaccurate values of phase difference to be computed for some SARIn waveforms at the boundaries of the SARIn mask, is solved in cooperation with ESA and Dr. Scagliola from ARESYS S.r.l.. The upcoming CS Baseline D L1b products will include this improvement which will benefit any application that exploits the phase information from SARIn L1b products near the boundaries of the SARIn mask.

The second part of the project describes the work carried out at the NASA Jet Propulsion Laboratory (JPL) in cooperation with Dr. Kwok and Dr. Armitage. Here, a second sea ice processor (MPASIP) is developed to investigate if the number of valid sea ice as well as lead measurements could be increased by processing multiple peaks of single CS SARIn waveforms, using the associated phase information, to further reduce the sea ice freeboard and thickness uncertainties. From Sentinel-1 SAR images, it is shown that the contributions from sea ice reflections close to the satellite nadir and specular returns from off-nadir leads can potentially be separated for some SARIn waveforms. Additionally, using the SARIn phase information enables to discard echoes generating from land and to retrieve freeboard heights closer to the coast compared to other available sea ice products.

Radar freeboard retrievals from MPASIP show a general good agreement with estimates from the Alfred Wagner Institute (AWI) and a general overestimation over multi-year ice (MYI) compared to the JPL processor. The comparison of sea ice freeboard and thickness estimates with OIB airborne data shows a good correlation ($\sim$0.7) and indicates that MPASIP and AWI overestimations in MYI regions are retracker-dependent. The analysis in SARIn areas reveals a larger correlation of MPASIP sea ice freeboard and thickness with OIB estimates compared to AWI. This is possibly due to a better sampling of the local sea surface of MPASIP, achieved by processing additional parts of the SARIn waveforms representing returns from off-nadir leads. Comparing MPASIP and ASIP, the increased amount of both lead ($\sim$5 times) and sea ice ($\sim$2.5 times) measurements, obtained by processing multiple peaks of single SARIn waveforms, results in an average reduction of the gridded random freeboard and thickness uncertainties of 54% and 52%, respectively. This corresponds to a reduction in the total sea ice thickness uncertainty of $\sim$30%, when the systematic contributions from the snow depth and density are taken into account.

Dansk resumé

Havis spiller en fundamental rolle I det globale klima system. Ved at ændre albedoen af Jorden's overflade regulerer den vekselvirkningen mellem atmosfæren og havet. Observationer fra satellitter og ubåde har påvist en drastisk reduktion af havisens udbredelse, og også en reduktion af havisens tykkelse i Arktis gennem de seneste 30 år. Satellit altimetri måler havisens fribord, det vil sige den del af havisen der stikker op over havets overflade, som kan konverteres til istykkelser. Ved konversionen fra fribord til tykkelse, er fribordet og den hermed forbundne nøjagtighed behæftet med fejl, som typisk er 10 gange større for istykkelsen. Det er således yderst vigtigt både at forbedre nøjagtigheden af fribordet samt at minimere den behæftede fejl.

Den største kilde til fribordets usikkerhed, udover bidraget fra den manglende viden om snelaget, stammer fra den manglende viden om det eksakte havniveau i isdækkede områder. Satellitten CryoSat-2 (CS) har evnen til at måle med en interferometrisk måleteknik (SARIn), som gør det muligt at inddrage målinger fra sprækker i isdækket, der ikke ligger lige under satellitens nadir lokation, og som ellers vil blive kasseret med CS's standard måleteknik, kaldet SAR. Faktisk kan fase informationen, der er tilgængelig med SARIn teknikken, bruges til at korrigere for den ekstra afstand til sprækkerne, grundet dens placering længere væk fra nadir. Ved at korrigere for denne faktor, er det muligt at inkludere flere målinger af havniveauet i processeringen. Dette giver I sidste ende større nøjagtighed på de enkelte målinger og reducerer usikkerheden af det lokale midlede havniveau.

Fase informationen fra SARIn teknikken bliver p.t. ikke brugt af forskerne til at bestemme havisens fribord og tykkelse, sandsynligvist da kun det er en relativt lille del af det Arktiske Ocean, hvor CS opererer med SARIn teknikken. På trods af ændringer i SARIn dækningen gennem årene, opererer CS stadigvæk i SARIn langs kyststrækningerne i hele det Arktiske Ocean. I denne afhandling, gives en vurdering af potentialet og begrænsningerne ved at anvende data fra CS med den interferometriske måleteknik specielt med henblik på at estimere havisens fribord og tykkelse. Udover at være interessant for havis forskere, vil sådanne en analyse bidrage til forslag og design af fremtidige satellit altimetri missioner, der kun anvender SARIn måleteknik.

Første del af afhandlingen undersøger, hvordan fase informationen fra målinger af CS i SARIn påvirker estimereingen af havisens fribord og tykkelse, samt deres tilhørende usikkerheder. Til dette formål er der, på DTU, udviklet en processor (ASIP) til at beregne havisens fribord og tykkelse i Arktis ud fra pulsformen (waveforms) i CS SAR samt SARIn L1B data produkter både ved en ren standard SAR processering, som kun anvender information fra direkte analyse af pulsformen tæt på nadir, samt ved i tillæg at anvende fase informationen målt med CS SARIn måleteknik til også at inkludere målinger væk fra nadir. Det viser sig, at målinger opsamlet af CS SARIn, kan detektere sprækker i haveisen med stor nøjagtighed i op til 2 km fra satellittens nadir lokation og ved yderligere at bruge fase informationen kan korrigere for den overestimerede afstand til denne. Sammenlignes CS estimater af havisens fribord beregnet med ASIP, med tilsvarende flymålinger fra ESA CryoVEx og NASA Operation IceBridge (OIB) kampagner, kan det påvises at inkluderes fase informationen, reduceres usikkerheden på den enkelte CS måling af fribordet uden at introducere målebias på den midlede fribordshøjde.

En analyse af afvigelser mellem SAR og SARIn fribordet på grænserne, hvor CS skifter fra SAR til SARIn måleteknik, som forventes at eksistere grundet den større støj behæftet til SARIn målingerne i forhold til SAR målingerne, viser at kontinuiteten mellem de to måleteknikker kan bevares. Ved at korrigere for den overestimerede afstand, forårsaget af låsning af satellitens signal på sprækker i isen placeret væk fra satellitens nadir lokation, er det muligt at inkludere flere målinger i processeringen end ved anvendelse af en standard SAR processerings rutine. Antallet af de processerede målinger øges signifikant. I SARIn områder, resulterer dette i en reduktion på henholdsvist 14% og 13% af usikkerhed af fribords og tykkelses estimater i et grid, når der sammenlignes med SAR referencen. Under udførelsen af analysen i denne del af afhandlingen, blev der fundet en fejl i ESA Baseline C IPF1, som er den processor der er ansvarlig for at beregne SAR og SARIn L1B waveforms. Fejlen, der forårsagede ukorrekte værdier af fase forskellen beregnet af de første SARIn waveforms på grænsen af SARIn masken, er blevet løst i samarbejde med ESA og Dr. Scagliola from ARESYS S.r.l..ESA's kommende CS Baseline D L1b data produkt vil inkludere denne forbedring, som vil påvirke og forbedre resultater af alle applikationer der anvender fase informationen fra SARIn L1b data tæt på grænserne af SARIn masken.

Anden del af afhandlingen, beskriver et studie der blev udført på NASA Jet Propulsion Laboratory (JPL) i samarbejde med Dr. Kwok and Dr. Armitage. Her blev en anden havis processor (MPASIP) udviklet for at undersøge om antallet af valide målinger af havis og sprækker i isen kan blive øget ved at processere multiple overflade refleksioner fra en enkelt waveform. Dette kan gøres, ved anvendelse af fase informationen, for yderligere at kunne reducere usikkerheden på fribord og tykkelse. Sammenligninger med Sentinel-1 SAR billeder, viser at reflektioner fra havis tæt på nadir og reflektioner fra sprækker der ligger væk fra nadir potentielt kan adskilles for nogle SARIn waveforms. Yderligere, gør SARIn fase informationen det muligt at kassere retur signaler, der stammer fra land, hvilket resulterer i at havisens fribord kan estimeres tættere på kysten sammenlignet med eksisterende havis produkter.

Radar fribordet estimeret ved brug af MPASIP stemmer generelt godt overens med tilsvarende estimater fra Alfred Wagner Institute (AWI), og begge disse overestimerer fribordet over flerårs-is når de sammenlignes med data fra JPL processoren. Sammenligningen af havisens fribord og tykkelse korrelerer godt (0.7) med OIB flydata og indikerer at det at MPASIP og AWI overestimerer i områder dækket af flerårs-is er forårsaget af den valgte re-tracker. Analysen i SARIn områderne afslører en større korrelation af MPASIP havis fribord og tykkelser med OIB målinger, når der sammenlignes med AWI. Dette er muligvis fordi MPASIP er bedre til at bestemme det lokale havniveau, da den også anvender information om det lokale havniveau fra sprækker der ligger væk fra nadir. Sammenlignes MPASIP and ASIP, øges antallet af valide målinger af både sprækker ($\sim$5 gange) og havis ($\sim$2.5 gange), således at målinger der inkluderer multiple reflektioner fra enkelte waveforms, resulterer i en reduktion på 54% og 52% af usikkerheden af fribordet og tykkelsen på grid-produktet. Dette svarer til en reduktion i usikkerheden af havisens tykkelse på $\sim$30%, når det systematiske bidrag fra sne dybde og densitet er medregnet.

Acknowledgements

First of all, I would like to thank my main supervisor, René Forsberg, for giving me the possibility to work on this project and for always encouraging my participation in a fair number of international conferences and workshops. A big thank you goes to my co-supervisor, Henriette Skourup, for the large amount of time she spent giving me feedback during the past three years, even when it was outside of regular working time. Thanks to my colleagues at DTU Space, for the continuous support, the mini-breaks and the extra care they took of me during stressful periods. Special thanks to Gaia Piccioni, Valentina Barletta and Louise Sandberg Sørensen for taking the time to read this work and for providing valuable feedback.

I would like to thank Ron Kwok for giving me the chance to spend 7 months at the Jet Propulsion Laboratory, during which both he and Tom Armitage gladly shared their expertise with me. Thanks for the interesting discussions and for contributing to deepen my knowledge about the CryoSat-2 mission, and more. I am especially grateful to Johan Nillson, Fernando Paolo, Tom Armitage, Veronica Nieves, Mike DeFlorio and Blake Margett, for making Pasadena feel like home and, sometimes, even better.

Thanks to all the fellow researchers I met around the world during these three years and to the ESRIN crew. You guys have been the cherry on top of the cake in every single trip.

A warm thank you goes to my family for always showing me unconditional love and understanding and to my nephew, Thomas, for all his sincere, pure, and contagious smiles that gave me an extra boost to keep pushing through tough days.

Finally, I would like to express all my gratitude to Anthie for being a great companion during this journey we shared. Thanks for all the support and the incredible amount of hours you spent listening to my discussions about Arctic sea ice... Now, I can finally smell the freeboard!

Contents

List of Figures

List of Tables

Abbreviations

AEM	Airborne ElectroMagnetic induction sounder
AGU	American Geophysical Union
ALS	Airborne Laser Scanner
AO	Arctic Oscillation
ASIP	Arctic Sea Ice Processor
ASIRAS	Airborne SAR Interferometric RAdar System
ATM	Airborne Topographic Mapper
AWI	Alfred Wagner Institute
BRF	Burst Repetition Frequency
CNES	French National Space Agency
CryoVEx	CryoSat Validation Experiment
CS	CryoSat-2
DEM	Digital Elevation Model
DMI	Danish Meteorological Institute
DORIS	Doppler Orbitography and Radiopositioning Integrated by Satellite
ECMWF	European Centre for Medium-range Weather Forecast
EM	Electromagnetic probe
ESA	European Space Agency
FBR	Full Bit Rate
FYI	First-year ice
GDAL	Geospatial Data Abstraction Library
GIM	Global Ionospheric Map
GPS	Global Positioning System
GSHHG	Global Self-consistent, Hierarchical, High-resolution Geography Database

IPF1	Instrument Processing Facility L1b
ISRO	The Indian Space Research Organization
JPL	Jet Propulsion Laboratory
LRM	Low Resolution Mode
MPASIP	Multi-peak Arctic Sea Ice Processor
MSS	Mean sea surface
MYI	Multi-year ice
NASA	National Aeronautics and Space Administration
NSIDC	National Snow and Ice Data Center
OCOG	Offest Center Of Gravity
OIB	NASA Operation IceBridge
ONC	Off-nadir range correction
OSI SAF	Ocean and Sea Ice Satellite Application Facility
POCA	Point of closest approach
POD	Precise Orbit Determination
PP	Pulse peakiness
PRF	Pulse Repetition Frequency
S1	Sentinel-1
SAR	Synthetic Aperture Radar
SARIn	SAR Interferometric Mode
SIRAL	SAR Interferometric Radar ALtimeter
SRAL	SAR ALtimeter
SSA	Sea surface anomaly
SSH	Sea surface height
TEC	Total Electron Content
ULS	Upward Looking Sonar
W99	Warren 99 climatology
WB	Wingham Box
WGS84	World Geodetic System 1984

Chapter 1

Introduction

1.1 Motivation

Sea ice is one of the most significant climate parameters interacting with several feedback processes of the global climate system. Changes in the sea ice cover represent one of the most visible components of climate change, with the sea ice extent influencing directly the albedo of our planet [Laxon et al., 2013]. Furthermore, variations in the ice volume reflect changes in the heat budget of the Arctic [Laxon et al., 2013] and can influence the climate at a global scale. To represent these changes, coupled atmosphere-ocean models require the knowledge of the sea ice mass balance. Besides the scientific interest as a climate indicator, knowledge of the sea ice cover and thickness are important for the shipping and fishery industries as well as for exploration and off-shore activities [Ulaby et al., 1986]. Remote sensing records of Arctic sea ice now span over several decades. Since the 1980s, satellite observations from passive radiometers have shown a rapid reduction of the ice-covered area in the Arctic [Comiso et al., 1991] which, together with evidences about the thinning of Arctic sea ice from submarine data [Rothrock et al., 1999; Kwok et al., 2009], may cause a reduction of the sea ice volume at an even faster rate than observed for sea ice extent [Desch et al., 2017].

In order to understand our changing climate and make Arctic navigation even safer, an extensive and continuous monitoring of the Arctic sea ice cover is necessary. Satellite observations guarantee a good spatial as well as temporal coverage. Estimating the sea ice volume from satellite observations requires the knowledge of the sea ice extent and thickness. While the extent can be measured directly by satellites using passive radiometry, the estimation of the thickness is more challenging. This parameter can be estimated, assuming hydrostatic equilibrium [Laxon et al., 2003], from the measurement of the sea ice freeboard, i.e. the height of the ice surface above the local sea level. For the last 25 years, satellite altimetry has been used to measure directly the sea ice freeboard by Laxon et al. [2003]; Kwok et al. [2009]; Laxon et al. [2013]; Kwok & Cunningham [2015]; Armitage & Ridout [2015]; Tilling et al. [2018] and more. However, in the freeboard-to-thickness conversion the freeboard and the associated errors are typically multiplied by a factor of $\sim$9.6 [Wingham et al., 2006], thus, it is fundamental to both improve the accuracy of freeboard estimates as well as to minimise their uncertainty.

The second largest source of freeboard uncertainty, after the contribution due to the lack of knowledge of the Arctic snow cover [Giles et al., 2007], originates from the poor knowledge of the sea surface height (SSH) in ice-covered regions [Ricker et al., 2014]. The uncertainty of the SSH throughout the Arctic Ocean highly depends on the amount of leads detected by the satellite as well as by their spatial distribution. Armitage & Davidson [2014] have demonstrated that CryoSat-2's (CS) interferometric mode (SARIn) enables to process waveforms whose power echo is dominated by the strong reflection from off-nadir leads, which are usually discarded in

common SAR altimetry data processing. In fact, the available phase information can be used to correct for the associated range error and to retrieve a larger number of valid SSH measurements which, ultimately, increases the accuracy as well as reduces the uncertainty of the area-averaged SSH. An additional consequence of the larger number of SSH measurements, not discussed by Armitage & Davidson [2014], is the increase in the amount of valid freeboard retrievals which would also contribute to reduce the uncertainty of the area-averaged freeboard estimates.

Despite this finding, no publicly available product to date includes the SARIn phase information in the estimation of sea ice freeboard and thickness. While the main reason might be the scarce SARIn coverage of the Arctic Ocean, a more detailed assessment of how CS phase information could benefit sea ice freeboard and thickness retrievals would be not only interesting for the sea ice community and climate-related studies, but it would inform the proposal and design of future satellite altimetry missions planning to operate in SARIn mode over the entire Arctic. Additionally, CS still operates in SARIn mode along the entire coast of the Arctic Ocean and, as shown by e.g. Abulaitijiang et al. [2015], the phase information can be used to retrieve a larger amount of valid height measurements in regions with a complicated topography.

1.2 Objectives

This study investigates how the larger amount of waveforms which is possible to process in the SARIn mode, thanks to the available phase information, affects both the accuracy and the uncertainty of Arctic sea ice freeboard and thickness retrievals. Furthermore, a processing scheme inspired by the concept of swath processing [Gray et al., 2013] is proposed, aimed at maximising the amount of information that can be extracted from CS SARIn waveforms over sea ice-covered regions. This approach is used to investigate if processing multiple peaks of single SARIn waveforms could further reduce the uncertainty of Arctic freeboard heights, especially in regions with a sparse lead distribution. CS SARIn phase information is also used to estimate Arctic sea ice freeboard and thickness closer to the coast than other available sea ice products, where CS permanently acquires data in SARIn mode.

1.3 Scientific contributions

The work carried out during this PhD project is partly described in the manuscripts published, or accepted for publications, in international scientific impact journals. Section 1.3.1 provides a list of these scientific contributions. Additionally, oral and poster presentations given to international scientific conferences are provided in section 1.3.2. Journal articles and poster contributions are included in Appendix A and B, respectively, at the end of this manuscript. The abstracts summarising oral presentations are instead provided here.

1.3.1 Journal papers

1. **Uncertainty reduction of Arctic sea ice freeboard from CryoSat-2 interferometric mode**
   A. Di Bella, H. Skourup, J. Bouffard, T. Parrinello
   Published in *Advances in Space Research, vol. 62, no. 6, pp.1251–1264, Jun. 2018 (online in Mar. 2018)*. See Appendix A.1

2. **Improving CryoSat SARIn L1b products to account for inaccurate phase difference: impact on sea ice freeboard retrieval**
   A. Di Bella, M. Scagliola, L. Maestri, H. Skourup, R. Forsberg
   Accepted for publication after minor revisions in *IEEE Geoscience and Remote Sensing Letters, Mar. 2019*. See Appendix A.2

1.3.2 Conference contributions

1. **Validation of CryoSat-2 Performance over Arctic Sea Ice**
   A. Di Bella, H. Skourup, J. Bouffard, T. Parrinello
   Poster presentation at the *Living Planet Symposium 2016, Prague, Czech Republic, 9–13 May 2016*. See Appendix B.1

2. **Evaluation of Sentinel-3 SAR Performance over Arctic Sea Ice**
   A. Di Bella, S. B. Simonsen, H. Skourup, L. S. Sørensen, R. Forsberg
   Oral presentation at the *AGU Fall Meeting 2016, San Francisco, CA, USA, 12–16 Dec. 2016*

   Sea ice is a fundamental component of the Earth climate system since it influences directly the albedo of our planet and regulates the heat exchange between the atmosphere and the ocean. Global weather patterns and climate are therefore strictly connected to the presence and properties of sea ice which represents an important element in short- and long-term climate modelling.
   The launch of the EC/ESA's Sentinel-3 mission offers the opportunity to prolong the observation of sea ice topography and dynamics as well as it provides essential near real-time information for ocean and weather forecasting. In particular, the SAR radar altimeter (SRAL) carried on board of this satellite enables to estimate sea ice thickness in ice-covered areas by measuring directly the sea ice freeboard.
   This work evaluates Sentinel-3 SAR performance over Arctic sea ice using laser altimetry data collected during a Sentinel-3 underflight – the first with the SRAL instrument operating in SAR mode – performed as a part of the CryoVEx 2016 campaign. Snow freeboard heights derived from airborne laser scanner measurements are used to validate the sea ice freeboard obtained by processing Sentinel-3 SAR level 1b waveforms. We present the results of the freeboard comparison from a statistical point of view.

3. **Evaluation of CryoSat-2 SARIn vs. SAR Arctic Sea Ice Freeboard**
   A. Di Bella, H. Skourup, R. Forsberg
   Oral presentation at the *AGU Fall Meeting 2017, New Orleans, LA, USA, 11–15 Dec. 2017*

   Earth climate is a complex system which behaviour is dictated by the interaction among many components. Sea ice, one of these fundamental components, interacts directly with the oceans and the atmosphere playing an important role in defining heat exchange processes and, thus, impacting weather patterns on a global scale. Sea ice thickness estimates have

notably improved in the last couple of decades, however, the uncertainty of such estimates is still significant.
For the past 7 years, the ESA CryoSat-2 (CS2) mission has provided a unique opportunity to observe polar regions due to its extended coverage up to 88° N/S. The SIRAL radar altimeter on board CS2 enables the sea ice community to estimate sea ice thickness by measuring the sea ice freeboard. Studies by Armitage & Davidson [2014] and Di Bella et al. [2018] showed that the interferometric capabilities of SIRAL can be used to retrieve an increased number of valid sea surface heights in sea ice covered regions and thus reduce the random uncertainty of the estimated freeboards, especially in areas with a sparse lead distribution.
This study focuses on the comparison between sea ice freeboard estimates obtained by processing L1B SARIn data inside the Wingham box – an area in the Arctic Ocean where SIRAL has acquired SARIn data for 4 years – and those obtained by processing L1B SAR data in the area surrounding the box. This comparison evaluates CS2 performance on Arctic sea ice from a statistical perspective by analysing the continuity of freeboard estimates in areas where SIRAL switches between SAR and SARIn acquisition modes. Data collected during the Operation IceBridge and CryoVEx field campaigns are included in the study as an additional validation.
Besides investigating the possibility of including the phase information from SIRAL in currently available freeboard estimates, this results provide valuable information for a possible SARIn CryoSat follow-on mission.

4. **Greenlandic coastal sea ice freeboard and thickness from CryoSat-2 SARIn data**
A. Di Bella, R. Kwok, T. Armitage, H. Skourup, R. Forsberg
Poster presentation at the *25 Years of Progress in Radar Altimetry, Ponta Delgada, Azores, 24–29 September 2018*. See Appendix B.2

5. **Multi-peak Retracking of CryoSat Waveforms over Arctic Sea Ice**
A. Di Bella, R. Kwok, T. Armitage, H. Skourup, R. Forsberg
Accepted for poster presentation at the *Living Planet Symposium 2019, Milan, Italy, 13–17 May 2019*

By measuring directly the sea ice freeboard, satellite altimetry has proven to be a powerful tool to estimate sea ice thickness from space for the last 25 years.
Since 2010, the ESA's CryoSat-2 (CS2) radar altimetry mission has made a significant contribution to this field. Compared to previously launched missions, CS2 enabled the observation of Arctic sea ice at latitudes up to 88N at a higher along-track ground resolution, when operating in SAR and SAR Interferometric (SARIn) modes. Previous studies showed how the phase information available in the SARIn mode can be used to reduce the uncertainty of the sea surface height in ice-covered regions [Armitage & Davidson, 2014] and, consequently, the uncertainty of freeboard retrievals [Di Bella et al., 2018].
This work investigates how retracking more than one peak in level 1b SARIn waveforms – in combination with the respective phase information – could increase the amount of valid sea ice as well as sea surface height measurements, so as to ultimately reduce even further the uncertainty of freeboard estimates. The challenges and limitations of this method will be identified with the support of Sentinel-1 SAR images and airborne validation data from the ESA CryoVEx and NASA Operation IceBridge campaigns.

1.4 Structure of the thesis

This thesis is partly based on the content of the journal publications listed in section 1.3.1 and attached in full length in Appendix A. While the motivation behind the study as well as its objectives have been respectively stated in sections 1.1 and 1.2, the rest of the thesis is organised as follows.

Chapter 2 covers the state of the Arctic sea ice describing seasonal cycles, sea ice extent and thickness distribution, snow cover and the importance of sea ice in the climate system.

Chapter 3 introduces the CryoSat-2 (CS) mission as well as the basic theory of satellite altimetry and waveform retracking which is used throughout the thesis.

Chapter 4 focuses on the techniques used to estimate sea ice freeboard and thickness, and the respective uncertainties, from satellite radar altimetry.

Chapter 5 describes the data used in this work and some of the instruments used to collect them.

Chapter 6 investigates the possible advantages of using the CS SARIn phase information in the estimation of Arctic sea ice freeboard and thickness, using the first of the two sea ice processors developed in this study (ASIP). The content of this chapter is to be considered complementary to the work described in [Di Bella et al., 2018] and [Di Bella et al., 2019] which can be found in Appendix A.

Chapter 7 describes the work carried out during a 7-month stay at the NASA Jet Propulsion Laboratory (JPL) which investigates the possibility to further reduce the uncertainties of Arctic sea ice freeboard and thickness retrievals by processing SARIn waveforms according to a "swath-like" processing technique. A manuscript describing the results obtained at JPL is currently in preparation and is not attached to the thesis. The content of the current draft is expanded in this chapter which describes the algorithms behind the second sea ice processor (MPASIP), developed at JPL, together with related results.

Chapter 8 finally summarises the work of the entire PhD project and provides some concluding remarks and ideas for future work.

Chapter 2

The Arctic sea ice

The Arctic Ocean (figure 2.1) is partially covered by sea ice all year round. The average thickness of the Arctic sea ice ranges between 2 m and 3 m and varies with the season. Sea ice interacts with several processes of the global climate system. Changes in the sea ice cover influence in particular (1) the surface albedo of our planet, i.e. the fraction of solar radiation that is reflected back into space, (2) the exchange of heat and gases between the ocean and the atmosphere and (3) the circulation of the ocean by altering its salinity. This chapter aims at providing an overview of the Arctic sea ice cover and its connections to the global climate system. The next sections describe the main ice types, the basic processes driving its seasonal cycle as well as variations in the extent and thickness distribution.

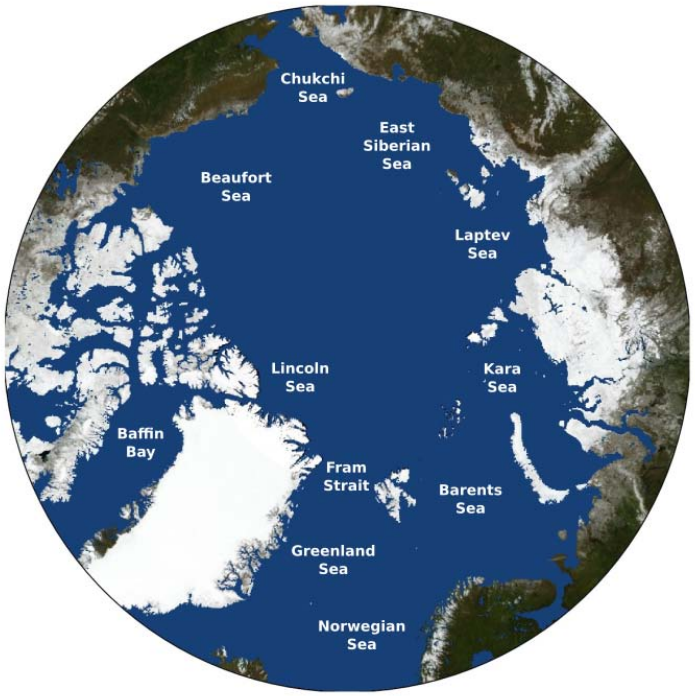

Figure 2.1: Map of the Arctic Ocean. Background: NASA Blue Marble

2.1 The Arctic sea ice cover

On large scales, the Arctic sea ice is mainly characterised in terms of extent (section 2.2) and thickness (section 2.3). Sea ice extent has been observed since 1979 with passive microwave satellites [Comiso et al., 1991]. Arctic-wide sea ice thickness is more complicated to determine, mainly because satellites are only able to measure the upper part of the ice (chapter 4). Nevertheless, Arctic sea ice is usually classified according to its thickness which directly relates to the age of the ice and its physical properties. The ice thickness varies in response to thermodynamic processes (growth and melt) and dynamic forcing (ocean and wind circulation).

2.1.1 Thermodynamic growth and sea ice types

Arctic sea ice can be mainly grouped into new ice, young ice, first-year ice and multi-year ice, although a larger number of categories exist in the literature [World Meteorological Organization, 2014].

New ice and young ice are less than 0.1 m thick and between 0.1 m and 0.3 m thick, respectively. They represent the initial stage of sea ice formation and, during fall, young ice grows rapidly into *first-year ice* (FYI) reaching a maximum thickness of 2 m by thermodynamic growth alone. This kind of ice has a very smooth surface and is relatively dense, as part of the salt present in the ocean accumulates into droplets, called brine, and freezes together with the water.

During the melt season, typically from May to September, most of the FYI and thinner ice classes melt. The ice that survives at least one summer's melt is called *multi-year ice* (MYI) and is more than 2 m thick, usually between 3–4 m. Due to the melt and refreeze of the surface happening during summer and early winter, MYI has a rougher surface than FYI. The difference in roughness between these two kinds of ice enables the estimation of the ice type by active microwave sensing [Gohin & Cavanié, 1994]. MYI is less dense than FYI since over time the brine migrates downward through holes and channels in the ice, leaving behind air pockets, and eventually reaches back into the ocean. Additionally, the freshwater from summer melt ponds travels through the cracks and holes in the ice, washing out remaining brine. MYI has a much smaller annual growth cycle than FYI, of approximately 0.40–0.45 m [Maykut & Untersteiner, 1971].

2.1.2 Dynamic forcing

Winds and currents in the Arctic Ocean cause horizontal transport and deformation of the sea ice cover, heavily influencing the geographic distribution of the thickness. In divergent areas the sea ice fractures exposing the sea surface to the cold atmosphere. These cracks in the sea ice, the *leads*, rapidly refreeze at subzero temperatures. Leads play an important role in the heat exchange between the atmosphere and the ocean in the Arctic. Furthermore, in this study they are used to determine the local sea surface height in ice-covered regions, enabling the estimation of sea ice thickness from satellite altimetry (see chapter 4).

In convergent areas sea ice is pushed together and thickness increases following rafting or ridging processes. While rafting describes ice floes below 1 m overriding each other, ridges are formed when ice breaks into pieces and piles up on top of each other. Ridging is common in regions where FYI collides with MYI as well as where drifting ice meets landfast ice along the coast. Ridges can reach more than 1 m height above [Duncan et al., 2018] and several meters below the sea level.

The circulation of the sea ice cover is closely coupled to the circulation of the ocean surface layer and both are primarily driven by winds (figure 2.2). Cold water, with a relatively low concentration of salt compared to Arctic seawater, enters the Arctic Ocean through the Bering

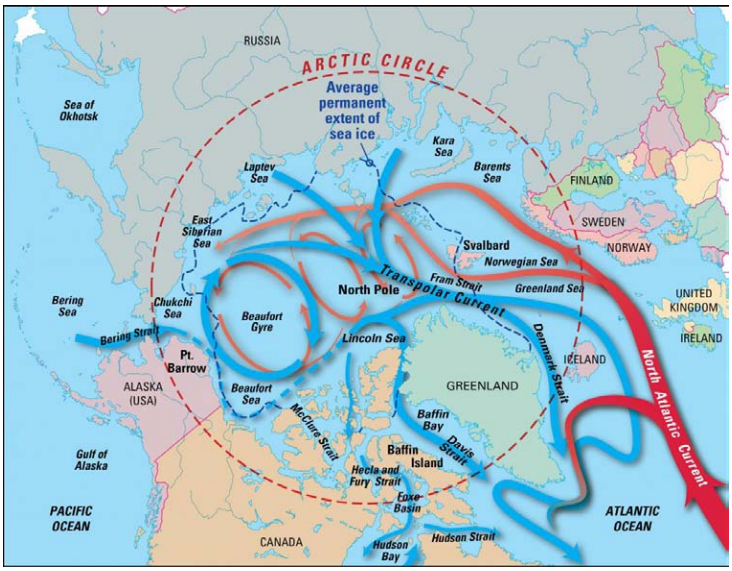

Figure 2.2: Circulation patterns in the Arctic Ocean. Red arrows indicate warm salty water from the North Atlantic, while blue arrows are cold fresh water. Credit: Jack Cook, Woods Hole Oceanographic Institution

Strait to get to the Chukchi Sea where, in winter, cold air freezes seawater into sea ice. During this process, salt is released into surface waters which become denser and sink, creating the halocline layer. This layer lies on top of warmer and denser water coming from the Atlantic Ocean through the Fram Strait and the Barents Sea. From the Chukchi Sea, fresh surface water and sea ice are swept into the main wind-driven circular current of the Arctic Ocean, the anticyclonic *Beaufort Gyre*. Between the Beaufort Gyre and a weaker circulation system in the Eurasian basin, the *Transpolar Drift* transports sea ice from the East Siberian Sea, Laptev Sea and Kara Sea out of the Arctic region (figure 2.2). The largest part of multi-year sea ice leaves the Arctic Ocean through the Fram Strait, branching around either side of Iceland, to reach the warmer North Atlantic waters, where it deteriorates. Smaller fractions of MYI can reach the Atlantic by drifting to Baffin Bay, through the Nares Strait, or through the Canadian Archipelago. These main circulation patterns define the geographic variations of sea ice thickness in the Arctic, resulting in thicker ice along the northern coasts of the Canadian Archipelago and Greenland compared to the rest of the Arctic.

The strength and location of the main surface currents in the Arctic are mainly determined by wind patterns controlled by changes in the atmospheric pressure system. The *Arctic Oscillation* (AO) index [Rigor et al., 2002] is a climate index describing the state of the atmospheric circulation in the Arctic with respect to that of mid latitudes. More in details, it measures the principal time varying component of the Northern hemisphere's sea level pressure anomaly [Thompson & Wallace, 1998]. Changes in the AO index cause changes in the sea ice motion which, in turn, affects the geographical concentration (section 2.2) as well as the thickness distribution (section 2.3). A positive AO index is associated with lower than normal sea level pressure over the Arctic and higher than normal pressure at mid-latitudes. This generates cyclonic winds which slow down the Beaufort Gyre and strengthen the Transpolar Drift. During this state, the transport of sea ice from coastal areas out of the Arctic basin through the Fram Strait increases, together with the amount of leads and the production of new sea ice in the East Siberian and Laptev Seas. Therefore, a positive AO index is generally associated with a decrease in the extent as well as a thinning of sea ice [Rigor et al., 2002].

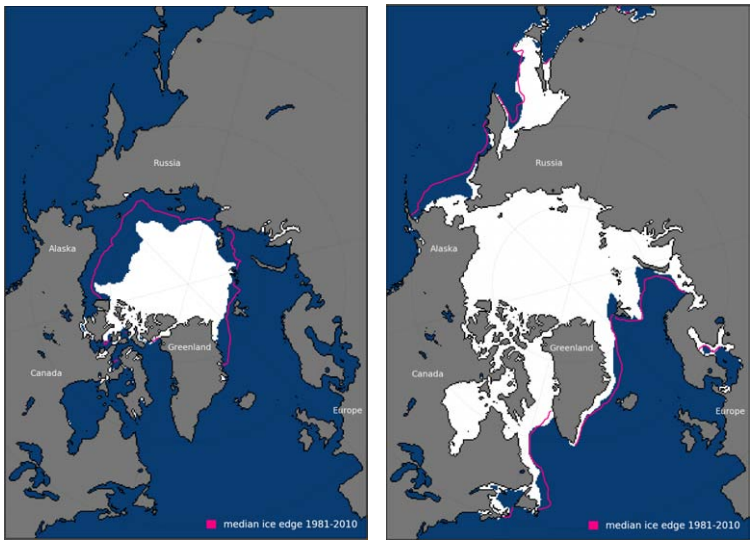

(a) **(b)**

Figure 2.3: Arctic sea ice extent. (a) Seasonal minimum in September 2017 and (b) Seasonal maximum in March 2018. Credit: National Snow and Ice Data Center (NSIDC)

On the contrary, a negative AO index indicates a higher than normal sea level pressure in the Arctic and a lower than normal pressure at mid-latitudes. The consequently anticyclonic winds strengthen the Beaufort Gyre which tends to recirculate the ice longer before being exported out of the Arctic through the Fram Strait [Steele et al., 2004]. Thus, a negative AO index generally favours thicker ice, although this was not the case during winter 2009/10 [Stroeve et al., 2011].

Armitage et al. [2017] estimated geostrophic currents throughout the Arctic Ocean from 2003 to 2014, a period of rapid environmental change in the Arctic. They found an acceleration of the Beaufort Gyre after 2007 relative to 2003–2006, when strong atmospheric circulation, record low sea ice extent, loss of MYI and significant thinning of the ice resulted in high surface stress and spin-up of the ocean currents. In the same study, they point out that in 2013, the Beaufort Gyre moved 300 km to the northwest of its 2003 position.

2.2 Arctic sea ice extent

In order to measure the amount of sea ice in the Arctic Ocean using remote sensing techniques, this region is divided into a grid. The percentage of sea ice within each grid cell is referred to as ice concentration. The Arctic sea ice extent is commonly defined as the area in the Arctic Ocean having an ice concentration of at least 15% [Bamber & Kwok, 2004].

Passive microwave satellites have been used to measure sea ice concentration since 1979 [Comiso et al., 1991], taking advantage of the different radiation emitted by ice and water. However, this also means that sea ice concentration is hard to measure during the summer due to the large amount of moisture present in the atmosphere as well as because surface melt cannot be distinguished from open water.

The Arctic sea ice starts forming in October and reaches its maximum in March, which marks the end of the growth season. Starting typically from May, the ice melts throughout the Arctic summer and reaches the minimum extent in September, when about 2/3 of the ice have disappeared (figure 2.3).

Since 1979 both the Arctic sea ice minimum and maximum extents have seen a constant

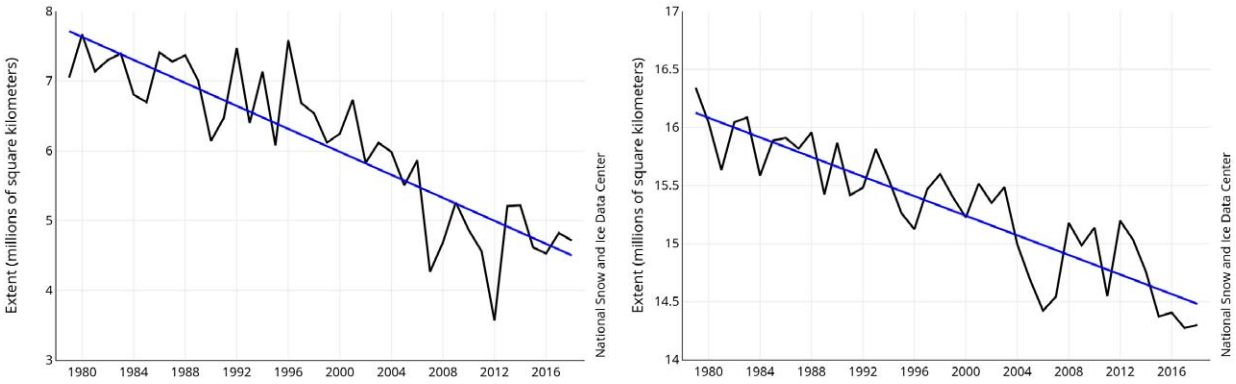

Figure 2.4: Average monthly Arctic sea ice extent (black curve) for the period 1979–2018. (a) Average extent for the month of September and (b) for the month of March. The fitted linear trend is -12.8% and -2.7%, respectively. Credit: National Snow and Ice Data Center (NSIDC)

decrease, with a trend of -12.8% and -2.7% per decade, respectively [National Snow and Ice Data Center (NSIDC)] (figure 2.4). September 17, 2012 saw the lowest record of sea ice extent since 1979, with an extent of $3.39 \cdot 10^6$ km^2, which was $2.95 \cdot 10^6$ km^2 lower than the 1981–2010 median value [National Snow and Ice Data Center (NSIDC)]. This record was 18% lower than the former record of minimum ice extent, observed in 2007 [Perovich et al., 2012]. Both the minima in 2007 and 2012 were caused by the shrinking and thinning of the sea ice cover during the previous years in combination with anomalous atmospheric forcing [Maslanik et al., 2007; Lindsay et al., 2009; Perovich et al., 2008; Stroeve et al., 2012]

For reference, monthly averages of sea ice extent from NSIDC can be observed in figure 2.5, where the 1981–2010 median extent is compared to the averages for 2007, 2012, 2016, 2017 and 2018.

2.3 Arctic sea ice thickness distribution

Sea ice thickness is one of the most challenging sea ice parameters to be measured mainly because of the high variability of, and low accessibility to, the bottom part of the ice. Sea ice thickness can be measured in various ways, the most commonly used being: in-situ measurements, Upward Looking Sonar (ULS), electromagnetic sensors (EM) and airborne and satellite altimetry. Satellite passive microwave has been shown to be able to retrieve the thickness up to 0.5 m, although this technique does not provide consistent measurements for thicker ice [Kaleschke et al., 2012].

In-situ measurements provide the most accurate sea ice thickness estimates but, due to their limited availability and spatial coverage, they are mainly useful to validate other datasets [Haas et al., 1997]. ULS, measuring the ice from below the sea level, have shown a decrease in thickness of 42% between 1958 and 1976 [Rothrock et al., 1999] and a 43% thinning in the period 1976–96 [Wadhams & Davis, 2000], both corresponding to about 1 m thinning of the ice. Helicopter EM measurements exploits the contrast of electrical conductivity between the sea ice and ocean layers. The EM probe, also known as "bird" for the way it hangs out of the helicopter, measures the distance between the probe and the water, while a laser altimeter in the bird determines the system height above the ice or snow surface. Measurements collected over the Transpolar Drift in 2001, 2004 and 2007 showed a 53% reduction of modal sea ice thickness [Haas et al., 2008]. Several other local surveys based on in-situ and EM ice thickness measurements exist in

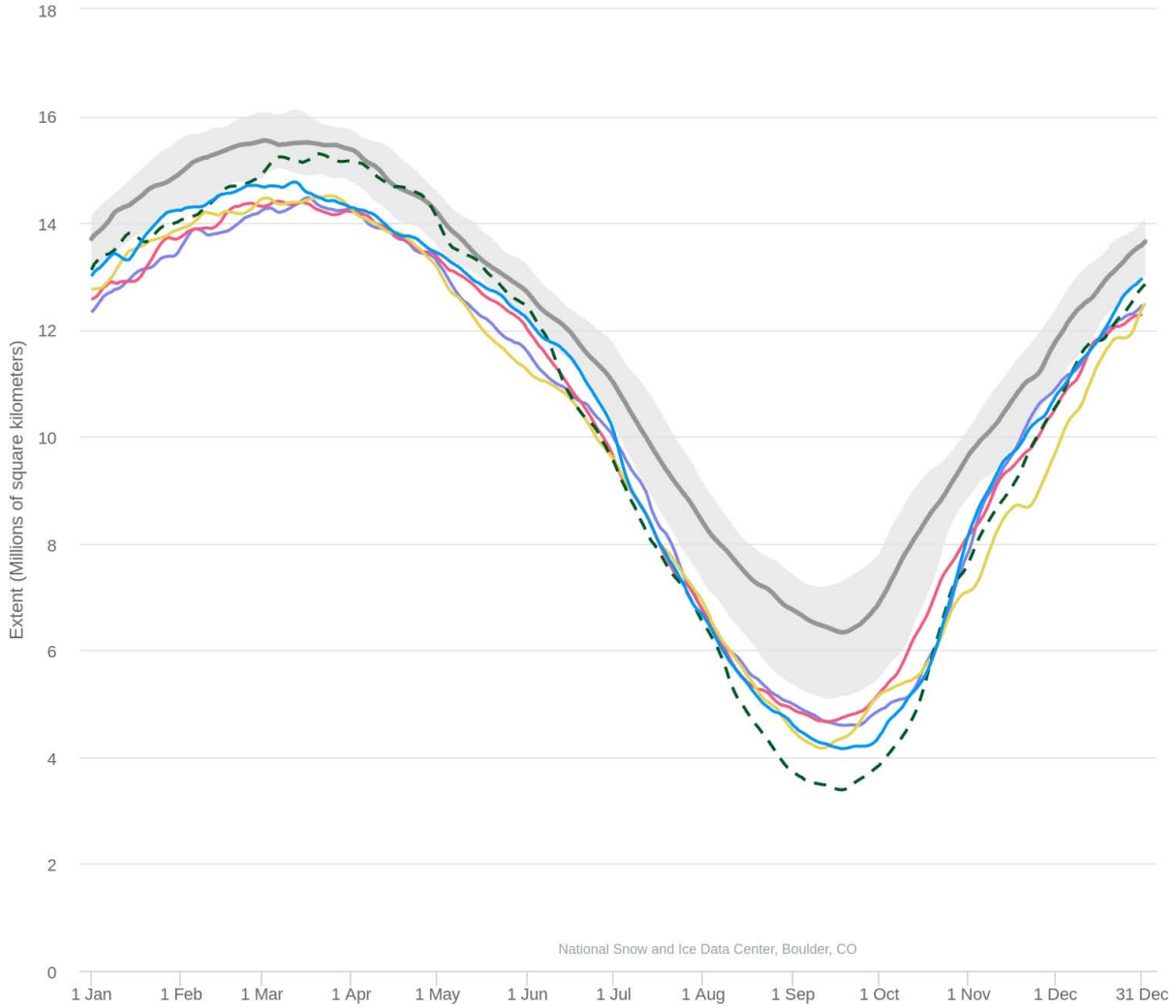

Figure 2.5: Monthly Arctic sea ice extent, median for the period 1979–2018 (grey curve) with interdecile range (grey shaded area). For comparison, averages from 2007 (blue), 2012 (dashed), 2016 (yellow), 2017 (red) and 2018 (purple) are shown. Credit: National Snow and Ice Data Center (NSIDC)

the literature showing similar trends [Renner et al., 2014; Krumpen et al., 2016].

While in-situ and airborne measurements provide reliable thickness estimates, they are limited in spatial and temporal coverage. Laxon et al. [2003] showed the first Arctic sea ice thickness map from satellite altimetry covering up to 81.5°N. The basic theory behind altimetry, the focus of this study, and its use in the estimation of sea ice thickness will be covered in chapters 3 and 4, respectively. Using radar altimetry data Laxon et al. [2003] revealed a high-frequency interannual variability in the mean Arctic ice thickness between 1993 and 2001. Kwok et al. [2009] used 5 years of laser altimetry data to find a remarkable thinning of ∼0.6 m in MYI over the period 2003–2008, along with a more than 42% decrease in MYI coverage since 2005.

Sea ice thinning can occur for different reasons, where surface and bottom melt can be linked to higher air temperatures and to the advection of warm water into the Arctic, respectively. The thinning found by Laxon et al. [2003] is suggested to be linked mainly to changes in the amount of summer melt. Wadhams [1997] found a linear relationship between melt rate and sea ice thinning, where bottom melt is the main factor causing the thinning. Changes in circulation can increase the transport of MYI out of the Arctic basin (section 2.1.2) and start a feedback

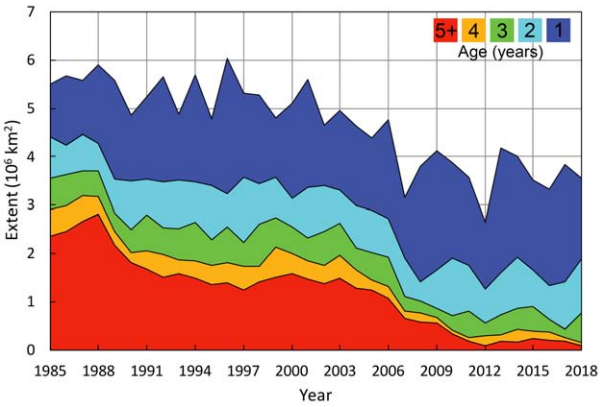

Figure 2.6: Time series of the age of multi-year ice at the end of each summer melt season since 1985. Credit: M. Tschudi, S. Stewart, University of Colorado, Boulder, and W. Meier, J. Stroeve, NSIDC

mechanism resulting in an overall thinner ice cover. FYI melts more easily than MYI, increasing the summer open water extent. This allows for an increased absorption of solar radiation which melts the ice, warms the water and promotes creation of thinner FYI [Lindsay & Zhang, 2005]. Stroeve et al. [2012] observed an increased variability in sea ice thickness after 1990, which might be coupled to changes in the MYI and FYI fractional coverage during spring, also reported by Nghiem et al. [2007]. This is linked with a strong positive AO index favouring the transport of thick sea ice out of the Arctic basin which is substituted by younger and thinner ice.

Another way to assess the thickness of the ice, at least in a qualitative sense, is by looking at the sea ice age, where older ice is generally thicker than younger ice. Figure 2.6 shows that, over the satellite record, there has been a significant decline in coverage of the oldest, thickest ice.

2.4 Snow loading

Snow is one of the most reflective and insulative natural materials on Earth [Webster et al., 2018]. It is thus an integral part of the sea ice and climate system. Knowledge of snow depth is also required to estimate sea ice thickness using freeboard measurements made with satellite altimeters (see chapter 4).

The general thinning of the Arctic sea ice discussed in section 2.3 is likely coupled with the negative trends in snow depth found over the last half-century by Warren et al. [1999]; Webster et al. [2014]. Such trend, together with the thinning snow cover simulated by various models [Hezel et al., 2012; Blanchard-Wrigglesworth et al., 2018], point to a clear and unidirectional response of the snow cover to Arctic sea ice loss: summer ice loss increases solar absorption and warming in the upper ocean [Perovich et al., 2007]. This delays sea ice formation in the autumn and reduces the total snow accumulation, as snow does not accumulate on the ocean surface. A thinner snow cover exposes sea ice to solar radiation earlier the following spring, which contributes to the positive albedo feedback mechanism by decreasing the surface albedo [Holland & Landrum, 2015]. Consequently, the enhanced sea ice loss and ocean warming further delay sea ice formation in the subsequent autumn, which further reduces snow accumulation.

The Arctic snow cover has a high spatial variability. Large scale variability in snow depth is mainly dependent on sea ice type and thickness. While the thick MYI carries the full seasonal snow load, FYI has only a fraction of it, depending on the time at which the growth started. Locally, the snow cover shows a large spatial variability as it is affected by winds and topography, making snow on sea ice processes very complicated [Webster et al., 2018].

Currently, accurate pan-Arctic observations of the snow depth on sea ice are lacking. Valuable in-situ measurements have been collected throughout the years in various regions of the Arctic. However, measurement campaigns have been sparse in both temporal and spatial coverage and do not provide a complete picture of the Arctic snow cover, especially in terms of its interannual variability.

Airborne radar measurements of snow depth have been collected by the NASA Operation IceBridge team since 2009 every year in March and April. This dataset complements in situ measurements and it has been used to validate both models and snow estimation from satellite. Despite being extremely useful, Operation IceBridge measurements do not cover in general the Eurasian basin.

The most used snow depth estimates in Arctic-wide sea ice freeboard and thickness retrieval come from the climatology developed by Warren et al. [1999] (W99), based on measurements performed mainly in the central Arctic, at Soviet drifting stations in the period 1954–91. Although being an old climatology, a good agreement with modern airborne and in situ measurements of snow depth on multi-year sea ice has been shown by recent studies [Kurtz & Farrell, 2011; Newman et al., 2014; Haas et al., 2017]. On the other hand, the W99 climatology is less consistent with recent measurements of snow depth on FYI, as some of the regions now covered by FYI were dominated by MYI during the 37 years of measurements used by the W99 climatology [Newman et al., 2014]. To account for that, it has been shown that by scaling down the snow load provided by the W99 climatology on FYI [Kurtz & Farrell, 2011], radar estimates of sea ice thickness are more consistent with airborne validation data [Laxon et al., 2013; Kwok & Cunningham, 2015]. Despite the good results obtained with this configuration, a more updated and consistent knowledge of the snow on sea ice is needed, as the W99 climatology does not provide any information on the interannual variability of the snow cover.

Recently, dual-frequency radar altimetry has been used to estimate snow depth on Arctic sea ice from satellites [Guerreiro et al., 2016; Lawrence et al., 2018]. This method has shown a good potential, with root-mean-square errors of 5–7 cm when compared to airborne snow radar measurements from Operation IceBridge. However, the coverage of these products cannot reach further than 81.5°N, limited by the orbit inclination of one of the spacecraft. This area might be extended to 88°N with the NASA ICESat-2 mission (section 3.1), launched in September 2018. The potential for Arctic snow depth estimation using ICESat-2 and CryoSat-2 data is explored by Kwok & Markus [2017].

Chapter 3

Satellite altimetry and CryoSat-2

This chapter provides the background knowledge about satellite altimetry necessary to understand the work carried out during the PhD project. Section 3.1 briefly describes past and current satellite missions, putting into perspective CryoSat-2, the mission providing most of the data used in this study which is introduced in section 3.2. Section 3.3 provides the basic theory of altimetry systems, while section 3.4 describes the geophysical corrections applied to satellite altimetry measurements so as to obtain accurate height estimates.

3.1 Satellite altimetry missions

This section describes some of satellite altimetry missions that have mapped, or are currently mapping, the Arctic Ocean and have been used to estimate sea ice thickness. This list should not be considered exhaustive, especially with regard to altimetry missions sensing the land and the oceans at latitudes lower than 60°N.

3.1.1 Past missions

The first Arctic sea ice thickness map from satellite altimetry was shown by Laxon et al. [2003] using data from the European Remote Sensing satellites ERS-1 and ERS-2. These missions, covering up to 81.5° N/S [ESA, 2000, 2011], operated between 1991-2000 and 1995-2011 respectively and were equipped with a K_u-band (13.8 GHz) Radar Altimeter (RA).

In 2002 the European Space Agency (ESA) launched Envisat, a spacecraft which carried on board an improved radar altimeter (RA-2, 13.575 GHz) [ESA, 2012] with a nominal footprint of 2-10 km [Connor et al., 2009]. This mission covered the same area as ERS-1 and ERS-2, however, with a better accuracy of the height estimates [Rose, 2013] providing a valuable dataset for sea ice thickness studies [Giles et al., 2008; Connor et al., 2009]. In 2012 ESA suddenly lost contact with the spacecraft.

The Ice, Cloud, and Land Elevation Satellite (ICESat) was a NASA's laser altimetry mission dedicated to measure ice sheet mass balance, cloud and aerosol heights, as well as land topography and vegetation characteristics. It operated between 2003 and 2010 contributing, with an increased coverage up to 86° N/S and a ground footprint of only 65 m [Schutz et al., 2005], to advancing our knowledge of the Earth's sea ice cover and the entire cryosphere. Examples of sea-ice-related studies based on ICESat measurements are Kwok [2004]; Forsberg & Skourup [2005]; Kwok et al. [2007]; Zwally et al. [2008]; Farrell et al. [2009]; Connor et al. [2013]

3.1.2 Current missions

There are currently several altimetry missions observing the poles of our planet. CryoSat-2, launched in 2010, is the focus of this study and will be described in more details in section 3.2.

The Indian Space Research Organization (ISRO) and the French National Space Agency (CNES) joined forces to design the SARAL mission, launched in February 2013. This spacecraft, covering up to 81.5° N/S carries the AltiKa instrument, a K_a-band (35.75 GHz) altimeter [CNES, 2013] with a pulse-limited ground resolution of 1.4 km [Guerreiro et al., 2016]. The higher frequency of AltiKa has been used to assess the potential of estimating snow depth on Arctic sea ice from dual frequency altimetry [Guerreiro et al., 2016; Lawrence et al., 2018] as well as to assess the signal penetration into the snowpack at K_u- and K_a-bands [Armitage & Ridout, 2015].

In February 2016, as a part of the Copernicus programme, ESA and the European Union launched the first satellite of the tandem mission Sentinel-3, dedicated to monitoring and operational oceanography. The constellation was completed in April 2018 with the launch of Sentinel-3B. The two spacecraft, also measuring regions up to 81.5° N/S, have been equipped with the SAR ALtimeter (SRAL) operating at K_u- and C-band (13.575/5.41 GHz). While the C-band is used to correct range delay errors due to the varying density of electrons in the ionosphere, the K_u-band is the main frequency for altimetry range measurements [ESA, 2016]. At this frequency, the ground footprint is approximately 1600 m in the across-track direction and, thanks to on-ground SAR processing (see section 3.2), only 300 m in the along-track direction.

Finally, NASA's ICESat-2 was launched in September 2018. This spacecraft carries a photon-counting laser altimeter that will allow scientists to measure, with unprecedented detail, the elevation of ice sheets, glaciers and sea ice [Markus et al., 2017]. Although the data are not available to the public yet, first results on sea ice presented at the AGU Fall Meeting 2018 by NASA/JPL scientists look very promising.

3.2 CryoSat-2

CryoSat-2 is an ESA satellite radar altimetry mission launched on April 8, 2010. Its objective is to determine the global variations in the thickness of both continental ice sheets and sea ice [ESA, 2015]. For the last nine years, this satellite has made a great contribution to the precise monitoring of Earth's cryosphere, surpassing its design specifications [Parrinello et al., 2018], as well as to the study of sea level, coastal areas, marine gravity and inland waters. CryoSat-2 has now long exceeded the originally planned 3 years in orbit and, with both the space and ground segment in an excellent state, the mission is fit to continue the exploitation phase until the middle of the next decade [Parrinello et al., 2018].

CryoSat-2, hereinafter CryoSat (CS), has been revolutionary compared to previous missions in at least two ways. With its non-sun-synchronous orbit having an inclination of 92°, CS has been the first altimetry mission able to observe our planet up to 88° N/S – latitudes reached only recently by NASA's ICESat-2 – covering more than 4.6 million km^2 of unexplored areas over the poles [Parrinello et al., 2018]. Its drifting orbit has a quasi repeat cycle of 369 days (30 days sub-cycle) and offers a high-density coverage at the poles, while still collecting sufficient measurements down to the South of Greenland [Parrinello et al., 2018].

CS is equipped with the K_u-band SAR Interferometric Radar ALtimeter (SIRAL) which can operate in three different acquisition modes, depending on the observed geographical area (figure 3.1): the Low Resolution Mode (LRM), the Synthetic Aperture Radar mode (SAR) and the SAR Interferometric mode (SARIn).

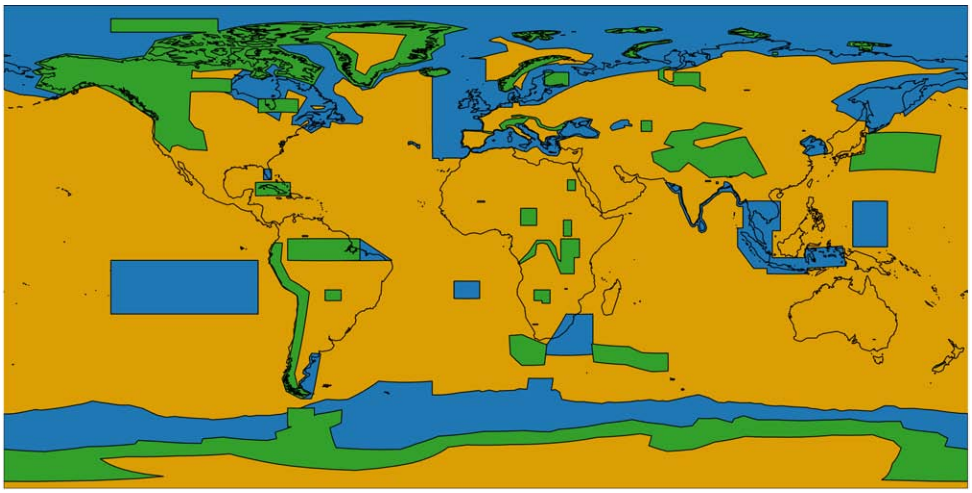

Figure 3.1: CryoSat-2 mode mask version 3.4, valid from October 2012 to July 2014, showing regions where SIRAL operates in LRM (yellow), SAR (blue) and SARIn (green) mode

Low Resolution Mode

The Low Resolution Mode (LRM) is used mainly over land, ocean and ice sheet interiors. When in this mode, CS operates as a conventional pulse-limited radar altimeter. This means that the area illuminated on the ground around the point of closest approach (POCA) depends exclusively on the height of the satellite (H) and on the compressed pulse length (B). The radius of the illuminated area is defined as

$$r = \sqrt{H\frac{c}{B}} \tag{3.1}$$

where c is the speed of light in vacuum. Using the parameters in table 3.1, the CS pulse-limited illuminated area (left-hand side of figure 3.2) is about 2.15 km^2, corresponding to an area which is ∼1.65 km wide in both the along- and across-track directions [ESA, 2015].

Synthetic Aperture Radar mode

The Synthetic Aperture Radar (SAR) mode is used mainly over flat areas of sea ice and some ice sheets. In this mode, SIRAL sends a burst of pulses (right-hand side of figure 3.2) and, by exploiting their coherence, the along-track resolution is improved performing Delay/Doppler processing on-ground [Raney, 1998]. Since the band of Doppler frequencies that is unambiguously sampled by the pulse repetition frequency (PRF) goes from $-PRF/2$ to $PRF/2$, and 64 different sharpened beams are equally spaced in the Doppler domain, the width of the sharpened beam-limited area results in

$$\Delta x = H\frac{\lambda_0}{2v}\frac{PRF}{64} \tag{3.2}$$

where the carrier frequency f_0 defines $\lambda_0 = 1/f_0$, the carrier wavelength. v is the spacecraft velocity [ESA, 2015]. By substituting the values from table 3.1 in equation 3.2, the CS pulse-Doppler-limited area can be approximated by a 0.5 km^2 rectangle (figure 3.2), defined in the across-track direction as the pulse-limited width (∼1.65 km) and as the sharpened beam-limited area width in the along-track direction (∼305 m) [ESA, 2015]. The resulting enhanced along-track resolution enables the measurement of floating sea ice as well as the indirect estimation of sea ice thickness, due to the better sampling of small sea ice floes as well as narrow leads.

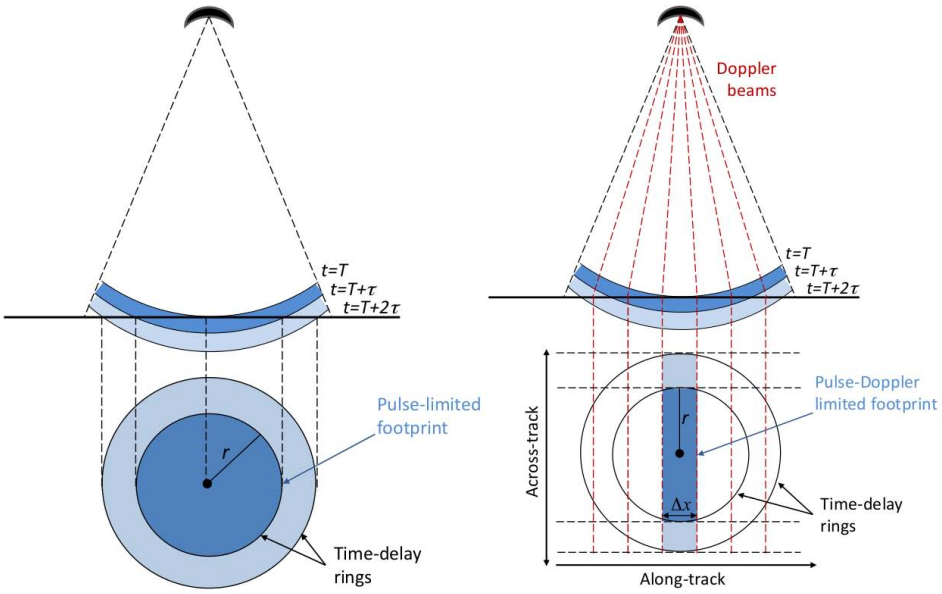

Figure 3.2: Pulse-limited footprint for LRM (left) and Pulse-Doppler-limited footprint for SAR and SARIn modes. Credit: [ESA, 2015]

This mode additionally enables to reduce the random noise on measurements, i.e. the speckle noise, using a technique known as multilooking. In fact, the aforementioned series of bursts is sent so that the associated illuminated areas on the ground overlap when the satellite moves, as shown in figure 3.3. In this way, the measurement of a specific location is the average of a stack of waveforms representing "looks" from different angles.

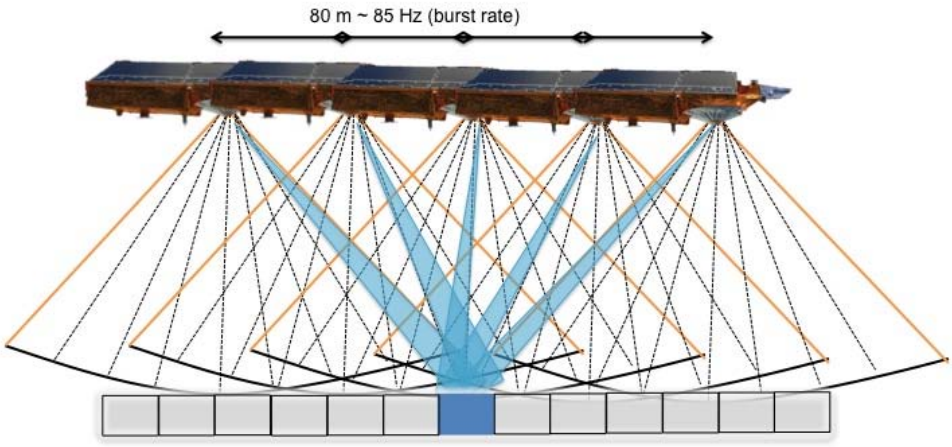

Figure 3.3: Geometry of measurement for five consecutive bursts for the CryoSat-2 SAR and SARIn modes. The blue rectangle represents a multilooked Doppler cell. Credit: [ESA, 2015]

SAR Interferometric mode

The SAR Interferometric (SARIn) mode is used around the ice sheet margins and over mountain glaciers, where the terrain is sloping and thus contributing to large measurement errors in conventional altimetry. When operating in this mode, SAR processing is combined with across-track interferometry exploiting the echoes received by a second across-track antenna mounted approximately 1 m apart. This functionality allows SIRAL to determine the angle to the POCA, and thus the across-track point where the echo originated, enabling the study of areas with a complex topography. The illuminated area for this operational mode is the same as for SAR. More details about this mode are provided in the next chapters as the exploitation of this mode frames the work of this thesis.

In the Arctic Ocean, SIRAL operates most of the time in SAR mode. However, a small region between 80-85°N and 100–140°W (figure 3.1) was selected to test the SARIn capabilities over sea ice [Armitage & Davidson, 2014]. This area is known as the Wingham box, after the British scientist who firstly proposed the CS mission to ESA, and it has been active since CS launch in 2010 until October 2014. Post October 2014, SIRAL has acquired data in SAR mode also in the Wingham box. This study uses data acquired from CS in the SAR and SARIn modes. More details about the satellite mission and these two acquisition modes can be found in table 3.1.

Figure 3.4: Artistic representation of CryoSat-2 in orbit. Credit: ESA

3.3 The Principle of Altimetry

Altimeters are nadir-pointing instruments that emit an electromagnetic wave and measure the echo reflected by the surface. They can be flown on aircraft to cover extended areas as well as on satellites to obtain measurements at a global scale. Altimeters indirectly measure the distance, or range, between the point where the wave is generated and a reflecting surface or object on the ground. This is done in principle by measuring the time (t) between the moment when the electromagnetic pulse is transmitted and when the reflection is received back, i.e. the two-way travel time. Assuming propagation in vacuum, the range (R_0) can be computed as

$$R_0 = \frac{ct}{2} \tag{3.3}$$

Parameter	Symbol	Value (SAR/SARIn)
Mean altitude	H	725 km
Geometric factor	η	1.113
Satellite velocity	v	7435 ms^{-1}
Carrier frequency	f_0	13.575 GHz
Receive bandwidth	B	320 MHz
Pulse Repetition Frequency	PRF	18.182 kHz
Burst Repetition Frequency	BRF	85.7 Hz / 21.4 Hz

Table 3.1: Operating parameters of CryoSat-2 as in Galin et al. [2013] and Wingham et al. [2006]

In order to obtain accurate range measurements, the preliminary range R_0 needs to be corrected for a variety of factors and effects [Vignudelli et al., 2011]. The most important can be grouped into three categories, namely instrument, atmospheric and tidal corrections.

Instrument corrections take care of the non-random part of the measurement error associated to the instrument. They are derived from characterisation and ground calibration data as well as from periodic on-board calibrations and can correct e.g. for bias and drift errors [ESA, 2015]. Atmospheric and tidal corrections (section 3.4) are applied to altimetry measurements to account for the interaction of the electromagnetic wave with certain layers of the atmosphere and to correct for tidal effects, respectively. The corrected range (R) is obtained by adding these corrections (R_i) to the preliminary range

$$R = R_0 + \sum_i R_i \tag{3.4}$$

It is worth noticing that the sign in equation 3.4 changes between satellite products and, sometimes, might even differ between the type of correction. An example is the Operation IceBridge IDCSI4 product [Kurtz et al., 2015], where atmospheric and tidal corrections need to be applied with opposite signs [Harbeck, personal communication]. The height of the sensed surface (h) can finally be computed as

$$h = H - R \tag{3.5}$$

where H is the altitude of the platform carrying the altimeter. In airborne altimetry this altitude is determined using the Global Positioning System (GPS). This system is sometimes also used for satellites, in combination with other solutions. CS, for instance, relies on the Doppler Orbitography and Radiopositioning Integrated by Satellite (DORIS) tracking system, which detects and measures the Doppler shift on signals broadcast from a network of over 50 radio beacons around the world [ESA, 2015]. These signals are used for the Precise Orbit Determination (POD) which allows to reach an accuracy of ∼6 cm [Wingham et al., 2006] in the radial direction. Such a small error is essential to accurately measure the height of the ice surface.

All elevations are measured with respect to a specific surface. Typical reference surfaces are e.g. the geoid and the reference ellipsoid (figure 3.5). The geoid is an equipotential surface which approximates the mean sea level surface if only gravitational and centrifugal forces were acting on the oceans. Thus, the distribution of masses inside the Earth determines the spatial variations of the geoid. The reference ellipsoid is a mathematically defined surface which approximates the

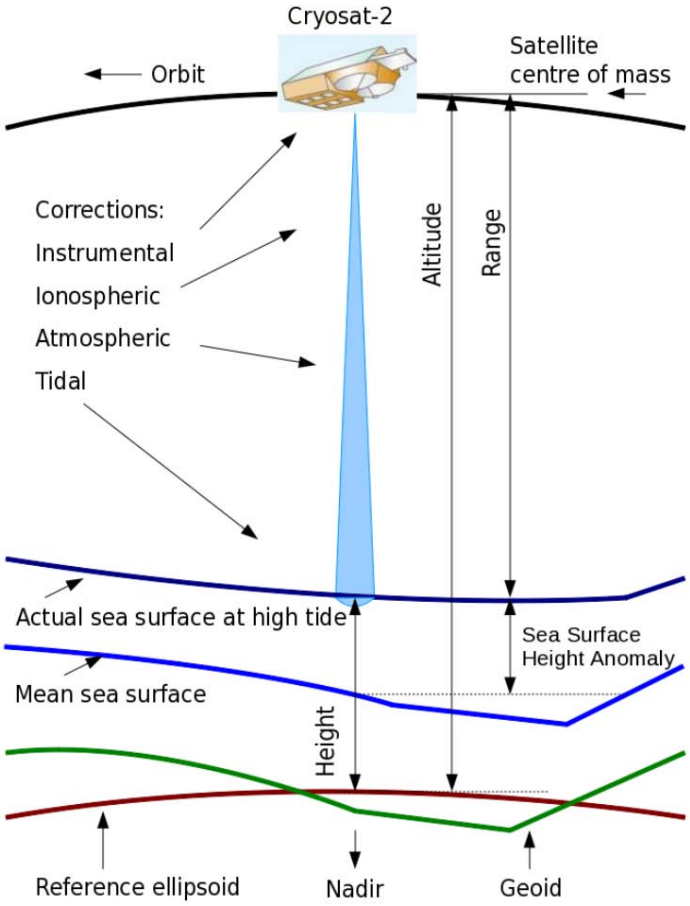

Figure 3.5: Basic altimetry terms and applicable corrections over open ocean for satellite altimetry. Credit: [ESA, 2015]

geoid. There exist several different reference ellipsoids [Hofmann-Wellenhof & Moritz, 2006] and in this study all elevations are referenced to the World Geodetic System 1984 (WGS84).

A summary of the basic altimetry terms and corrections over open ocean is shown in figure 3.5. Although the drawing refers to satellite altimetry, the same terminology is applicable to airborne altimetry, the only difference being that the ionospheric and atmospheric corrections in the figure should not be applied to the latter.

3.3.1 Waveforms and retracking

In altimetry the range to an object or surface on the ground, R in equation 3.3, is determined from the reflected echo received at the satellite antenna, the so-called waveform. The shape of the waveform strongly depends on the reflecting surface. In order to understand how this echo is formed, figure 3.6 shows the temporal evolution of a radar pulse over a flat and horizontal diffuse scattering surface, like the ocean. The figure refers to the case in which a conventional radar is used, which is valid for CS when operating in the LRM acquisition mode.

The pulse transmitted by the altimeter propagates with a spherical front which intercepts the surface at nadir at the time $T0$. In this moment, a fraction of the transmitted power is reflected back to the satellite marking the beginning of the leading edge. The samples on the leading edge generate from reflections coming from points close to the satellite nadir and can be associated with the fast increase of the illuminated area with time, defining the ground

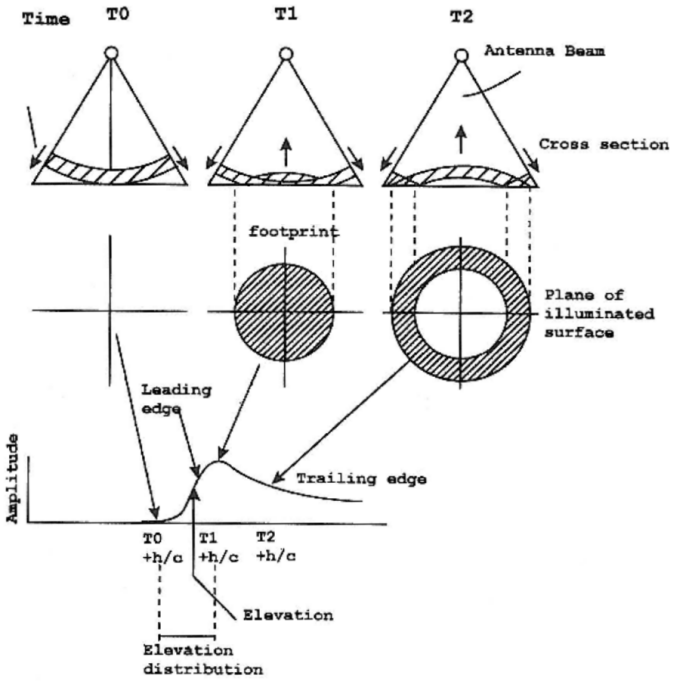

Figure 3.6: The development of a radar pulse over a planar and horizontal ocean surface. Modified from [Ridley & Partington, 1988]

footprint. At the time $T1$ the back of the pulse also intercepts the surface and the illuminated area reaches its maximum together with the received power. After the intersection of the entire pulse, the illuminated area grows into an expanding ring, so that the samples on the trailing edge correspond to echoes generated from points increasingly further away from nadir. The decreasing power is not due to a decrease in the illuminated area, which remains constant at its maximum [Robinson, 1985], but to the attenuation coming from the antenna beam pattern. Due to the discrete nature of the received echo, which is sampled by the altimeter, the time on the x axis is expressed in samples which are known as range bins or range gates. Thus, each waveform sample covers a specific range (Δr) and time delay (Δt) which can be computed for CS as $\Delta r = c/4B$ and $\Delta t = 1/2B$ [ESA, 2015]. With a chirp bandwidth $B = 320$ MHz, $\Delta r \approx 23.42$ cm and $\Delta t \approx 1.5625$ ns for both SAR and SARIn modes. These values are valid starting from the Baseline B data release, where oversampling is applied to raw complex SAR and SARIn echoes in the Full Bit Rate (FBR) to level 1b (L1b) processor to avoid aliasing over specular surfaces [ESA, 2015]. However, despite the increased sampling, the range resolution has not changed as it is fixed by the instrument impulse response as $\sim$46.84 cm ($c/2B$).

The altimeter is set to receive echoes only in a specific range window, determined by the on-board tracker system, around the expected surface elevation. Typical autonomous tracking systems can work in open and closed loops. An open-loop tracking system positions the range window using a-priori knowledge from a high-resolution Digital Elevation Model (DEM) stored on board [ESA, 2015]. Errors in the DEM and changes in topography happening at a scale higher than the DEM resolution can cause the altimeter to lose track. On the other hand, in a closed-loop system the range window is positioned based on the on-board near real time analysis of previous waveforms, which increases the chances for the altimeter to maintain the signal inside the range window. For this reason, CS uses a closed-loop tracking system during science acquisitions, which improves performance in coastal regions, sloping ice sheets and sea ice. Since the Baseline C release, CS uses a $\sim$60 m and a $\sim$240 m range window for its SAR and SARIn

mode, respectively. The SARIn range window was chosen to be 4 times larger than the SAR range window to account for the slope variation in ice sheet margins [ESA, 2015].

The on-board tracker centres the range window around the expected surface height and provides the 2-way travel time in equation 3.3 to a reference point, which for CS corresponds to the center of the range window (figure 3.7). However, due to the size of the waveform sample and depending on the surface roughness, the range provided by the on-board tracker can be several metres off. In order to obtain a more accurate range measurement, and thus height estimate, post-processing retracking is necessary. Retracking is, in principle, the procedure through which (1) a point in the range window, most likely to represent the range to the surface, is chosen, the so-called retracking point and (2) the departure of this point from the reference point in the range window is computed. The resulting retracked range (R_r) is obtained as

$$R_r = R + \Delta R_r \tag{3.6}$$

where

$$\Delta R_r = \Delta r(r_r - r_t) \tag{3.7}$$

is the retracking correction. Here, r_r is the range bin of the retracked point and r_t is the range bin which the time provided by the on-board tracker refers to ((a) and (b) in figure 3.7, respectively). Equation 3.5 can be then updated to obtain a more accurate height estimate including both the retracking and the geophysical corrections

$$h = H - (R_0 + \Delta R_r + \Delta R_{corr}) \tag{3.8}$$

The exact retracking point, usually located somewhere on the waveform's leading edge, depends on the kind of retracker used. In the literature, there exist many retracking algorithms and it is beyond the scope of this work to describe all of them. However, an important distinction can be made between physical and empirical retrackers. Physical retrackers try to fit the altimeter waveform with one computed by a physical model. These models take into account e.g. the altimeter impulse response and surface properties to determine the microwave scattering [Brown, 1977]. While being more comprehensive, these retrackers need a great deal of knowledge which is not easily available in sea ice-covered regions, especially considering the large variability of surface types and their associated backscattering properties which can be found within the radar footprint [Kurtz et al., 2014].

Empirical retrackers can be either based on statistical properties or they can try to fit an empirical function to the waveform. An example of the statistical kind is the Offset Center Of Gravity (OCOG) retracker [Wingham et al., 1986], which defines a rectangle around the waveform's center of gravity and calculates the width and amplitude of the waveform. It is a simple and robust solution, easy to implement, and it is still used on board of several satellites.

The threshold retracker used by Davis [1997] identifies the retracking point as the first range bin exceeding a specific percentage of the waveform's maximum power. The algorithm used in this work to retrieve surface elevations is also an empirical threshold retracker although based largely on the one suggested by Ricker et al. [2014], explained in more details in sections 6.2 and 7.2.

The β-retracker [Martin et al., 1983] is an empirical retracker that tries to fit a functional form of the returned power to the waveform. The Ice Altimetry Group at NASA's Goddard Space Flight Center (GSFC) has developed a series of retracking algorithms for ice sheets and sea ice based on this method [Rose, 2013].

Another empirical retracker was recently proposed by Kurtz et al. [2014] which developed a new method to fit CS L1b waveforms using an empirical model, but with physical basis. In their study,

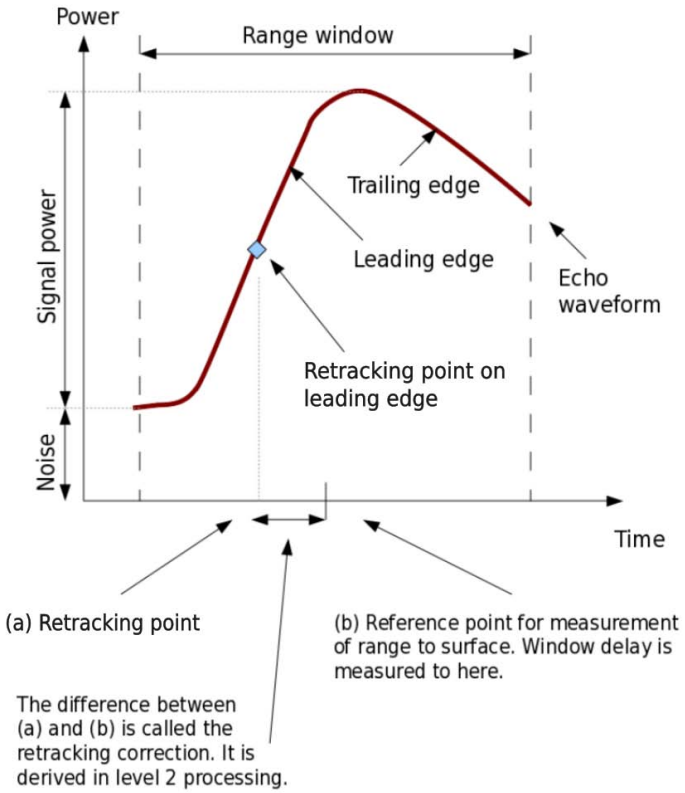

Figure 3.7: Idealised radar altimeter waveform from a diffused scattering surface (e.g. ocean). Modified from [ESA, 2015]

Kurtz et al. [2014] showed that their method can obtain improved results over empirical threshold retrackers suggesting that the waveform-fitting technique is capable of better reconciling the sea ice thickness data record from laser and radar altimetry data sets through the usage of consistent physical assumptions [Kurtz et al., 2014].

3.3.2 Airborne laser altimetry

The concepts presented in the previous sections can in principle be applied also to airborne laser altimetry which is used in this study as a mean of validation. The main difference between radar and laser altimetry is the frequency of the electromagnetic wave transmitted. While radars usually operate in the microwave regime, having carrier frequencies in the order of GHz and wavelengths of a few centimetres, lasers use electromagnetic waves in the visible and near-infrared part of the electromagnetic spectrum with frequencies as high as a few hundreds of THz and wavelengths around the nanometre.

The much higher frequency of lasers leads to a very low beam divergence which, together with the much lower altitude of an aircraft compared to a satellite, result in a very small ground footprint. Typical airborne laser footprints are in the order of metres and, as a consequence, small scale features are better resolved compared with what is possible to achieve with radars on board satellites.

3.4 Geophysical corrections

Geophysical corrections have to be applied to CS range measurements in order to obtain a more accurate height estimate. This section lists the geophysical corrections used in this study together with their source. Only corrections included in the CS product are used in this work and, for each one of them, a typical winter magnitude at 80°N averaged over 1 month and 10^4 km^2 from Wingham et al. [2006] is provided.

3.4.1 Atmospheric corrections

The signal transmitted by the satellite travels several hundreds of kilometres to the ground and back. On its way, it crosses the ionosphere and the troposphere, which refractive indices can change significantly the propagation speed of the signal. Additionally, variations in the sea surface height can be caused by atmospheric pressure and by winds. These corrections are obtained from different sources, mainly from models, and if not applied can cause significant errors on the measured range.

Ionospheric correction

The ionosphere is the part of the atmosphere going from approximately 75 km to 1000 km above the Earth. Being exposed to high energy particles coming from Sun and cosmic rays, this layer is made by ionized gas. For this reason, the Total Electron Content (TEC) in the ionosphere is not only latitude-dependent, but it varies between day and night and, in general, with solar activity. The ionospheric correction available in the CS product is derived from the Global Ionospheric Map (GIM), which uses GPS measurements, as well as from the Bent model. The GIM (`http://iono.jpl.nasa.gov/gim.html`) is the nominal choice with the Bent model (`http://modelweb.gsfc.nasa.gov/ionos/bent.html`) available as an alternative solution if GIM data are not available [ESA, 2015].
This correction ranges between 0.06 m and 0.12 m, with a typical value of 0.015 cm in the Arctic.

Tropospheric correction

The troposphere is the lower part of the atmosphere and it extends from 9 km to 16 km at the poles and the equator, respectively. It consists of a wet and a dry components which have to be modelled independently [Rose, 2013]. Both corrections are provided by Meteo-France based on pressure and temperature grids from the European Centre for Medium-range Weather Forecast (ECMWF).
The wet tropospheric correction accounts for the delay due to liquid water in the atmosphere. It has typically a range of 0 to 0.5 m [ESA, 2015] with a typical value of 0.01 m in the Arctic.
The dry tropospheric correction accounts for the path delay caused by other gases such as oxygen and nitrogen. Ranging from 1.7 m to 2.5 m [ESA, 2015], it has a typical value of 2.3 m at 80°N, being the largest of all the applied geophysical corrections.

Inverse barometric correction

The inverse barometric correction compensates for the atmospheric loading on the oceans, i.e., the variations in sea surface height due to atmospheric pressure variations. This correction, also provided by Meteo-France, has a typical range from -0.15 m to 0.15 m. A representative winter value for the Arctic is 0.03 m.

3.4.2 Tidal corrections

Tidal corrections account for the effects caused by the gravitational attraction of other celestial bodies, both on the oceans and the Earth's crust, as well as for other crust deformations due to the weight of the ocean and to variations in the centrifugal force of our planet. When all the following tidal corrections are applied, CS elevations are put in a tide-free system, i.e. a system in which the permanent tidal deformation is removed from the shape of the Earth.

Ocean tide correction

The ocean tide correction removes the effects of local tides caused by the Moon. This correction is provided by the FES2004 ocean tide model [Lyard et al., 2006] and ranges between -0.5 m and 0.5 m. A typical value for the Arctic Ocean at 80°N is 0.03 m.
Although newer ocean tidal models, with a better resolution, have been proven to perform better in the Arctic [Renganathan, 2010], this study uses the FES2004 correction included in the CS product.

Long-period equilibrium tide correction

The long-period equilibrium tide correction removes tidal effects due to the Sun. The FES2004 ocean tide model also provides an estimate for this correction, ranging between -0.05 m and 0.01 m [Rose, 2013]. A typical value in the Arctic is 0.0075 m.

Ocean loading tide correction

The ocean loading tide correction removes the deformation of the Earth's crust due to the weight of the overlying oceans. This correction, provided by the FES2004 loading tide model, has a typical range from -0.02 m to 0.02 m with an average value of 0.002 m in the Arctic.

Solid Earth tide correction

The solid Earth tide correction removes the deformation of the Earth due to the gravitational attraction of the Sun and the Moon. This correction, typically ranging between -0.3 m and 0.3 m, is computed using the Cartwright Edden Earth tide model [Cartwright & Edden, 1973]. A typical winter magnitude at 80°N is 0.015 m.

Geocentric polar tide correction

The geocentric polar tide correction removes the long-period distortion of the Earth's crust caused by variations in the centrifugal force as the geographic location of the Earth's rotational axis changes. According to [Wahr, 1985], this correction typically ranges from -0.02 m to 0.02 m. An average value for this correction in the Arctic is 0.0025 m.

Chapter 4

Sea ice measurements from satellite radar altimetry

Sea ice thickness cannot be measured directly from satellite radar altimetry, but it can be inferred from the knowledge of the sea ice freeboard, i.e. the height of the ice above the local sea surface. This chapter describes the basic concepts and assumptions used to measure sea ice freeboard from satellite radar altimetry as well as to estimate sea ice thickness. Although this work focuses on the random part of the freeboard and thickness uncertainties, an overview of their total uncertainties is provided. For a recent and more complete analysis of the biases and uncertainties affecting CS sea ice freeboard and thickness estimates, the reader is referred to [Ricker et al., 2014].

4.1 Sea ice freeboard

In remote sensing of the ice-covered oceans, the term freeboard (F) is generally used to describe the height of the surface sensed by the instrument (h) above the local sea surface height (SSH)

$$F = h - SSH \tag{4.1}$$

In the Arctic Ocean, sea ice is usually covered by snow, as shown by the schematic representation in figure 4.1. In this case, it is important to distinguish between the *snow freeboard* (F_s) and the *sea ice freeboard* (F_i) which represent the height above the local sea surface of the air/snow and snow/ice interface, respectively. Assuming a normal incident angle, the penetration depth of an electromagnetic wave into a material depends mainly on the frequency of the transmitted signal, the dielectric constant of the material and its physical structure. Due to the very high frequency of the transmitted pulse, the lasers altimeters used in this study (ALS and ATM, section 5.2) practically do not penetrate the snow cover [Deems et al., 2013] and are used to measure the snow freeboard.

Laboratory measurements showed that radars operating at K_u-band, like SIRAL, can penetrate a layer of cold and dry snow [Beaven et al., 1995]. However, field measurements carried out by Willatt et al. [2010] showed that, in Antarctica, this was the case only where no morphological features or flooding were observed in the snow pack. Willatt et al. [2011] performed a similar analysis on Arctic sea ice showing a strong relationship between penetration depth at K_u-band and snow temperature. With temperatures close to freezing, the main scattering surface appeared to be closer to the snow/ice interface than the air/snow interface in only 25% of the radar returns, as compared to the 80% of the returns at lower temperatures [Willatt et al., 2011]. These considerations lead to the necessity to define the so-called *radar freeboard* (F_r), i.e., the freeboard

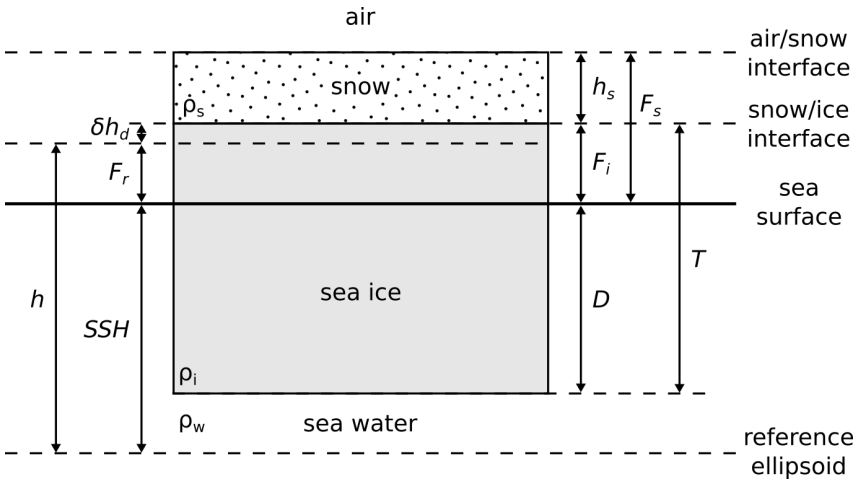

Figure 4.1: Schematic drawing showing the radar (F_r), sea ice (F_i) and snow (F_s) freeboard as well as the sea ice draft (D) and total thickness (T). The radar freeboard is shown considering only the correction for the path delay (δh_s), caused by a layer of snow of depth h_s, assuming the main radar scattering horizon to coincide with the snow/ice interface. The elevation measured by CS (h) and the sea surface height (SSH) are relative to the reference ellipsoid. ρ_s, ρ_i and ρ_w represent the density of snow, sea ice and water, respectively

as measured directly by CS. In this case, the main scattering horizon lies somewhere in between the air/snow and snow/ice interfaces. A snow layer on top of the sea ice has the additional effect of slowing down the signal [Willatt et al., 2010], due to its refractive index being larger than one.

As anticipated in chapter 2, in sea ice-covered regions the local SSH is given by the leads. The sea ice freeboard is measured from satellite altimetry by discriminating between echoes coming from these openings in the ice and those coming from the sea ice itself [Laxon et al., 2003]. The very different roughness and physical structure of these two surfaces determines the shape of the radar altimetry waveforms [Drinkwater, 1991; Laxon, 1994]. Waveforms generating from reflections from leads, quasi-specular surfaces, resemble the impulse response of SIRAL, i.e., they are very "peaky" and have a very high maximum power compared to ocean and sea ice waveforms, which have a more diffusive look (figure 4.2). The accuracy of the SSH estimated from satellite altimetry therefore depends on the amount and geographical distribution of the detected leads. To improve the SSH accuracy, it is common to detrend the retracked elevations using a mean sea surface (MSS) and to use the sea surface anomaly (SSA) instead, to determine the freeboard. In fact, subtracting the MSS from the elevations removes the major component of the height measurement due to the geoid [Skourup et al., 2017] as well as higher frequency variations in the SSH. Since $SSH = MSS + SSA$, the radar freeboard can be determined by subtracting the interpolated SSA from the sea ice elevation anomalies as

$$F_r = h - MSS - SSA \tag{4.2}$$

In this study all elevations are detrended using the DTU18 MSS [Andersen et al., 2017]. The sea ice freeboard can then be estimated from the radar freeboard as

$$F_i = F_r + (\delta h_p + \delta h_d) \tag{4.3}$$

where δh_p is the bias due to scattering from the air/snow interface, related to the aforementioned penetration issue, and δh_d is the bias for the delay due to the lower propagation speed in the snow layer. While the scattering from the air/snow interface always results in a radar freeboard larger than the sea ice freeboard, the reduced propagation speed into snow always displaces the

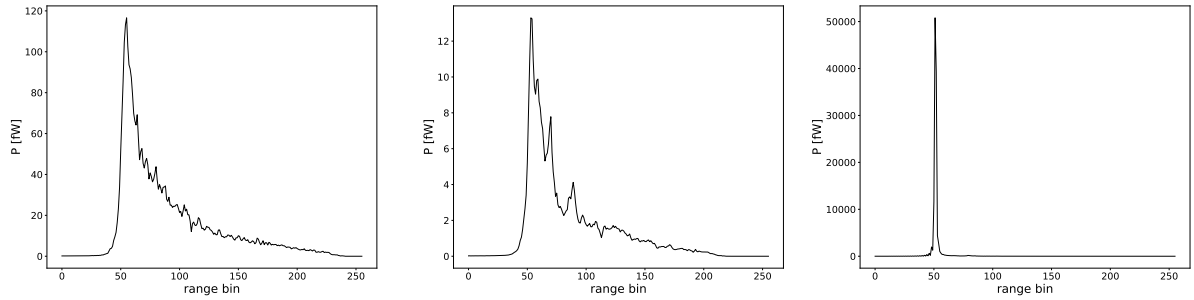

Figure 4.2: Examples of CS SAR waveforms over ocean (a), multi-year sea ice (b) and a lead (c). The maximum power of first-year sea ice waveforms can be up to 10 times larger than the one shown in (b), due to the smoother surface of young ice

main scattering surface away from the radar. Thus, the value of δh_p in equation 4.3 is always negative while that of δh_d is always positive. The effect of these competing corrections has been simulated by Kwok [2014] which concluded that, when these corrections are not applied, the residual error for snow layers thicker than 20 cm might be significant.

Due to the poor knowledge of radar penetration into snow, related to the poor knowledge of the snow properties in the Arctic basin, in this study the basic assumption is that the main scattering horizon for CS coincides with the snow/ice interface, although it is acknowledged that this will introduce a bias in the final freeboard and thickness estimates. Considering only the delay correction

$$F_i \approx F_r + \delta h_d \tag{4.4}$$

The path-delay correction can be estimated as

$$\delta h_d = h_s \left(\frac{c}{c_s} - 1 \right) \tag{4.5}$$

where h_s is the snow depth and

$$c_s = \frac{c}{\sqrt{1 + 1.7\rho_s + 0.7\rho_s^2}} \tag{4.6}$$

is the propagation speed in snow, parametrised following Tiuri et al. [1984] as a function of the snow density (ρ_s) expressed in g/cm^3. Following Kwok & Cunningham [2015], the snow depth and density used in this study are the time- and space-varying estimates from the W99 climatology [Warren et al., 1999]. To account for the reduction of the MYI fraction observed in the last half-century discussed in section 2.4, the W99 snow depth on FYI is halved as suggested in [Kurtz & Farrell, 2011; Laxon et al., 2013].

In the Arctic summer, especially between June and August, surface melt drives the formation of melt ponds on Arctic sea ice. As observed by Armitage et al. [2016], melt ponds are seen by the satellite as specular surfaces and it is hard to distinguish them from leads. Also, the increased snow water content displaces the main scattering horizon for sea ice waveforms towards the air/snow interface. For these reasons in this work, freeboard and thickness are estimated only during autumn and winter months, in the period from October to April.

4.1.1 Sea ice freeboard uncertainty

Assuming the different error sources to be uncorrelated, the uncertainty of a single height estimate over sea ice from CS (σ_h) can be written as

$$\begin{aligned} \sigma_h^2 &= \sigma_H^2 + \sigma_R^2 \\ &\approx \sigma_H^2 + \sigma_{speckle}^2 + \sigma_{corr}^2 + \sigma_s^2 \end{aligned} \tag{4.7}$$

where σ_H is the uncertainty of the satellite altitude and σ_R is the uncertainty in the range measured by the radar. The range uncertainty is equal, to a first approximation, to the sum of the error due to random fluctuations in the incoherent radar echoes [Elachi, 1987], known as speckle noise ($\sigma_{speckle}$), the uncertainty of the atmospheric and tidal corrections applied to the measured range (σ_{corr}) and the uncertainty caused by a snow layer on top of the ice (σ_s). This last contribution includes both the uncertainties in the penetration and the path-delay corrections. It has to be noticed that, in this definition, possible errors coming from the on-board tracking system as well as retracker-dependent errors are neglected.

The contribution of the SIRAL instrument system error to the total elevation estimate has been analysed in details by Wingham et al. [2006], which attributed a 6 cm error arising from orbit determination procedures and a speckle noise of 10 cm and 14 cm for SAR and SARIn "single shot" acquisitions, respectively. The mode-dependent value of speckle noise is due to the lower burst repetition frequency (BRF) of the SARIn mode compared to that of the SAR mode (section 3.2). These two contributions, assumed to be uncorrelated, can be summed in quadrature to obtain the total random height uncertainty for a CS L1b measurement (σ_{L1b})

$$\sigma_{L1b}^2 = \sigma_H^2 + \sigma_{speckle}^2 \tag{4.8}$$

giving a value of 11.6 and 15.2 cm for SAR and SARIn modes, respectively [Wingham et al., 2006].

Since the freeboard is a relative measurement, the uncertainties of the geophysical corrections will tend to cancel each other out. Ricker et al. [2016] analysed the impact of geophysical corrections on sea ice freeboard retrievals from CS, concluding that major parts of the Arctic are not noticeably affected by the corrections being applied or not, with the exception of areas with very low lead density. Here, they find that only the 7.17% and 2.69% of all valid CS freeboard grid cells are affected by the ocean tides and the inverse barometric correction by more than 1 cm, representing by far the major contributions among the impacts of the individual corrections [Ricker et al., 2016]. This shows how the impact of geophysical corrections depends mainly on the performance of the interpolation between subsequent leads, used to retrieve the SSH, and the magnitude of the corrections applied [Ricker et al., 2016]. Thus, the uncertainty due to the geophysical corrections is considered in this work to be minimal and to be accounted for in the estimation of the SSH uncertainty.

According to equation 4.2, the uncertainty of the radar freeboard (σ_{F_r}), where the effect of the snow layer on the ice is not accounted for, is assumed to be governed by the total random height uncertainty and the accuracy of the actual SSA. These two uncertainties are considered to be uncorrelated and can be combined as

$$\sigma_{F_r}^2 = \sigma_{L1b}^2 + \sigma_{SSA}^2 \tag{4.9}$$

where σ_{SSA} is the uncertainty of the SSA. σ_{SSA} generally depends on the amount of detected leads and will be discussed more in details in chapters 6 and 7, since it represents a very important aspect of this work.

The uncertainty of the sea ice freeboard is by definition larger than the uncertainty of the radar freeboard, as it includes also errors connected to the snow loading. Assuming that the radar penetrates completely the snow pack and that all uncertainties are uncorrelated, the sea ice freeboard uncertainty (σ_{F_i}) can be written as

$$\sigma_{F_i}^2 = \sigma_{F_r}^2 + \sigma_{\delta h_d}^2 \tag{4.10}$$

where the uncertainty due to the path-delay correction ($\sigma_{\delta h_d}$) can be computed using Gaussian propagation of the uncertainty (Appendix C) on equation 4.5, resulting in

$$\sigma_{\delta h_d}^2 = \left(\frac{c}{c_s} - 1\right)^2 \sigma_{h_s}^2 + \left(-\frac{h_s c}{c_s^2}\right)^2 \sigma_{c_s}^2 \tag{4.11}$$

While the uncertainty of the snow depth (σ_{h_s}) is provided by the W99 climatology, the uncertainty of the propagation speed in snow (σ_{c_s}) can be determined from equation 4.6 to be

$$\sigma_{c_s} = -\frac{c(14\rho_s + 17)}{20(7/10\rho_s^2 + 17/10\rho_s + 1)^{3/2}} \tag{4.12}$$

As in [Ricker et al., 2014], also in this study the uncertainties of the W99 snow depth and density, due to interannual variabilities, are assumed to be systematic and are not treated as random uncertainties. Therefore, in this work the random part of the uncertainty of the radar and sea ice freeboard is considered to be the same.

If the SSA is estimated using a single lead measurement, $\sigma_{SSA} = \sigma_{L1b}$. Thus, according to equation 4.9 the uncertainty of the radar freeboard on a single CS measurement is bounded by $\sigma_{L1b} < \sigma_{F_r} \leq 2\sigma_{L1b}$ and it could reach values as high as 23 cm for SAR and 30 cm for SARIn. In order to ensure that the contribution to the error in ice freeboard and thickness estimates due to the random noise is lower than the error due to other uncertainties, e.g. snow loading, freeboard estimates are averaged together [Laxon et al., 2013], as the uncertainty will decrease with the square-root of the number of averaged measurements. As a reference, Giles & Hvidegaard [2006] provide a typical uncertainty for the radar-estimated sea ice freeboard of 3 cm, averaging at least 50 individual freeboard estimates. Due to CS 30-days repeat sub-cycle, in this work data are averaged over a month to provide maps with regular spatial coverage over the Arctic. Throughout this study, freeboard estimates are gridded on a 25-km EASE-Grid 2.0 [Brodzik et al., 2012] following the procedure described in Appendix C.

4.2 Sea ice thickness

Analyses of nearly-coincident airborne laser and submarine sonar profiles in the Arctic were used by Comiso et al. [1991] and Wadhams et al. [1992] to conclude that the sea ice thickness can be derived by assuming the sea ice is in hydrostatic equilibrium with the surrounding water. With the bottom of the sea ice not accessible to altimeters, this assumption enables to estimate the sea ice thickness (T) from the sea ice freeboard [Laxon et al., 2003] following

$$T = F_i \frac{\rho_w}{\rho_w - \rho_i} + h_s \frac{\rho_s}{\rho_w - \rho_i} \tag{4.13}$$

where ρ_w and ρ_i are the density of water and sea ice, respectively. During winter, water density can vary between about 1024 and 1027 kg/m^3 [Pavlov, 1998] while ice density can vary significantly depending on the method used to estimate it [Alexandrov et al., 2010]. In general, a main distinction can be made between FYI and MYI, the latter having a lower density due to the inclusion of proportionally less brine and more air in subsequent summers [Kwok & Cunningham,

2015]. In this study a fixed water density of 1025 kg/m^3 and ice densities of 917 and 882 kg/m^3 for FYI and MYI, respectively, are used in the freeboard to thickness conversion. These values are based on in-situ ice and snow data from 689 observation sites, obtained during the Sever expeditions in the 1980s and reported by Alexandrov et al. [2010].

4.2.1 Sea ice thickness uncertainty

In the freeboard-to-thickness conversion the sea ice freeboard and its uncertainty are multiplied by a factor ∼9.6 [Wingham et al., 2006], so that small errors in the estimation of freeboard will lead to large errors in the sea ice thickness. Assuming the various uncertainty contributions to be uncorrelated, they can be combined via Gaussian propagation of the uncertainty to get the total uncertainty of the sea ice thickness (σ_T) as

$$\sigma_T^2 = \left(\frac{\rho_w}{\rho_w - \rho_i}\right)^2 \sigma_{F_i}^2 + \left(\frac{\rho_w F_i + \rho_s h_s}{(\rho_w - \rho_i)^2}\right)^2 \sigma_{\rho_i}^2 + \left(\frac{\rho_s}{\rho_w - \rho_i}\right)^2 \sigma_{h_s}^2 + \left(\frac{h_s}{\rho_w - \rho_i}\right)^2 \sigma_{\rho_s}^2 \qquad (4.14)$$

where the negligible contribution due to variations in sea water density is not included in the estimation [Kurtz et al., 2013]. The uncertainty of the snow density (σ_{ρ_s}) is provided by the W99 climatology, while the uncertainty of the ice density (σ_{ρ_i}) is taken in this study as 35 and 23 kg/m^3 for FYI and MYI, respectively, from [Alexandrov et al., 2010]. Giles et al. [2007] provided a typical error of 46 cm for radar derived sea ice thickness, assuming a 3 cm sea ice freeboard uncertainty from [Giles & Hvidegaard, 2006]. In the same study, Giles et al. [2007] compute values for each of the contributions to the total sea ice thickness uncertainty showing that, while the largest contribution is attributed to the snow depth uncertainty (∼32 cm), sea ice freeboard uncertainty is the second largest contribution (∼28 cm). These results highlight how important it is to achieve more precise freeboard estimates.

As for the sea ice freeboard, the uncertainty contributions due to snow depth and density from Warren 99 are considered to be systematic, so that the random part of the sea ice thickness uncertainty is approximated by the first two terms of equation 4.14. Sea ice thickness estimates are also averaged into a 25-km grid to bring the random uncertainty to reasonable levels.

It is important to remember that, throughout this work, all the uncertainty contributions are assumed to be uncorrelated, although it is acknowledged that the total radar freeboard and thickness uncertainties are an approximation resulting from a lack of knowledge of the covariance of individual error contributions [Ricker et al., 2014].

Chapter 5

Data

In this study, CryoSat-2 data are used to estimate sea ice freeboard and thickness in the Arctic Ocean. In order to validate these results, several other datasets based on airborne and satellite measurements are used. The following sections provide some details about such datasets.

5.1 CryoSat-2

As mentioned in section 3.2, in the Arctic region CryoSat-2 (CS) operates mainly in SAR mode, with the exception of coastal areas where data are acquired in SARIn mode. Until October 2014, the SARIn mode was extended to the Wingham Box (figure 5.1) to test SARIn capabilities.

This work uses both SAR and SARIn 20 Hz level 1b (L1b) waveforms processed with the Baseline C processor, downloaded from ESA CryoSat ftp server (`ftp://science-pds.cryosat.esa.int`). Since the focus of this study is the processing of SARIn waveforms, data acquired before October 2014 are used to assess the potential and limitations of this mode, both in the Wingham box and in coastal areas. For the period Jan–Mar 2014, the results shown in this thesis are based on a reprocessed dataset due to an issue in the Baseline C data, identified during this study, which affected the phase difference of some of the SARIn waveforms [Di Bella et al., 2019]. The Full Bit Rate (FBR) dataset (level 0) was reprocessed by Dr. Scagliola at *Aresys S.r.l.*.

For further information about the data product, the reader is referred to the CryoSat-2 Product Handbook [ESA, 2015] and the Product Format Specification documents available at the CryoSat WiKi page (`https://wiki.services.eoportal.org/tiki-index.php?page=CryoSat%20Wiki`).

5.2 Airborne data

Data collected during airborne campaigns are used as a mean of validation for height, freeboard and thickness estimates. Some of the airborne data used in this work were collected during CS underflights, so as to measure a surface similar to the one seen by the satellite. The processing of this kind of data is explained in more detail in [Di Bella et al., 2018].

5.2.1 ESA CryoVEx

Part of the validation of CS freeboard estimates is performed using data collected during the *CryoSat Validation Experiment* (CryoVEx), a series of campaigns which started in 2003 and is still running in the present (next campaign is planned for Mar–Apr 2019). Born as a joint effort between ESA, DTU Space, the Alfred Wegener Institute (AWI) and other European and

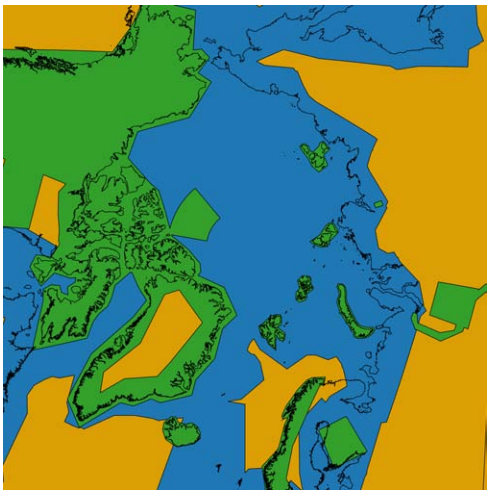

Figure 5.1: CryoSat-2 mode mask version 3.4, same as in figure 3.1, but shown here only for the Arctic region (Arctic Polar Stereographic projection). In blue regions SIRAL operates in SAR mode while the SARIn mode is used in green regions. Yellow regions correspond to areas where SIRAL operates in LRM mode, not relevant in this work

Canadian Institutes, CryoVEx objective was, and is, to provide pre- and post-launch reference datasets for CS over sea- and land ice [Skourup et al., 2012].

Although slightly different every year, these campaigns usually include both work on the ground and the collection of airborne data. The most common aircraft set-up consists of the *Airborne Laser Scanner* (ALS), the *Airborne SAR Interferometric RAdar System* (ASIRAS), an *Airborne ElectroMagnetic induction sounder* (AEM) and a camera to take nadir-looking photos, together with a GPS and an *Inertial Navigation System* (INS) to determine the location and the attitude of the aircraft. In this work, only data from ALS and ASIRAS are used.

The ALS is a conventional airborne laser scanner of type RIEGL LMS-Q240i-60 operating at a wavelength of 904 nm, with a pulse repetition frequency of 10 kHz. The typical resolution of the raw data is approximately 1×1 m in a 300 m wide swath at the nominal flight altitude of 300 m. The vertical accuracy is in the order of 10 cm depending primarily on uncertainties in the kinematic GPS solutions [Skourup et al., 2012]. ALS data were processed at DTU Space to obtain a level 1 product containing the geolocated elevations above the WGS84 reference ellipsoid together with the relative timestamps.

The ASIRAS radar is an airborne version of the SIRAL radar altimeter onboard CS. It operates at K_u-band (13.5 GHz) with a footprint size of 10 m in the across- and 3 m in the along-track directions, when operating in Low Altitude Mode with low resolution (LAMa) at a standard flight height of 300 m [Skourup et al., 2012]. The ASIRAS data used in this study were processed by AWI as part of the ESA CryoVal-SI project to obtain a level 2 product containing the geolocated freeboard heights.

5.2.2 NASA Operation IceBridge

NASA's *Operation IceBridge* (OIB) started in 2009 with the aim to collect airborne remote sensing measurements bridging the gap between NASA's ICESat and ICESat-2 satellite missions. With yearly campaigns carried out every March and April, it is, to date, the largest airborne survey of Earth's polar ice ever flown. OIB aircraft carry on board a series of laser altimeters, radars, gravimeters, magnetometers and cameras to characterise annual changes in thickness of sea ice, glaciers, and ice sheets.

This study uses data from the *IceBridge L4 Sea Ice Freeboard, Snow Depth, and Thickness, Quick Look* product, distributed by NSIDC, as for 2014 the fully consolidated products (IDCSI4, [Kurtz et al., 2015]) are not yet available. As the name suggests, this dataset provides estimates of sea ice freeboard, snow depth and thickness, determined from the *Airborne Topographic Mapper* (ATM), the *Snow Radar* and the *KT-19 radiometer*. All measurements are averaged along track and provided at a ground resolution of 40 m [Kurtz et al., 2015].

ATM is a scanning LIDAR operating at a wavelength of 532 nm, with a pulse repetition frequency of 5 kHz. The nominal across-track resolution is 400 m with an average point density of one laser shot per 10 m^2 [Rose, 2013]. Over sea ice, the elevation accuracy is expected to be better than 10 cm by incorporating measurements from GPS receivers and INS attitude sensors [Farrell et al., 2012a].

The ultra-wideband snow radar was built by the Center for Remote Sensing of Ice Sheets (CReSIS), University of Kansas. It operates over the frequency range from 2 to 8 GHz to map near-surface internal layers in polar firn with a vertical resolution of ∼5 cm [Panzer et al., 2013].

The KT-19 is a radiometer that measures the brightness temperature of the surface beneath the aircraft. Exploiting the different brightness temperatures of ice and water, it can accurately measure the temperature of leads larger than 40 metres [source: NASA].

The Quick Look product relies on the surface temperature from the KT-19 instrument to identify leads, rather than using the DMS and CAMBOT digital imaging systems as described by Onana et al. [2013], as well as the use of near real-time GPS data. For this reason, they have a larger uncertainty than the consolidated product (documentation available via `http://nsidc.org/data/icebridge/evaluation-products.html`).

5.3 SAR images

To assess CS lead detection capabilities, SAR imagery from Envisat and Sentinel-1 satellites are used in this work. The *Wide Swath Mode* (WSM) level 1b products (version 6.02) of the *Advanced Synthetic Aperture Radar* (ASAR) instrument on board of Envisat are available at the ESA Earth Online portal (`https://earth.esa.int/`). In this mode, ASAR has a ground range and azimuth resolution of 150×150 m [ESA, 2007].

Data from the *C-SAR* instrument on board of Sentinel-1 are downloaded from the Copernicus Open Access Hub (`https://scihub.copernicus.eu/dhus`). The Extra Wide swath (EW) imaging mode is used in this study due to its wide coverage and short revisit times. The SAR images in the level 1 Ground Range Detected (GRD) products used in this work cover a 400 km swath at a resolution of 93×87 m in the ground range and azimuth directions, respectively [ESA-MPC, 2016]. The images are geocoded, and sometimes resampled to a lower resolution, using the Geospatial Data Abstraction Library (GDAL).

5.4 OSI SAF

The sea ice concentration and sea ice type information used in this work is provided by the *EUMETSAT Ocean and Sea Ice Satellite Application Facility* (OSI SAF) system. The OSI SAF group is currently formed by Météo-France (MF), as a leading institute, the Danish Meteorological Institute (DMI), the French Research Institute for Exploitation of the Sea (Ifremer), the Royal Netherlands Meteorological Institute and the Norwegian Meteorological Institute (MET Norway).

The sea ice concentration product *OSI-401-b* is produced under the responsibility of MET Norway and DMI and is distributed on a 10 km Polar Stereographic grid. It uses a combination of brightness temperatures from microwave radiometry and numerical weather prediction (NWP)

data from the *European Centre for Medium-Range Weather Forecasts* (ECMWF) [Tonboe et al., 2017]. The algorithm has been implemented so that data from different sensors can be processed. Currently, data from the *Special Sensor Microwave Imager Sounder* (SSMIS) are used, while previous to 19/01/2013 results were based on measurements from the *Special Sensor Microwave/Imager* (SSM/I). For more details about the product and the algorithm, the reader is referred to [Tonboe et al., 2017].

The sea ice type product *OSI-403-c*, also provided on a 10 km Polar Stereographic grid, combines data from passive microwave radiometry from the *Advanced Microwave Scanning Radiometer 2* (AMSR2) (SSIM or SSM/I were used before 2017), the *Advanced SCATterometer* (ASCAT) and ECMWF data for atmospheric corrections. Particularly important are the data from the ASCAT instrument which measures the backscatter and takes advantage of the difference between the relative isotropic behaviour over sea ice and the strong anisotropic behaviour over water. Data are combined using a Bayesian multi-sensor approach. For more details on the subject see [Aaboe et al., 2018].

5.5 Coastline

Filtering measurements acquired on land is an obvious, while important, step in sea ice freeboard and thickness estimation, especially in coastal areas and regions characterised by fjords and small islands. The first part of this study (chapter 6) relies on the surface classification provided in the CS product, which is based on the coastline from the *Global Self-consistent, Hierarchical, High-resolution Geography Database* (GSHHG) [Wessel & Smith, 1996]. This dataset is used by many mapping tools e.g. the *Generic Mapping Tool* (GMT).

As in this study the GSHHG dataset is found to be not accurate in northeastern Greenland (section 7.2.1), the second part of this work, testing CS SARIn capabilities also in coastal areas, performs surface classification using a high-resolution land polygons dataset from the *OpenStreetMapData* project (`http://openstreetmapdata.com/data/land-polygons`). This dataset is derived from OpenStreetMap data (© OpenStreetMap contributors) and available under the Open Data Commons Open Database License (ODbL).

Chapter 6

The DTU Arctic Sea Ice Processor

6.1 Introduction

Reflections from off-nadir leads can dominate the power echo of radar altimetry waveforms, causing the onboard tracker to "snag" and overestimate the two-way travel time used to compute the range to the ground. In common SAR altimetry data processing, these snagged waveforms are usually discarded as it is not possible to correct for the associated range error. The SARIn phase information can, on the other hand, be used to correct for the overestimation of the range and to retrieve a larger number of valid SSH measurements which, as shown by Armitage & Davidson [2014], reduces the area-averaged SSH uncertainty in ice-covered regions. Despite the fact that this could directly reduce the random uncertainty of sea ice freeboard and thickness estimates, no publicly available sea ice freeboard/thickness product makes use of the SARIn phase information. The main objective of this part of the study is to investigate how the phase information provided by the CS SARIn acquisition mode affects Arctic sea ice freeboard and thickness retrievals and their corresponding random uncertainties. To do so, a system capable of processing CS L1b waveforms according to a "regular" SAR processing scheme as well as by using the SARIn phase information is implemented. The regular processing scheme, where the phase information is not exploited, represents the reference case and is used throughout this study. To quantify differences in the uncertainty of freeboard retrievals, this has to be computed using a consistent method between different processors, which is fulfilled by using the reference case described above. Along-track freeboard retrievals are validated using both airborne measurements and satellite SAR images and the implications connected to the use of the SARIn phase information are discussed.

Section 6.2 describes the algorithm and methods developed for the so-called *DTU Arctic Sea Ice Processor* (*DTU ASIP*). The most important results are both presented and discussed in section 6.3 and a summary of the main findings is finally provided in section 6.4.

The content of these chapters has to be considered complementary to the information provided in [Di Bella et al., 2018] and [Di Bella et al., 2019], attached in full length in Appendix A.1 and A.2, respectively. This means that the main focus of the next pages is set on the results obtained after the publication of the manuscripts. Sea ice freeboard and thickness maps additional to the ones shown in this chapter can be found in Appendix D.

6.2 Methods

This chapter aims at describing the data processing chain developed at DTU to process CS Baseline C 20 Hz SAR and SARIn L1b waveforms in the Arctic Ocean. The final product

produced by the software includes point estimates of radar freeboard, sea ice freeboard and sea ice thickness with their respective estimates of random uncertainty. The study carried out by Di Bella et al. [2018] (Appendix A.1) uses the first implementation of the orbit processing algorithm presented in this chapter. Since then, the algorithm has evolved and turned into the DTU ASIP processor, hereinafter just referred to as ASIP. The next sections provide more information about each of the steps performed by ASIP, summarised by the block diagram in figure 6.2. In-depth technical details are provided in this chapter only if not already given by Di Bella et al. [2018] and for procedures not common to regular altimetry processing schemes, which are instead just described in a more general way.

An important difference is made throughout the next sections between the two ASIP processing modes, referred to as *SAR* and *SARIn* processing modes. In the ASIP SAR processing mode all waveforms are treated as SAR echoes, i.e., the phase information available in the SARIn acquisition mode is discarded. On the contrary, the phase of SARIn waveforms is exploited in the ASIP SARIn processing mode (figure 6.1). These two modes correspond to the SIN_0 and SIN cases described in Di Bella et al. [2018].

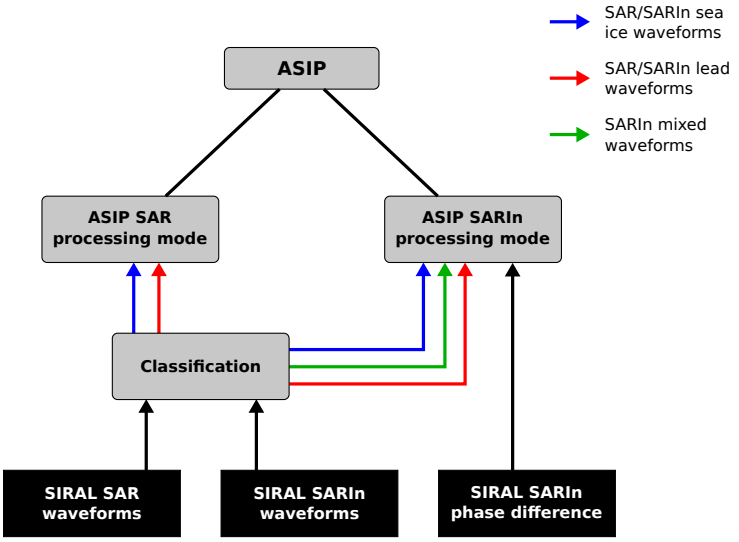

Figure 6.1: The DTU ASIP SAR and SARIn processing modes

6.2.1 Pre-processing

This study deals with data acquired by CS in the Arctic Ocean at latitudes higher than 65°N. The waveform ingestion algorithm takes care of this first rough geographical filtering.
During the pre-processing step, an UTC timestamp is assigned to each waveform and some basics operations are performed, like (1) the *DORIS Ultra Stable Oscillator Drift* (USO Drift) correction is applied to the CS window delay[(1)] [ESA, 2015], (2) the power of the waveforms is converted from counts to Watts [ESA, 2015] and (3) the local bearing from one satellite footprint to the next, i.e. the clockwise angle measured from the North line to the line joining the centres of the two footprints, is computed based on the relations in Williams [2011].
Finally, only for SARIn waveforms, the power is divided by a factor 2[(2)] and faulty coherence values larger than 1 are set to 0.

[(1)] Window delay is the name given to the time measured from the transmission of the pulse to the reception of the ground reflection, referenced to the center of the range window (section 3.3.1)

[(2)] Due to an issue in the Baseline C Instrument Processing Facility L1b (IPF1) used by ESA to compute the L1b waveforms, the power of SARIn waveforms has double its real value. This information, not reported in the

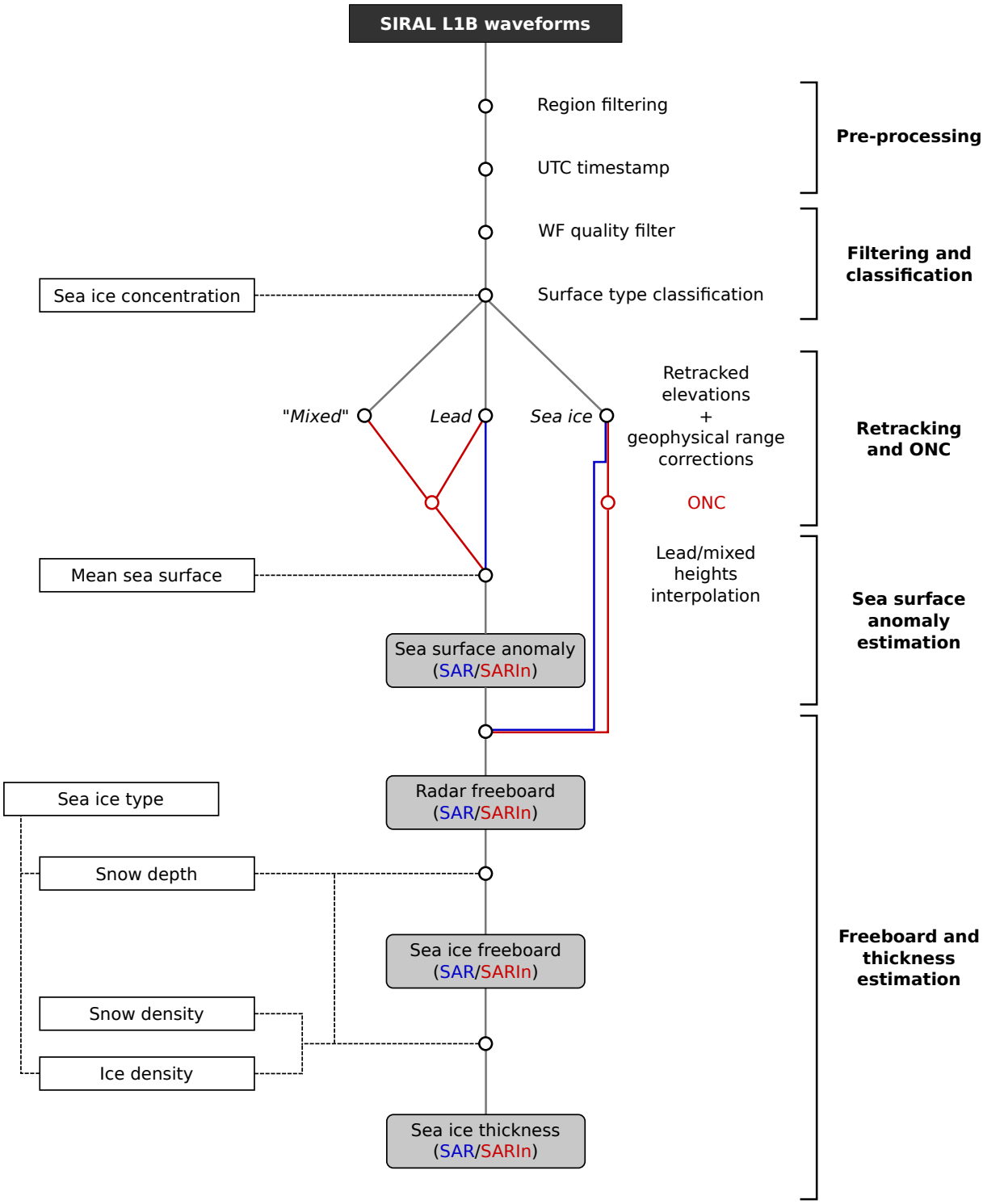

Figure 6.2: Diagram summarising the DTU ASIP freeboard and thickness retrieval algorithm. The blue and the red colours represent the two different processing modes, SAR and $SARIn$. Sections 6.2.1–6.2.5 provide more information about each one of the steps highlighted in bold to the right-hand side of the diagram

official CS documentation, was acquired at the CS Quality Working Group #7 meeting, which took place on 26–28 November 2018 at ESRIN, Frascati, Italy

6.2.2 Filtering and classification

Basic waveform filtering is performed according to the L1b product quality flags as described in ESA [2015]. Surface classification is also carried out using the product flag, where only data acquired over the ocean are selected. The OSI SAF sea ice concentration product is then used to select waveforms contained in grid cells having a sea ice concentration larger than 50%.
Additional filtering is performed using thresholds for the Signal to Noise Ratio (SNR) and the Pulse Peakiness (PP) of the waveforms, as described in Di Bella et al. [2018]. In the ASIP processor the number of range bins used to compute the waveforms' thermal noise is increased from 5 for SARIn only [Di Bella et al., 2018] to 20 for SAR and 80 for SARIn (SARIn waveforms have 4 times the number of range bins compared to SAR, hence the difference). This step is carried out to filter out waveforms too noisy to allow for the identification of a clear leading edge as well as echoes likely coming from the ocean [Di Bella et al., 2018].

Waveform classification is performed as in Armitage & Davidson [2014] using two thresholds for the PP values, namely a *high* ($PP_h = 0.25$) and a *low* ($PP_l = 0.1$, whereas 0.045 is used by Di Bella et al. [2018]) threshold. Waveforms with $PP > PP_h$ present a purely specular feature which can be associated to a reflection coming from a lead relatively close to the satellite nadir. On the other hand, waveforms with $PP < PP_l$ have a purely diffusive look which is the result of the radar signal being reflected by a rough surface, like sea ice. Waveforms with $PP_l < PP < PP_h$ usually present both specular and diffusive features and, in this study, they are referred to as *mixed*. While SAR mixed waveforms are always discarded, SARIn mixed waveforms might be processed.

A first difference between ASIP SAR and SARIn processing modes is based on the way mixed waveforms are treated. In the SAR processing mode, SARIn mixed waveforms are discarded and the phase information provided by the SARIn mode is not used, i.e., all waveforms are processed according to a regular SAR altimetry processing scheme. In the SARIn processing mode, instead, SARIn mixed waveforms with $PP > 0.10$ (differently from $PP > 0.09$ used in Di Bella et al. [2018]) are processed together with their phase information (figure 6.3).

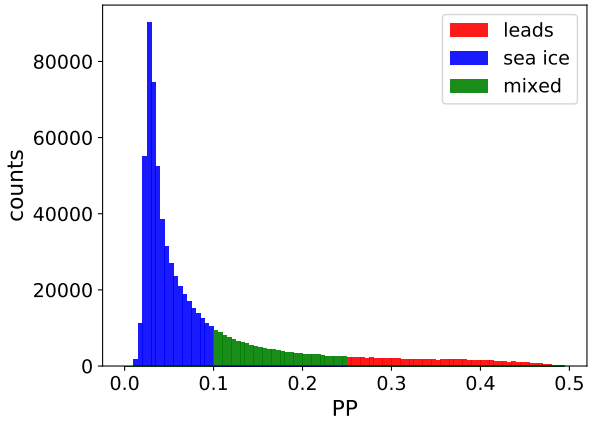

Figure 6.3: Distribution of waveform Pulse Peakiness (PP) for March 2014. In the ASIP SAR processing mode only leads (red) and sea ice (blue) waveforms are processed, while the SARIn processing mode uses also "mixed" echoes (green)

6.2.3 Retracking and Off-Nadir Correction (ONC)

Retracking is performed in the exact same way as described in Di Bella et al. [2018], where a *Threshold First-Maximum Retracker Algorithm* with a 50% peak power threshold (TFMRA50),

based on the retracker used in Ricker et al. [2014], is implemented to retrack sea ice waveforms. An additional power threshold is used so that the power of the first peak is at least 40% of the maximum waveform power. This step is necessary to suppress noisy peaks on the waveform leading edge, characterising especially SARin echoes. A similar retracker is developed in the ASIP processing scheme to retrack the 50% of the maximum waveform power in both leads and mixed waveforms. All elevations are corrected applying the atmospheric and tidal corrections described in section 3.4.

In the SARIn processing mode, ASIP applies a range correction to SARIn elevations to account for the overestimated range caused by SIRAL snagging on echoes coming from off-nadir leads. In fact, as shown by Armitage & Davidson [2014], the strong scattering of leads up to several kilometres from the satellite nadir can dominate the power echo causing the onboard tracker to "snag" and overestimate the two-way travel time (figure 6.4). The interferometric capabilities of CS enable to infer the across-track angle of return to the off-nadir lead (θ) and, thus, to determine its across-track distance from nadir (d) as well as a geometric correction to account for the associated range error. This Off-Nadir range Correction (ONC) can be estimated as

$$ONC = \frac{\eta R_m}{2}\left(\rho^2 - 2\rho\alpha\right) \tag{6.1}$$

where η is a geometric factor used to correct for the curvature of the Earth [Wingham et al., 2004; Galin et al., 2013], R_m is the measured range to the lead and ρ is the angle between the local vertical and the lead direction. The across-track slope β (figure 6.4) is converted to an across-track angle to the POCA through $\alpha = \beta/\eta$ [Armitage & Davidson, 2014]. While in Di Bella et al. [2018] the ONC is applied only to lead and mixed waveforms, i.e. to the specular parts of the echoes, ASIP applies such a correction to sea ice waveforms too. This correction is usually negligible for sea ice as, in the absence of leads inside the SIRAL footprint, the echo received should be dominated by scattering from regions close to the satellite nadir. However, sometimes the roughness distribution at the footprint scale might cause the main scattering to generate from specific areas inside the footprint. In this case, the phase information would improve the elevation accuracy of sea ice too.

To compensate for the larger noise in front of the leading edge of SARIn waveforms, compared to SAR waveforms, a dedicated SARIn elevation filter is developed. Histograms of detrended sea ice elevations are computed for each 25-km segment along track and height estimates more than 30 cm larger than the segment mode are discarded (see section 6.3.3).

The uncertainty of the ONC (σ_{ONC}) is defined in Armitage & Davidson [2014] as

$$\sigma^2_{ONC} \simeq \eta^2 R_m^2 \left(|\rho - \alpha|^2 \sigma_\rho^2 + \rho^2 \sigma_\alpha^2\right) \tag{6.2}$$

where σ_ρ and σ_α are the uncertainties of the angles ρ and α, respectively. While the value of σ_ρ is assumed in this work to be 90 μrad, based on the estimations made by Galin et al. [2013], σ_α depends on the across-track slope β. In their study, Armitage & Davidson [2014] used a geoid to detrend the elevations so that the remaining components of σ_α in their work arise from the local dynamic topography, tidal variations in the SSH and from the method used to interpolate the across-track slope of the geoid. Farrell et al. [2012b] estimate these contributions to be equal to 20 μrad. By subtracting a MSS from the retracked elevations, σ_α would be lower than this estimate, as the mean dynamic topography would also be removed. However, precise estimates of uncertainty for the DTU18 MSS used in this work are not available, so that 20 μrad is also used by ASIP as a value for σ_α.

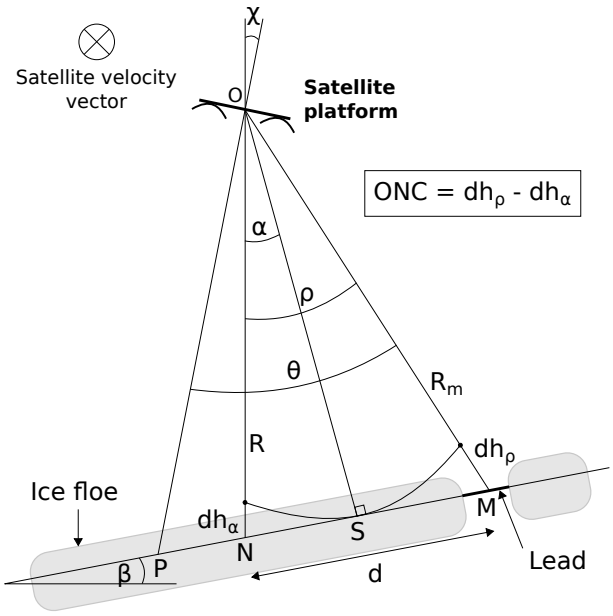

Figure 6.4: Geometry for the off-nadir range correction (ONC), adapted from Armitage & Davidson [2014]. In the drawing, OP is the antenna boresight direction, with χ being the satellite platform roll angle measured from the satellite nadir (N). θ is the angle measured by the interferometer between the antenna boresight direction and the lead (M), and ρ is the angle between the nadir and the lead. R and R_m are the ranges to the nadir and to the lead, respectively, while d is the across-track distance to the lead (NM). β is the across-track surface slope and α the angle between the nadir and the POCA (S). dh_ρ and dh_α are the range errors due to the off-nadir ranging and across-track slope, respectively, and the total range correction is given by $ONC = dh_\rho - dh_\alpha$. In the drawing the satellite velocity vector enters the page

6.2.4 Sea surface anomaly estimation

As already mentioned in section 4.1, all retracked elevations are detrended using the DTU18 MSS (differently from Di Bella et al. [2018], where the DTU15 MSS is used) to improve the accuracy of the local SSH (section 4.1). In the ASIP SAR processing mode, the sea surface anomaly (SSA) at the sea ice locations is obtained by along-track linear interpolation of the detrended lead elevations and by applying a running mean filter with 25-km width to smooth jumps that can occur in dense lead clusters due to the signal noise [Ricker et al., 2014]. The same procedure is applied in the SARIn processing mode, but using the elevations from both leads and mixed echoes. However, only mixed echoes with a retracked elevation within ±15 cm from the SAR SSA, tested on along-track segments of 25 km, are retained (this additional check is not performed in Di Bella et al. [2018]). In segments where the SAR SSA is not available, its along-track mean is used instead. In both processing modes, the value of SSA is set to be invalid at sea ice locations further than 100 km from the closest lead, as interpolation is not considered accurate enough to describe local changes in the SSA at such scales.

The SSA uncertainty (σ_{SSA}) depends on the abundance of detected leads which are needed for an accurate interpolation of the SSA [Ricker et al., 2014]. Thus, in the SAR processing mode σ_{SSA} is determined by taking the standard deviation of the lead heights within the same 25-km moving window used to estimate the SSA [Di Bella et al., 2018]. If only one lead elevation is used, then the uncertainty equals the total random uncertainty of a single CS measurement, σ_{L1b} (section 4.1.1). In the case that no leads are found, σ_{SSA} takes the value of the deviation of the interpolated SSA from the mean CS sea ice elevation inside the moving window [Ricker et al., 2014]. The same approach is used to determine σ_{SSA} in the SARIn processing mode, with

the difference that both lead and mixed echoes are used. Additionally, in the case of a single detected lead inside the moving window, the total SSA uncertainty includes the contribution from the ONC, i.e., $\sigma^2_{SSA} = \sigma^2_{L1b} + \sigma^2_{ONC}$.

6.2.5 Freeboard and thickness estimation

The radar freeboard is estimated by subtracting the local SSA from each sea ice elevation anomaly (equation 4.2). The sea ice freeboard is then obtained by correcting the radar freeboard for the lower propagation speed into the snow pack, using time- and space-varying estimates of snow depth and density from the W99 climatology, in combination with the OSI SAF sea ice type (section 4). In the regional study by Di Bella et al. [2018], an area-averaged snow depth estimate derived from OIB data is used instead.
The random uncertainty of both radar and sea ice freeboard is considered to be the same (section 4.1.1) and equal to $\sigma^2_F = \sigma^2_{L1b} + \sigma^2_{SSA}$, assuming the error contributions to be uncorrelated. Sea ice freeboard estimates outside the interval $-\sigma_F < F_i < 2 \text{ m} + \sigma_F$ are discarded.

Sea ice thickness values are computed from freeboard heights according to equation 4.13, using water (ρ_w) and ice (ρ_i) densities from Alexandrov et al. [2010]. According to section 4.2.1, ASIP computes the random part of the sea ice thickness uncertainty as

$$\sigma^2_T = \left(\frac{\rho_w}{\rho_w - \rho_i}\right)^2 \sigma^2_F + \left(\frac{\rho_w F_i + \rho_s h_s}{(\rho_w - \rho_i)^2}\right)^2 \sigma^2_{\rho_i} \tag{6.3}$$

where h_s and ρ_s are the aforementioned snow depth and density, respectively.

6.3 Results and discussion

In this section, the effect of the phase information on freeboard and thickness retrievals is assessed using the results from the ASIP processor. Focus is put on radar freeboard uncertainty, as systematic uncertainties contributions, e.g. from snow loading, cannot be reduced by this kind of waveform processing. SARIn freeboard estimates are validated in section 6.3.1 using airborne data, while section 6.3.2 summarises the results of an analysis showing large negative freeboard at the boundary of the SARIn acquisition mask. These two sections summarise the results in [Di Bella et al., 2018] and [Di Bella et al., 2019], attached respectively in Appendix A.1 and A.2, where these subjects are discussed in more details. Section 6.3.3 also focuses on the behaviour of freeboard retrievals at the boundary of the SARIn acquisition mask and, finally, differences in the freeboard and thickness uncertainty are discussed in section 6.3.4. Sea ice freeboard and thickness maps for additional months are available in Appendix D.

6.3.1 Airborne validation

Summary of Appendix A.1
Di Bella et al. [2018] analyse sea ice freeboard heights estimated by processing CS SARIn L1b waveforms (SIRAL) inside the Wingham Box (WB), along orbit #10565. The results are validated using measurements from airborne laser (ALS) and radar (ASIRAS) altimetry acquired during the ESA CryoVEx 2012 campaign as well as snow radar measurements from NASA Operation IceBridge 2012. Additionally, the possible reduction in the random freeboard uncertainty is investigated comparing two scenarios, i.e. a SAR-like and a SARIn acquisition (equivalent to the ASIP SAR and SARIn processing modes).

Using spatially coincident SAR imagery from the ASAR instrument onboard Envisat, CS is shown to be able to accurately detect off-nadir leads up to a distance of 2300 m from the satellite

nadir. No spatial correlation is observed at the footprint scale between SIRAL sea ice freeboard and both ALS snow and ASIRAS sea ice freeboard, which is mainly attributed to the different instrument ground footprint size as well as to the difference in the estimated SSAs. Even after the ONC is applied, the SSA in the SARIn processing mode shows some values significantly lower than its along-track mean. A deeper analysis relates these heights with waveforms having a value of PP close to the cutoff threshold of 0.09, suggesting that this threshold might be too low. For this reason, the current version of ASIP uses only lead heights from mixed echoes within ±15 cm from the SSA estimated in the SAR processing mode.

A very good agreement is observed between the along-track mean ASIRAS and SIRAL radar freeboards taking into account the respective uncertainties and the different threshold (40%) used to retrack ASIRAS waveforms. It is observed that including in the SARIn processing mode ∼35% of the waveforms discarded in the SAR processing mode reduces the average random freeboard uncertainty of ∼29%[(3)] without introducing a bias on the average freeboard.

These results set the stage for a more thorough analysis. Di Bella et al. [2018] used only CS SARIn data which are noisier than SAR echoes. While this is taken into account in the contribution to the freeboard uncertainty, using a lower σ_{L1b} for SAR than for SARIn waveforms, the uncertainty of the SSA, determined as the standard deviation of the lead heights, would also be reduced in a real SAR acquisition. Furthermore, these results refer to a single CS track so that, in order to better quantify the possible reduction of the freeboard uncertainty brought by the SARIn phase information, more data, including SAR acquisitions, should be included in the study.

6.3.2 Inaccurate SARIn phase difference: impact on sea ice freeboard retrieval

Summary of Appendix A.2

Based on the results in Di Bella et al. [2018], CS L1b SAR and SARIn waveforms are processed to assess the quality of SARIn sea ice freeboard retrievals in the Arctic. Processing pan-Arctic Baseline C L1b products, exploiting the SARIn phase information, shows large negative freeboard estimates at the boundary of the SARIn acquisition mask. The analysis of CS waveform stacks[(4)] reveals an issue in the first 19 SARIn bursts when entering the SARIn mask, where one of the calibrations is not applied by the ESA's SAR/SARIn IPF1 (the system responsible of computing the L1b waveforms). A patch dealing with this issue, which affects the quality of the phase information of the first ∼40 SARIn waveforms, is developed and 4 months worth of data, for the period January-April 2014, are produced by Dr. Scagliola from ARESYS S.r.l., using the updated IPF1.

Using the reprocessed dataset, an improved quality of the freeboard retrievals at the SARIn boundaries is observed. The negative pattern observed using estimates from the Baseline C products disappears using the updated IPF1 processor, and the negative freeboard heights around the WB are reduced from 17.4% to 0.6% (this low amount is caused by the noise on CS measurements).

This update will be included in the new CS SAR/SARIn IPF1 producing the upcoming Baseline D L1b products. Improvements are expected not only for sea ice freeboard retrieval, but for any application that exploits the phase information in the SARIn L1b products. Areas up to ∼12 km inside the SARIn acquisition mask, corresponding to the maximum along-track distance

(3) The 40% stated in Di Bella et al. [2018] refers to the square of the uncertainty and should be amended with the value provided here

(4) A waveform stack is a set of waveforms before the multilooking procedure is performed (section 3.2), also known as single looks

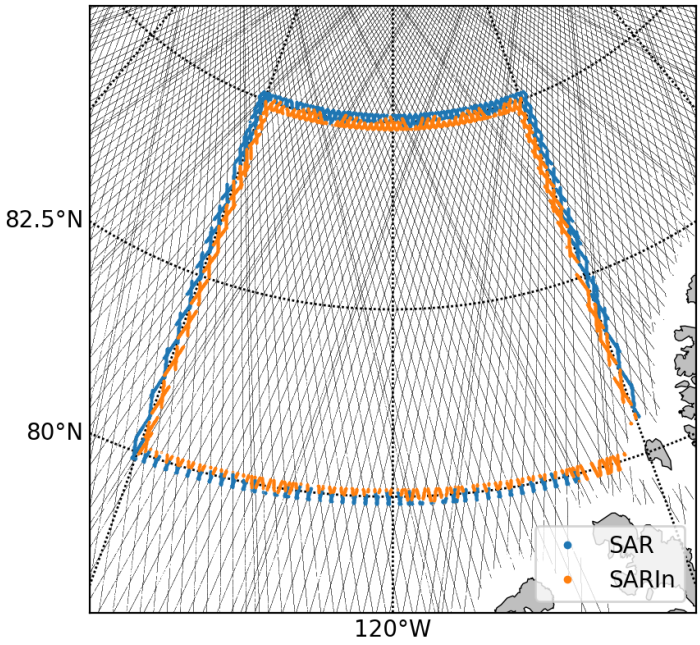

Figure 6.5: Region of interest for the freeboard continuity analysis. The region extends ∼10 km inside and outside of the Wingham Box (80–85°N, 100–140°W). Black lines represent all CS orbits during March 2014, while the blue and the orange dots are respectively the freeboard measurements from SAR and SARIn waveforms used in the analysis

on the ground covered by 40 20 Hz CS waveforms, will benefit from the increased accuracy of the SARIn phase difference. The improvement for inland water monitoring applications will be significant, especially w.r.t. monitoring small water bodies and narrow rivers, where discarding the first ∼40 waveforms might not always be a viable option.

6.3.3 Freeboard continuity between SAR and SARIn areas

This section aims to assess possible differences between the sea ice freeboard computed from SAR and SARIn waveforms, in either cases where the SARIn phase information is or is not used. To do so, CS data from March 2014 are processed with ASIP in both the SAR and SARIn processing modes and freeboard retrievals at the boundary of the WB are analysed. The following results are obtained using the reprocessed dataset mentioned in section 6.3.2.

Average values of sea ice SAR ($\overline{F}_{SAR}$) and SARIn ($\overline{F}_{SARIn}$) freeboard heights are compared in an area extending ∼10 km inside and outside the WB, as shown in figure 6.5. Table 6.1 summarises the results together with the number of valid freeboard measurement for each case. Average freeboards are expressed in centimetres and the first decimal digit, not scientifically significant given the typical magnitude of the freeboard uncertainty of a few centimetres, is retained just to discuss the trend observed in the results.

The average sea ice freeboard should not change significantly at the analysed scales, as confirmed by the results from the ASIP SAR processing mode, where both SAR and SARIn freeboard are estimated as 41.1 cm. On the other hand, when using the phase information in the ASIP SARIn processing mode, the average SAR and SARIn freeboard seem to slightly differ by 1.3 cm. The SAR freeboard is 0.5 cm smaller than in the case where the phase information is discarded, which is attributed to the larger average value of SSA. While in principle the SARIn phase information is not expected to affect results from SAR waveforms, this result is explained

Mode filter applied		
	ASIP SAR	**ASIP SARIn**
$\overline{\mathbf{F}}_{\mathbf{SAR}}$ / $\overline{\mathbf{F}}_{\mathbf{SARIn}}$	41.1 / 41.1	40.6 / 41.9
$\overline{\mathbf{SSA}}_{\mathbf{SAR}}$ / $\overline{\mathbf{SSA}}_{\mathbf{SARIn}}$	20.0 / 20.3	21.5 / 23.6
$\overline{\mathbf{ONC}}_{\mathbf{SAR}}$ / $\overline{\mathbf{ONC}}_{\mathbf{SARIn}}$	0.0 / 0.0	0.0 / 2.7
$\mathbf{N}_{\mathbf{SAR}}$ / $\mathbf{N}_{\mathbf{SARIn}}$	9735 / 7922	11366 / 9991

Table 6.1: Average values of sea ice freeboard (F), sea surface anomaly (SSA) and off-nadir range correction (ONC) computed from the SAR and SARIn waveforms in figure 6.5 by the DTU ASIP SAR and SARIn processing modes for March 2014. The values correspond to the case in which the SARIn sea ice elevation mode filter (section 6.2.3) is applied. The total number of available freeboard estimates (N) is also provided

as follows: As shown by Armitage & Davidson [2014] and Di Bella et al. [2018], applying the ONC to SARIn lead height estimates gives a higher SSA (23.6 vs. 20.3 cm from table 6.1). In areas where SIRAL switches between SAR and SARIn acquisition modes, this difference propagates to the SAR SSA because of the along-track interpolation.

On the other hand, the average freeboard from the ASIP SARIn processing mode is found to be larger than the one computed by the SAR processing mode (41.9 vs. 41.1 cm). This happens because in the ASIP SARIn processing mode, the ONC is also added to sea ice elevations (section 6.2.3), which tends to increase the freeboard estimates. In fact, the median value of ONC applied to sea ice elevations in this analysis is ∼1.3 cm, which corresponds to the difference between the SAR and SARIn freeboard values computed in the ASIP SARIn processing mode (table 6.1). It is likely that the SARIn freeboard heights are more accurate than the SAR estimates since (1) the SSA is better sampled in SARIn regions by the increased amount of lead heights compared to SAR regions, and (2) the ONC correction enables to correct for range overestimation also for echoes coming from sea ice. This difference in the accuracy, however, slightly affects the freeboard continuity across the SAR and SARIn geographical areas. This result suggests that, when combining SAR and SARIn data, it might be more consistent to add the ONC only to lead elevations, like in Di Bella et al. [2018].

The residual freeboard differences not explained numerically by changes in the average SSA and ONC values in table 6.1 are due to the fact that the SARIn processing mode includes ∼14% more valid freeboard retrievals compared to the SAR processing mode (N_{SAR} vs. N_{SARIn}). In any case, the magnitude of the difference between the mean sea ice SAR and SARIn freeboard observed when introducing the SARIn phase information in the processing (in this case ∼1 cm), will depend on the amount of leads detected at the boundaries of the SARIn acquisition mask as well as on the performance of the SSA interpolation.

In order to justify the necessity of the along-track mode filter applied to SARIn sea ice elevations (section 6.2.3), table 6.2 shows the results of the same freeboard comparison if SARIn sea ice elevations are not filtered (the average SSAs and ONCs are not reported because their value does not change). While this step discards ∼7–10% of SARIn waveforms, when no filter is applied, the SAR and SARIn freeboard estimates differ of ∼4 cm around the WB for both the ASIP SAR and SARIn processing modes. This difference is not attributed to the use of the SARIn phase information and, as mentioned in section 6.2.3, it is due to the larger noise in front of the leading edge of SARIn waveforms when compared to SAR waveforms. An example of the typical elevation profile crossing the WB is provided in figure 6.6a, where it is possible to see the

Mode filter not applied		
	ASIP SAR	**ASIP SARIn**
$\overline{\mathbf{F}}_{\mathbf{SAR}}$ / $\overline{\mathbf{F}}_{\mathbf{SARIn}}$	41.1 / 45.0	40.6 / 45.0
$\mathbf{N}_{\mathbf{SAR}}$ / $\mathbf{N}_{\mathbf{SARIn}}$	9735 / 8708	11366 / 10720

Table 6.2: Average values of sea ice freeboard (F) and number of available freeboard retrievals (N) for the region of interest in figure 6.5 for March 2014, if the SARIn sea ice elevation mode filter is not applied

effect of the along-track mode filter. The waveform corresponding to the sea ice elevation circled in yellow is shown in figure 6.6b and is representative for the majority of filtered sea ice elevations. The dashed green line indicates the retracking point selected by the ASIP retracker, where the 40% power threshold used in the peak detection algorithm is not sufficient to classify the first peak as noise. The shape of this kind of waveforms is found to be quite common when SIRAL operates in SARIn mode and it suggests the two peaks next to the main peak to be caused by the contribution of side lobes from the instrument impulse response (section 7.2.1). The consequent overestimation of the sea ice surface is therefore retracker-dependent. While some physical retrackers, waveform fitting algorithms or more sophisticated peak detection algorithms might not be as sensitive, the empirical threshold retracker used by ASIP requires this additional filter to better reconcile SAR and SARIn sea ice freeboard, and thus thickness, estimates.

6.3.4 Uncertainty reduction

Figure 6.7 (6.8) shows a comparison of gridded radar freeboard (sea ice thickness) estimates and their uncertainties for March 2014, obtained by the ASIP SAR and SARIn processing modes. The correspondent grid cell statistics relative to regions inside the SARIn mask is provided in table 6.3.

	ASIP SAR	**ASIP SARIn**	**Difference**
$\overline{F}_r$ [cm]	17.1	17.9	+0.8 cm
$\overline{\sigma}_F$ [cm]	4.2	3.6	−14%
$\overline{T}$ [m]	2.27	2.30	+0.03 m
$\overline{\sigma}_T$ [m]	0.38	0.33	−13%

Table 6.3: Grid cell statistics for SARIn regions. Average radar freeboard (F_r) and sea ice thickness (T) together with the respective random uncertainties (σ_F and σ_T) are computed for the ASIP SAR and SARIn processing modes. The percentage in the last column is the variation of the results obtained in the SARIn processing mode with respect to those obtained in the SAR processing mode

While no major variations can be observed in the Arctic freeboard maps from the two processing modes, their difference (ASIP SARIn − ASIP SAR, figure 6.7e) does show deviations at the grid cell level up to ±5 cm in the SARIn acquisition mask (red dashed line). These differences, are dependent on the additional leads detected locally by the ASIP SARIn mode, while differences in the grid cells surrounding the WB are due to the along-track interpolation of the SSA. The mean difference between the radar freeboard (ASIP SARIn − ASIP SAR) is 0.8 cm, consistent with the analysis performed in section 6.3.3, which translates in a 3 cm difference in sea ice thickness (table 6.3).

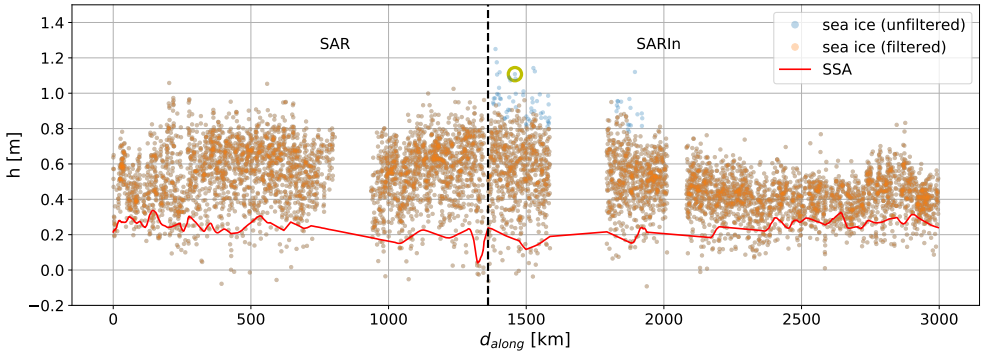

(a)

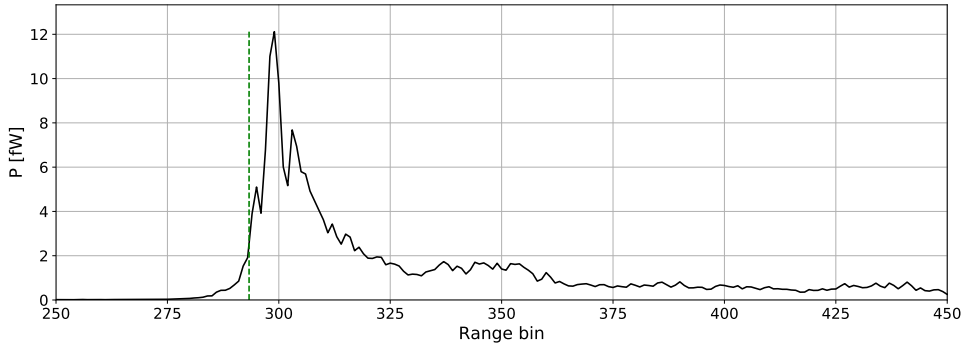

(b)

Figure 6.6: Example of elevation profile crossing the Wingham Box (a) when the sea ice elevation filter is not applied (blue dots) and when it is applied (orange dots). In the plot, the orange dots cover the blue ones. Red line is the interpolated sea surface anomaly. All elevations are detrended using the DTU18 MSS and the black vertical line represents the boundary of the WB. The waveform corresponding to the sea ice elevation circled in yellow is shown in (b) where the noise in front of the leading edge causes the retracker to retrack the 50% (green dashed line) of possibly the wrong peak

The fact that the gridded random radar freeboard and thickness uncertainties decrease with $\sqrt{N}$, where N is the number of freeboard estimates in a grid cell, results in the latitude-dependent gradient observed in figures 6.7b, 6.7d, 6.8b and 6.8d. This is also the reason why the uncertainty increases at the ice edge, where less freeboard retrievals are available. Larger uncertainties are also observed in land-fast regions, e.g. the Laptev Sea [Ricker et al., 2014], and in the MYI area north of Canada and Greenland. This is in general expected when no leads are detected, as the algorithm assigns the uncertainty as the deviation of the interpolated SSA from the mean sea ice elevation.

The reduction of the gridded random radar freeboard uncertainty obtained with the ASIP SARIn processing mode can be observed in figure 6.7f. The average reduction is estimated to be ∼14% (table 6.3) considering only areas inside the SARIn acquisition mask. As expected, in areas outside the mask no uncertainty reduction is observed, apart from some small reductions around the WB due to the interpolation of the SSA. Variations in the random uncertainty are mainly governed by the amount of detected leads which is summarised in table 6.4. The Arctic-wide number of leads detected by the ASIP SARIn is only ∼11% larger of the amount detected by the ASIP SAR mode, due to the scarce SARIn coverage of the Arctic Ocean. On the other hand, when considering only areas inside the SARIn mask, the amount of detected leads triples in the ASIP SARIn mode (280% in SARIn areas and 307% inside the WB). A larger number of

detected leads, decreases the grid cell averaged uncertainty in two ways, (1) it decreases the average point uncertainty of the SSA and (2) it increases the amount of valid freeboard retrievals inside a grid cell (due to the constraint of the maximum distance of a freeboard estimate from a lead, set in ASIP to 100 km). Table 6.5 shows that, in March 2014, an average reduction of 16% in the freeboard point uncertainty and a 36% increase in the number of valid freeboard retrievals is achieved by the ASIP SARIn processing mode. Similar improvements are achieved for the random sea ice thickness uncertainty at both the point and grid levels. If the systematic contributions to the sea ice thickness uncertainty from the snow depth and snow density are included in the error budget, the 13% reduction in the random uncertainty observed in March 2014 translates into a reduction in the total sea ice thickness uncertainty from 51 to 47 cm, i.e., ∼8%.

	N. of leads		
Region	**ASIP SAR**	**ASIP SARIn**	**Difference [%]**
Arctic	425037	471130	111
SARIn mask	25565	71658	280
WB	3448	10578	307

Table 6.4: Number of lead measurements performed in both the SAR and SARIn processing mode by ASIP in the entire Arctic Ocean, in SARIn regions and inside the Wingham Box (WB). The percentage in the last column is the variation of the results obtained in the SARIn processing mode with respect to those obtained in the SAR processing mode

	ASIP SAR	**ASIP SARIn**	**Difference [%]**
$\overline{\sigma}_F$ [cm]	28.6	23.9	−16
N_F	173388	235064	+36
$\overline{\sigma}_T$ [m]	2.25	1.93	−14
N_T	172043	233693	+36

Table 6.5: Point statistics for SARIn regions. Average freeboard and thickness random uncertainties (σ_F and σ_T) together with the number of valid retrievals (N) are computed for the ASIP SAR and SARIn processing modes. The percentage in the last column is the variation of the results obtained in the SARIn processing mode with respect to those obtained in the SAR processing mode

6.4 Summary and conclusions

An Arctic sea ice processor has been developed at DTU to investigate how the phase information available in the CS SIRAL SARIn acquisition mode affects freeboard and thickness estimates in the Arctic Ocean. The processor (ASIP) can process CS L1b waveforms according to a regular SAR processing scheme (ASIP SAR processing mode), which is used as a reference case in this study, as well as it can use the SARIn phase information where available (ASIP SARIn processing mode).

Along-track validation is performed using ASAR SAR images as well as airborne laser (ALS) and radar (ASIRAS) altimetry. Using the SARIn phase information, SIRAL is capable to pinpoint

off-nadir leads up to 2.3 km from the satellite nadir and to correct for most of the overestimated ranges. No spatial correlation is found at the footprint scale between SIRAL sea ice freeboard and both snow and sea ice freeboard from airborne laser and radar altimetry, which is mainly attributed to the different instrument footprint size [Haas et al., 2016]. A good agreement is found between SIRAL and ASIRAS sea ice freeboard, considering the respective uncertainties, as well as between SIRAL and ALS sea ice freeboard (computed from the snow freeboard using area-averaged snow depth estimates from NASA Operation IceBridge (OIB) snow radar).

Pan-Arctic sea ice freeboard retrievals obtained with the ASIP SARIn processing mode show a pattern of large negative freeboard heights along the CS SARIn mask. An analysis performed in cooperation with ARESYS S.r.l. [Di Bella et al., 2019] highlights an issue in the phase difference of some of the SARIn waveforms included in the current Baseline C L1b products. The upcoming Baseline D data release will include a patch developed as a result of this analysis, improving the accuracy of the SARIn phase difference along the boundaries of the SARIn acquisition mask.

The continuity of sea ice freeboard between regions where SIRAL operates in SAR and SARIn mode is investigated in a region of interest around the Wingham Box (WB), using data from March 2014. CS waveforms are processed in both the ASIP SAR and SARIn processing modes to assess the impact of the phase information. By using the phase information, a difference of 1.3 cm between the SAR and SARIn mean sea ice freeboard estimates is found across the WB. By applying the off-nadir range correction (ONC) only to lead heights, and not to sea ice elevations, this difference approaches zero. However, it is likely that the freeboard estimate from ASIP SARIn mode be more accurate than the one from ASIP SAR mode, as the phase information allows for a better local sampling of the SSA as well as for the correction of the overestimated range for both leads and sea ice.

By increasing the amount of detected leads and by correcting for the overestimated range due to snagging, the gridded uncertainty of ASIP SARIn freeboard and thickness estimates is reduced by 14% and 13%, respectively, when compared to the ASIP SAR reference case. Although the magnitude of this reduction depends on the actual geographical distribution of leads, it is likely that there will always be an improvement when SARIn waveforms are processed including the phase information. Despite the lower relative reduction obtained when considering the systematic error contributions from the snow loading ($\sim$8%), radar freeboard uncertainty is still the second largest contribution to the total sea ice thickness uncertainty.

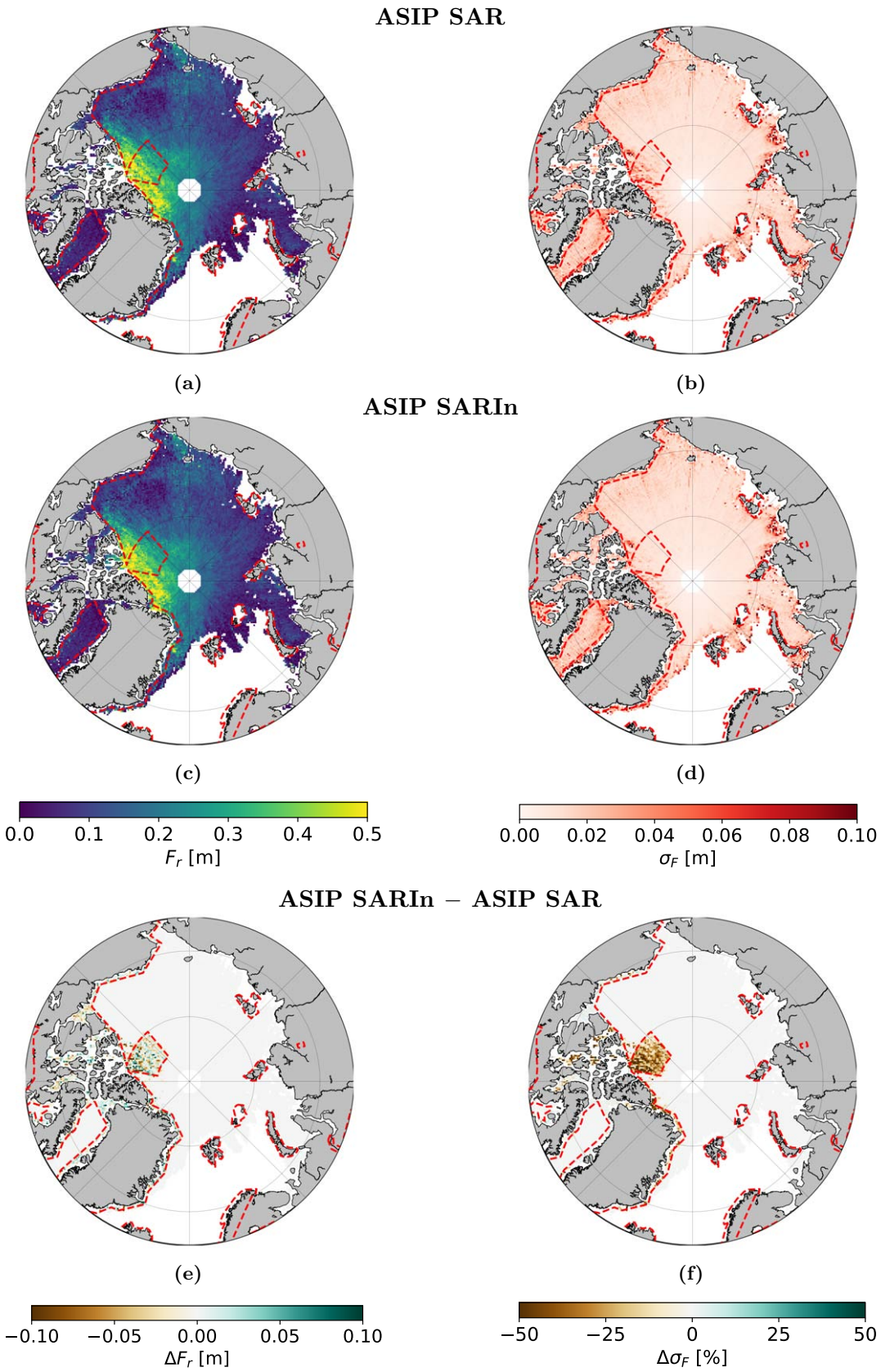

Figure 6.7: Arctic radar freeboard maps and random uncertainties for March 2014 from the DTU ASIP SAR ((a) and (b)) and SARIn processing mode ((c) and (d)). (e) is the difference (c)−(a) and (f) represents the percentage of variation of (d) with respect to (b)

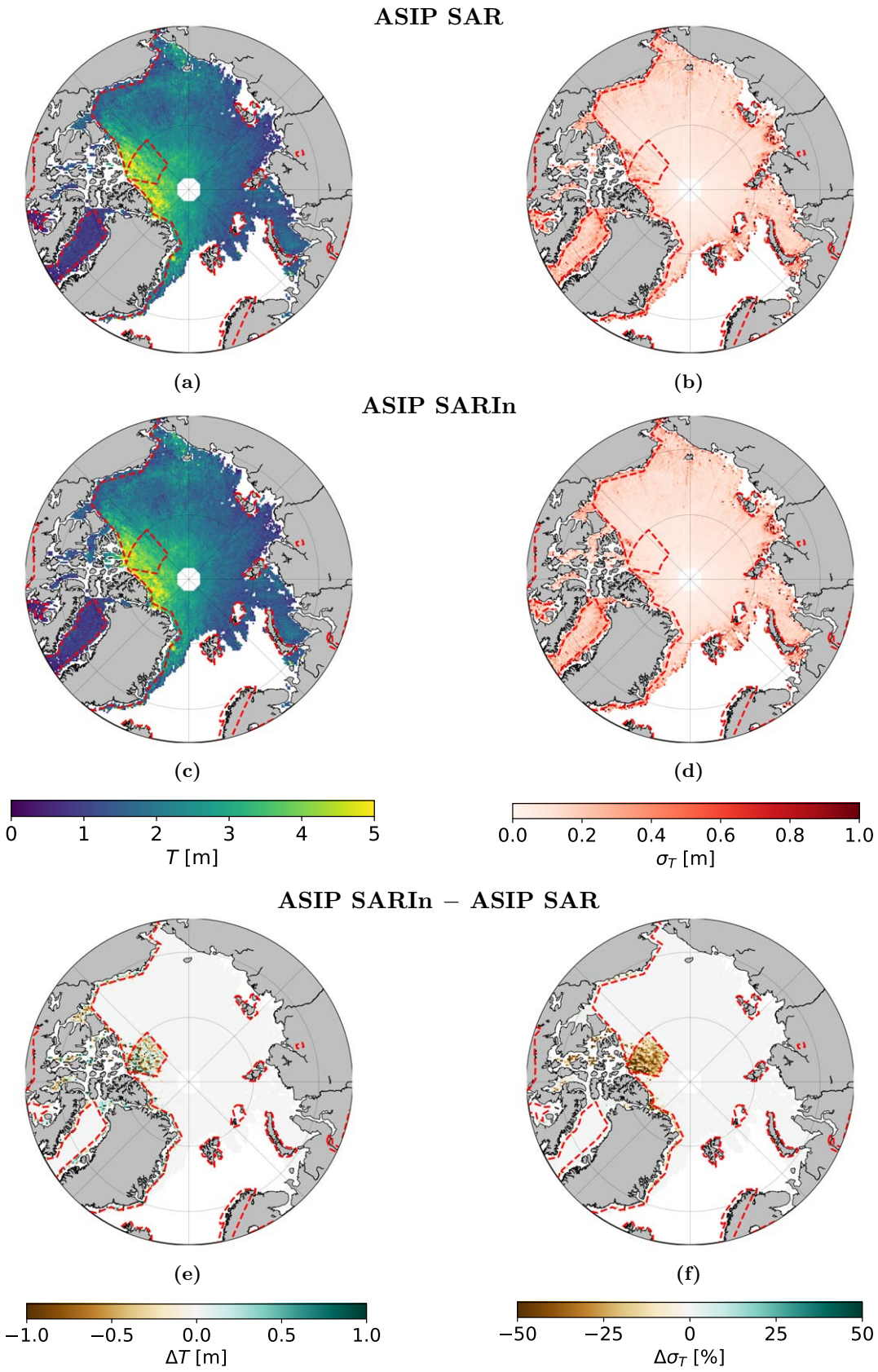

Figure 6.8: Arctic sea ice thickness maps and random part of the thickness uncertainty for March 2014 from the DTU ASIP SAR ((a) and (b)) and SARIn processing mode ((c) and (d)). (e) is the difference (c)−(a) and (f) represents the percentage of variation of (d) with respect to (b)

Chapter 7

The JPL/DTU Multi-Peak Arctic Sea Ice Processor

7.1 Introduction

Despite the reduction of the sea ice freeboard and thickness random uncertainties discussed in the previous chapter, the question if the capabilities of the CS SARIn acquisition mode could be exploited any further for sea ice applications, still stands.

Swath processing of CS L1b SARIn waveforms [Gray et al., 2013] has been shown to be able to provide across-track elevations in regions with a complex topography, like ice sheets and ice caps [Nilsson et al., 2016; Foresta et al., 2016]. Despite the relative flatness characterising the ocean and sea ice-covered regions, processing multiple parts of a CS SARIn waveforms together with the associated phase information might have the advantage of increasing the amount of elevation estimates per waveform.

Most of the times in sea ice-covered regions, the snagging of the onboard tracker due to an off-nadir lead results in a broadened leading edge of the waveform. However, depending on the across-track distance of the lead from the nadir, the typical diffusive and specular features associated to reflections from sea ice floes and leads, respectively, could potentially be separated in the range bin space. This would result in the theoretical possibility to get an elevation estimate, from a single waveform, for both the sea ice at nadir and a lead located several kilometres across-track from it. Consequently, the number of valid freeboard retrievals as well as lead measurements would increase which, as shown in chapter 6, would reduce the random part of the sea ice freeboard and thickness uncertainties.

This chapter presents the sea ice processor developed at the NASA Jet Propulsion Laboratory (JPL) as a part of this PhD project, referred to in this work as the *JPL/DTU Multi-Peak Arctic Sea Ice Processor* (*MPASIP*). This processor is used to investigate how retracking more than one peak in single L1b SARIn waveforms, in combination with the respective phase information, could increase the amount of valid sea ice as well as sea surface height measurements, so as to possibly reduce even further the random uncertainty of sea ice freeboard and thickness estimates.

Section 7.2 describes the methods used by MPASIP to process CS data while in section 7.3 the potential, challenges and limitations of this method are identified with the support of Sentinel-1 SAR images, external CS sea ice products as well as airborne measurements from the NASA Operation IceBridge campaigns. Finally, section 7.4 summarises the work presented in this chapter and provides some concluding remarks.

Sea ice freeboard and thickness maps additional to the ones shown in this chapter can be found in Appendix E.

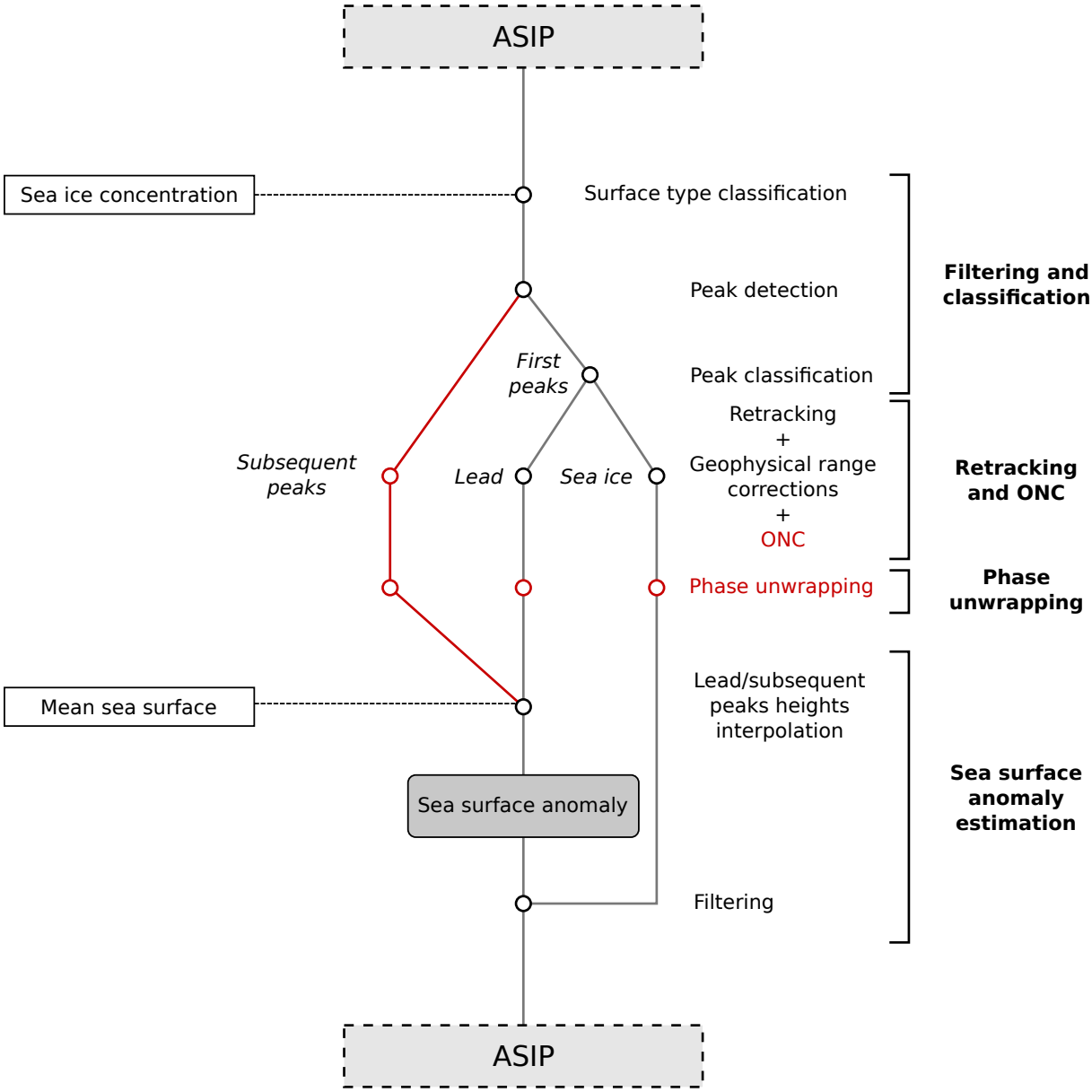

Figure 7.1: Diagram summarising MPASIP waveform processing steps. Only the procedures which differ from the ASIP processor (figure 6.2) are shown. The red colour marks the steps performed only on *SARIn* waveforms. Sections 7.2.1–7.2.4 provide more information about each one of the steps highlighted in bold to the right-hand side of the diagram

7.2 Methods

This section provides technical details about the algorithm used by MPASIP to process CS Baseline C 20 Hz SAR and SARIn L1b waveforms. MPASIP and ASIP share some of the orbit processing chain, thus, only the procedures which differ from ASIP are described in this section. Figure 7.1 shows a diagram summarising these steps, for which more details are provided in the following sections.

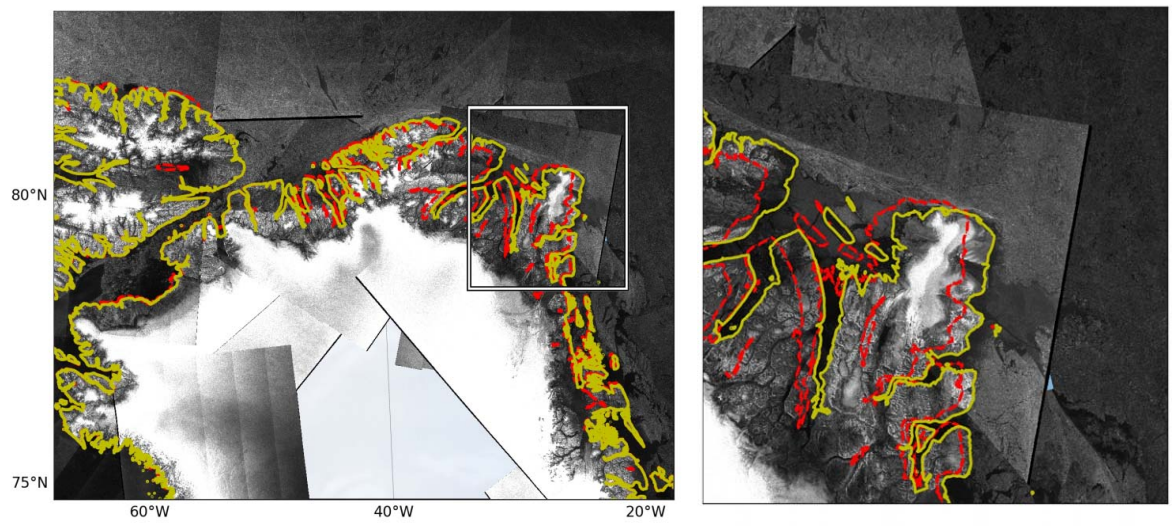

(a) (b)

Figure 7.2: Comparison between the GSHHG coastline (red), on which the surface flag in the CS L1b product is based, and the OpenStreetMapData coastline (yellow). Both coastlines are overlapped on a Sentinel-1 mosaic of Northern Greenland created using images from March 2015. The area inside the white box in (a) is enlarged in (b), showing the better accuracy of the OpenStreetMapData compared to the GSHHG coastline which is more than 20 km off in the area shown

7.2.1 Filtering and classification

Pre-processing and waveform quality filtering is performed in the same way as in the ASIP processor, with the only difference being that measurements close to the coast, with a sea ice concentration value set to invalid in the OSI SAF product, are also retained. Additionally, land filtering is performed using a high-resolution coastline (section 5.5), as the surface flag in the CS product is found not to be reliable in the region around northern Greenland (figure 7.2).

As for ASIP, SAR waveforms with $0.1 < PP < 0.25$ are discarded since the snagging effect, which cannot be corrected for in the SAR mode, is considered to affect significantly the elevations retrieved from these waveforms.

Peak detection algorithm

CS waveforms are oversampled in the frequency domain by a factor 16 [Kwok & Cunningham, 2015] to refine the position of the peaks, as this is not accurately described by the original waveform samples. Figure 7.3 shows how this is especially true for specular returns. The peak detection algorithm performs several steps in order to select only those peaks of the oversampled waveform that might correspond to relevant reflections on ground. Firstly, it selects all waveform peaks above an absolute noise threshold of 5 fW, identified through the analysis of a large amount of waveforms as a good threshold to filter out noisy peaks (as a comparison, the maximum power of a sea ice waveform ranges between 15 and several hundreds fW, depending on the roughness of the ice).

Waveforms generated from strong and specular reflections from leads look very much like the signal transmitted by CS (figure 7.3). For SIRAL, the compressed pulse (s) as a function of the

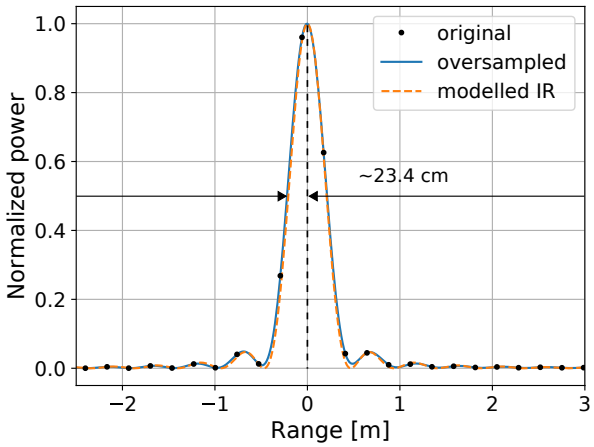

Figure 7.3: Example of a CS waveform from a quasi-specular surface (black dots) oversampled by a factor 16 in the frequency domain (blue curve). The oversampled waveform is compared with the SIRAL compressed pulse (dashed orange curve) showing that, from near-specular surfaces, the width of the return at its half-power point is approximately the width of the SIRAL compressed pulse (∼46.8 cm). The half-width (W_p) is used by MPASIP for the peak classification

range (r) is accurately described by the function [Galin et al., 2013]

$$s(r) = \mathrm{sinc}^2\left(\frac{2\pi B_w r}{c}\right) \tag{7.1}$$

where $\mathrm{sinc}(x) = \sin(x)/x$, B_w is the radar bandwidth and c is the speed of light. As already mentioned in section 3.3.1, this function also defines the instrument range resolution of ∼46.84 cm as the width of the main lobe at the half-power point (figure 7.3).

As suggested in section 6.3.3, the noise on the leading edge of SARIn waveforms might be caused by the side lobes of SIRAL's impulse response shown in figure (figure 7.3). For this reason, a dedicated side lobes filter is developed in MPASIP. The instrument impulse response is computed for each waveform in the range bin space as shown in figure 7.4 and peaks close to the location of the first two strongest side lobes are discarded. A tolerance of ±1/4 of a range bin in the peak location is allowed, to account for the fact that that the received waveform is not the perfect copy of the modelled instrument impulse response, due to measurement noise and the interaction with ground. This procedure is performed for strong and specular reflections from leads as well as more diffusive power echoes, as also some of the CS sea ice waveforms seem to be affected by this issue. Figure 7.4 shows an example of peaks discarded because containing contributions from side lobes.

While only the first significant peak is selected in SAR waveforms, additional peaks are retained in SARIn echoes, where an important distinction is made between *first* and *subsequent* peaks. While the first peak of a waveform is the one representing the main reflection on ground, and the one commonly being retracked, subsequent peaks on the trailing edge result from scattering increasingly further away from the POCA (section 3.3.1). While the area illuminated on ground by the altimeter expands as a ring, scattering occurs at both sides of the POCA. A measure of the extent to which the received power originates from one of the two sides of the POCA, rather than a mixture of the two, is provided by the cross-channel coherence [Wingham et al., 2004], provided in the CS L1b product. Dominant features on the ground, e.g. leads, are characterised by a high value of coherence, indicating that the power received in specular waveforms comes from predominantly one distinct location in the footprint that can be determined using the interferometric phase measurement [Armitage & Davidson, 2014]. For these reasons,

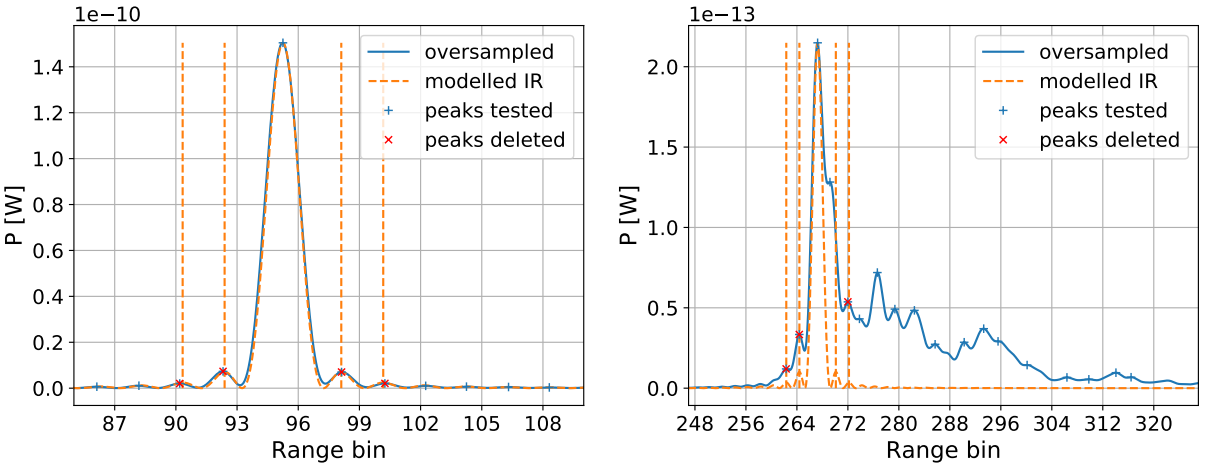

(a) (b)

Figure 7.4: Example of peaks discarded by the side lobe filter for a quasi-specular return from a lead (a) and for a more diffusive waveform (b)

once the first relevant peak is identified, subsequent peaks in SARIn waveforms are filtered so that only those having a coherence larger than 0.9 are retained.

Peak classification

Classification is carried out at this stage only for the first peak of the waveforms. The approach used here is not based on the PP, as this is a parameter that describes the shape of the entire waveform, but it relies on a combination of the peak power (P_p) and the half-width of the peak at the half-power point (W_p) [Kwok & Morison, 2015] (figure 7.3). An analysis of these two parameters in the Arctic Ocean from first unambiguous peaks shows that the population of specular returns, having high P_p and narrow W_p, is marked by a distinct mode in the top left corner of the joint distributions in figure 7.5. An unambiguous peak is a peak with a clearly-defined leading edge, i.e., without any local minima in the range interval between its half- and peak-power points [Kwok & Morison, 2015].

In this work, the thresholds of minimum $P_p = 40$ dBf and maximum $W_p = 30$ cm used to identify sea surface returns by Kwok & Morison [2015] have been relaxed to 30 dBf and 35 cm, respectively. Thus, peaks having $P_p > 30$ dBf and W_p to the left of the red dashed line in figure 7.5 are considered specular returns from leads, while those not meeting these conditions are classified as reflections coming from sea ice. Subsequent peaks, on the other hand, are harder to classify. Echoes from off-nadir leads will not be as specular as those generating in regions close to the satellite nadir and their power will be much lower too, due to the attenuation from the antenna beam pattern. For this reason, subsequent peaks are not classified at this stage, but assumed to be all generated by relevant reflections from off-nadir leads.

7.2.2 Retracking and Off-Nadir Correction (ONC)

MPASIP uses different retrackers for sea ice and lead peaks. Sea ice peaks are retracked using a 50% threshold retracker, while lead peaks are retracked at the range bin where the peak power occurs. In order to avoid biases introduced by the different retrackers, a correction is added to the elevations estimated from lead peaks. This correction is chosen as the minimum value between the measured peak W_p and a maximum value of 35 cm.

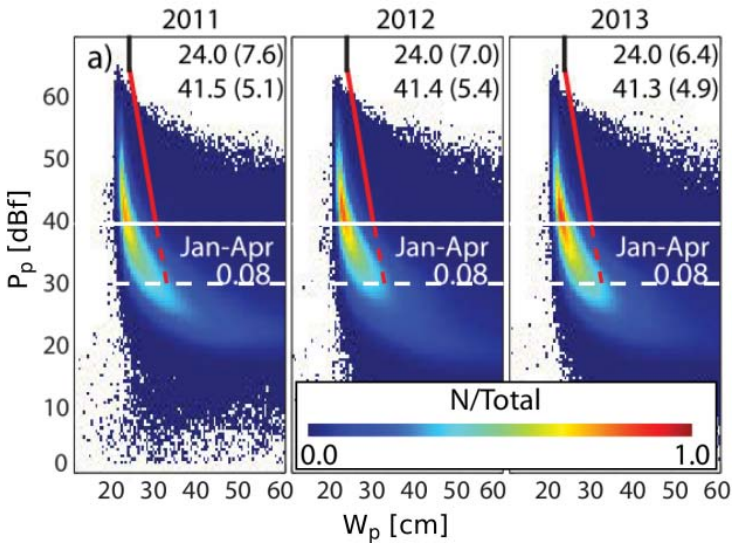

Figure 7.5: Joint distribution of peak power (P_p) and width of the leading edge (W_p) for first unambiguous peaks of CS waveforms acquired in the Arctic in the period Jan–Apr 2011 and 2013. Quantities in the top-right corner are the mean and standard deviation of P_p and W_p at the mode of the distributions. In this work, sea surface returns are those samples with $P_p > 30$ dBf (above dashed white line) and W_p to the left of the black and dashed red lines. The values in the centre of the panels are the fractional coverage of those samples designated as sea surface returns by Kwok & Morison [2015] using the thresholds identified by the solid white and solid red lines. Figure modified from [Kwok & Morison, 2015]

In the case of first lead peaks, W_p is always lower than 35 cm and adding this correction to the estimated elevation is equivalent to use a 50% threshold retracker (this can be observed also in figure 7.3). The only difference, for SARIn waveforms, is that the phase difference used to compute the ONC is the value at the peak-power point and not the one at the half-power point. However, in strong specular reflections from leads close to the satellite nadir, the phase evolution between the half- and the peak-power point is limited to less than a range bin and it can be considered negligible. With regard to subsequent peaks, they might easily have a value of W_p larger than 35 cm due to antenna attenuations and, assuming they generate from leads, due the larger fraction of the signal scattered away from the satellite compared to a lead located at nadir. However, the maximum correction is set in this work to 35 cm, following the assumption that significant reflections from off-nadir leads should not have a leading edge broader than this value.

As for the ASIP processor, the SARIn differential phase is used to compute the ONC to be applied to elevations from both sea ice and lead returns estimated from SARIn waveforms.

7.2.3 Phase unwrapping

The phase difference provided in the CS SARIn L1b product is wrapped in the interval $(-\pi, +\pi]$. This means that, if parts of the waveforms generate from reflections further than ∼7 km away from the satellite nadir [Abulaitijiang et al., 2015], the phase difference will be discontinuous, showing sudden jumps between the interval extremes. As discussed in section 6.2.3, the phase difference is used to compute the across-track distance of the main scattering location on ground from the satellite nadir as well as the corresponding ONC value applied to the retracked height. Thus, in order to compute an accurate ONC correction, the phase needs to be unwrapped.

Phase unwrapping is in general a very challenging task in digital signal processing, mainly due to the noise affecting real-world measurements and because a starting "true" absolute value of phase is generally required to avoid phase unwrapping errors. However, using some basic

assumptions, the one-dimensional phase unwrapping of the CS SARIn differential phase can be heavily simplified.

In relatively flat areas like the Arctic Ocean, it is safe to assume that the main reflection, identified by the first significant peak of the waveform, comes from a region close to the satellite nadir, and thus, that the phase at its retracking point is not wrapped. Also, assuming that the phase value between two consecutive gates is not aliased, their absolute difference should not be larger than π. Following these assumptions, phase unwrapping can therefore be performed starting from the phase value at the retracking point of the first peak and looking for discontinuities in the phase until the retracking point of the last detected peak (as phase jumps outside this interval will not affect the retracked heights). When jumps are found, 2π is either added or subtracted to the phase value, depending on the sign of the difference between the phase at the two consecutive gates.

The noise affecting phase measurements can, in principle, generate "false" phase wraps. During phase unwrapping procedures, these false wraps affect all the values of phase to the right of the gate at which they occur. If more than one false wrap occurs, the unwrapping error will accumulate. To account for the effect of the noise in the phase measurements, phase unwrapping is performed by MPASIP in 3 independent iterations using different thresholds to detect phase jumps (1.9π, 1.5π and π). During every iteration, a new value of ONC is computed and added to the retracked height (MSS-detrended). If the deviation of the new height estimate from the MSS is lower than it was before the phase unwrapping procedure, the new value of phase difference is chosen over the old one. This test is considered to be reliable enough as height errors from a wrapped phase cause an underestimation of the retracked heights in the order of several tens of metres.

After phase unwrapping is performed on SARIn waveforms, the across-track location of the main scattering regions is again tested against the high-resolution coastline, to discard echoes possibly generated on land.

7.2.4 Sea surface anomaly estimation

As for ASIP, the DTU18 MSS is subtracted from all retracked elevations. The sea surface anomaly (SSA) is determined along every orbit in 25-km fixed segments. Tie points for the SSA value are estimated as the average of the heights inside each segment, using exclusively strong specular returns, i.e., first peaks classified as leads. This "reference" SSA is interpolated segment-wise along the entire track allowing a maximum interpolation extent of 4 segments, i.e., the reference SSA is not assigned to points further than ∼100 km from a lead measurement. The final SSA is then estimated for each segment as the weighted average of the elevations from both lead peaks and the subsequent peaks detected on the waveform trailing edge, inside the segment. Only subsequent peaks with a retracked elevation within ±15 cm from the segment reference SSA are used. The uncertainty of each height estimate, used as a weight in the estimation of the segment average SSA, includes the contributions from the random uncertainty of a CS height measurement as well as from the ONC uncertainty, i.e. it is equal to $\sqrt{\sigma_{L1b}^2 + \sigma_{ONC}^2}$. The SSA in valid segments is interpolated linearly to the rest of the track allowing, as for the SSA tie points, a maximum distance between lead measurements of ∼100 km.

The total uncertainty of the SSA (σ_{SSA}) is assigned for each segment as the standard deviation of the lead elevations inside the segment, including elevations from subsequent peaks. As for ASIP, in the case that no leads are found in a segment, σ_{SSA} takes the value of the deviation of the interpolated SSA from the mean CS sea ice elevation inside the segment.

A final test is performed to look for echoes possibly generating on land and missed by previous land filtering: all elevations 2 m above the segment reference SSA, or 3 m above the local MSS if

no SSA tie points are available, are discarded. Furthermore, SARIn sea ice elevations generating more than 800 m across track from the satellite nadir, i.e. outside the SIRAL pulse-limited footprint, are also discarded.

The radar freeboard, sea ice freeboard, sea ice thickness and the respective uncertainties are finally estimated according to section 6.2.5.

7.3 Results and discussion

This section presents the results obtained by the MPASIP processor. Section 7.3.1 aims at validating the peak detection and classification algorithms described in section 7.2.1 and at assessing the general lead detection capabilities of CS. In section 7.3.2, the radar freeboard estimates obtained by MPASIP are compared to those generated by the Alfred Wagner Institute (AWI) and the NASA Jet Propulsion Laboratory (JPL). Additional validation is performed in section 7.3.3 by comparing these three products to airborne measurements from the NASA Operation IceBridge (OIB) campaign. Finally, section 7.3.4 discusses the uncertainties of the sea ice freeboard and thickness estimates from MPASIP.

7.3.1 Lead detection

Sentinel-1 (S1) SAR images are used in this work to assess CS lead detection capabilities as well as to investigate which kind of features on ground are associated with the subsequent peaks detected on the trailing edge of SARIn waveforms. Figure 7.6a shows a CS track north of Ellesmere Island from April 22, 2015 (orbit #26703) overlapped to a S1 mosaic from March 2015. The dashed red line represents the CS SARIn acquisition mask, where SIRAL operates in SARIn mode (next to the coast). Figure 7.6b zooms in onto the CS track, which is plotted on top of a S1 image acquired ∼1 hour before the CS pass. No sea ice drift correction is applied to the SAR image as the drift is considered to be smaller than the image resolution (∼100 m) on this time scale. Here, one can see the results of the peak classification introduced in section 7.2.1, where blue dots are returns from sea ice, red dots are reflections from leads and orange dots are subsequent peaks which are not classified as leads. Focussing on the SARIn region, the yellow box in figure 7.6b is enlarged in figure 7.6c showing how every measurement, relocated across-track using the SARIn phase information, corresponds to a black spot in the SAR image. Being the SAR instrument onboard S1 a side-looking radar, dark spots in S1 images indicate regions with a low surface roughness, like leads and very smooth ice. This indicates that most of the subsequent peaks detected by MPASIP correspond to actual ground features, although it has to be noticed that they might not always coincide with the real sea surface, as open leads in the Arctic refreeze rapidly in March.

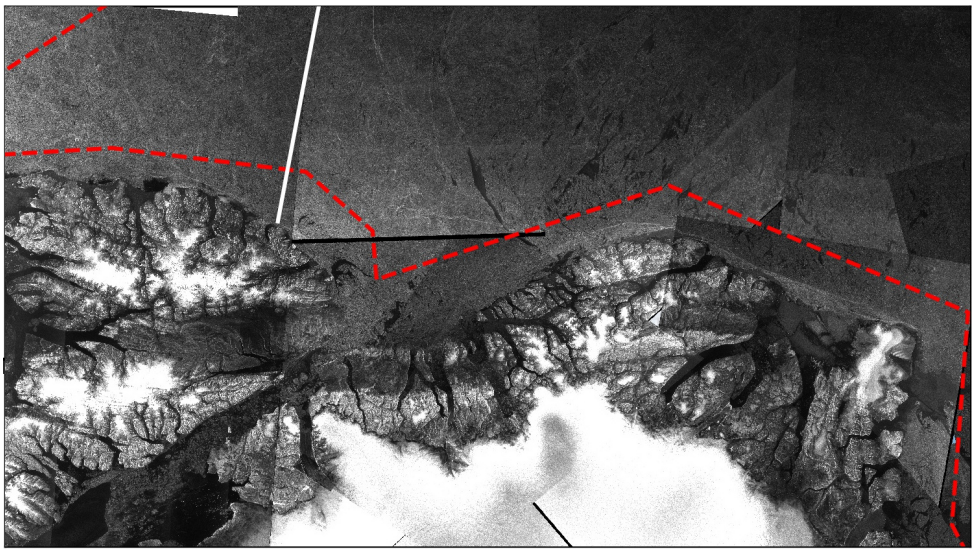

(a)

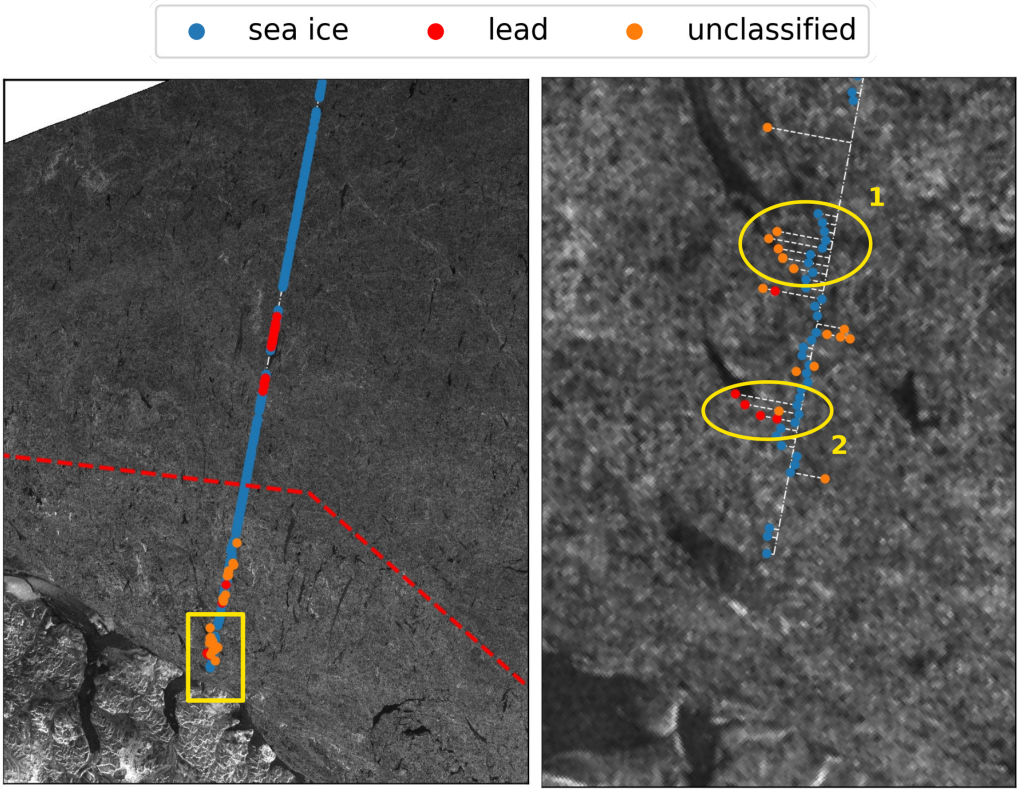

(b) (c)

Figure 7.6: Sentinel-1 (S1) mosaic of Northern Greenland and part of the Lincoln Sea showing in white the analysed CS track (a). Results of the classification performed by MPASIP overlapped to a S1 SAR image acquired ∼1 hour before the CS pass (b), the yellow box is enlarged in (c) showing the two regions used in the text. The red dashed line marks the transition from the SARIn acquisition area (over the coast) to the SAR mode area

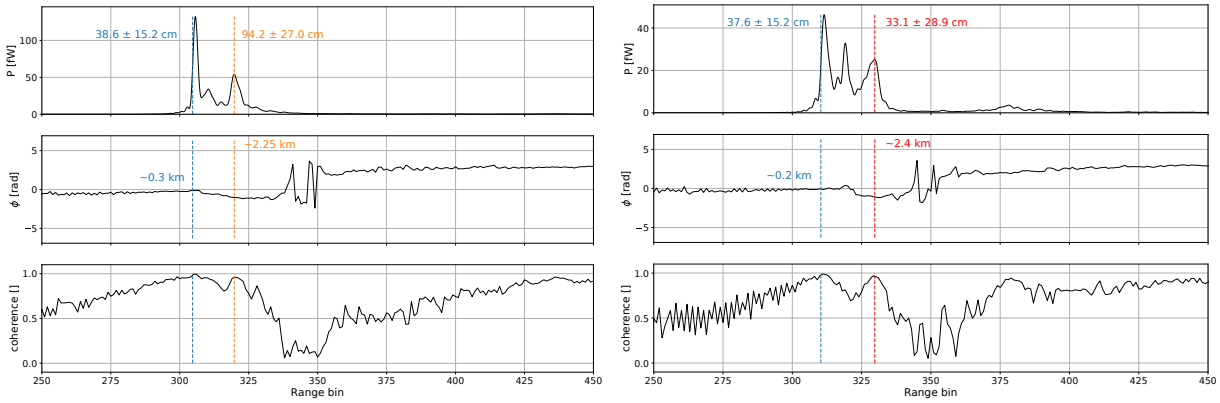

(a) **(b)**

Figure 7.7: Example of a representative waveform (top panels) for region 1 (a) and region 2 (b) in figure 7.6c. Middle panels show the phase difference and bottom panels the coherence. Dashed vertical lines represent the retracking points of sea ice peaks (blue), leads (red) and unclassified subsequent peaks (orange). The same color code is used to indicate the elevations in the top panel and the distance of the reflections from the satellite nadir in the middle panel. Height estimates shown for leads and subsequent peaks are already corrected to account for the retracker-dependent difference discussed in section 7.2.2

An analysis of region 1, circled in yellow in figure 7.6c shows that some of the points classified as sea ice follow the boundary of a small lead. While the height underestimation due to the snagging on the onboard tracker is corrected for, using the SARIn phase information, the possible misclassification results in an underestimation of the sea ice freeboard. This is also what possibly happens between 84.1–84.4°N in the elevation profile shown in figure 7.8, where sea ice elevations are close in value to the local sea surface anomaly. This is not likely to be the case as, given the geographical location and the time of the year, this region should be characterised by thick multi-year ice. This example suggests that the further tuning of the thresholds used to classify the first peaks of the waveforms might lead to more accurate freeboard estimates by MPASIP. Figure 7.6c also shows that all of the off-nadir points detected in region 1 are not classified as leads, even if they follow closely the shape of a lead in the SAR image. A representative waveform for this region can be seen in figure 7.7a (top panel) together with its phase difference (middle panel) and coherence (bottom panel). While the second peak has a high coherence (it generates from a specific location inside the SIRAL footprint) and a value of phase information which accurately pin points the reflection from a possible lead in the SAR image, the final retracked height (94.2 cm) is not ±15 cm from the reference SSA (21.6 cm) computed using the SSA tie points marked in green in figure 7.8. This happens for all subsequent peaks in region 1, identified by the orange crosses inside the yellow circle of figure 7.8. Nevertheless, the first peak of these waveforms is always successfully retracked.

On the other hand, most of the waveforms in region 2 (figure 7.6c) provide a height measurement of both sea ice and SSA. As shown by the representative waveform in figure 7.7b, the second peak is not selected due to a coherence value lower than 0.9, while the third is. The peak is classified as a lead return as its retracked height falls in the interval of ±15 cm from the reference SSA. Figure 7.7 also shows how, the larger the distance from the satellite nadir, the larger the uncertainty on the final height estimate due to the contribution from σ_{ONC} (section 7.2.4).

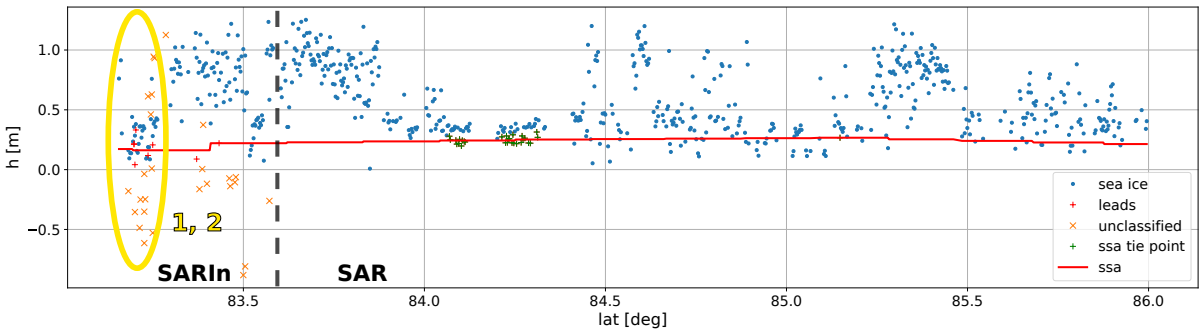

Figure 7.8: Elevation profile, detrended using the DTU18 MSS, for the track shown in figure 7.6b. Sea ice elevations lower than the sea surface anomaly (SSA), corresponding to negative freeboard heights, are due to the noise on CS measurements (section 6.2.5)

Region	MPASIP–AWI	MPASIP–JPL	AWI–JPL
Arctic	0.3	2.1	1.7
SARIn mask	1.5	1.7	2.1

Table 7.1: Average differential radar freeboard in cm relative to figure 7.9 computed using only the grid cells overlapping for each difference

7.3.2 Comparison with external products

In this section, radar freeboard retrievals from the MPASIP are compared to the estimates from the current Alfred Wagner Institute (AWI) L2i product as well as to the estimates produced by Dr. Kwok at the NASA Jet Propulsion Laboratory (JPL). The AWI and JPL products are produced using different techniques, however, in both of them the SARIn phase information is not used. It has to be noticed that these datasets are not used as a source of absolute validation, but to assess general trends in the MPASIP processor as well as to show the sensitivity of sea ice freeboard heights to different processing algorithms.

Figure 7.9 shows radar freeboard estimates for March 2014 from MPASIP, AWI and JPL as well as differential radar freeboard of the 3 products, MPASIP–AWI, MPASIP–JPL and AWI–JPL (average values in table 7.1). In the AWI product, radar freeboard estimates are not filtered for possible outliers, as opposed to their sea ice freeboard, and include large negative values. In the following comparison, AWI radar freeboard heights lower than the radar freeboard uncertainty provided in their product are filtered out, not to bias the results. The OSI SAF sea ice type classification from March 15, 2014 is additionally shown in figure 7.10 and used as a reference in the discussion.

A good agreement is found Arctic-wide between the MPASIP and the AWI radar freeboard, with differences ranging between ±2 cm and averaging to 0 in most regions. An average difference of 1.5 cm is found for MPASIP–AWI in SARIn areas and local differences of ±7 cm are observed in the Wingham Box (WB) and the Lincoln Sea. While the signal in the WB could be related to the height estimates from subsequent peaks included in the MPASIP SARIn processing technique, the smaller MPASIP freeboard in the Lincoln Sea compared to AWI, where SIRAL operates in SAR mode, suggests that the reasons for these differences could be several.

To better understand the nature of these differences, figure 7.11 shows the deviation of the MPASIP sea surface anomalies (SSA) from the AWI SSA. The general underestimation of the SSA from MPASIP compared to AWI is due to some differences in the signal processing

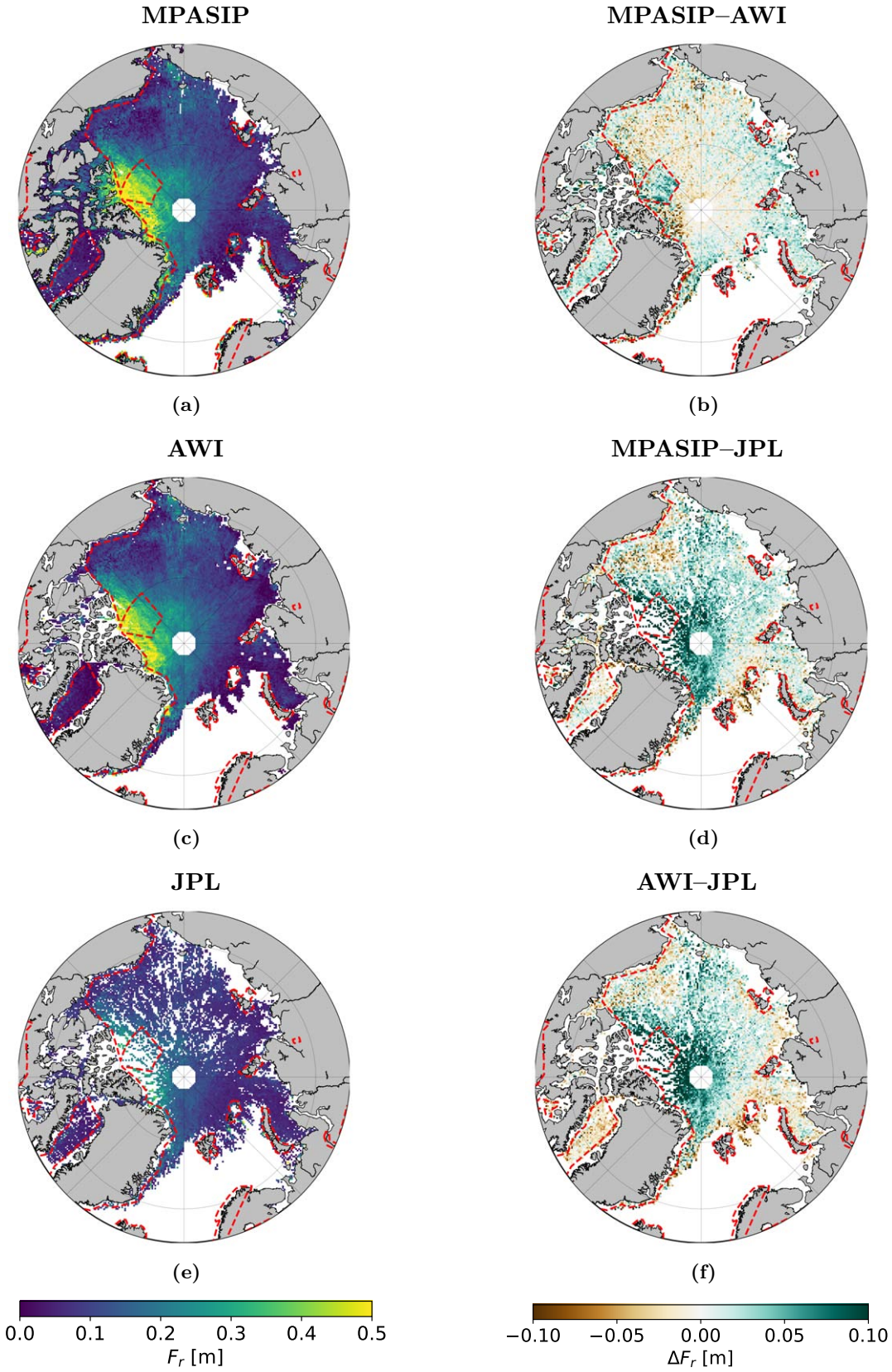

Figure 7.9: Radar sea ice freeboard for March 2014 as estimated by the MPASIP (a), AWI (c) and JPL (e) processors. The differences MPASIP–AWI, MPASIP–JPL and AWI–JPL are shown in the right column (b-d-f). The dashed red line represents the CS SARIn acquisition mask

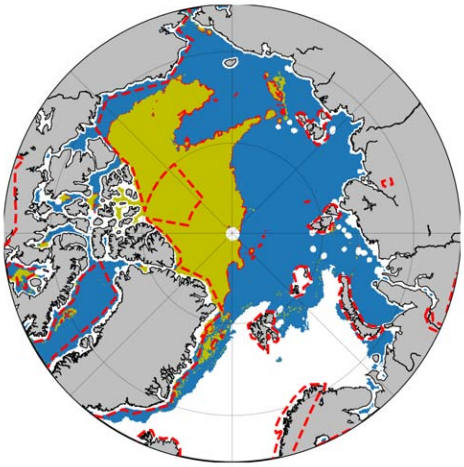

Figure 7.10: OSI SAF ice type for March 15, 2014. First-year ice is shown in blue and multi-year ice in yellow. Red areas indicate an ambiguous ice type

performed by the two processors. Despite using a similar 50% threshold retracker, the AWI processor applies a smoothing filter to the interpolated (factor 10) waveforms. This filter has in general the effect of displacing the leading edge of both leads and sea ice waveforms towards the radar, resulting in larger absolute height estimates. The size of the window used in the filtering by the AWI processor is 11 and 21 samples for SAR and SARIn waveforms, respectively, to account for the larger noise of SARIn echoes, compared to SAR (sections 4.1.1 and 6.3.3). An analysis performed on specular returns in March 2014, not shown here, estimates an average difference in the absolute height estimates of ∼2 and ∼5 cm when the smoothing is applied to respectively SAR and SARIn waveforms compared to when it is not applied. It has to be noticed that this should not affect freeboard estimates as also the leading edge of sea ice echoes is displaced in a similar way. However, it might be interesting to better quantify the impact of the smoothing procedure on the final retrieved elevations when applied to specular and diffusive returns. Part of the difference between the MPASIP and AWI SSAs might also be explained by the fact that the AWI processor additionally applies the residual CS range errors, reported in Scagliola & Fornari [2017] to be 4.7 ± 4 and 1.7 ± 3.5 cm for SAR and SARIn measurements, respectively. While these residual errors do not affect the relative measure of freeboard (apart from the SAR/SARIn boundaries, depending on the amount of leads detected), they do result in higher absolute elevations. These residual errors are not accounted for in the MPASIP processor as they have not yet been associated to systematic biases [Scagliola, personal communication]. Removing the average bias between the MPASIP and AWI SSAs from figure 7.11a, enables a better graphic visualisation of possible regional patterns in the differential SSA, as shown in figure 7.11b. Here, a lower SSA can still be observed in western region of the WB. This could partly be related to the height estimates from subsequent peaks of SARIn waveforms processed by MPASIP. The analysis of a large number of elevation profiles in SARIn areas, showed the statistical tendency for subsequent peaks to have lower elevations than the reference SSA estimated from just strong specular returns. From this analysis, it seems like the ONC might not completely correct for the range overestimation of all detected subsequent peaks, as also noticed by Di Bella et al. [2018]. Despite the ±15 cm threshold from the reference SSA set to select only possibly relevant sea surface heights from subsequent peaks, including all of them without any further classification will have the effect to lower the average along-track SSA, and hence, to increase the corresponding values of freeboard. This suggests that further investigation might be required to better identify only relevant subsequent peaks on the trailing edge of SARIn

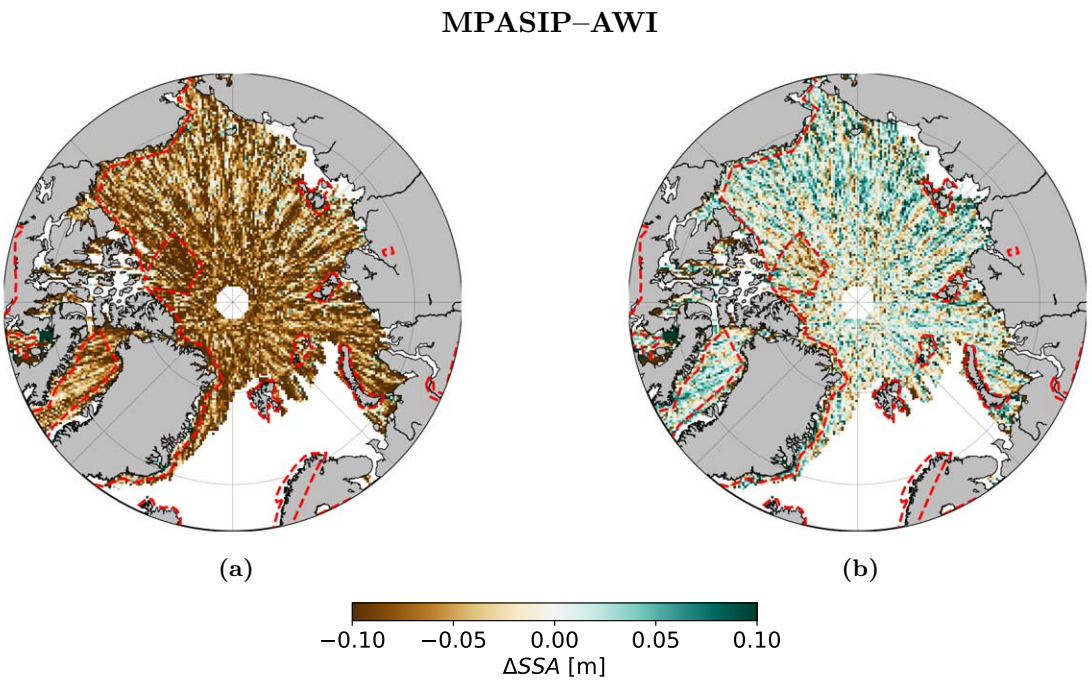

Figure 7.11: Difference between the sea surface anomaly (SSA) estimated by MPASIP and AWI (a) and same plot after the mean difference between the two fields is removed (b)

waveforms. However, the lower height estimates from some of the subsequent peaks might also be due to the empirical maximum retracking correction of 35 cm, discussed in section 7.2.2, not being large enough to account for the different retracking techniques used for sea ice and both leads and subsequent peaks.

Figure 7.11b, does not show any clear pattern in the differential SSA in the rest of the Lincoln Sea which could explain the smaller MPASIP freeboard observed in this region compared to the AWI product (figure 7.9b). This suggests that the reason for the different radar freeboard values in this area might be due to the MPASIP misclassification of some snagged waveforms as sea ice, discussed in section 7.3.1, which would result in an underestimation of the radar freeboard. It is speculated that this could also be the reason for the slightly smaller MPASIP freeboard, compared to AWI, in regions covered by multi-year ice (MYI), as the absolute difference between the ice and the sea surface would be larger on thicker ice than on thin first-year ice (FYI).

The difference MPASIP–JPL in figure 7.9d shows a general overestimation of the radar freeboard by MPASIP compared to JPL, reaching up to 10 cm over the thick MYI north of Greenland and the Canadian Archipelago. It is hard to evaluate retrievals inside the WB as the JPL dataset discards many waveforms in this area due to the snagging caused by off-nadir leads [Kwok, personal communication]. This difference is likely attributed to the snow layer on top of the sea ice. As discussed in section 4.1, the main scattering horizon of CS signals is likely located somewhere between the air/snow and snow/ice interfaces. The radar not penetrating completely the snow pack would result in an overestimated freeboard height. JPL elevations are obtained using a retracker which takes the range to the ice surface as the centroid of the waveform area in the interval between the range location of the selected peak and 1.5 times the range to the half-power point on the leading edge of that peak [Kwok & Cunningham, 2015]. The retracking point selected by this method would generally correspond to a leading edge power threshold larger than 50% which would result in smaller radar freeboards [Ricker et al., 2014]. Additionally, based on simulations, Kwok [2014] suggested that this kind of retracker could be less sensitive to

the broadening of the waveform leading edge caused by scattering from the air/snow interface. This could explain the larger freeboard differences between MPASIP and JPL retrievals over MYI compared to the difference over FYI, as MYI carries a thicker layer of snow (section 2.4). The smaller radar freeboard measured in the Beaufort Sea by MPASIP compared to JPL is likely due to the misclassification of some snagged waveforms as sea ice, discussed in section 7.3.1. At the time of writing, SSAs estimates from JPL were not available so that possible freeboard differences attributed to the way in which MPASIP determines the SSA are not investigated here.

The same general pattern of overestimated freeboard, especially over MYI, is observed in figure 7.9f showing the difference AWI–JPL. This further support the hypothesis that this difference might be retracker-dependent, as AWI uses a 50% threshold algorithm like MPASIP. The underestimation of freeboard in the Beaufort Sea from AWI compared to JPL might again be due to the more conservative filtering of snagged waveforms performed by JPL compared to AWI, although further investigation in this region is required.

The radar freeboard heights in figure 7.9 show a larger geographical coverage of MPASIP compared to AWI and JPL, especially in coastal areas, e.g. the Canadian Archipelago, the Nares Strait and Greenland's northern and eastern fjords. The northern coast of Greenland is enlarged in figure 7.12 which shows the single valid radar freeboard retrievals as well as their gridded average for MPASIP, AWI and JPL processors. While AWI product does not estimate freeboard closer than 20–30 km from the coast, probably using only CS measurements contained into grid cells for which a valid OSI SAF sea ice type is available, MPASIP and JPL retrieve estimates very close to the coastline. The JPL product discards many measurements due to snagging and probably also many waveforms contaminated by reflections from land. MPASIP, on the other hand, retrieves a larger amount of valid surface measurements by using the SARIn phase information, resulting in the increased coverage shown in figure 7.12. This additionally suggests the potential for MPASIP to estimate sea ice freeboard and thickness in coastal areas, although a more thorough validation in these regions is needed. Valid MPASIP freeboard heights seem located on land in figure 7.12a because these plots use the inaccurate GSHHG coastline (see also figure 7.2).

7.3.3 Airborne validation

To put into context the differences of freeboard estimates presented in the previous section, results from the MPASIP, AWI and JPL processors for March 2014 are compared to airborne measurements from the NASA Operation IceBridge (OIB) 2014 campaign (quicklook products, see section 5.2.2). All CS and OIB measurements acquired between March 12–31 are included in the comparison. The corresponding OIB tracks are plotted in blue in figure 7.13.

The following analysis focuses on radar freeboard, sea ice freeboard and sea ice thickness to separate the impact of the proposed SARIn processing scheme on the results, from differences attributed to the snow depth, snow density, ice type and ice densities used in the conversion of the radar freeboard to sea ice freeboard and thickness. All parameters are averaged to the same 25-km grid used throughout the study (Appendix C) prior to comparison and differences in the correlation, mean difference and standard deviation between satellite and airborne datasets are discussed. In order to make the comparison fair in terms of how representative satellite and airborne samples are for a single grid cell, only grid cells with a minimum of 10 CS measurement and at least 100 OIB measurements are used. The values are chosen considering the case in which a single CS and OIB tracks would cross a grid cell. These quantities would ensure 3 and 4 km of sampled ground, considering the along-track resolutions of 300 and 40 m for CS and the OIB datset, respectively. OIB estimates of sea ice freeboard are obtained by subtracting

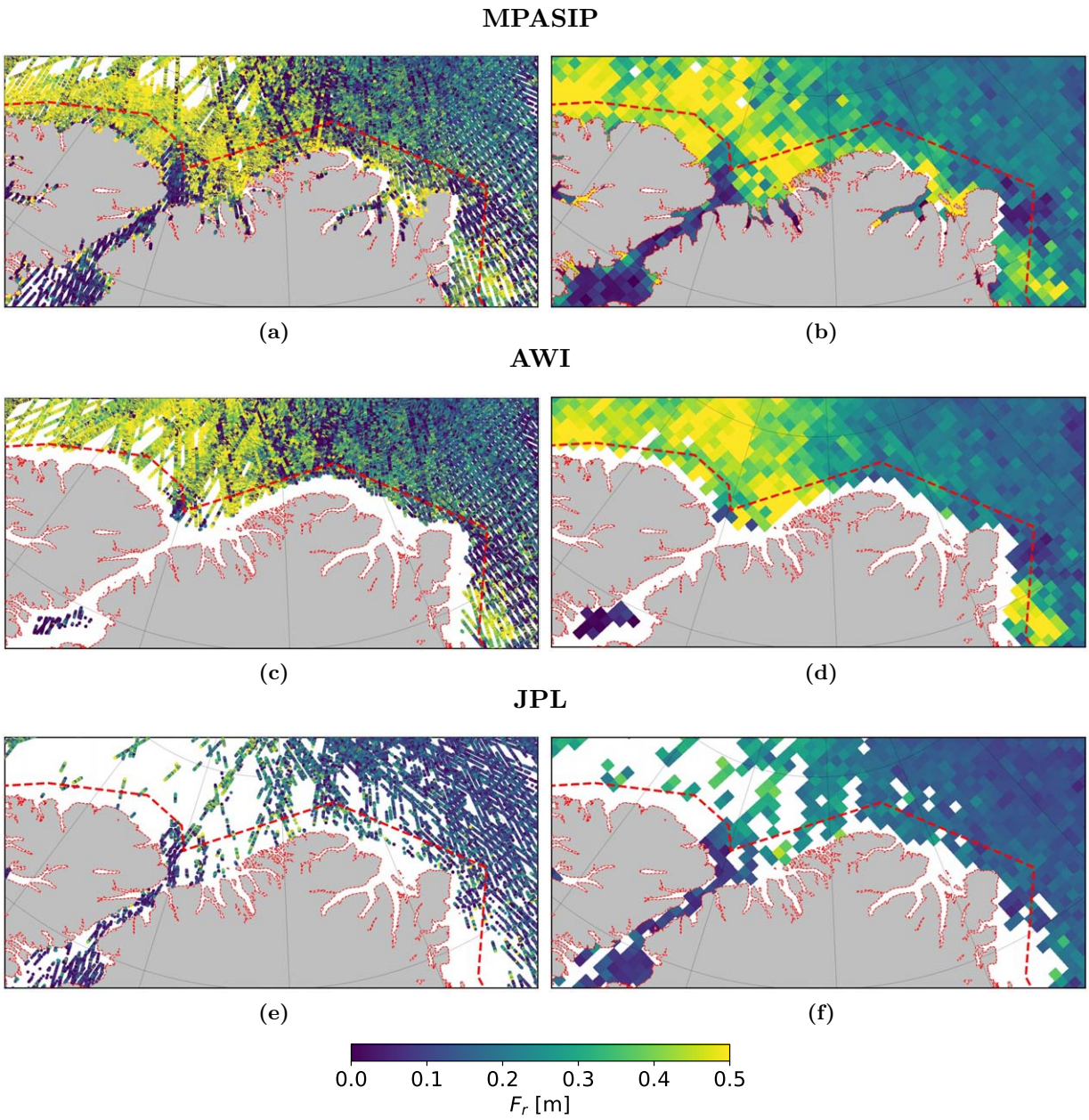

Figure 7.12: Radar sea ice freeboard for March 2014 along the coast of Greenland as estimated by the MPASIP (a), AWI (c) and JPL (e) processors. The gridded averages are shown in the right column (b-d-f). The dashed red line represents the CS SARIn acquisition mask

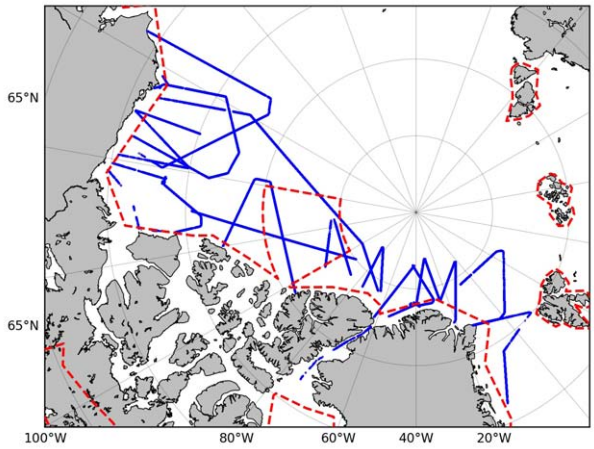

Figure 7.13: NASA Operation IceBridge data from the 2014 campaign used in the analysis in section 7.3.3. The dashed red line indicates the boundaries of the CS SARIn acquisition mask

the snow depth provided in the product from the mean snow freeboard measured by the laser scanner onboard the aircraft. To simulate a radar freeboard retrieval, the computed OIB sea ice freeboard is decreased by subtracting the δ_d correction from it, accounting for the path delay caused by a snow layer to a radar signal (section 4.1). This correction is computed according to equations 4.5 and 4.6 using a constant snow density of 320 kg/m^3 [Kurtz et al., 2013]. This step is performed to account for the fact that the snow depth used by MPASIP, AWI and JPL is derived from a snow climatology while OIB ice bridge uses measurements performed by the snow radar onboard the aircraft.

The results of the comparison are summarised in table 7.2. All three processors show similar values of correlations with the OIB dataset for radar and sea ice freeboard as well as sea ice thickness. A correlation higher than 0.5 is found for all parameters, with the best match observed in the thickness comparison (∼0.7). The thickness correlations found here have values comparable to the ones obtained in similar studies by Laxon et al. [2013] (0.61) and Kwok & Cunningham [2015] (0.53) which used OIB data from the 2011–12 campaigns. Figure 7.14 shows the comparison of the three thickness estimates from CS with those from OIB. Freeboard values are not plotted as they have a correlation very similar to the thickness.

MPASIP–OIB shows a 5 cm average difference in the radar freeboard, compared to the 4 and –2 cm for AWI–OIB and JPL–OIB, respectively. Similarly, the differences between the CS and OIB sea ice freeboard are 7, 6 and 1 cm for MPASIP, AWI and JPL, respectively. Since OIB measurements are mainly performed on MYI (figure 7.13), the lower estimate of freeboard from the JPL dataset is probably due to the different retracker, which might be less affected by the scattering from the air/snow interface (section 7.3.2). This is further visible in the reduced standard deviation of the radar freeboard heights from JPL (7 cm) compared to the standard deviations of MPASIP and AWI (12 and 11 cm). Deviations of the CS radar and sea ice freeboard from the airborne estimates from OIB are very similar for MPASIP and AWI, indicating comparable performance.

MPASIP, AWI and JPL mean differences from the OIB thickness estimates are 12, 2 and –14 cm, respectively. These results are based on specific assumptions of snow depth and density as well as ice densities. MPASIP and AWI should have similar results as they both use snow depths and densities from a modified W99 climatology as well as ice densities from Alexandrov et al. [2010]. However, an analysis of the snow density shows differences of ±50 kg/m^3 in the values used by MPASIP and AWI for the region of interest to this comparison, which require further

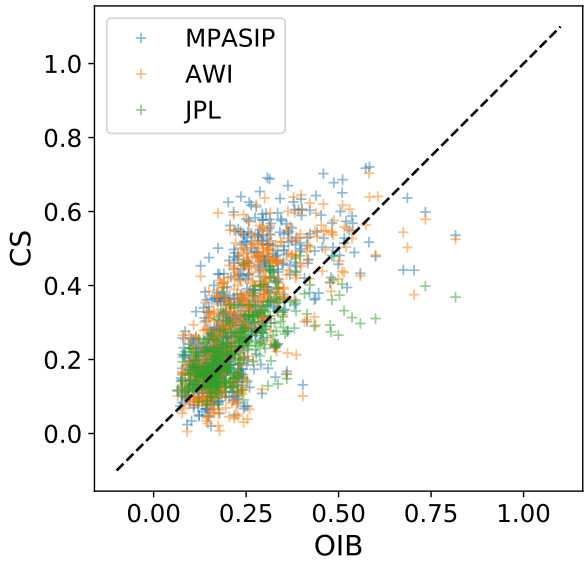

Figure 7.14: Comparison of the March 2014 sea ice thickness estimates produced by the MPASIP, AWI and JPL processors (CS data) with estimates from the NASA Operation IceBridge (OIB) 2014 campaign

All data			
	MPASIP	**AWI**	**JPL**
$\mathbf{r_{F_r}}$	0.61	0.63	0.59
$\mathbf{\Delta F_r}$	0.05 ± 0.12	0.04 ± 0.11	−0.02 ± 0.07
$\mathbf{r_{F_i}}$	0.69	0.70	0.68
$\mathbf{\Delta F_i}$	0.07 ± 0.12	0.06 ± 0.11	0.01 ± 0.08
$\mathbf{r_T}$	0.71	0.73	0.71
$\mathbf{\Delta T}$	0.12 ± 0.84	0.02 ± 0.82	−0.14 ± 0.74
$\mathbf{N_c}$	639	614	384

Table 7.2: Statistics for the comparison between MPASIP, AWI and JPL radar freeboard (F_r), sea ice freeboard (F_i) and sea ice thickness (T) with airborne data from the OIB 2014 campaign. Grid correlations (r) as well as mean deviations in m from OIB estimates (Δ) ± the standard deviation are provided for each parameter. The number of coincident grid cells used in the analysis (N_c) is also provided

investigation. JPL uses time-varying snow densities and the snow depth is corrected differently for thin freeboard [Kwok, personal communication]. Also, a single ice density is used for FYI and MYI, so that differences in the final mean ice thickness are to be expected. These results are based on the analysis of a different number of grid cells, specifically 639, 614 and 384 for MPASIP, AWI and JPL, respectively.

In order to assess possible improvements brought by the MPASIP processing scheme, the same comparison is performed using only grid cells where SIRAL operates in SARIn mode. The results are summarised in table 7.3. The mean deviation of the MPASIP and AWI radar (sea ice) freeboard heights from OIB estimates is 13 (15) and 13 (14) cm, respectively, showing again similar performance for these two processors in the analysed regions. The lower difference of

SARIn areas			
	MPASIP	**AWI**	**JPL**
$\mathbf{r_{F_r}}$	0.32	0.27	0.39
$\mathbf{\Delta F_r}$	0.13 ± 0.15	0.13 ± 0.13	−0.03 ± 0.07
$\mathbf{r_{F_i}}$	0.45	0.34	0.58
$\mathbf{\Delta F_i}$	0.15 ± 0.15	0.14 ± 0.12	−0.01 ± 0.07
$\mathbf{r_T}$	0.55	0.45	0.71
$\mathbf{\Delta T}$	0.34 ± 1.02	0.24 ± 0.91	−0.34 ± 0.57
$\mathbf{N_c}$	144	116	28

Table 7.3: Statistics for the comparison between MPASIP, AWI and JPL radar freeboard (F_r), sea ice freeboard (F_i) and sea ice thickness (T) with airborne data from the OIB 2014 campaign using only data from regions where SIRAL operates in SARIn mode. Grid correlations (r) as well as mean deviations in m from OIB estimates (Δ) ± the standard deviation are provided for each parameter. The number of coincident grid cells used in the analysis (N_c) is also provided

the AWI–OIB sea ice thickness compared to MPASIP–OIB is due to the differences in the snow density used by the 2 processors, previously discussed.

In SARIn areas, a general drop in the correlations is observed for all parameters and processors, with the exception of the JPL sea ice thickness which is stable at 0.71. The correlation of the radar and sea ice freeboard as well as thickness is always larger for MPASIP than for AWI, as opposed to the case where also SAR grid cells are included in the analysis. This possibly indicates a better sampling of the SSA due to the increased amount of lead measurements performed by MPASIP in SARIn regions (section 7.3.4).

In general, JPL results seem to be the most consistent in terms of correlations as well as mean differences and standard deviations with the OIB dataset. Part of the reason could be the number of grid cell used for the analysis by every processor, namely 144, 116 and 28 grid cells for MPASIP, AWI and JPL, respectively. The JPL classification algorithm seems to be more selective about the data to process, obtaining a better match of radar and sea ice freeboard with OIB retrievals, at the expense of the spatial coverage. With regard to the sea ice thickness, AWI estimates tend to have the best agreement with OIB estimates in terms of mean deviation. The slightly higher standard deviation of MPASIP results compared to AWI suggests a somewhat larger noise in the parameters retrieved by MPASIP which might be due to the higher noise of lead heights from subsequent peaks used by the MPASIP processor. However, it has to be noticed that the retracking of subsequent peaks in MPASIP, in its current version, is far from being optimal. Just as an example, the maximum correction added to lead heights from subsequent peaks is empirically limited to a maximum of 35 cm (section 7.2.2). This value does not represent the half-power point for most of the wider subsequent peaks, so that the SSA in regions with clusters of subsequent peaks might be lower than in reality, suffering from a retracker-dependent bias.

7.3.4 Uncertainty reduction

As discussed in section 6.3.4, the possible reduction of the random part of the freeboard uncertainty is mainly governed by the amount of detected leads. The amount of lead measurements (L)

Region	L	L_0 (%)	$L_{ASIP-SAR}$ (%)	$WF_{p>1}$/WF (%)
SARIn mask	145725	97204 (149.9)	25565 (570)	45759/755780 (6.1)
WB	21797	1741 (1252.0)	3448 (632)	19937/184760 (10.8)

Table 7.4: Number of lead measurements performed by MPASIP (L) and ASIP SAR ($L_{ASIP-SAR}$) in SARIn regions and inside the Wingham Box (WB) in March 2014. L_0 is the number of waveforms where the first peak is classified as a lead by MPASIP. The amount of waveforms with more than one usable peak ($WF_{p>1}$) with respect to the total amount of waveforms (WF) for ASIP is also provided. Percentage values between parentheses in columns L_0 and $L_{ASIP-SAR}$ are computed as L/L_0 and $L/L_{ASIP-SAR}$, respectively

performed in March 2014 by MPASIP, including subsequent peaks, inside the SARIn mask and inside the Wingham Box (WB) are provided in table 7.4. The values for the entire Arctic Ocean are not reported here due to the reduced area in which SIRAL operates in SARIn mode. In order to assess the increase in the number of lead measurements attributed to the processing of subsequent peaks, L is compared with two parameters: the number of waveforms where the first peak is classified as a lead (L_0) and the number of leads detected in the same month by the ASIP SAR processor ($L_{ASIP-SAR}$). L_0 can be considered a measure of the improvement, in terms of lead detection, attributed to the processing of the subsequent peaks compared to the case in which MPASIP would only use the first significant peak of the waveforms. On the other hand, $L_{ASIP-SAR}$ is provided as a reference representing the case of a regular SAR processing scheme.

In the SARIn mask (WB), the total number of lead measurements performed by MPASIP is ∼1.5 (∼12) times larger when subsequent peaks are retracked than when they are not. Compared to the ASIP SAR processor, MPASIP measures ∼5 and ∼6 times more leads in the SARIn region and the WB, respectively. Although these values show a significant increase in the amount of lead measurements performed by the MPASIP processor, one should notice that (1) the MPASIP processor uses echoes generating closer to the coast compared to the ASIP SAR processor which should be taken into account in the comparison of L and $L_{ASIP-SAR}$ for SARIn areas, and (2) some of the subsequent peaks classified as leads might not be actual leads, as discussed in section 7.3.2. Thus, repeating this analysis with an improved classification and retracking algorithms might provide a better match with external sea ice freeboard and thickness products but a somewhat lower amount of lead measurements. Table 7.4 additionally provides a count of the amount of waveforms with more than one usable peak ($WF_{p>1}$) with respect to the total amount of waveforms (WF), showing that multiple peaks are used only in 6.1% and 10.8% of the waveforms in the SARIn mask and inside the WB, respectively. This value will vary according to the actual geographical lead distribution since significant subsequent peaks are detected only when off-nadir leads are within few kilometres from the satellite nadir.

The amount of lead heights retrieved by MPASIP affects both the average SSA point uncertainty and the number of valid freeboard retrievals in a grid cell (section 6.3.4). This can be observed in table 7.5 which reports the average point random uncertainties of freeboard ($\overline{\sigma}_F$) and thickness ($\overline{\sigma}_T$) estimates as well as the number of valid freeboard (N_F) and thickness (N_T) retrievals. All values refer to data acquired in the SARIn area and are compared with the reference values provided by ASIP SAR. Uncertainty reductions of 37% and 24% are observed for the sea ice freeboard and thickness, respectively, and are attributed to the increased number of lead measurements which reduces the average point SSA uncertainty. The larger number of detected leads also results in the ∼3-fold increase of the number of valid freeboard and thickness estimates for MPASIP, when compared to ASIP SAR. Once again, it has to be noticed that the increase in N_F and N_T is partly due to measurements performed only by MPASIP in coastal

	MPASIP	**ASIP SAR**	**Variation [%]**
$\overline{\sigma}_F$ [cm]	18.1	28.6	−37
N_F	631911	173388	+265
$\overline{\sigma}_T$ [m]	1.70	2.25	−24
N_T	624585	172043	+263

Table 7.5: Point statistics for SARIn regions. Average freeboard and thickness random uncertainties (σ_F and σ_T) together with the number of valid retrievals (N) are computed for the MPASIP and compared to the values for the ASIP SAR processor provided in section 6.3.4. The value in the last column is the percentage of variation obtained by MPASIP with respect to ASIP SAR

areas.

Figure 7.15 shows the gridded radar freeboard and uncertainty for March 2014 from MPASIP and ASIP SAR as well as the corresponding differences. The increased coverage of MPASIP can be observed in figure 7.15a. While this shows a potential for freeboard and thickness estimation in the Canadian archipelago and coastal areas, proper validation in these areas needs to be performed. Furthermore, it is likely that until an updated pan-Arctic snow depth product is available to the sea ice community, thickness estimates from the Canadian archipelago would not be accurate as the W99 climatology does not have a sufficiently representative sampling for the snow depth in that area [Ricker et al., 2014].

Looking at the difference between radar freeboard estimates in figure 7.15e, one can notice a good agreement between MPASIP and ASIP SAR in regions where CS operates in SAR mode, with slightly lower values for MPASIP. This is likely due to the side lobe filter applied by MPASIP, which takes additional care of the noise in front of the waveforms leading edge, as well as by the additional power threshold used by MPASIP to detect strong reflections from leads. This additional constraint further filters out possible snagged waveforms which tends to lower the absolute value of the SSA and, thus, to increase the freeboard. MPASIP shows a larger freeboard in SARIn areas compared to ASIP SAR, with an average difference of ∼3 cm (table 7.6). This overestimation, observed also in the comparison between MPASIP and the AWI, JPL and OIB datasets (sections 7.3.2 and 7.3.3), is attributed to possible inaccuracies in the MPASIP classification and retracking algorithms, resulting into some subsequent peaks not representing significant reflections from off-nadir leads being included in the processing (section 7.3.2).

Figure 7.15f shows the percentage of reduction of the radar freeboard uncertainty obtained from MPASIP compared to the uncertainty of the ASIP SAR radar freeboard. The increase in the random uncertainty in the central Arctic, around the WB and in the Chukchi Sea is due to the different approach used by MPASIP and ASIP to compute the uncertainty of the SSA. When no lead is detected, both processors assign the deviation of the interpolated SSA from the local sea ice elevation as an uncertainty of the SSA. However, while ASIP uses a 25-km moving window to detect lead heights and compute their standard deviation, MPASIP uses fixed 25-km segments. Thus, in areas characterised by sparse lead measurements, the uncertainty of the ASIP SSA will be substantially lower than the one from MPASIP. Also, due to the aforementioned extra power threshold used for lead detection by MPASIP, areas with fewer leads will be more common. The moving-window approach used by ASIP is found to be more fair than the fixed-window used by MPASIP, as in the latter case points located just hundreds of metres from a lead, but pertaining to a different segment where no leads are detected, will be assigned a larger value of SSA uncertainty. For this reason, the MPASIP SSA estimation algorithm will be updated in the

	MPASIP	ASIP SAR	Variation
$\overline{F}_r$ [cm]	20.1	17.1	+3 cm
$\overline{\sigma}_F$ [cm]	1.9	4.2	−54%
$\overline{T}$ [m]	2.38	2.27	+0.11 m
$\overline{\sigma}_T$ [m]	0.18	0.38	−52%

Table 7.6: Grid cell statistics for SARIn regions. Average radar freeboard (F_r) and sea ice thickness (T) together with the respective random uncertainties (σ_F and σ_T) are computed for the MPASIP and compared to the values for the ASIP SAR processor provided in section 6.3.4. The variation expressed in the last column refers to the difference MPASIP–ASIP SAR

near future to inherit the moving-window approach used by ASIP.

On the other hand, in regions where many lead measurements are available, the two uncertainties will have more similar values and can be compared safely. From figure 7.15f and table 7.6 it can be observed that in SARIn areas the random gridded freeboard uncertainty is reduced from 4.2 to 1.9 cm (∼54%) when comparing values from MPASIP and ASIP SAR. In the current version of MPASIP, this value should probably not be considered as an actual, but more as a potential reduction of the uncertainty, due to the current biases in the absolute value of radar freeboard discussed in sections 7.3.2 and 7.3.3.

Plots of sea ice thickness and the respective uncertainties are not shown here as they follow the same pattern as the radar freeboard and its related uncertainties (as shown in section 6.3.4). Table 7.6 shows a potential reduction of the SARIn random thickness uncertainty of ∼52% with an ∼11 cm overestimation when comparing results from MPASIP and ASIP SAR. If the systematic contributions to the sea ice thickness uncertainty from the snow depth and snow density are included in the error budget, the 52% reduction in the random uncertainty observed in March 2014 translates into a reduction in the total sea ice thickness uncertainty from 51 to 35 cm, i.e., ∼30%.

7.4 Summary and conclusions

An Arctic sea ice processor is developed at JPL, as a part of this PhD project, to assess the potential and limitations of the CS SARIn acquisition mode with regard to sea ice freeboard and thickness estimation in the Arctic Ocean. In particular, the sea ice processor (MPASIP) is designed to process several parts of single CS SARIn L1b waveforms and to investigate if more than one valid surface height estimate can be retrieved from single waveforms in sea ice-covered regions. In regular sea ice altimetry processing schemes, only the first significant peak of a waveform is usually retracked, as it is associated with echoes coming from regions close to the satellite nadir. MPASIP investigates if additional height estimates can be obtained by retracking peaks further down the trailing edge of SARIn waveforms, together with the associated phase information.

The lead detection capabilities of CS as well as the peak detection and classification algorithms are validated using Sentinel-1 (S1) SAR images. It is shown that single SIRAL waveforms can show contributions from both the sea ice at nadir and specular reflections from off-nadir leads. The phase information provided by SIRAL can be used to accurately determine the across-track location of such reflections and to separate those generating from the sea ice at nadir from the scattering happening further away from the satellite track. A good match is found between

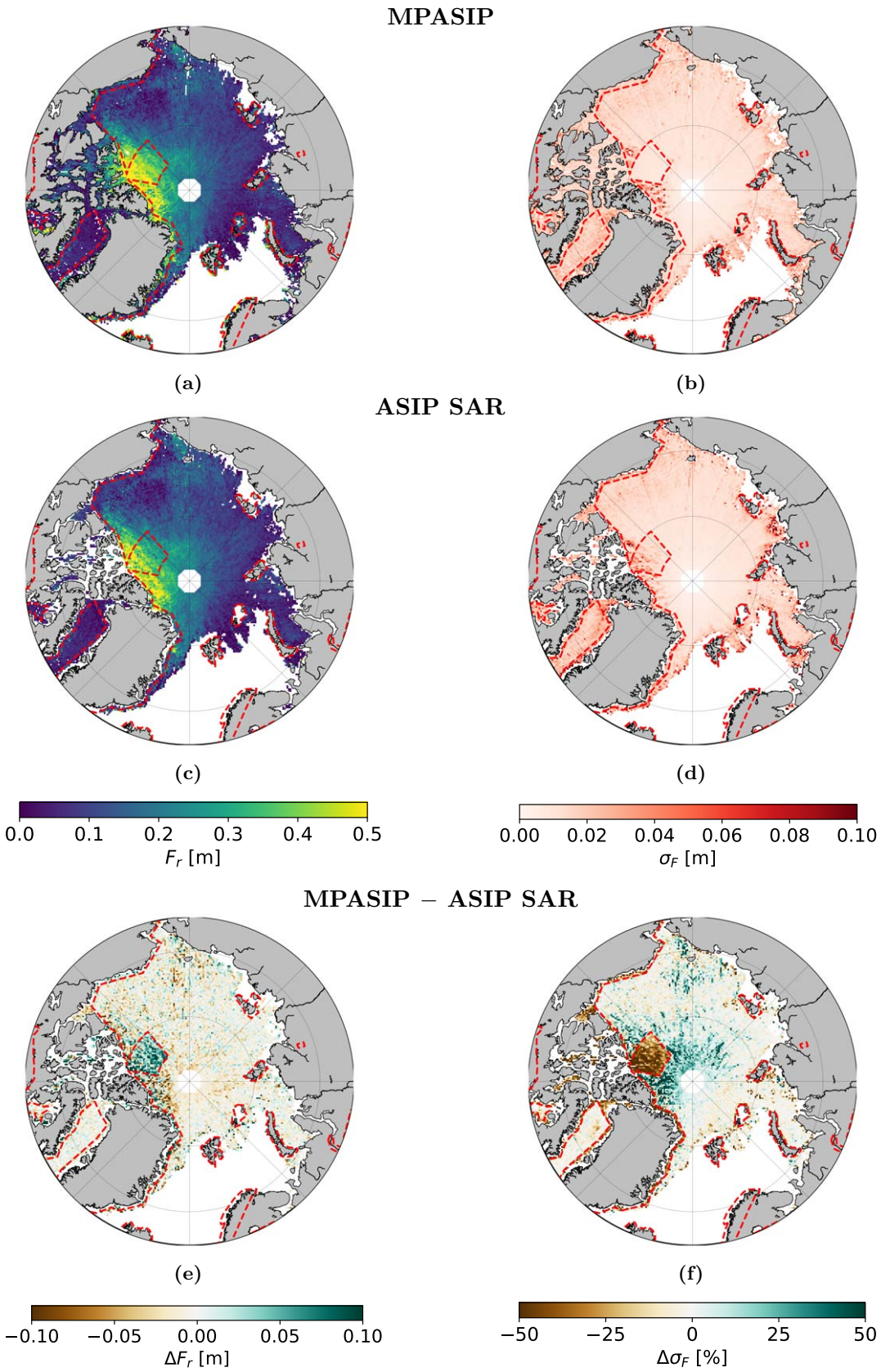

Figure 7.15: Arctic radar freeboard maps and random uncertainties for March 2014 from MPASIP ((a) and (b)) and ASIP SAR ((c) and (d)). (e) is the difference (a)−(c) and (f) represents the percentage of variation of (b) with respect to (d)

peaks classified by MPASIP as off-nadir leads and ground features visible in S1 SAR images, although the thresholds used in the classification might need further tuning to avoid some snagged waveforms to be classified as ice.

The radar freeboard estimates obtained from MPASIP in March 2014 are compared with those generated by AWI and JPL. Both the MPASIP and AWI estimates show an overestimation of the radar freeboard compared to the estimates from JPL, especially over MYI. This difference can be partly attributed to the partial penetration of the CS signal into the snow pack and the fact that the retracker used in the JPL product is less sensitive to scattering from the air/snow interface [Kwok, 2014]. A general good agreement is found between MPASIP and AWI freeboard heights with some local discrepancies inside the Wingham Box (WB). The larger MPASIP freeboard observed in the WB compared to AWI (∼2 cm) is found to be partially caused by a slight underestimation of the SSA in SARIn areas by MPASIP. This lower SSA is due to the inclusion of height estimates from some of the retracked subsequent peaks on the trailing edge of SARIn waveforms. This suggests further investigation towards (1) an improved characterisation of subsequent peaks for SARIn waveforms, so as to select only the most relevant peaks and (2) a tailored retracking procedure applied to these peaks, as part of the MPASIP freeboard overestimation might be attributed to the different retrackers used for sea ice and lead/subsequent peaks. Nevertheless, a large number of subsequent peaks seem to provide valid sea surface height measurements.

Radar and sea ice freeboard as well as thickness retrievals from the MPASIP, AWI and JPL processors are additionally compared to gridded airborne estimates from the OIB campaign in March 2014. While all products show a good correlation with the OIB dataset (0.6–0.7), MPASIP and AWI tend to overestimate the sea ice freeboard (7 and 6 cm, respectively), whereas JPL estimates show the best match with the airborne data (–1 cm). Limiting the analysis to SARIn regions shows a similar trend, with differences of 15 and 14 cm in the sea ice freeboard computed respectively by MPASIP and AWI and only 1 cm for JPL, supporting the hypothesis that this deviation might be retracker-dependent. While correlation values generally drop for all parameters in SARIn regions, MPASIP shows a higher correlation of the sea ice freeboard with the OIB dataset compared to AWI (0.45 vs. 0.34) which might reflect the better sampling of the local SSA due to the increased amount of lead measurements.

By including relevant peaks on the trailing edge of SARIn waveforms, MPASIP performs ∼5 times more lead measurements in SARIn regions than the ASIP SAR processor (chapter 6), which is considered in this study the reference case for a regular SAR processing scheme. Despite the lower accuracy of height measurements from off-nadir leads compared to specular returns from the satellite nadir, the larger number of sea surface height measurements ultimately reduces the average random uncertainty of the SSA as well as it increases the number of valid freeboard and thickness retrievals in SARIn regions. In March 2014, MPASIP exhibits a ∼50% potential reduction of the grid-averaged random sea ice freeboard and thickness uncertainties, compared to the reference value provided by the ASIP SAR processor. This translates into a ∼30% reduction of the total thickness uncertainty, when systematic contributions from the snow depth and density are taken into account. These values are based on the assumption that contributions from all error sources are uncorrelated, although further investigation is needed to determine the covariance of individual error contributions.

The potential for coastal freeboard and thickness estimation is suggested by the significantly increased freeboard heights retrieved by MPASIP along the northern coast of Greenland compared to the AWI and JPL processors. Further investigation should include a thorough validation of these estimates using in-situ and airborne measurements.

Chapter 8

Project conclusions and perspectives

Sea ice is one of the most significant climate parameters interacting with several feedback processes of the global climate system. Besides the scientific interest as a climate indicator, knowledge of the sea ice cover and thickness are important for the shipping and fishery industries as well as for exploration and off-shore activities [Ulaby et al., 1986]. Since the 1980's, a combination of satellite observations from passive radiometers and submarine data have shown a rapid reduction of the ice-covered area and a general thinning of Arctic sea ice [Comiso et al., 1991; Rothrock et al., 1999; Kwok et al., 2009]. For the past 25 years, satellite altimetry has been used to infer sea ice thickness from the direct measurement of the sea ice freeboard, i.e. the height of the ice surface above the local sea level. However, in the freeboard-to-thickness conversion the freeboard and the associated errors are typically multiplied by a factor of $\sim$10 [Wingham et al., 2006], thus, it is fundamental to both improve the accuracy of freeboard estimates as well as to minimise their uncertainty.

The largest source of freeboard uncertainty, after the contribution due to the lack of knowledge of the Arctic snow cover, originates from the poor knowledge of the sea surface height (SSH) in ice-covered regions [Ricker et al., 2014]. Armitage & Davidson [2014] have demonstrated that CryoSat-2's (CS) interferometric mode (SARIn) enables to process waveforms whose power echo is dominated by the strong reflection from off-nadir leads, referred to as "snagged" waveforms, which are usually discarded in common SAR altimetry data processing. In fact, the available phase information can be used to correct for the associated range error and to retrieve a larger number of valid SSH measurements which, ultimately, increases the accuracy as well as reduces the uncertainty of the area-averaged SSH. The SARIn phase information is currently not used by the scientific community in the sea ice freeboard and thickness estimation, probably because of the scarce SARIn coverage of the Arctic Ocean. In this work, an assessment of the potential and limitations of the CS SARIn mode with respect to the estimation of the sea ice freeboard and thickness in the Arctic is performed. Besides being of interest to the sea ice community, such an assessment could inform the proposal and design of future SARIn-only satellite altimetry missions.

Following up on the work by Armitage & Davidson [2014], the first part of this project was aimed at investigating how the phase information provided by the CS SARIn acquisition mode affects Arctic sea ice freeboard and thickness retrievals as well as their corresponding random uncertainties. An Arctic sea ice processor (ASIP) was developed at DTU to process CS SAR and SARIn L1b waveforms according to a regular SAR processing scheme, where only the power echoes are used, as well as by using the SARIn phase information.

It is shown that CS SARIn mode can accurately detect off-nadir leads up to $\sim$2 km from the satellite nadir and correct for the associated range overestimation using the interferometric information. The comparison of along-track sea ice freeboard estimates from ASIP with airborne

measurements from the ESA CryoVEx and NASA Operation IceBridge (OIB) campaigns concludes that, by using the phase information, the average random freeboard uncertainty of single CS freeboard estimates can potentially be reduced without introducing a bias on the average freeboard heights.

A difference in the SAR and SARIn freeboard heights of ∼4 cm is found at the boundary of the SARIn acquisition mask if no extra care is taken to deal with the larger, compared to SAR, noise on the leading edge of SARIn waveforms. This difference does not depend on the inclusion of the SARIn phase information in the processing. After overestimated SARIn sea ice elevations are filtered out, no bias is found between the SAR and SARIn freeboard heights at the boundaries of the SARIn mask when the interferometric phase information is used and the off-nadir range correction (ONC) is applied only to lead heights.

By correcting for the overestimated range due to the snagging effect, it is possible to process more waveforms than in a regular SAR processing scheme. The larger amount of both the processed waveforms and the detected leads is then increased significantly. This results in a 14% and 13% reduction of the gridded random uncertainty of freeboard and thickness estimates, respectively, in SARIn areas when compared to the the results from the regular SAR reference case.

During the analysis performed in this part of the study, an issue in the ESA Baseline C IPF1, the processor responsible of computing SAR and SARIn L1b waveforms, has been detected. This issue causes inaccurate values of phase difference to be computed for some waveforms at the boundaries of the SARIn mask. Working closely with ESA and Dr. Scagliola from ARESYS S.r.l., the issue has been solved and the upcoming CS Baseline D L1b products will feature more accurate values of phase difference in regions where SIRAL switches from the SAR to the SARIn acquisition mode. Improvements are expected not only for sea ice freeboard retrieval, but for any application that exploits the phase information from SARIn L1b products in regions close to the boundaries of the SARIn mask.

By using the interferometric information available in the SARIn acquisition mode, one could potentially get more than one valid height estimate per waveform. The second part of the project describes the work carried out at the NASA Jet Propulsion Laboratory (JPL) in cooperation with Dr. Kwok and Dr. Armitage. Here, a second sea ice processor (MPASIP) was developed to investigate if the number of valid sea ice as well as lead measurements could be increased by processing multiple peaks of single CS SARIn waveforms, using the associated phase information, so as to further reduce the sea ice freeboard and thickness uncertainties.

From Sentinel-1 (S1) SAR images, it has been shown that the contributions from sea ice reflections close to the satellite nadir can potentially be separated from specular returns from off-nadir leads, for some SARIn waveforms. MPASIP's peak detection and classification algorithms perform well when compared with S1 images, although some of the thresholds currently used in the classification can be improved in order to process only the most relevant parts of SARIn waveforms.

Radar freeboard retrievals from MPASIP showed a general good agreement with estimates from the Alfred Wagner Institute (AWI) and the JPL processors, taking into account retracker-dependent differences. MPASIP and AWI, both using a 50% threshold retracker, overestimate freeboard heights compared to JPL especially over multi-year ice (MYI), where scattering from a thick layer of snow displaces the retracking point towards the satellite (the reatracker used by JPL is shown to be less sensitive to this phenomenon). An average 1.5 cm difference when subtracting AWI from MPASIP radar freeboard is found in SARIn areas, which is attributed to the lower sea surface anomaly (SSA) estimated by MPASIP compared to AWI. The underestimation of the SSA is found to be caused by the retracked heights of some of the additional peaks of the

SARIn waveforms processed by MPASIP. This result indicates that the current algorithm can be improved so as to filter out those subsequent peaks on the trailing edge of SARIn waveforms which provide inaccurate height estimates.

The comparison of sea ice freeboard and thickness estimates from MPASIP, AWI and JPL with those from OIB data shows a good correlation (∼0.7) and confirms the general retracker-dependent overestimation of MPASIP and AWI estimates. When considering only data in SARIn areas, JPL data show the best agreement with OIB estimates, although the number of compared grid cells is 5 to 6 times lower than for MPASIP and AWI product. The comparison between both MPASIP and AWI with the OIB dataset shows reduced correlations and increased average deviations of freeboard and thickness estimates in SARIn areas, when compared to the values computed for all regions covered by OIB data. In SARIn areas only, MPASIP shows a larger correlation with OIB estimates than AWI does, possibly due to a better sampling of the local SSA by MPASIP. In fact, MPASIP is shown to perform ∼5 times more lead measurements than those performed by the regular SAR processor (ASIP).

Comparing MPASIP and ASIP, the increased amount of both lead (∼5 times) and sea ice (∼2.5 times) measurements obtained by processing multiple peaks of single SARIn waveforms results in an average reduction of the gridded random freeboard and thickness uncertainties of 54% and 52%, respectively. This corresponds to a reduction in the total sea ice thickness uncertainty of ∼30% (from ∼51 to ∼35 cm), when the systematic contributions from the snow depth and density are taken into account. The uncertainty estimates computed in this project are based on the assumption that contributions from all error sources are uncorrelated. It is acknowledged, however, that they are just an approximation resulting from the lack of knowledge of the covariance of individual error contributions. Nevertheless, the achieved reduction of the random uncertainty in SARIn areas is significant and suggests that a satellite altimetry mission operating in SARIn mode over the entire Arctic could provide more accurate estimates of sea ice freeboard and thickness.

8.1 Future work

In the coming months, the focus will be put on (1) improving the algorithm behind the MPASIP processor, (2) validating MPASIP sea ice freeboard and thickness retrievals in coastal regions and (3) working towards an operational version of MPASIP.

Despite sharing parts of the processing chain, the development of the ASIP and MPASIP sea ice processors took a significant amount of the time available in this project. The higher complexity of MPASIP posed several technical challenges and, despite the good results shown in chapter 7, there are several ideas to improve the current version of the processor. The concept behind MPASIP evolved throughout the project from a simple 2-peak retracking system to something looking more like a swath processor. A first obvious step will be to look more into procedures commonly performed in swath processing, e.g. the smoothing of the along-track interferogram [Gray et al., 2013] which could reduce the noise of the SARIn phase difference. However, this would result in a reduced slant range resolution, which might be too low for the accuracy required by freeboard estimation.

The first-peak classification algorithm will be improved, using along-track airborne validation data, to further filter out possible snagged waveforms currently classified as sea ice. Furthermore, statistical analyses will be performed in search of significant peak parameters to aid peak classification, so as to ensure that only significant contributions from the trailing edge of SARIn waveforms will be included in the processing. Finally, the upcoming Baseline D L1b products will provide a more accurate value of phase difference due to recent updates in the processing of

the CS star tracker data [Scagliola, personal communication] which might further improve the accuracy of the ONC.

Altimetry in coastal regions has proven to be more challenging than over open ocean due to e.g. land footprint contamination and degradation of geophysical corrections [Cipollini et al., 2017]. With a reduced along-track resolution of ∼300 m, CS can potentially estimate elevations quite close to the coast, depending on the complexity of the coastal profile and the orientation of the CS orbit. Abulaitijiang et al. [2015] showed that, when operating in SARIn mode, CS is able to retrieve valid sea surface height estimates up to ∼13 km away from the satellite nadir when flying over fjords in Eastern Greenland. MPASIP shows how the interferometric capabilities of CS can be used to measure freeboard heights closer to the coast compared to available sea ice products. Airborne data from the CryoVEx and OIB campaigns will be used in the coming months to validate retrievals in coastal regions so as to assess the potential for coastal freeboard and thickness estimations from the CS SARIn mode.

Finally, focus will be put on the overall optimisation of MPASIP, aiming at the distribution of sea ice freeboard and thickness products to the public. These products will have the advantage, over the ones currently available, to potentially provide freeboard and thickness estimates in coastal regions, increasingly important and relevant to society in connection to fishery, shipping and other off-shore activities [Pugh & Woodworth, 2014]. Additionally, they will feature smaller random uncertainties in SARIn regions, the second largest contribution to the total sea ice thickness uncertainty, thanks to the phase information provided by CS in these regions.

References

Aaboe, H., Breivik, L.-A., Eastwood, S., & Lavergne, T. (2018). Global Sea Ice Edge and Type Product User's Manual. OSI-402-c and OSI-403-c.
URL http://osisaf.met.no/docs/osisaf_cdop3_ss2_pum_ice-conc_v1p6.pdf

Abulaitijiang, A., Andersen, O. B., & Stenseng, L. (2015). Coastal sea level from inland CryoSat-2 interferometric SAR altimetry. *Geophysical Research Letters*, *42*(6), 1841–1847.

Alexandrov, V., Sandven, S., Wahlin, J., & Johannessen, O. M. (2010). The relation between sea ice thickness and freeboard in the Arctic. *The Cryosphere*, *4*, 373–380.
URL www.the-cryosphere.net/4/373/2010/

Andersen, O., Knudsen, P., Kenyon, S., Factor, J., & Holmes, S. (2017). Global gravity field from recent satellites (dtu15) - arctic improvements. *First Break*, *35*(12), 37–40.

Armitage, T. W. K., Bacon, S., Ridout, A. L., Petty, A. A., Wolbach, S., & Tsamados, M. (2017). Arctic Ocean surface geostrophic circulation 2003–2014. *The Cryosphere*, *11*, 1767–1780.
URL https://www.the-cryosphere.net/11/1767/2017/tc-11-1767-2017.pdf

Armitage, T. W. K., Bacon, S., Ridout, A. L., Thomas, S. F., Aksenov, Y., & Wingham, D. J. (2016). Arctic sea surface height variability and change from satellite radar altimetry and GRACE, 2003–2014. *Journal of Geophysical Research: Oceans*, *121*(6), 4302–4322.
URL https://eprints.soton.ac.uk/401159/1/jgrc21773.pdf

Armitage, T. W. K., & Davidson, M. W. J. (2014). Using the interferometric capabilities of the ESA CryoSat-2 mission to improve the accuracy of sea ice freeboard retrievals. *IEEE Transactions on Geoscience and Remote Sensing*, *52*(1), 529–536.

Armitage, T. W. K., & Ridout, A. L. (2015). Arctic sea ice freeboard from AltiKa and comparison with CryoSat-2 and Operation IceBridge. *Geophysical Research Letters*, *42*(16), 6724–6731.

Bamber, J., & Kwok, R. (2004). Remote-sensing techniques. In J. Bamber, & A. Payne (Eds.) *Mass balance of the cryosphere: observations and modelling of contemporary and future change*, (pp. 337–366). United Kingdom: Cambridge University Press.

Beaven, S., Lockhart, G., Gogineni, S., Hosseinmostafa, A., Jazek, K., Gow, A., Perovich, D., Fung, A., & Tjuatja, S. (1995). Laboratory measurements of radar backscatter from bare and snow-covered saline ice sheets. *International Journal of Remote Sensing*, *16*(5), 851–876.

Blanchard-Wrigglesworth, E., Webster, M. A., Farrell, S. L., & Bitz, C. M. (2018). Reconstruction of Snow on Arctic Sea Ice. *Journal of Geophysical Research: Oceans*, *123*(5), 3588–3602.
URL http://doi.wiley.com/10.1002/2017JC013364

Brodzik, M. J., Billingsley, B., Haran, T., Raup, B., Savoie, M. H., Brodzik, M. J., Billingsley, B., Haran, T., Raup, B., & Savoie, M. H. (2012). EASE-Grid 2.0: Incremental but Significant Improvements for Earth-Gridded Data Sets. *ISPRS International Journal of Geo-Information*, *1*(1), 32–45.
URL http://www.mdpi.com/2220-9964/1/1/32

Brown, G. (1977). The average impulse response of a rough surface and its applications. *IEEE Transactions on Antennas and Propagation*, *25*(1), 67–74.
URL http://ieeexplore.ieee.org/document/1141536/

Cartwright, D. E., & Edden, A. C. (1973). Corrected Tables of Tidal Harmonics. *Geophysical Journal International*, *33*(3), 253–264.
URL https://academic.oup.com/gji/article-lookup/doi/10.1111/j.1365-246X.1973.tb03420.x

Cipollini, P., Benveniste, J., Birol, F., Joana, M., Obligis, E., Passaro, M., Strub, P. T., Valladeau, G., Vignudelli, S., & Wilkin, J. (2017). Satellite Altimetry in Coastal Regions. In D. Stammer, & A. Cazenave (Eds.) *Satellite Altimetry Over Oceans and Land Surfaces*, chap. 11. CRC Press.

CNES (2013). SARAL/AltiKa Products Handbook. Doc ref.: SALP-MU-M-OP-15984-CN.
URL https://www.aviso.altimetry.fr/fileadmin/documents/data/tools/SARAL_Altika_products_handbook.pdf

Comiso, J. C., Wadhams, P., Krabill, W. B., Swift, R. N., Crawford, J. P., & Tucker, W. B. (1991). Top/bottom multisensor remote sensing of Arctic sea ice. *Journal of Geophysical Research: Oceans*, *96*(C2), 2693–2709.
URL http://doi.wiley.com/10.1029/90JC02466

Connor, L. N., Farrell, S. L., McAdoo, D. C., Krabill, W. B., & Manizade, S. (2013). Validating ICESat Over Thick Sea Ice in the Northern Canada Basin. *IEEE Transactions on Geoscience and Remote Sensing*, *51*(4), 2188–2200.
URL http://ieeexplore.ieee.org/document/6311459/

Connor, L. N., Laxon, S. W., Ridout, A. L., Krabill, W. B., & McAdoo, D. C. (2009). Comparison of Envisat radar and airborne laser altimeter measurements over Arctic sea ice. *Remote Sensing of Environment*, *113*(3), 563–570.
URL https://www.sciencedirect.com/science/article/pii/S0034425708003283

Davis, C. (1997). A robust threshold retracking algorithm for measuring ice-sheet surface elevation change from satellite radar altimeters. *IEEE Transactions on Geoscience and Remote Sensing*, *35*(4), 974–979.
URL http://ieeexplore.ieee.org/document/602540/

Deems, J. S., Painter, T. H., & Finnegan, D. C. (2013). Lidar measurement of snow depth: a review. *Journal of Glaciology*, *59*(215), 467–479.
URL https://www.cambridge.org/core/product/identifier/S0022143000204462/type/journal{_}article

Desch, S. J., Smith, N., Groppi, C., Vargas, P., Jackson, R., Kalyaan, A., Nguyen, P., Probst, L., Rubin, M. E., Singleton, H., Truitt, A., Zaw, P. P., & Hartnett, H. E. (2017). Arctic ice management. *Earth's Future*, *5*(1), 107–127.

Di Bella, A., Scagliola, M., Maestri, L., Skourup, H., & Forsberg, R. (2019). Improving CryoSat SARIn L1b products to account for inaccurate phase difference: impact on sea ice freeboard retrieval. Accepted for publication in *IEEE Geoscience and Remote Sensing Letters*.

Di Bella, A., Skourup, H., Bouffard, J., & Parrinello, T. (2018). Uncertainty reduction of Arctic sea ice freeboard from CryoSat-2 interferometric mode. *Advances in Space Research*, *62*(6), 1251–1264.
URL https://doi.org/10.1016/j.asr.2018.03.018

Drinkwater, M. R. (1991). Kuband airborne radar altimeter observations of marginal sea ice during the 1984 Marginal Ice Zone Experiment. *Journal of Geophysical Research*, *96*(C3), 4555–4572.

Duncan, K., Farrell, S. L., Connor, L. N., Richter-Menge, J., Hutchings, J. K., & Dominguez, R. (2018). High-resolution airborne observations of sea-ice pressure ridge sail height. *Annals of Glaciology*, *59*(76pt2), 137–147.
URL https://www.cambridge.org/core/product/identifier/S0260305518000022/type/journal{_}article

Elachi, C. (1987). *Spaceborne radar remote sensing: applications and techniques*. IEEE Press.

ESA (2000). ERS-1 - eoPortal Directory - Satellite Missions.
URL https://eoportal.org/web/eoportal/satellite-missions/e/ers-1

ESA (2007). ASAR Product Handbook.
URL http://envisat.esa.int/handbooks/asar/CNTR.html

ESA (2011). ERS-2 - eoPortal Directory - Satellite Missions.
URL https://eoportal.org/web/eoportal/satellite-missions/e/ers-2

ESA (2012). Envisat - eoPortal Directory - Satellite Missions.
URL https://eoportal.org/web/eoportal/satellite-missions/e/envisat

ESA (2015). CryoSat-2 Product Handbook – Intermediary Working Version.

ESA (2016). User Guides - Sentinel-3 Altimetry - Operating modes - Sentinel Online.
URL https://sentinel.esa.int/web/sentinel/user-guides/sentinel-3-altimetry/overview/modes

ESA-MPC (2016). Sentinel-1 Product Definition. Doc. n.: S1-RS-MDA-52-7440.
URL https://sentinel.esa.int/documents/247904/1877131/Sentinel-1-Product-Definition

Farrell, S. L., Kurtz, N., Connor, L. N., Elder, B. C., Leuschen, C., Markus, T., McAdoo, D. C., Panzer, B., Richter-Menge, J., & Sonntag, J. G. (2012a). A First Assessment of IceBridge Snow and Ice Thickness Data Over Arctic Sea Ice. *IEEE Transactions on Geoscience and Remote Sensing*, *50*(6), 2098–2111.
URL http://ieeexplore.ieee.org/document/6081925/

Farrell, S. L., Laxon, S. W., McAdoo, D. C., Yi, D., & Zwally, H. J. (2009). Five years of Arctic sea ice freeboard measurements from the Ice, Cloud and land Elevation Satellite. *Journal of Geophysical Research*, *114*(C4), C04008.
URL http://doi.wiley.com/10.1029/2008JC005074

Farrell, S. L., McAdoo, D. C., Laxon, S. W., Zwally, H. J., Yi, D., Ridout, A., & Giles, K. (2012b). Mean dynamic topography of the Arctic Ocean. *Geophysical Research Letters*, *39*(1), n/a–n/a.
URL http://doi.wiley.com/10.1029/2011GL050052

Foresta, L., Gourmelen, N., Pálsson, F., Nienow, P., Björnsson, H., & Shepherd, A. (2016). Surface elevation change and mass balance of Icelandic ice caps derived from swath mode CryoSat-2 altimetry. *Geophysical Research Letters*, *43*(23), 12,138–12,145.
URL http://doi.wiley.com/10.1002/2016GL071485

Forsberg, R., & Skourup, H. (2005). Arctic Ocean gravity, geoid and sea-ice freeboard heights from ICESat and GRACE. *Geophysical Research Letters*, *32*(21), L21502.
URL http://doi.wiley.com/10.1029/2005GL023711

Galin, N., Wingham, D. J., Cullen, R., Fornari, M., Smith, W. H. F., & Abdalla, S. (2013). Calibration of the CryoSat-2 interferometer and measurement of across-track ocean slope. *IEEE Transactions on Geoscience and Remote Sensing*, *51*(1), 57–72.

Giles, K., Laxon, S., Wingham, D., Wallis, D., Krabill, W., Leuschen, C., McAdoo, D., Manizade, S., & Raney, R. (2007). Combined airborne laser and radar altimeter measurements over the Fram Strait in May 2002. *Remote Sensing of Environment*, *111*(2-3), 182–194.
URL https://www.sciencedirect.com/science/article/pii/S0034425707002817

Giles, K. A., & Hvidegaard, S. M. (2006). Comparison of space borne radar altimetry and airborne laser altimetry over sea ice in the Fram Strait. *International Journal of Remote Sensing*, *27*(15), 3105–3113.
URL https://www.tandfonline.com/doi/full/10.1080/01431160600563273

Giles, K. A., Laxon, S. W., & Ridout, A. L. (2008). Circumpolar thinning of Arctic sea ice following the 2007 record ice extent minimum. *Geophysical Research Letters*, *35*(22), L22502.
URL http://doi.wiley.com/10.1029/2008GL035710

Gohin, F., & Cavanié, A. (1994). A first try at identification of sea ice using the three beam scatterometer of ERS-1. *International Journal of Remote Sensing*, *15*(6), 1221–1228.
URL https://www.tandfonline.com/doi/full/10.1080/01431169408954156

Gray, L., Burgess, D., Copland, L., Cullen, R., Galin, N., Hawley, R., & Helm, V. (2013). Interferometric swath processing of Cryosat data for glacial ice topography. *Cryosphere*, *7*(6), 1857–1867.

Guerreiro, K., Fleury, S., Zakharova, E., Rémy, F., & Kouraev, A. (2016). Potential for estimation of snow depth on Arctic sea ice from CryoSat-2 and SARAL/AltiKa missions. *Remote Sensing of Environment*, *186*, 339–349.
URL https://www.sciencedirect.com/science/article/pii/S0034425716302711

Haas, C., Beckers, J., King, J., Silis, A., Stroeve, J., Wilkinson, J., Notenboom, B., Schweiger, A., & Hendricks, S. (2017). Ice and Snow Thickness Variability and Change in the High Arctic Ocean Observed by In Situ Measurements. *Geophysical Research Letters*, *44*(20), 10,462–10,469.

Haas, C., Gerland, S., Eicken, H., & Miller, H. (1997). Comparison of sea-ice thickness measurements under summer and winter conditions in the Arctic using a small electromagnetic induction device. *GEOPHYSICS*, *62*(3), 749–757.
URL http://library.seg.org/doi/10.1190/1.1444184

Haas, C., Hendricks, S., Ricker, R., King, J., Beckers, H., J. Skourup, Farrell, S. L., Baker, S., & Gaudelli, J. (2016). *CryoVal-SI: CryoSat Sea Ice Product Validation using CryoVex and IceBridge campaign data*, 1.1 ed. Technical Note 3: Assessment of Different Sources of Uncertainty. Doc. No.: CVSI–TN–WP3–3001.

Haas, C., Pfaffling, A., Hendricks, S., Rabenstein, L., Etienne, J.-L., & Rigor, I. (2008). Reduced ice thickness in Arctic Transpolar Drift favors rapid ice retreat. *Geophysical Research Letters*, *35*(17), L17501.
URL http://doi.wiley.com/10.1029/2008GL034457

Hezel, P. J., Zhang, X., Bitz, C. M., Kelly, B. P., & Massonnet, F. (2012). Projected decline in spring snow depth on Arctic sea ice caused by progressively later autumn open ocean freeze-up this century. *Geophysical Research Letters*, *39*(17), n/a–n/a.
URL http://doi.wiley.com/10.1029/2012GL052794

Hofmann-Wellenhof, B., & Moritz, H. (2006). Physical geodesy (second, corrected edition). *Physical Geodesy (second, Corrected Edition)*, (pp. 1–403).

Holland, M. M., & Landrum, L. (2015). Factors affecting projected Arctic surface shortwave heating and albedo change in coupled climate models. *Philosophical transactions. Series A, Mathematical, physical, and engineering sciences*, *373*(2045).
URL http://www.ncbi.nlm.nih.gov/pubmed/26032318http://www.pubmedcentral.nih.gov/articlerender.fcgi?artid=PMC4455713

Kaleschke, L., Tian-Kunze, X., Maaß, N., Mäkynen, M., & Drusch, M. (2012). Sea ice thickness retrieval from SMOS brightness temperatures during the Arctic freeze-up period. *Geophysical Research Letters*, *39*(5), n/a–n/a.
URL http://doi.wiley.com/10.1029/2012GL050916

Krumpen, T., Gerdes, R., Haas, C., Hendricks, S., Herber, A., Selyuzhenok, V., Smedsrud, L., & Spreen, G. (2016). Recent summer sea ice thickness surveys in Fram Strait and associated ice volume fluxes. *The Cryosphere*, *10*(2), 523–534.
URL https://www.the-cryosphere.net/10/523/2016/

Kurtz, N., Studinger, M. S., Harbeck, J., Onana, V., & Yi, D. (2015). IceBridge L4 Sea Ice Freeboard, Snow Depth, and Thickness, Version 1. *Boulder, Colorado USA. NASA National Snow and Ice Data Center Distributed Active Archive Center*.

Kurtz, N. T., & Farrell, S. L. (2011). Large-scale surveys of snow depth on Arctic sea ice from Operation IceBridge. *Geophysical Research Letters*, *38*(20), n/a–n/a.
URL http://doi.wiley.com/10.1029/2011GL049216

Kurtz, N. T., Farrell, S. L., Studinger, M., Galin, N., Harbeck, J. P., Lindsay, R., Onana, V. D., Panzer, B., & Sonntag, J. G. (2013). Sea ice thickness, freeboard, and snow depth products from Operation IceBridge airborne data. *The Cryosphere*, *7*(4), 1035–1056.
URL https://www.the-cryosphere.net/7/1035/2013/

Kurtz, N. T., Galin, N., & Studinger, M. (2014). An improved CryoSat-2 sea ice freeboard retrieval algorithm through the use of waveform fitting. *Cryosphere*, *8*(4), 1217–1237.

Kwok, R. (2004). Annual cycles of multiyear sea ice coverage of the Arctic Ocean: 1999–2003. *Journal of Geophysical Research*, *109*(C11), C11004.
URL http://doi.wiley.com/10.1029/2003JC002238

Kwok, R. (2014). Simulated effects of a snow layer on retrieval of CryoSat-2 sea ice freeboard. *Geophysical Research Letters*, *41*(14), 5014–5020.

Kwok, R., & Cunningham, G. F. (2015). Variability of Arctic sea ice thickness and volume from CryoSat-2. *Philosophical Transactions of the Royal Society of London A: Mathematical, Physical and Engineering Sciences*, *373*(2045), 20140157.
URL http://rsta.royalsocietypublishing.org/content/373/2045/20140157{%}5Cnhttp://rsta.royalsocietypublishing.org/content/373/2045/20140157.abstract

Kwok, R., Cunningham, G. F., Wensnahan, M., Rigor, I., Zwally, H. J., & Yi, D. (2009). Thinning and volume loss of the Arctic Ocean sea ice cover: 2003-2008. *Journal of Geophysical Research - Part C - Oceans*, *114*(C7), C07005.

Kwok, R., Cunningham, G. F., Zwally, H. J., & Yi, D. (2007). Ice, Cloud, and land Elevation Satellite (ICESat) over Arctic sea ice: Retrieval of freeboard. *Journal of Geophysical Research*, *112*(C12), C12013.
URL http://doi.wiley.com/10.1029/2006JC003978

Kwok, R., & Markus, T. (2017). Potential basin-scale estimates of Arctic snow depth with sea ice freeboards from CryoSat-2 and ICESat-2: An exploratory analysis.

Kwok, R., & Morison, J. (2015). Sea surface height and dynamic topography of the ice-covered oceans fromCryoSat-2: 2011–2014. *Journal of Geophysical Research*, *121*, 674–692.

Lawrence, I., Tsamados, M., Stroeve, J., Armitage, T., & Ridout, A. (2018). Estimating snow depth over Arctic sea ice from calibrated dual-frequency radar freeboards. *The Cryosphere*, (March), 1–21.

Laxon, S., Peacock, N., & Smith, D. (2003). High interannual variability of sea ice thickness in the Arctic region. *Nature*, *425*(6961), 947–950.

Laxon, S. W. (1994). Sea ice altimeter processing scheme at the EODC. *International Journal of Remote Sensing*, *15*(4), 915–924.
URL https://www.tandfonline.com/doi/full/10.1080/01431169408954124

Laxon, S. W., Giles, K. A., Ridout, A. L., Wingham, D. J., Willatt, R., Cullen, R., Kwok, R., Schweiger, A., Zhang, J., Haas, C., Hendricks, S., Krishfield, R., Kurtz, N., Farrell, S., & Davidson, M. (2013). CryoSat-2 estimates of Arctic sea ice thickness and volume. *Geophysical Research Letters*, *40*(4), 732–737.

Lindsay, R. W., & Zhang, J. (2005). The Thinning of Arctic Sea Ice, 1988–2003: Have We Passed a Tipping Point? *Journal of Climate*, *18*(22), 4879–4894.
URL http://journals.ametsoc.org/doi/abs/10.1175/JCLI3587.1

Lindsay, R. W., Zhang, J., Schweiger, A., Steele, M., Stern, H., Lindsay, R. W., Zhang, J., Schweiger, A., Steele, M., & Stern, H. (2009). Arctic Sea Ice Retreat in 2007 Follows Thinning Trend. *Journal of Climate*, *22*(1), 165–176.
URL http://journals.ametsoc.org/doi/abs/10.1175/2008JCLI2521.1

Lyard, F., Lefevre, F., Letellier, T., & Francis, O. (2006). Modelling the global ocean tides: modern insights from FES2004. *Ocean Dynamics*, *56*(5-6), 394–415.
URL http://link.springer.com/10.1007/s10236-006-0086-x

Markus, T., Neumann, T., Martino, A., Abdalati, W., Brunt, K., Csatho, B., Farrell, S., Fricker, H., Gardner, A., Harding, D., Jasinski, M., Kwok, R., Magruder, L., Lubin, D., Luthcke, S., Morison, J., Nelson, R., Neuenschwander, A., Palm, S., Popescu, S., Shum, C., Schutz, B. E., Smith, B., Yang, Y., & Zwally, J. (2017). The Ice, Cloud, and land Elevation Satellite-2 (ICESat-2): Science requirements, concept, and implementation. *Remote Sensing of Environment*, *190*, 260–273.
URL https://www.sciencedirect.com/science/article/pii/S0034425716305089

Martin, T. V., Zwally, H. J., Brenner, A. C., & Bindschadler, R. A. (1983). Analysis and retracking of continental ice sheet radar altimeter waveforms. *Journal of Geophysical Research*, *88*(C3), 1608.
URL http://doi.wiley.com/10.1029/JC088iC03p01608

Maslanik, J. A., Fowler, C., Stroeve, J., Drobot, S., Zwally, J., Yi, D., & Emery, W. (2007). A younger, thinner Arctic ice cover: Increased potential for rapid, extensive sea-ice loss. *Geophysical Research Letters*, *34*(24), L24501.
URL http://doi.wiley.com/10.1029/2007GL032043

Maykut, G. A., & Untersteiner, N. (1971). Some results from a time-dependent thermodynamic model of sea ice. *Journal of Geophysical Research*, *76*(6), 1550–1575.
URL http://doi.wiley.com/10.1029/JC076i006p01550

Newman, T., Farrell, S. L., Richter-Menge, J., Connor, L. N., Kurtz, N. T., Elder, B. C., & McAdoo, D. (2014). Assessment of radar-derived snow depth over Arctic sea ice. *Journal of Geophysical Research : Oceans*, *119*(12), 8578–8602.
URL https://doi.org/10.1002/2014JC010284

Nghiem, S. V., Rigor, I. G., Perovich, D. K., Clemente-Colón, P., Weatherly, J. W., & Neumann, G. (2007). Rapid reduction of Arctic perennial sea ice. *Geophysical Research Letters*, *34*(19), L19504.
URL http://doi.wiley.com/10.1029/2007GL031138

Nilsson, J., Gardner, A., Sandberg Sørensen, L., & Forsberg, R. (2016). Improved retrieval of land ice topography from CryoSat-2 data and its impact for volume-change estimation of the Greenland Ice Sheet. *The Cryosphere*, *10*, 2953–2969.
URL www.the-cryosphere.net/10/2953/2016/

Onana, V.-D.-P., Kurtz, N. T., Farrell, S. L., Koenig, L. S., Studinger, M., & Harbeck, J. P. (2013). A Sea-Ice Lead Detection Algorithm for Use With High-Resolution Airborne Visible Imagery. *IEEE Transactions on Geoscience and Remote Sensing*, *51*(1), 38–56.
URL http://ieeexplore.ieee.org/document/6236136/

Panzer, B., Gomez-Garcia, D., Leuschen, C., Paden, J., Rodriguez-Morales, F., Patel, A., Markus, T., Holt, B., & Gogineni, P. (2013). An ultra-wideband, microwave radar for measuring snow thickness on sea ice and mapping near-surface internal layers in polar firn. *Journal of Glaciology*, *59*(214), 244–254.
URL https://www.cambridge.org/core/product/identifier/S0022143000204292/type/journal{_}article

Parrinello, T., Shepherd, A., Bouffard, J., Badessi, S., Casal, T., Davidson, M., Fornari, M., Maestroni, E., & Scagliola, M. (2018). CryoSat: ESA's ice mission – Eight years in space. *Advances in Space Research*, *62*(6), 1178–1190.
URL https://www.sciencedirect.com/science/article/pii/S0273117718303296

Pavlov, V. K. (1998). Circulation in ice-covered waters. In M. Leppäranta (Ed.) *Physics of the Ice-covered Seas*, vol. 2, (pp. 447–482). Helsinki University Printing House.

Perovich, D., Meier, W., Tschudi, M., Gerland, S., & Richter-Menge, J. (2012). Sea ice. In *Arctic Report Card: Update for 2012*, (pp. 37–42). Available at `ftp://ftp.oar.noaa.gov/arctic/documents/ArcticReportCard_full_report2012.pdf`.

Perovich, D. K., Light, B., Eicken, H., Jones, K. F., Runciman, K., & Nghiem, S. V. (2007). Increasing solar heating of the Arctic Ocean and adjacent seas, 1979–2005: Attribution and role in the ice-albedo feedback. *Geophysical Research Letters*, *34*(19), L19505.
URL `http://doi.wiley.com/10.1029/2007GL031480`

Perovich, D. K., Richter-Menge, J. A., Jones, K. F., & Light, B. (2008). Sunlight, water, and ice: Extreme Arctic sea ice melt during the summer of 2007. *Geophysical Research Letters*, *35*(11), L11501.
URL `http://doi.wiley.com/10.1029/2008GL034007`

Pugh, D., & Woodworth, P. (2014). *Sea-Level Science: Understanding Tides, Surges, Tsunamis and Mean Sea-Level Changes*. Cambridge University Press.

Raney, R. (1998). The delay/Doppler radar altimeter. *IEEE Transactions on Geoscience and Remote Sensing*, *36*(5), 1578–1588.
URL `http://ieeexplore.ieee.org/document/718861/`

Renganathan, V. (2010). *Arctic Sea Ice Freeboard Heights from Satellite Altimetry*. Ph.D. thesis, University of Calgary.

Renner, A. H. H., Gerland, S., Haas, C., Spreen, G., Beckers, J. F., Hansen, E., Nicolaus, M., & Goodwin, H. (2014). Evidence of Arctic sea ice thinning from direct observations. *Geophysical Research Letters*, *41*(14), 5029–5036.
URL `http://doi.wiley.com/10.1002/2014GL060369`

Ricker, R., Hendricks, S., & Beckers, J. F. (2016). The Impact of Geophysical Corrections on Sea-Ice Freeboard Retrieved from Satellite Altimetry. *Remote Sensing*, *8*(4), 1–15.

Ricker, R., Hendricks, S., Helm, V., Skourup, H., & Davidson, M. (2014). Sensitivity of CryoSat-2 Arctic sea-ice freeboard and thickness on radar-waveform interpretation. *Cryosphere*, *8*(4), 1607–1622.

Ridley, J. K., & Partington, K. C. (1988). A model of satellite radar altimeter return from ice sheets. *International Journal of Remote Sensing*, *9*(4), 601–624.
URL `https://www.tandfonline.com/doi/full/10.1080/01431168808954881`

Rigor, I. G., Wallace, J. M., Colony, R. L., Rigor, I. G., Wallace, J. M., & Colony, R. L. (2002). Response of Sea Ice to the Arctic Oscillation. *Journal of Climate*, *15*(18), 2648–2663.

Robinson, I. S. (1985). *Satellite oceanography. An introduction for oceanographers and remote-sensing scientists*. Ellis Horwood.

Rose, S. K. (2013). *Measurements of sea ice by satellite and airborne altimetry*. Ph.D. thesis, DTU Space.
URL `http://forskningsbasen.deff.dk/Share.external?sp=S2b70450d-62a5-4de2-b255-dec7fc9b5f8b{&}sp=Sdtu`

Rothrock, D. a., Yu, Y., & Maykut, G. a. (1999). Thinning of the Arctic sea-ice cover. *Geophysical Research Letters*, *26*(23), 3469.

Scagliola, M., & Fornari, M. (2017). Known biases in CryoSat Level1b products. Doc. N.: C2-TN-ARS-GS-5135.

Schutz, B. E., Zwally, H. J., Shuman, C. A., Hancock, D., & DiMarzio, J. P. (2005). Overview of the ICESat Mission. *Geophysical Research Letters*, *32*(21), L21S01.
URL http://doi.wiley.com/10.1029/2005GL024009

Skourup, H., Einarsson, I., Forsberg, R., Haas, C., Helms, V., Hvidegaard, S. M., Nilsson, J., Olesen, A. V., & Olesen, A. K. (2012). ESA CryoVEx 2012. Campaign report.

Skourup, H., Farrell, S. L., Hendricks, S., Ricker, R., Armitage, T. W. K., Ridout, A., Andersen, O. B., Haas, C., & Baker, S. (2017). An Assessment of State-of-the-Art Mean Sea Surface and Geoid Models of the Arctic Ocean: Implications for Sea Ice Freeboard Retrieval. *Journal of Geophysical Research: Oceans*.
URL http://doi.wiley.com/10.1002/2017JC013176

Steele, M., Morison, J., Ermold, W., Rigor, I., Ortmeyer, M., & Shimada, K. (2004). Circulation of summer Pacific halocline water in the Arctic Ocean. *Journal of Geophysical Research*, *109*(C2), C02027.
URL http://doi.wiley.com/10.1029/2003JC002009

Stroeve, J. C., Maslanik, J., Serreze, M. C., Rigor, I., Meier, W., & Fowler, C. (2011). Sea ice response to an extreme negative phase of the Arctic Oscillation during winter 2009/2010. *Geophysical Research Letters*, *38*(2), n/a–n/a.
URL http://doi.wiley.com/10.1029/2010GL045662

Stroeve, J. C., Serreze, M. C., Holland, M. M., Kay, J. E., Malanik, J., & Barrett, A. P. (2012). The Arctic's rapidly shrinking sea ice cover: A research synthesis. *Climatic Change*, *110*(3-4), 1005–1027.

Taylor, J. R. (1997). *An Introduction to Error Analysis*, vol. 56. University Science Books, 2nd ed.

Thompson, D. W. J., & Wallace, J. M. (1998). The Arctic oscillation signature in the wintertime geopotential height and temperature fields. *Geophysical Research Letters*, *25*(9), 1297–1300.
URL http://doi.wiley.com/10.1029/98GL00950

Tilling, R. L., Ridout, A., & Shepherd, A. (2018). Estimating Arctic sea ice thickness and volume using CryoSat-2 radar altimeter data. *Advances in Space Research*, *62*(6), 1203–1225.
URL https://www.sciencedirect.com/science/article/pii/S0273117717307901

Tiuri, M., Sihvola, A., Nyfors, E., & Hallikaiken, M. (1984). The complex dielectric constant of snow at microwave frequencies. *IEEE Journal of Oceanic Engineering*, *9*(5), 377–382.
URL http://ieeexplore.ieee.org/document/1145645/

Tonboe, R., Lavelle, J., Pfeiffer, R.-H., & Howe, E. (2017). Product User Manual for OSI SAF Global Sea Ice Concentration. Product OSI-401-b.
URL http://osisaf.met.no/docs/osisaf_cdop3_ss2_pum_ice-conc_v1p6.pdf

Ulaby, F. T., Moore, R. K., & Fung, A. K. (1986). *Microwave Remote Sensing: Active and Passive. Vol. 3: From Theory to Applications*, vol. 3. Artech House,.

Vignudelli, S., Kostianoy, A. G., Cipollini, P., & Benveniste, J. (2011). *Coastal Altimetry*. Springer.

Wadhams, P. (1997). Ice thickness in the Arctic Ocean: The statistical reliability of experimental data. *Journal of Geophysical Research: Oceans*, *102*(C13), 27951–27959.
URL http://doi.wiley.com/10.1029/97JC02503

Wadhams, P., & Davis, N. R. (2000). Further evidence of ice thinning in the Arctic Ocean. *Geophysical Research Letters*, *27*(24), 3973–3975.
URL http://doi.wiley.com/10.1029/2000GL011802

Wadhams, P., Tucker, W. B., Krabill, W. B., Swift, R. N., Comiso, J. C., & Davis, N. R. (1992). Relationship between sea ice freeboard and draft in the Arctic Basin, and implications for ice thickness monitoring. *Journal of Geophysical Research*, *97*(C12), 20325.
URL http://doi.wiley.com/10.1029/92JC02014

Wahr, J. M. (1985). Deformation induced by polar motion. *Journal of Geophysical Research*, *90*(B11), 9363.
URL http://doi.wiley.com/10.1029/JB090iB11p09363

Warren, S. G., Rigor, I. G., Untersteiner, N., Radionov, V. F., Bryazgin, N. N., Aleksandrov, Y. I., & Colony, R. (1999). Snow depth on Arctic sea ice. *Journal of Climate*, *12*(6), 1814–1829.

Webster, M., Gerland, S., Holland, M., Hunke, E., Kwok, R., Lecomte, O., Massom, R., Perovich, D., & Sturm, M. (2018). Snow in the changing sea-ice systems. *Nature Climate Change*, *8*(11), 946–953.
URL http://dx.doi.org/10.1038/s41558-018-0286-7

Webster, M. A., Rigor, I. G., Nghiem, S. V., Kurtz, N. T., Farrell, S. L., Perovich, D. K., & Sturm, M. (2014). Interdecadal changes in snow depth on Arctic sea ice. *Journal of Geophysical Research: Oceans*, *119*(8), 5395–5406.
URL http://doi.wiley.com/10.1002/2014JC009985

Wessel, P., & Smith, W. H. F. (1996). A global, self-consistent, hierarchical, high-resolution shoreline database. *Journal of Geophysical Research: Solid Earth*, *101*(B4), 8741–8743.
URL http://doi.wiley.com/10.1029/96JB00104

Willatt, R., Laxon, S., Giles, K., Cullen, R., Haas, C., & Helm, V. (2011). Ku-band radar penetration into snow cover on Arctic sea ice using airborne data. *Annals of Glaciology*.

Willatt, R. C., Giles, K. A., Laxon, S. W., Stone-Drake, L., & Worby, A. P. (2010). Field investigations of Ku-band radar penetration into snow cover on antarctic sea ice. *IEEE Transactions on Geoscience and Remote Sensing*.

Williams, E. (2011). Aviation Formulary.

Wingham, D. J., Francis, C. R., Baker, S., Bouzinac, C., Brockley, D., Cullen, R., de Chateau-Thierry, P., Laxon, S. W., Mallow, U., Mavrocordatos, C., Phalippou, L., Ratier, G., Rey, L., Rostan, F., Viau, P., & Wallis, D. W. (2006). CryoSat: A mission to determine the fluctuations in Earth's land and marine ice fields. *Advances in Space Research*, *37*(4), 841–871.

Wingham, D. J., Phalippou, L., Mavrocordatos, C., & Wallis, D. (2004). The mean echo and echo cross product from a beamforming interferometric altimeter and their application to elevation measurement. *IEEE Transactions on Geoscience and Remote Sensing*, *42*(10), 2305–2323.

Wingham, D. J., Rapley, C., & Griffiths, H. (1986). New techniques in satellite altimeter tracking systems. *Proceedings of the 1986 International Geoscience and Remote Sensing Symposium (IGARSS'86)*.

World Meteorological Organization (2014). WMO Sea-ice nomenclature. TP 145.

Zwally, H. J., Yi, D., Kwok, R., & Zhao, Y. (2008). ICESat measurements of sea ice freeboard and estimates of sea ice thickness in the Weddell Sea. *Journal of Geophysical Research*, *113*(C2), C02S15.
URL `http://doi.wiley.com/10.1029/2007JC004284`

Appendix A

Journal papers

A.1 Uncertainty reduction of Arctic sea ice freeboard from CryoSat-2 interferometric mode

Available online at www.sciencedirect.com

ScienceDirect

Advances in Space Research 62 (2018) 1251–1264

ADVANCES IN SPACE RESEARCH (a COSPAR publication)

www.elsevier.com/locate/asr

Uncertainty reduction of Arctic sea ice freeboard from CryoSat-2 interferometric mode

A. Di Bella [a,*], H. Skourup [a], J. Bouffard [b], T. Parrinello [b]

[a] DTU Space, National Space Institute, Elektrovej 327, 2800 Kgs. Lyngby, Denmark
[b] ESA/ESRIN, Via Galileo Galilei C.P. 64, 00044 Frascati, Italy

Received 1 March 2017; received in revised form 22 February 2018; accepted 9 March 2018
Available online 17 March 2018

Abstract

A study by Armitage and Davidson (2014) has shown that the extra information from the CryoSat-2 (CS2) SARIn mode increases the number of valid sea surface height estimates which are usually discarded in the SAR mode due to snagging of the radar signal. As the number of valid detected leads increases, the uncertainty of the freeboard heights decreases.

In this study, the freeboard heights estimated by processing CS2 SARIn level 1b waveforms are validated using the information from airborne laser and radar altimetry as well as snow radar measurements acquired during the CryoVEx 2012 and Operation IceBridge 2012 campaigns, respectively. The possible reduction in the random freeboard uncertainty is investigated comparing two scenarios, i.e. a SAR-like and a SARIn acquisition.

A very good agreement is found between average airborne and satellite radar freeboards although, at the CS2 footprint scale, they do not show along-track spatial correlation. It is observed that using the extra phase information, CS2 is able to detect leads up to 2300 m off-nadir. A reduction in the total random freeboard uncertainty of ~40% is observed by taking advantage of the CS2 interferometric capabilities, which enable to include ~35% of the waveforms discarded in the SAR-like scenario.

Keywords: CryoSat-2; Sea ice; Freeboard; Uncertainty; SARIn; Altimetry

1. Introduction

Sea ice is one of the most significant climate parameters interacting with several feedback processes of the global climate system. Changes in the sea ice cover represent one of the most visible components of climate change influencing directly the albedo of our planet. Furthermore, variations in the ice volume reflect changes in the heat budget of the Arctic (Laxon et al., 2013) and can influence the climate at a global scale.

Remote sensing records of Arctic sea ice now span over several decades. Satellite observations show a rapid reduction of the ice-covered area in the Arctic (Comiso, 2012) especially during summers (Stroeve et al., 2012) which, together with evidences about the thinning of Arctic sea ice (Kwok and Rothrock, 2009), may cause a reduction of the sea ice volume at an even faster rate than observed for sea ice extent (Desch et al., 2017). Estimating the sea ice volume from satellite observations requires the knowledge of the sea ice extent and thickness. While the extent can be measured directly by satellites, the estimation of the thickness is more challenging. This parameter can be estimated, assuming hydrostatic equilibrium (Laxon et al., 2003), from the measurement of the sea ice freeboard, i.e. the height of the ice surface

* Corresponding author.
E-mail addresses: adia@space.dtu.dk (A. Di Bella), hsk@space.dtu.dk (H. Skourup), jerome.bouffard@esa.int (J. Bouffard), tommaso.parrinello@esa.int (T. Parrinello).

https://doi.org/10.1016/j.asr.2018.03.018
0273-1177/

above the local sea level. In principle, satellite altimetry can be used to measure directly the sea ice freeboard (Laxon et al., 2013; Kwok et al., 2009). In the freeboard-to-thickness conversion the freeboard and the associated errors are typically multiplied by a factor of ~9.6 (Wingham et al., 2006), thus, it is fundamental to both improve the accuracy of freeboard estimates as well as to minimise their uncertainty.

Armitage and Davidson (2014) have demonstrated that CryoSat-2's interferometric mode (SARIn) enables to process waveforms whose power echo is dominated by the strong reflection from off-nadir leads, as the available phase information can be used to correct for the associated range error. They found that such an error, if left unaccounted for, would cause a significant underestimation of the sea surface height which would, in turn, lead to an overestimation of freeboard heights. This study builds on their work to investigate how the decreased uncertainty of the sea surface height, obtained by including more waveforms in the analysis, affects the uncertainty of Arctic sea ice freeboard. Furthermore, airborne laser and radar altimetry as well as snow radar measurements are used to assess CryoSat-2 SARIn performance with regards to Arctic sea ice freeboard estimation.

The next section describes the datasets used in the study, while Section 3 provides the necessary theoretical background and the methodology used to process the data acquired by the different sensors. The estimated freeboard heights are presented and discussed in Section 4 together with snow depth estimates from several sources. Finally, Section 5 summarises the main findings of the study.

2. Data

2.1. CryoSat-2

A large part of this study deals with the processing of radar altimetry data from the *SAR Interferometric Radar Altimeter* (*SIRAL*) on board of *CryoSat-2* (*CS2*). Most of the time SIRAL operates in SAR mode over Arctic sea ice. However, a small region between 80–85°N and 100–140°W (Fig. 1) was selected to test the SARIn capabilities over sea ice (Armitage and Davidson, 2014). This area, known as the Wingham box, has been active since CS2 launch in 2010 until October 2014. Post October 2014, SIRAL has acquired data in SAR mode also in the Wingham box.

SARIn data acquired on the 5th of April 2012 along orbit #10565, inside the Wingham box, have been processed in this study (Fig. 1). In SARIn mode the CS2 footprint extends for ~1.65 km in the across-track direction and for ~305 m in the along-track direction (ESA, 2014).

This study uses 20 Hz SARIn waveforms (level 1b product) processed with the baseline C processor, downloaded from ESA CryoSat ftp client (ftp://science-pds.cryosat.esa.int).

2.2. CryoVEx 2012

Validation of CS2 freeboard estimates is performed using data collected during the *CryoSat Validation Experiment* (*CryoVEx*) 2012, a campaign which took place between the 25th of March and the 5th of May 2012. During the campaign, two aircraft were used to fly several sensors in order to collect data over sea- and land ice along selected CS2 ground tracks (Skourup et al., 2012). One of the aircraft carried an *airborne laser scanner* (*ALS*) and the *Airborne SAR Interferometric Radar System* (*ASIRAS*) which provided the data used in this study. Such data were also acquired on the 5th of April 2012 along the CS2 orbit #10565, inside the Wingham box (Fig. 1). The average time difference between the satellite pass (~14:00 h) and the aircraft pass (~18:30 h) is approximately 4.5 h.

The ALS is a conventional airborne laser scanner of type RIEGL LMS-Q240i-60 operating at a wavelength of 904 nm. Typical resolution of the raw data is approximately 1 × 1 m in a 300 m wide swath at the nominal flight altitude of 300 m. The vertical accuracy is in the order of 10 cm depending primarily on uncertainties in the kinematic GPS solutions. ALS data were processed at DTU Space to obtain a level 1 product containing the geo-located elevations above the WGS-84 reference ellipsoid together with the relative timestamps.

The ASIRAS radar is an airborne version of the SIRAL radar altimeter onboard CS2. It operates at 13.5 GHz with footprint size 10 m across track and 3 m along track in Low Altitude Mode with low resolution (LAMa) at a standard flight height of 300 m. The ASIRAS data used in this study were processed at the Alfred Wegener Institute (AWI) as part of the ESA CryoVal-SI project where they used a Threshold First Maximum Retracker Algorithm (TFMRA) with a 40% power threshold (Hendricks, personal communication) to obtain a level 2 product containing the geo-located freeboard heights.

2.3. Operation IceBridge

In order to account for the snow layer covering the sea ice, snow depth estimates from the *IceBridge L4 Sea Ice Freeboard, Snow Depth, and Thickness, Version 1* product (Kurtz et al., 2015) are included in the analysis. The data used in this study (*OIB*) were acquired during several flights performed between the 14th and the 29th of March 2012 (Fig. 1). At the 460 m nominal flight altitude the snow radar has a footprint size of 11 m across track and 14.5 m along track. The product, containing snow depths averaged every 40 m in the along-track direction (Kurtz et al., 2015), can be downloaded from the NASA NSIDC website (https://nsidc.org/icebridge/portal/).

2.4. Envisat

With regards to the capacity of CS2 to detect off-nadir leads, additional validation is performed using spatially

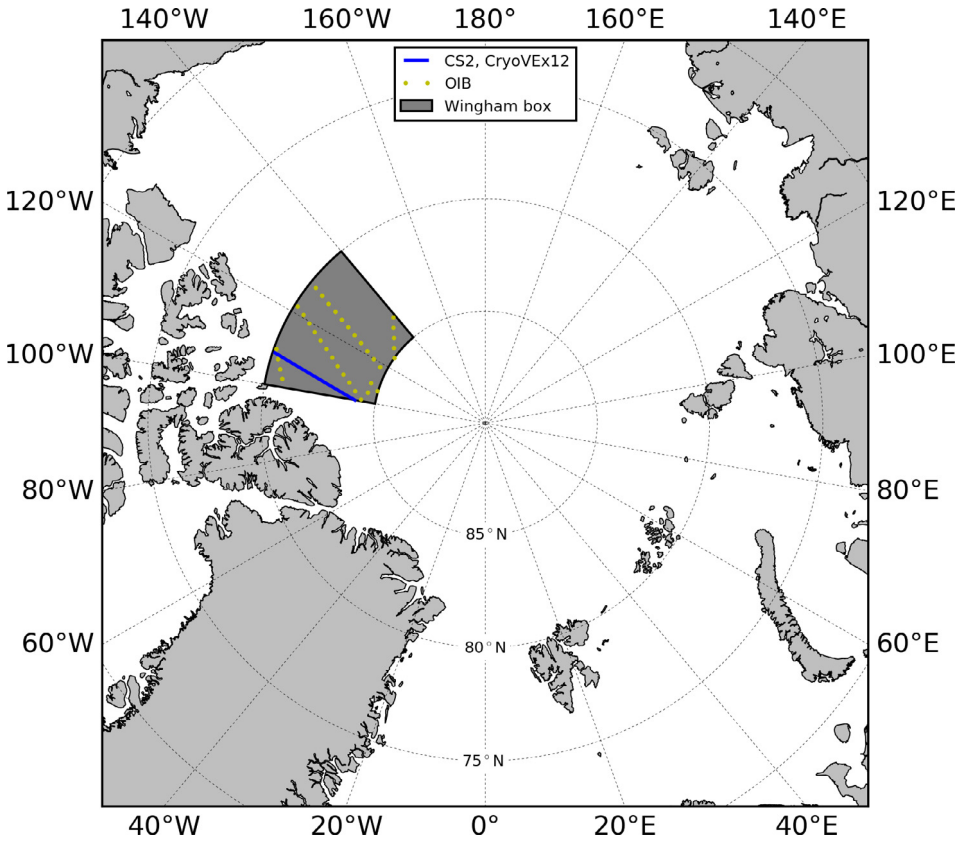

Fig. 1. Map of the Arctic Ocean. Wingham box (grey patch), where CryoSat-2 (CS2) was switched to SARIn mode (2010–2014), and tracks where the data have been acquired (blue line for CS2 and CryoVEx and yellow dots for Operation IceBridge (OIB)). (For interpretation of the references to colour in this figure legend, the reader is referred to the web version of this article.)

and almost temporally coincident SAR imagery from the *Advanced Synthetic Aperture Radar* (*ASAR*) instrument on board of Envisat, acquired just three days before losing contact with the satellite. The *Wide Swath Mode* level 1b product (version 6.02) used in this work is available at the ESA Earth Online portal (https://earth.esa.int/).

3. Methods

The main objectives of this study are (1) to make an assessment of Arctic sea ice freeboards derived from SIRAL measurements and (2) to investigate the possible reduction in the freeboard uncertainty achievable using SIRAL interferometric capabilities.

The first objective is accomplished by comparing SIRAL freeboard heights with those from ALS and ASIRAS as illustrated in Fig. 2. Snow depth estimates from the Warren climatology and the OIB snow radar are used as an additional input in Section 4 to discuss the results obtained in the study.

A detailed description of the processing steps applied to SIRAL, ALS and ASIRAS/OIB datasets is included in Sections 3.2, 3.3 and 3.4, respectively.

The possible reduction in the SIRAL freeboard uncertainty, introduced in Section 3.1.1, is investigated by comparing two scenarios: a SAR-like scenario, where ambiguous waveforms are discarded and the phase information not used, and a scenario in which some of the ambiguous waveforms are processed together with their phase information (Section 3.2).

3.1. Freeboard estimation

The definition of freeboard depends on the wavelength of the altimetry sensor used to observe sea ice and, thus, it differs for radar and laser altimetry. In general, one can say that the freeboard is determined by subtracting the local sea surface height from the height of the sensed surface as:

$$F = h - SSH \tag{1}$$

where h is the height of the sensed surface, snow for the ALS instrument and somewhere between snow and sea ice for SIRAL and ASIRAS, and SSH is the actual sea surface height. The actual SSH in regions covered by sea ice is determined by interpolating between lead height estimates. The elevations are first detrended using a mean sea surface (MSS) to improve the accuracy of the interpolated SSH. In fact, subtracting the MSS from the elevations removes the major component of the height measurement due to the geoid (Skourup et al., 2017) as well as it accounts for higher

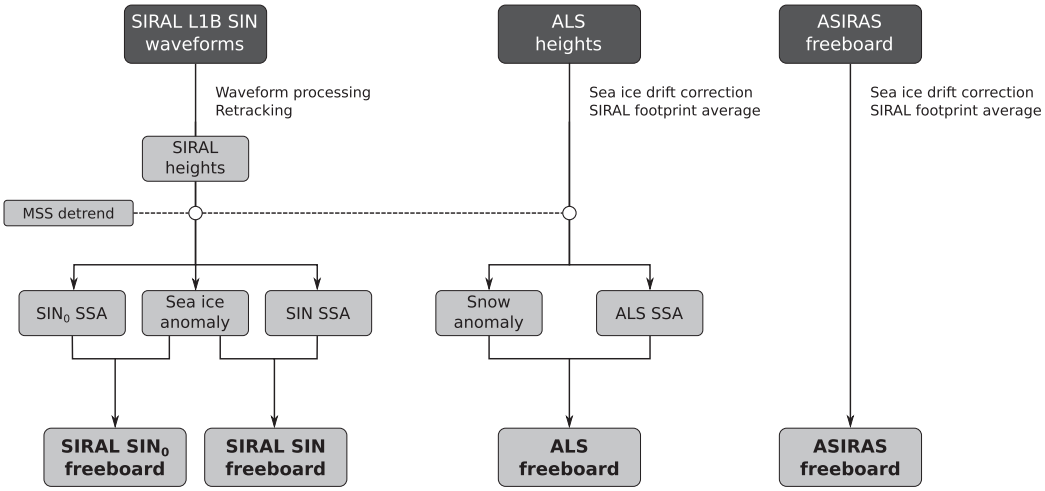

Fig. 2. Simplified block diagram illustrating the methods used to estimate freeboard from different sensors. The dark grey blocks on the top represent the datasets used in this study, described in detail in Section 2. The estimated freeboards, blocks with bold text at the bottom of the figure, are presented and discussed in Section 4. Everything else in between the top and the bottom blocks describes the processing steps applied to the respective datasets, which is the subject of Section 3.

frequency variations in the SSH. Since $SSH = MSS + SSA$, the freeboard can be determined as

$$F = h - MSS - SSA \tag{2}$$

where SSA is the sea surface anomaly (Fig. 3). In this study all elevations are detrended using the DTU15 MSS (Andersen et al., 2016).

As a layer of snow on the sea ice would reduce the radar propagation speed (Kurtz et al., 2014), a correction based on assumed snow depth, penetration and density should be applied to radar sea ice elevations (Section 3.2).

3.1.1. Freeboard uncertainty

The total uncertainty on a generic measurement is the result of the contributions from systematic and random uncertainties. While systematic errors can usually be corrected for, random errors can be minimised by increasing the number of measurements. This study focuses on the random part of the radar freeboard uncertainty since it is the quantity that could possibly be reduced by including more data into the analysis.

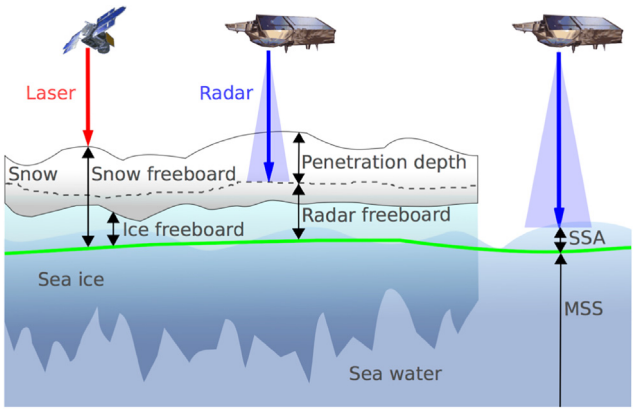

Fig. 3. Instrument-dependent freeboard. While laser altimeters like ALS sense the snow surface, the CryoSat-2 Ku-band radar altimeter (SIRAL) penetrates the snowpack, with a penetration depth dependent on snow properties. The drawing also shows that the actual sea surface height equals the sum of the mean sea surface (MSS) and the sea surface anomaly (SSA). Credits: (Ricker et al., 2014), CC BY 3.0.

Wingham et al. (2006) discusses different types of error from CS2 measurements over sea ice. Random errors originate from random fluctuations during measurements and are assumed to be governed by *instrument system errors*, affecting the range measurements, as well as by the *uncertainty on the actual sea surface height*, affecting directly freeboard retrievals (Ricker et al., 2014).

Concerning the SIRAL instrument system error, this contribution has been analysed in detail in Wingham et al. (2006) and it is found to be dominated by the SIRAL speckle noise for both SAR (0.10 m) and SARIn (0.14 m) modes. However, some errors also arise from orbit determination procedures (0.06 m) – which are again common to both modes – and from the accuracy of angle measurements (0.015 m) – for SARIn only. When these contributions are combined in a RSS fashion, they quantify the total elevation error associated to a single SIRAL level 1b measurement (σ_{l1b}) as 0.116 m for the SAR mode and 0.153 m for the SARIn mode.

On the other hand, the uncertainty of the actual sea surface height depends on the abundance of detected leads which are needed for an accurate interpolation of the sea surface anomaly (Ricker et al., 2014). The uncertainty of the sea surface anomaly (σ_{SSA}) is indeed determined by taking the standard deviation of the lead elevations detected along the track within a 25-km moving window. If no leads are detected inside the window, σ_{SSA} takes the value of the deviation of the interpolated SSA from the mean CS2 elevation (Ricker et al., 2014).

The instrument system error and the uncertainty of the actual sea surface height can be combined to obtain the

total random uncertainty of an individual radar freeboard measurement by adding up the variances

$$\sigma^2_{F_R} = \sigma^2_{l1b} + \sigma^2_{SSA} \tag{3}$$

This way of combining different sources of error would require them to be uncorrelated. This condition is probably not completely satisfied in this case, for instance, one could state that the speckle noise affects in some way the uncertainty of the SSA. However, due to the way in which σ_{SSA} is determined, its value is strongly governed by the number of detected leads and not by the error on the range measurement. Therefore, in this study the single uncertainties of the range measurements and sea surface anomaly are assumed to be uncorrelated, although it is acknowledged that the total radar freeboard uncertainty is an approximation resulting from a lack of knowledge of the covariance of individual error contributions (Ricker et al., 2014).

The random uncertainty of the ALS snow freeboard is estimated following the approach in Hvidegaard and Forsberg (2002) as

$$\sigma^2_{F_S} = \sigma^2_{ALS} + \sigma^2_{filt} \tag{4}$$

where σ_{ALS} is the vertical accuracy of the ALS instrument, reported in Skourup et al. (2012) to be approximately 0.10 m, and σ_{filt} is the error due to the filtering parameters chosen for the lead detection algorithm explained in Section 3.3.3. This value is estimated to be approximately 0.05 m (Hvidegaard and Forsberg, 2002).

3.2. SIRAL data processing

This section describes the methods used to estimate surface elevations from the SIRAL 20 Hz SARIn waveforms (3.2.1) as well as how the SIRAL SSA is determined (3.2.2).

3.2.1. Elevations

In the first place, the quality of the waveforms is assessed according to their *signal-to-noise ratio* (*SNR*), computed as

$$SNR = 10\log_{10}\left(\frac{P_{max}}{P_N}\right) \tag{5}$$

where P_{max} is the waveform maximum power and P_N is the thermal noise of the waveform, defined in Vignudelli et al. (2011) as

$$P_N = \frac{1}{5}\sum_{i=1}^{5} P_i \tag{6}$$

Here, P_i is the power at the i-th gate of the waveform. Waveforms having $SNR < 15$ dB are considered to be too noisy to allow for the identification of a clear leading edge and are therefore discarded. The value of this threshold is chosen using a trial and error approach based on the analysis of a large number of waveforms covering different areas of the Arctic Ocean (Di Bella, 2015).

The *pulse peakiness* (*PP*) of the remaining waveforms is computed as (Armitage and Davidson, 2014)

$$PP = \frac{P_{max}}{\sum_{i=1}^{N_g} P_i} \tag{7}$$

where N_g is the total number of gates. Waveforms having $PP < 0.012$ are discarded, since they are considered to be generated by reflections coming from the ocean. In this case, the PP threshold is derived from the results in Ricker et al. (2014).

Waveform classification is then performed taking inspiration from Armitage and Davidson (2014). Leads and sea ice are identified using two PP thresholds, namely a *high* threshold (PP_h) and a *low* one (PP_l).

All waveforms having $PP > PP_h$ present a purely specular feature which can be associated to a reflection coming from a lead relatively close to the satellite nadir. On the other hand, waveforms with $PP < PP_l$ are characterised by a purely diffusive feature which is the result of the radar signal being reflected by a rougher surface like sea ice. The value of PP_h and PP_l is set in this study to 0.25 and 0.045, respectively (Kildegaard Rose, 2013).

The remaining waveforms having $PP_l < PP < PP_h$ usually present both specular and diffusive features and they are classified in this study as *mixed*. In order to assess how the number of processed waveforms affects the total random freeboard uncertainty, two scenarios are defined:

- SIN_0, a SAR-like scenario where only waveforms with $PP > 0.25$ are processed and the phase information is discarded
- *SIN*, where waveforms with $PP > 0.09$ (Di Bella, 2015) are processed as they are considered to generate from leads. Additionally, the phase information is used to estimate the exact location of the scattering point on the ground.

Waveforms with $0.045 < PP < 0.09$ are not processed in this study because of their more ambiguous nature.

In this work sea ice waveforms are retracked with a 50% *Threshold First-Maximum Retracker Algorithm* (*TFMRA50*) (Ricker et al., 2014). In this way, the first local maximum of the waveform, usually associated with a return from ice floes, is retracked. The noise in front of the leading edge is suppressed by using a dynamic power threshold, defined as a percentage of the maximum power of the waveform. The first local maximum is then individuated as the first peak being larger than such a threshold. The exact retracking gate on the leading edge is finally obtained by linearly interpolating between the gates adjacent to ca. the 50% of the power of the first peak (for more details, see Ricker et al., 2014).

The same threshold retracker, adapted to retrack the peak corresponding to the maximum waveform power, instead of the first one, is used to retrack both leads and mixed waveforms.

The lower radar propagation speed through the snowpack is addressed by adding to the SIRAL sea ice elevations the correction

$$h_c = h_s\left(\frac{c}{c_s\,(\rho_s)} - 1\right) \tag{8}$$

where h_s is the snow depth and $c/c_s\,(\rho_s)$ is the ratio between the speed of light in space and in snow, dependent on the snow density ρ_s. Following Kwok and Cunningham (2015), the snow depth and density in Eq. (8) used in this study are the time- and space-varying estimates from the Warren climatology (W99) (Warren et al., 1999). Recent studies suggest that the W99 climatology does not represent very accurately the Arctic snow properties in the last years (Kurtz and Farrell, 2011; Newman et al., 2014), probably due to the decrease of multi-year ice (MYI) in the Arctic Ocean (Maslanik et al., 2011; Comiso, 2012; Polyakov et al., 2012). Modified versions of W99, scaling the snow depth values on first-year ice (FYI), have been suggested to partially overcome this issue (Laxon et al., 2013). However, in this work the classic version of W99 is used, based on the information available from the OSI-SAF sea ice type product on the 5th of April 2012, which shows mainly MYI inside the Wingham box (Fig. 4).

In the SIN scenario, where waveforms with a lower PP are included into the analysis, the strong reflection of scattering targets lying several kilometres away from nadir can contaminate the signal picked up by the radar (Armitage and Davidson, 2014; Abulaitijiang et al., 2015). A typical situation over sea ice is shown in Fig. 5 where the range R_m to an off-nadir lead is measured by the radar instead of the correct range R (Armitage and Davidson, 2014). Using the interferometric capabilities of CS2, it is possible to determine the across-track distance d to the scatterer and thus to correct the range measured by the satellite accordingly. In fact, when the scatterer – in this case the lead – is not exactly at nadir, the reflected signal travels different distances to the two SIRAL's antennas and therefore it is detected by them with two different phases. This difference can be used to compute the angle θ, subtended between the antenna boresight direction and the direction of the lead. Together with the roll angle provided by the star tracker on board of CS2, it is possible to compute the angle ρ measured from the local vertical to the direction of the lead (Armitage and Davidson, 2014). The across-track distance to the lead can then be calculated using the small-angle approximation as

$$d = R_m \sin(\rho) \simeq R_m \rho \tag{9}$$

and the consequent off-nadir range correction (ONC) is obtained through the relation

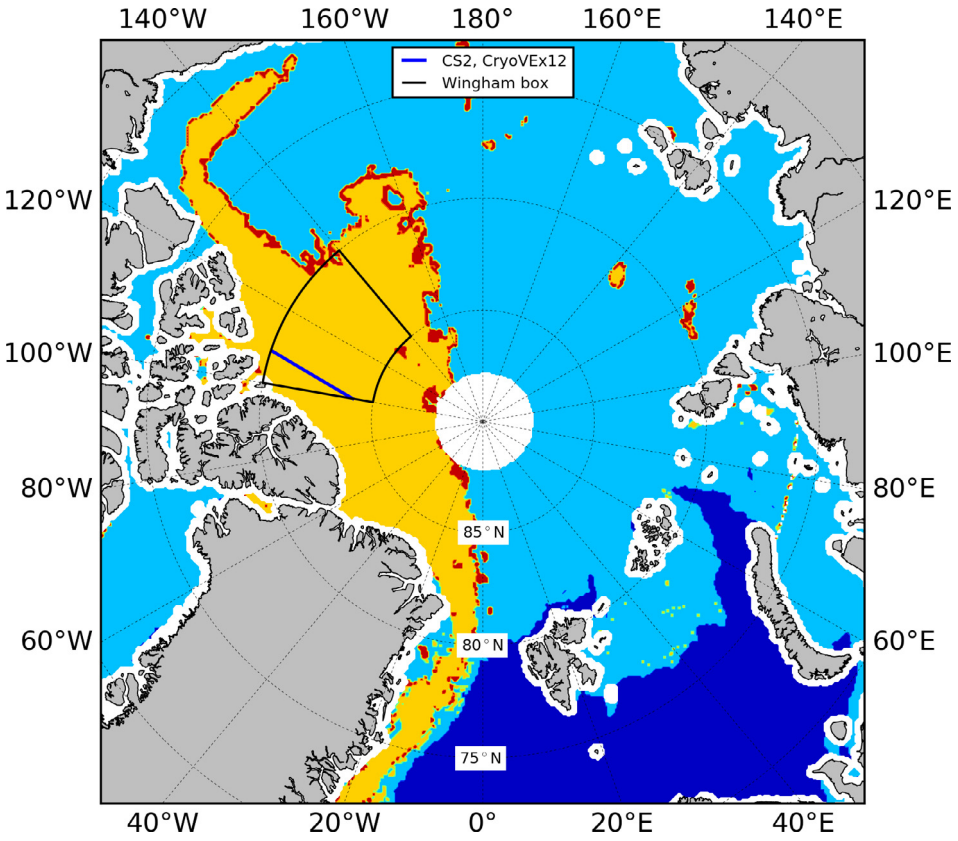

Fig. 4. Sea ice type from the OSI-SAF product on 5/4/2012, showing areas of open water (dark blue), first-year ice (light blue), multi-year ice (yellow) and ambiguous ice type (red). The dark blue line represents the track where the SIRAL, ASIRAS and ALS data used in this study have been acquired. (For interpretation of the references to colour in this figure legend, the reader is referred to the web version of this article.)

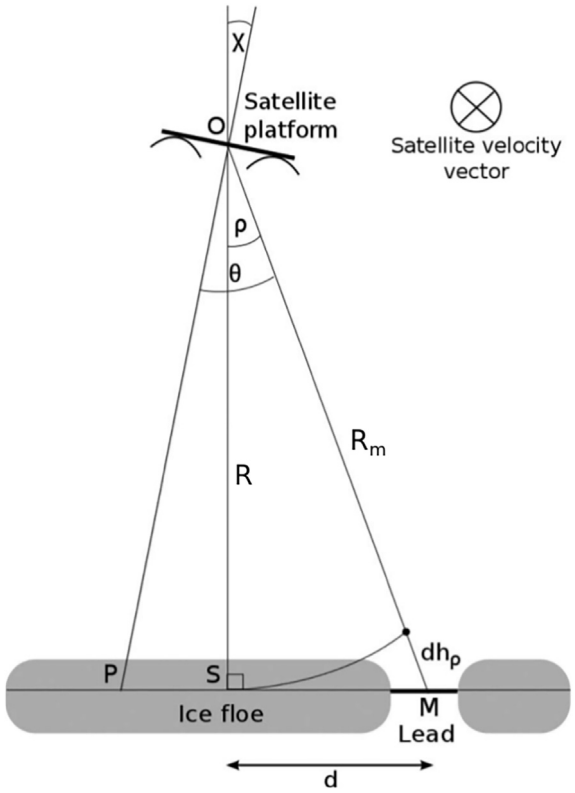

Fig. 5. Geometry for the off-nadir range correction (ONC). Off-nadir leads can cause an overestimation of the range, as $R_m > R$. The phase information available in the CryoSat-2 SARIn mode enables to compute the ONC (dh_ρ in the figure) and to correct for the range overestimation. In the drawing the satellite velocity vector enters the page. Modified from Armitage and Davidson (2014).

$$dh_\rho \simeq \eta R_m \frac{\rho^2}{2} \tag{10}$$

where η is a geometric factor used to correct for the curvature of the Earth (Wingham et al., 2004; Galin et al., 2013). The corrected range R in case of flat surface assumption is then obtained as

$$R = R_m - dh_\rho \tag{11}$$

The ONC is applied only in the SIN scenario.

3.2.2. Sea surface anomaly

The lead elevations obtained through the retracking procedure identify the local SSH. The local SSA is then obtained by subtracting from it the MSS at the lead locations, as

$$SSA = SSH - MSS \tag{12}$$

The SSA at the sea ice locations is obtained by along-track linear interpolation and, finally, by applying a running mean filter with 25-km width, to smooth jumps that can occur in dense lead clusters due to the signal noise (Ricker et al., 2014).

3.3. ALS data processing

3.3.1. Sea ice drift

In the first place, a sea ice drift correction is applied to the ALS measurements to account for the 4.5 h difference between the satellite and aircraft passes. Drift velocity vectors derived from repeated SAR images are provided by R. Saldo from DTU Space. The drift for each ALS measurement is obtained by using a nearest neighbour approach and is found to be very low in the area. As a consequence, the drift-corrected ALS measurements are shifted slightly to the West, but still within the CryoSat-2 footprint area (Di Bella, 2015).

3.3.2. Elevations

In order to compare heights and freeboard values from SIRAL and ALS, it is crucial to average the elevations retrieved by the ALS instrument to the SIRAL footprint. There exist many ways of doing it as discussed in Kildegaard Rose (2013). In this study, ALS measurements are averaged using their distance from the satellite nadir as a weight. Along the analysed track, each SIRAL footprint contains on average ~30,000 ALS point measurements, thus, lead heights will be averaged out during the process.

3.3.3. Sea surface anomaly

The determination of the ALS SSA requires a different approach from the one used for SIRAL since no information about the ALS waveforms is available in the data acquired for this study and, thus, leads cannot be identified in the way used for the radar case. In this study, the lead heights are extracted by looking for minima in the elevation profile following an approach similar to the one in Hvidegaard and Forsberg (2002). In the first place, the elevation profile is detrended using the MSS to remove the main features of the sea surface height. The minimum height is then found for 50 s intervals and these minima are averaged in groups of three. The resultant points are considered to represent lead elevations. This process is equivalent to apply a high-pass filter with a filtering parameter of approximately 150 s, which corresponds to about 10 km on ground considering that the aircraft flies at 250 km/h (Hvidegaard and Forsberg, 2002).

The SSA is finally obtained by linear interpolation of the lead elevations to the sea ice locations identified by SIRAL.

3.4. ASIRAS and OIB data processing

Level 2 freeboard heights from ASIRAS are corrected for sea ice drift and averaged to the SIRAL footprint as explained in Sections 3.3.1 and 3.3.2, respectively. The results are then compared directly to ALS and SIRAL freeboard estimates. No correction accounting for the lower radar propagation speed through the snow is applied to the ASIRAS freeboards as, at the time of writing, it was not clear if it was already applied by the AWI processor.

As shown in Fig. 1, OIB snow depths are not available exactly along the CS2/CryoVEx track. After a further 50-km along-track averaging, snow depth at the desired locations are obtained by linear interpolation of all OIB acquisitions inside the Wingham box. Even though the time of such acquisitions spans from 22 to 7 days prior the CS2 pass, no sea ice drift correction is applied so that the resulting along-track estimates represent solely a rough reference for snow depth in the study area during March 2012. Such a reference is used, together with snow depth estimates from the W99 climatology, to qualitatively assess the penetration of the Ku-band signal from ASIRAS and SIRAL into the snowpack.

4. Results and discussion

4.1. CS2 lead detection

In this work, the phase information provided by the CS2 SARIn acquisition mode is used to determine the across-track distance of leads from nadir and to compute the respective ONC (in the SIN scenario). Two examples showing the capability of SIRAL to detect off-nadir leads can be observed in Fig. 6 where the red dots represent the location of the waveforms classified as leads and relocated using the computed across-track distance. Dark areas in the Envisat image on the background correspond to a low value of backscatter coefficient which, for a slant-looking instrument like the ASAR, can be associated to specular surfaces, i.e. leads. It can be generally observed that the across-track distance computed using the phase information is quite accurate since practically every red dots lies on top of a black spot of the ASAR image. The furthest off-nadir lead detected by SIRAL is located at ~1500 m from the satellite nadir (Fig. 6a) but if, as a test, all mixed waveforms are included into the analysis, it turns out that SIRAL is able to pick up leads up to ~2300 m from nadir along this specific track (Fig. 6). However, as already discussed in Section 3.2.1, waveforms with $0.045 < PP < 0.09$ are mostly ambiguous and difficult to retrack and therefore discarded.

These examples show that the phase information available in the SARIn mode gives CS2 an excellent capacity to determine the across-track distance of the detected leads.

4.2. Elevations and SSAs

The top plot in Fig. 7 shows SIRAL lead height anomalies from the MSS, distributed around a mean value of ca. −1.01 m, with several points lying below −2 m. Large ONC values, computed for each lead height and shown in the middle plot, correspond to very low height anomalies suggesting the latter to be caused indeed by off-nadir leads. The bottom plot shows the height estimates corrected with the ONC, i.e. the sum of the top and middle plots, having a mean value of ca. −0.92 m. It is observed that some of the corrected heights are still close to −2 m which suggests that, in this case, the ONC is not able to completely correct every underestimated lead height. A deeper analysis relates these heights with waveforms having a value of PP close to the cutoff threshold of 0.09. This highlights the importance of the thresholds used for waveform classification and suggests that further investigation might be needed in that regards.

Fig. 8 shows in blue the height anomalies from the MSS and in red the SSAs obtained processing ALS (Fig. 8a) and SIRAL data (8b and c). As expected, average elevations from ALS (−0.38 m) are found to be larger than those from SIRAL (−0.56 m), as they generate from the air-snow interface while SIRAL Ku-band signal penetrates, at least partly, the snowpack. In the results from SIRAL it can be noticed that some of the retracked radar elevations lie below the corresponding SSA, which is mainly attributed to instrument noise on the measurements and to the uncertainty of the estimated SSAs.

The SSAs in Fig. 8 look quite different from each other. In particular, the SIN_0 SSA looks smoother than the others as only 15 leads are detected along the satellite track, compared to the 170 and 43 lead heights used in the SIN scenario and for the ALS SSA, respectively. The large variation in the SIN SSA observed around 83°(Fig. 8c) is caused by the underestimated lead heights visible in Fig. 7, thus, it is likely not to reflect a real variation of the SSA.

The ONC can correct for most of the underestimated lead heights which are then used to estimate the SSA. The SSA has a great impact on freeboard estimates as discussed further in Section 4.3.

4.3. Freeboard and uncertainty

In Figs. 9a–d the ALS snow freeboard and the ASIRAS radar freeboard are compared directly with the SIRAL radar freeboard estimated for the different scenarios (mean values in Table 1).

No spatial correlation is observed between satellite and airborne freeboards in any of the cases along the chosen track. The lack of correlation could depend on several factors. The first, and probably the most important, is the difference in the instruments' footprint size. Although ALS and ASIRAS data have been averaged along-track to the SIRAL footprint, the measurements cover only approximately 300 m and 10 m across-track, respectively, compared to the 1600 m covered by SIRAL. Thus, the instruments might be looking at different surfaces. While this would not affect significantly the average freeboard, it might affect spatial correlation at the footprint scale. Such a low correlation is also found as a result in the ESA CryoVal-SI project (Haas et al., 2016) where the authors show how additional along-track averaging on increasingly larger distances improves significantly the spatial correlation between SIRAL and airborne freeboards. The footprint issue is also supported by Fig. 9e which

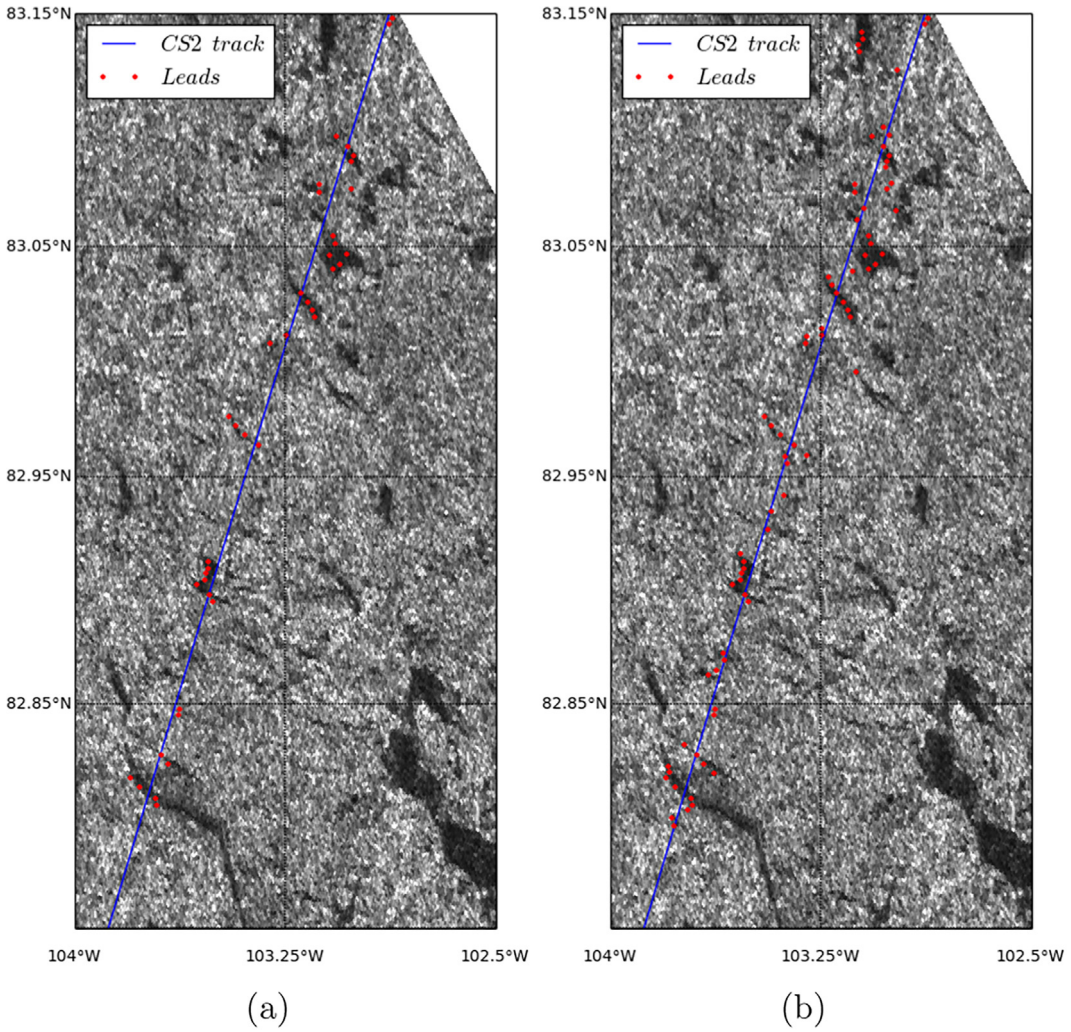

Fig. 6. Segment of CryoSat-2 (CS2) orbit (blue line) on top of an ASAR WSM image from Envisat. The leads detected by SIRAL (red dots) are relocated off-nadir using the SARIn phase information, showing an excellent match with the leads detected by the ASAR instrument (black pixels). In (a) all waveforms with pulse peakiness larger than 0.09 are processed as leads while in (b) the threshold is lowered to 0.045 in order to assess SIRAL lead detection capabilities. (For interpretation of the references to colour in this figure legend, the reader is referred to the web version of this article.)

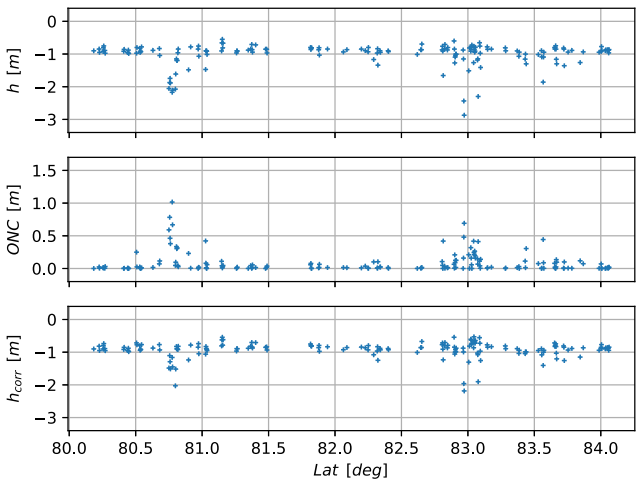

Fig. 7. SIRAL lead elevations (top), off-nadir correction (ONC) computed using the SARIn phase information (middle) and lead elevations after correction (bottom). All heights are relative to the MSS.

shows a good correlation (0.69) between ALS and ASIRAS freeboards.

Other factors impacting the spatial correlation are the algorithms used to estimate the SSA, as the SSA spatial variations reflect directly on the freeboard estimates, as well as the noise on measurements, as the number of representative measurements in a SIRAL footprint are: 1, ~100 and ~30,000 for SIRAL, ASIRAS and ALS, respectively.

With regards to the mean values, the snow freeboard tends to be larger than the radar freeboard for all cases, as expected. With a difference of 5 cm, ASIRAS and SIRAL freeboards are in good agreement, taking into account their respective uncertainties in Table 1. The agreement gets better if one considers that ASIRAS data have been retracked at AWI using a TFMRA with a 40% threshold. Lower thresholds lead, in fact, to higher values of freeboard as reported by Ricker et al. (2014), who estimated the average Arctic freeboard to be 6 cm larger when using a 40% threshold, instead of 50%, in March 2013 on MYI.

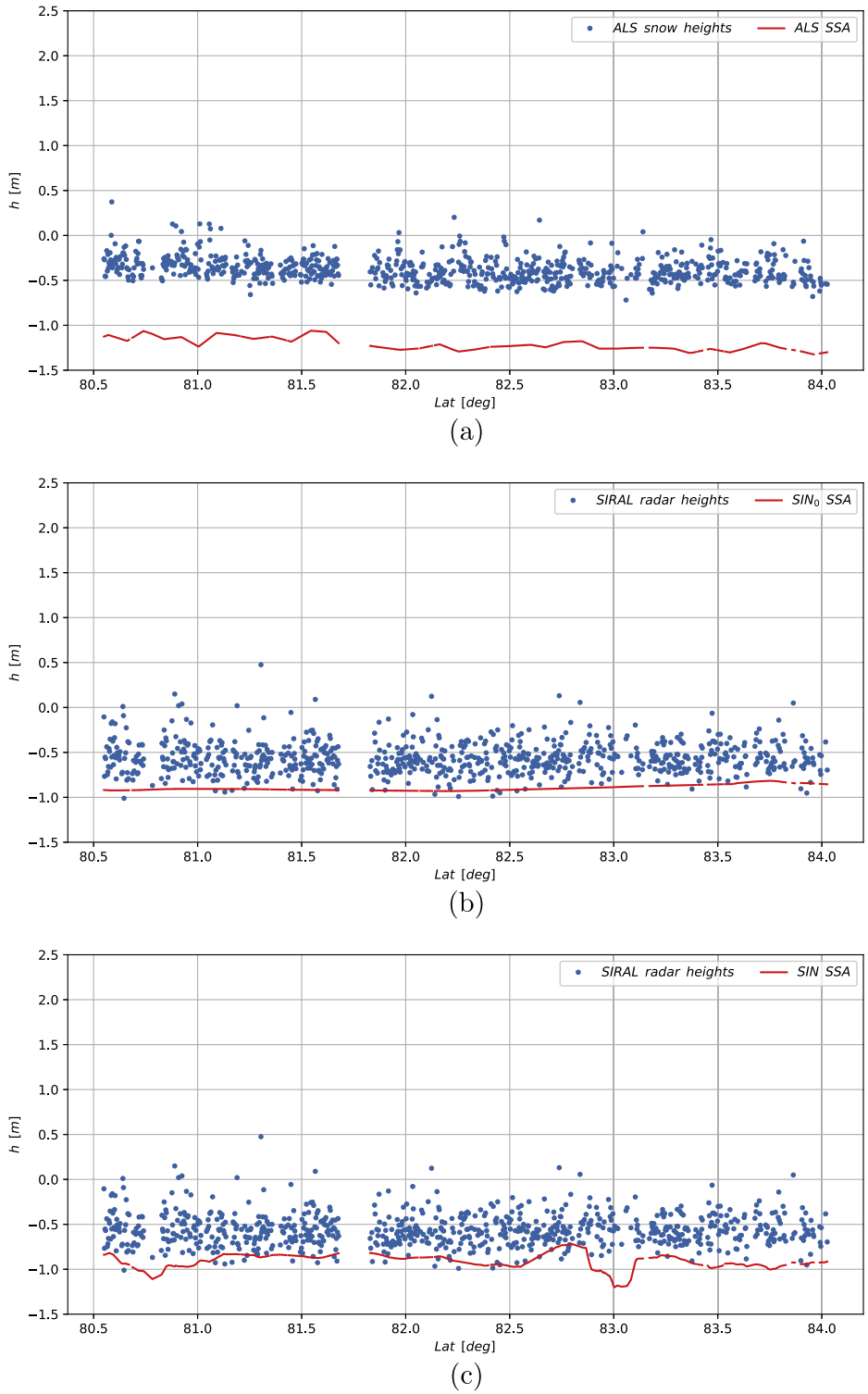

Fig. 8. Elevation profiles from ALS (a) and SIRAL for the SIN_0 (b) and SIN (c) scenarios, showed only at locations where valid coincident measurements from all instruments are available. The blue dots represent snow (ALS) and radar (SIRAL) heights above the MSS, while the red lines show the respective SSAs. (For interpretation of the references to colour in this figure legend, the reader is referred to the web version of this article.)

The SIN_0 and the SIN mean freeboard is found to be the same which suggests that processing ambiguous waveforms with their phase information would potentially not introduce a static bias on the absolute freeboard estimates, although further investigation in this direction is surely required.

The freeboard distribution for all cases can be observed in Fig. 10. Here, the ALS mode is shifted to the right

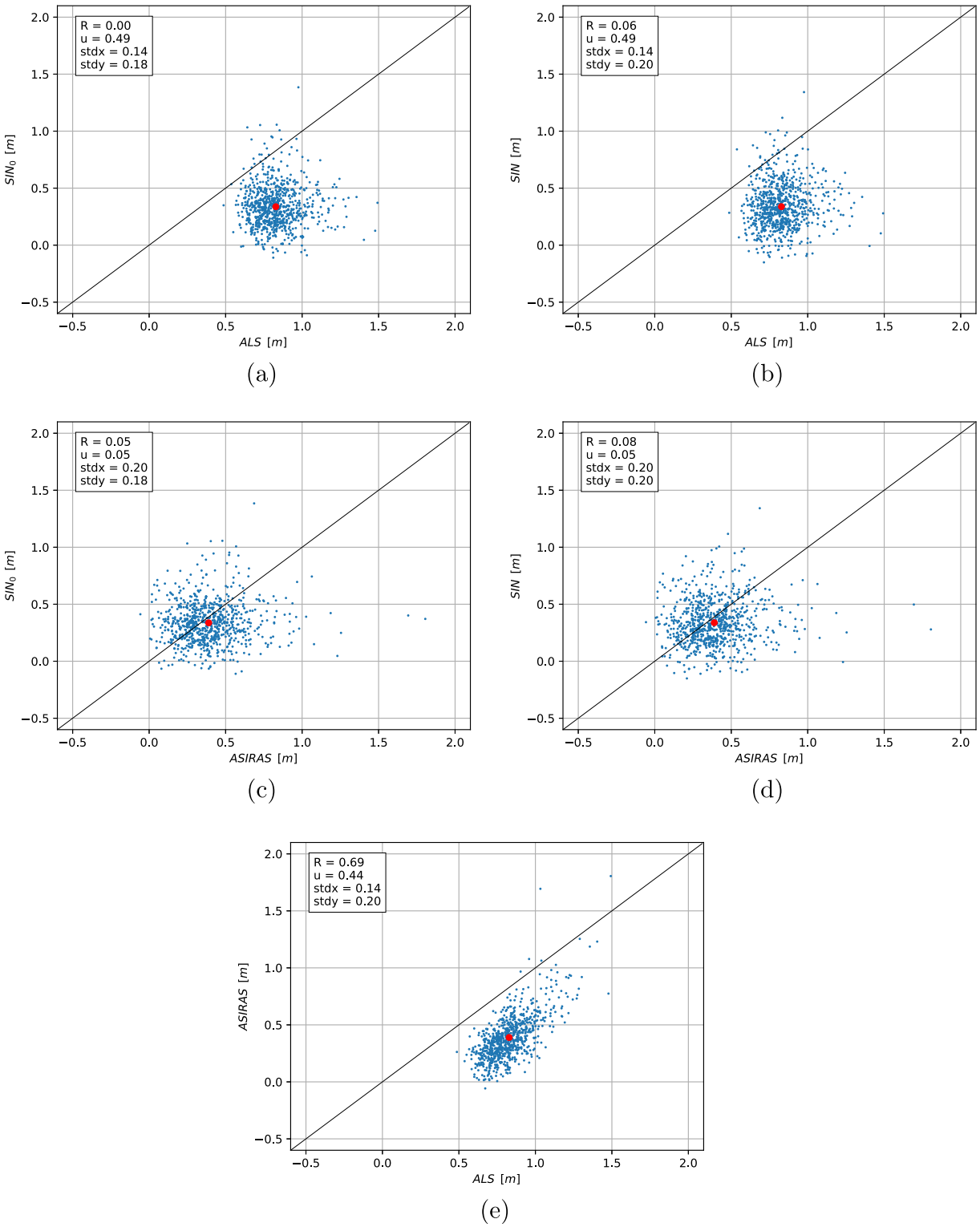

Fig. 9. Correlation plots for all satellite vs. airborne freeboards ((a) to (d)) and for ASIRAS vs. ALS (e). The top-left box in each plot shows values of correlation (R), mean difference (u) and standard deviation for the x (stdx) and y (stdy) axes.

compared to SIRAL and ASIRAS modes, as expected, since ALS senses the air-snow interface. Furthermore, the ASIRAS, SIN and SIN_0 modes lie all close to each other, supporting the fact that ASIRAS and SIRAL may have similar scattering horizons. The deviation of the radar freeboards from the snow freeboard might provide information about the average snow depth along the analysed track, topic further discussed in Section 4.4.

Fig. 11 shows the along-track snow and radar freeboards for all instruments and scenarios. While the shaded

Table 1
Mean values (μ_F) and associated uncertainties (σ_F^2) of the ALS, ASIRAS and SIRAL freeboards. $\Delta\mu_F$ are the deviations from the ALS snow freeboard and σ_{red}^2 represents the reduction of the uncertainty observed for the SIN scenario compared to the uncertainty of the SIN_0 scenario.

Scenario	$\mu_F \pm \sigma_F^2$ [m]	$\Delta\mu_F$ [m]	σ_{red}^2 [%]
ALS	0.83 ± 0.01	–	–
ASIRAS	0.39 ± 0.10	0.44	–
SIN_0	0.34 ± 0.10	0.49	–
SIN	0.34 ± 0.06	0.49	40

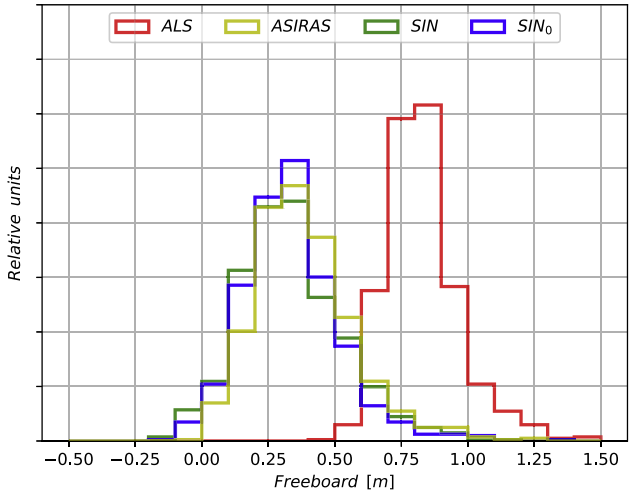

Fig. 10. Freeboard distribution corresponding to Fig. 11. The ALS mode, shifted to the right, and the good agreement between the radar modes support the idea that ASIRAS and SIRAL penetrate the snowpack and might have similar scattering horizons.

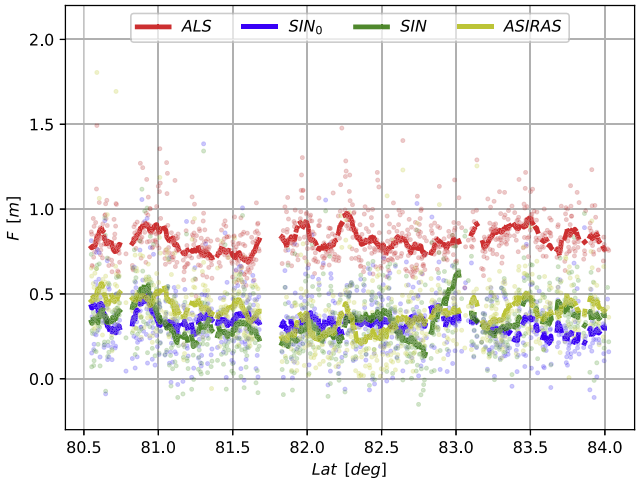

Fig. 11. Along-track snow and radar freeboards, showed only at locations where valid coincident ALS, ASIRAS and SIRAL measurements are available. The shaded dots represent estimates at the SIRAL footprint scale while the thick solid lines are the result of a 10-km running mean.

dots identify the freeboard estimated at the single SIRAL measurement locations, the thick solid lines are the result of a 10-km running mean applied to reduce noise and small-scale artefacts (Ricker et al., 2014). It can be observed that the snow freeboard lies on top of the radar freeboard along the entire track. In general, the radar freeboard does not have to follow exactly the same features presented by the snow freeboard since the scattering horizon for the SIRAL and ASIRAS instruments can have along-track profiles different from the air-snow interface. Nevertheless, this is observed quite clearly when comparing ALS and ASIRAS freeboards, while the SIRAL freeboard shows similar features only between approximately 80.5° and 81.25° and around 83.5°. An unexpected feature of the SIN freeboard is observed at latitudes between 82.6° and 83° and it is caused by the variation observed in the SIN SSA at the same latitudes (Fig. 8c) already discussed in Section 4.2.

The most interesting result of this study is perhaps the ~40% reduction in the total random freeboard uncertainty (σ_{red}^2 in Table 1), intended as the reduction of the uncertainty for the SIN scenario when compared to the SIN_0 case. Such a value could be further increased by processing larger datasets. However, it has to be noticed that the SIN_0 scenario emulates a SAR acquisition, but a real SAR acquisition would be less noisy than a SARIn one due to the higher burst repetition frequency (Wingham et al., 2006). While this is taken into account in the contribution to the freeboard uncertainty (σ_{l1b}), the standard deviation of the lead heights would be also slightly reduced in a real SAR acquisition. Nevertheless, the contribution due to the SSA (σ_{SSA}^2) is the quantity dominating the total freeboard uncertainty, which value is in turn governed by the number of leads detected along the track. For this reason, it is likely that there would always be a reduction in the total random freeboard uncertainty when including more leads and using the phase information available in the SIRAL SARIn acquisition mode.

Despite the lack of spatial correlation observed between satellite and airborne freeboards, due mainly to the different footprint size, a good agreement is found between average estimates when taking into account uncertainties and the presence of snow (further discussed in Section 4.4). Additionally, a significant reduction in the SIRAL random freeboard uncertainty is observed in the SIN scenario, due to the larger number of leads detected along the track.

4.4. Snow depth

In this section OIB snow depths are compared with snow depth estimates obtained by subtracting the ALS and the ASIRAS freeboard heights. Monthly values of snow depth from W99 are included as an additional reference.

Fig. 12 shows a comparison between the three snow depth estimates, namely W99, OIB and ALS-ASIRAS freeboard heights. The mean values are 0.36 ± 0.09 m, 0.31 ± 0.06 m and 0.44 ± 0.14 m, respectively. The different spatial variability is expected since ALS and ASIRAS measurements are averaged to the SIRAL footprint (~300 m

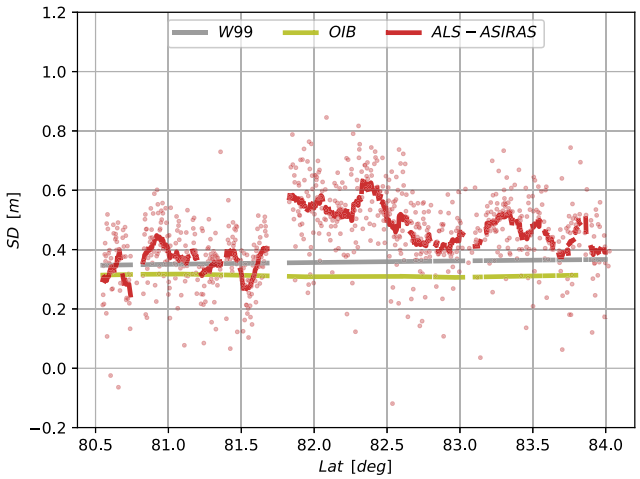

Fig. 12. Along-track snow depth estimates from the Warren climatology (W99), Operation IceBridge (OIB) and the ALS snow freeboard minus the ASIRAS radar freeboard. The thick solid red line is the result of a 10-km running mean applied to the shaded red dots. (For interpretation of the references to colour in this figure legend, the reader is referred to the web version of this article.)

along track), while OIB values are averaged 50 km along track and W99 values decrease following a second-degree polynomial outside the central Arctic Ocean (Warren et al., 1999). A good agreement is found for all estimates at latitudes between 80.5°and 81.6°, where the mean snow depth estimates from W99, OIB and ALS-ASIRAS equal 0.35 m, 0.32 m, and 0.35 m, respectively. On the other hand, from 81.8°to 84°ALS-ASIRAS snow depth seems to deviate from the other estimates up to ~0.25 m. This is the result of the simultaneous decrease in the ASIRAS freeboard and the slight increase in the ALS freeboard observed at the same range of latitudes (Fig. 11). These variations might be attributed to the way in which the ASIRAS data are processed, however, this is hard to assess as details about the ASIRAS processing were not available at the time this work was carried out. On the other hand, it should be remembered that estimates from the W99 climatology and OIB are only used as a reference in this study and that part of the deviation might be explained by actual snow accumulation.

The average snow depth estimates from W99, OIB and ALS-ASIRAS are additionally compared to the deviations of the average SIRAL radar freeboard from the average ALS freeboard ($\Delta\mu_F$ in Table 1). From Table 1 one can see that ALS-SIN$_0$ = ALS-SIN ≈ 0.49 m. This value does not agree in general with the snow depths from W99 and OIB, but it does agree with the ALS-ASIRAS estimate, taking into consideration the 0.10 m ASIRAS freeboard uncertainty. This supports the fact that collocated laser and Ku-band radar altimetry measurements could be a valuable combination to estimate snow depth during the spring, when the snow is usually cold and dry. However, during late summers, characterised by wet and warmer snow cover, Ku-band signals would probably not penetrate very much the snowpack. In this regard, it will be interesting to look at the results of the CryoVEx campaign which took place during the fall of 2016.

In general, without collocated accurate snow depth measurements it is not easy to assess snow depth variation, a reason why the authors strongly support the presence of in situ measurements in the coming CryoVEx field campaigns.

5. Conclusions

In this study, measurements from the ALS and ASIRAS instruments collected during the CryoVEx 2012 campaign are used to assess the performance of CS2 along a sea ice-covered track. This is accomplished through the comparison of the heights, SSAs and freeboards estimated using measurements from the three instruments as well as by considering snow depth estimates from the W99 climatology and the OIB campaign carried out in the spring of 2012. Additionally, the phase information provided by the SIRAL SARIn acquisition mode, already used by Armitage and Davidson (2014) to reduce the uncertainty of the sea surface height in ice-covered areas, is used to investigate the possible reduction in the Arctic radar freeboard uncertainty. This is achieved by defining two scenarios: SIN$_0$, emulating a SAR-like acquisition, and SIN, where the phase information is used to correct the retrieved lead elevations. In the latter scenario, leads are detected up to a distance of ~2300 m from the satellite nadir.

No spatial correlation is observed between SIRAL freeboards and both ALS and ASIRAS freeboards, which is mainly attributed to the different instrument ground footprint size as well as to the difference in the estimated SSAs. SSA determination is found to be a key aspect when estimating sea ice freeboard.

On the other hand, a very good agreement is observed between the mean ASIRAS (0.39 ± 0.10 m) and SIRAL radar freeboards (0.34 ± 0.10 m for the SIN$_0$ and 0.34 ± 0.06 m for the SIN scenarios), taking into account the respective uncertainties and the different threshold used during retracking (40% for ASIRAS and 50% for SIRAL). It is also observed that some features present in the snow freeboard profile from ALS can be found in the radar freeboards from SIRAL and ASIRAS which serves as an additional mean of validation.

Average snow depth estimates from OIB (0.31 ± 0.06 m) and the W99 climatology (0.36 ± 0.09 m) are comparable with the average ALS-ASIRAS freeboards (0.44 ± 0.14 m), suggesting that a combination of laser and Ku-band radar altimetry could be used to measure a layer of cold and dry snow. However, an assessment of the actual snow depth estimation capabilities of this method would require further validation which should include coincident snow depth estimates from snow radars and in situ measurements.

A reduction in the radar freeboard uncertainty is observed for the SIN scenario compared to the SIN$_0$ scenario. In general, one could say that the higher the number of processed waveforms, the lower the total random uncer-

tainty of the estimates – a concept further supported by the study in Di Bella (2015). It is observed that including in the SIN scenario ~35% of the waveforms discarded in the SIN_0 scenario, reduces the uncertainty of ~40% without introducing a bias on the average freeboard. These results suggest that by taking advantage of the SIRAL interferometric capabilities it is possible to significantly reduce the random part of the radar freeboard uncertainty. On the other hand, further investigation about the error sources affecting such estimates is necessary. In fact, the covariance of the individual error contributions is not taken into account in this work.

Acknowledgements

This work was supported by the project *Space-borne observations for detecting and forecasting sea ice cover extremes* (*SPICES*) funded mainly by the European Union's Horizon 2020 Programme. CryoSat-2 data and ASAR images were provided by the European Space Agency (ESA). The CryoVEx campaigns are part of ESA's Living Planet Programme and the airborne laser scanner data are provided by DTU Space. The ASIRAS data are part of the CryoVal-SI project and are provided by the Alfred Wagner Institute. The authors would like to thank Dr. Scagliola from ARESYS for valuable input during the project.

References

Abulaitijiang, A., Andersen, O.B., Stenseng, L., 2015. Coastal sea level from inland CryoSat-2 interferometric SAR altimetry. Geophys. Res. Lett. 42 (6), 1841–1847.

Andersen, O.B., Stenseng, L., Piccioni, G., Knudsen, P., 2016. The DTU15 MSS (Mean Sea Surface) and DTU15LAT (Lowest Astronomical Tide) reference surface. Proc. ESA Living Planet Symp., 2016

Armitage, T.W.K., Davidson, M.W.J., 2014. Using the interferometric capabilities of the ESA CryoSat-2 mission to improve the accuracy of sea ice freeboard retrievals. IEEE Trans. Geosci. Remote Sens. 52 (1), 529–536.

Comiso, J.C., 2012. Large decadal decline of the arctic multiyear ice cover. J. Clim. 25 (4), 1176–1193.

Desch, S.J., Smith, N., Groppi, C., Vargas, P., Jackson, R., Kalyaan, A., Nguyen, P., Probst, L., Rubin, M.E., Singleton, H., Spacek, A., Truitt, A., Zaw, P.P., Hartnett, H.E., 2017. Arctic ice management. Earths Future 5 (1), 107–127.

Di Bella, A., 2015. Validation of CryoSat-2 SARIn Performance over Arctic Sea Ice. Master's thesis, Technical University of Denmark. <http://findit.dtu.dk/en/catalog/2346508692>.

ESA, UCL, 2014. CryoSat Product Handbook. European Space Agency and University College London.

Galin, N., Wingham, D.J., Cullen, R., Fornari, M., Smith, W.H.F., Abdalla, S., 2013. Calibration of the CryoSat-2 interferometer and measurement of across-track ocean slope. IEEE Trans. Geosci. Remote Sens. 51 (1), 57–72.

Haas, C., Hendricks, S., Ricker, R., King, J., Beckers, J. Skourup, H., Farrell, S.L., Baker, S., Gaudelli, J., 2016. CryoVal-SI: CryoSat Sea Ice Product Validation using CryoVex and IceBridge campaign data. 1.1 Edition, Technical Note 3: Assessment of Different Sources of Uncertainty. Doc. No.: CVSI-TN-WP3-3001.

Hvidegaard, S., Forsberg, R., 2002. Sea-ice thickness from airborne laser altimetry over the Arctic Ocean north of Greenland. Geophys. Res. Lett. 29 (20), 13-1–13-4.

Kildegaard Rose, S., 2013. Measurements of sea ice by satellite and airborne altimetry. Ph.D. thesis, DTU Space. <http://orbit.dtu.dk/files/80537655/PhD_SKRose.pdf>.

Kurtz, N., Studinger, M.S., Harbeck, J., Onana, V., Yi, D., 2015. IceBridge L4 Sea Ice Freeboard, Snow Depth, and Thickness, Version 1. Boulder, Colorado USA. NASA National Snow and Ice Data Center Distributed Active Archive Center.

Kurtz, N.T., Farrell, S.L., 2011. Large-scale surveys of snow depth on arctic sea ice from operation icebridge. Geophys. Res. Lett. 38 (20). https://doi.org/10.1029/2011GL049216, n/a–n/a, l20505.

Kurtz, N.T., Galin, N., Studinger, M., 2014. An improved CryoSat-2 sea ice freeboard retrieval algorithm through the use of waveform fitting. Cryosphere 8 (4), 1217–1237.

Kwok, R., Cunningham, G.F., 2015. Variability of arctic sea ice thickness and volume from cryosat-2. Philos. Trans. Roy. Soc. A-Math. Phys. Eng. Sci. 373 (2045), 0157.

Kwok, R., Cunningham, G.F., Wensnahan, M., Rigor, I., Zwally, H.J., Yi, D., 2009. Thinning and volume loss of the Arctic Ocean sea ice cover: 2003-2008. J. Geophys. Res. – Part C - Oceans 114 (C7), C07005.

Kwok, R., Rothrock, D.A., 2009. Decline in Arctic sea ice thickness from submarine and ICESat records: 1958–2008. Geophys. Res. Lett. 36 (15), L15501.

Laxon, S., Peacock, N., Smith, D., 2003. High interannual variability of sea ice thickness in the arctic region. Nature 425 (6961), 947–950.

Laxon, S.W., Giles, K.A., Ridout, A.L., Wingham, D.J., Willatt, R., Cullen, R., Kwok, R., Schweiger, A., Zhang, J., Haas, C., Hendricks, S., Krishfield, R., Kurtz, N., Farrell, S., Davidson, M., 2013. CryoSat-2 estimates of Arctic sea ice thickness and volume. Geophys. Res. Lett. 40, 732–737.

Maslanik, J., Stroeve, J., Fowler, C., Emery, W., 2011. Distribution and trends in arctic sea ice age through spring 2011. Geophys. Res. Lett. 38 (13), L13502.

Newman, T., Farrell, S.L., Richter-Menge, J., Connor, L.N., Kurtz, N.T., Elder, B.C., McAdoo, D., 2014. Assessment of radar-derived snow depth over arctic sea ice. J. Geophys. Res.-Oceans 119 (12), 8578–8602.

Polyakov, I.V., Walsh, J.E., Kwok, R., 2012. Recent changes of arctic multiyear sea ice coverage and the likely causes. Bull. Am. Meteorol. Soc. 93 (2), 145–151.

Ricker, R., Hendricks, S., Helm, V., Skourup, H., Davidson, M., 2014. Sensitivity of CryoSat-2 Arctic sea-ice freeboard and thickness on radar-waveform interpretation. Cryosphere 8 (4), 1607–1622.

Skourup, H., Einarsson, I., Forsberg, R., Haas, C., Helms, V., Hvidegaard, S.M., Nilsson, J., Olesen, A.V., Olesen, A.K., 2012. ESA CryoVEx 2012.

Skourup, H., Farrell, S.L., Hendricks, S., Ricker, R., Armitage, T.W.K., Ridout, A., Andersen, O.B., Haas, C., Baker, S., 2017. An assessment of state-of-the-art mean sea surface and geoid models of the arctic ocean: implications for sea ice freeboard retrieval. J. Geophys. Res.: Oceans 122 (11), 8593–8613.

Stroeve, J.C., Serreze, M.C., Holland, M.M., Kay, J.E., Malanik, J., Barrett, A.P., 2012. The Arctic's rapidly shrinking sea ice cover: a research synthesis. Clim. Change 110 (3–4), 1005–1027.

Vignudelli, S., Kostianoy, A., Cipollini, P., Benveniste, J. (Eds.), 2011. Coastal Altimetry. Springer.

Warren, S., Rigor, I., Untersteiner, N., Radionov, V., Bryazgin, N., Aleksandrov, Y., Colony, R., 1999. Snow depth on arctic sea ice. J. Clim. 12 (6), 1814–1829.

Wingham, D., Francis, C., Baker, S., Bouzinac, C., Brockley, D., Cullen, R., de Chateau-Thierry, P., Laxon, S., Mallow, U., Mavrocordatos, C., Phalippou, L., Ratier, G., Rey, L., Rostan, F., Viau, P., Wallis, D., 2006. CryoSat: a mission to determine the fluctuations in Earths land and marine ice fields. Adv. Space Res. 37 (4), 841–871, natural Hazards and Oceanographic Processes from Satellite Data.

Wingham, D., Phalippou, L., Mavrocordatos, C., Wallis, D., 2004. The mean echo and echo cross product from a beamforming interferometric altimeter and their application to elevation measurement. IEEE Trans. Geosci. Remote Sens. 42 (10), 2305–2323.

A.2 Improving CryoSat SARIn L1b products to account for inaccurate phase difference: impact on sea ice freeboard retrieval

Improving CryoSat SARIn L1b products to account for inaccurate phase difference: impact on sea ice freeboard retrieval

Alessandro Di Bella, Michele Scagliola, Luca Maestri, Henriette Skourup, and Rene Forsberg

***Abstract*—CryoSat is the first mission carrying on board an altimeter instrument able to operate in Synthetic Aperture Radar Interferometric (SARIn) mode. CryoSat SARIn acquisitions have been exploited for different scientific applications that take advantage of the capability to determine the across-track angle of the first return and in particular they have been proved to reduce the uncertainty of sea ice freeboard retrievals. Nonetheless, the analysis of pan-Arctic freeboard obtained by processing CryoSat Baseline C L1b products has shown large negative freeboard estimates in correspondence of the beginning of SARIn acquisitions. Throughout the paper, the SARIn waveforms are analysed to identify the cause of this behaviour. An improvement of the CryoSat L1b processor is then prototyped and used to obtain a pan-Arctic freeboard dataset where the percentage of negative freeboard is successfully minimized.**

***Index Terms*—CryoSat, SARIn, altimetry, interferometry, sea ice freeboard.**

I. Introduction

The primary goals of the ESA's Earth Explorer CryoSat (CS), launched on the 8th of April 2010, are the precise monitoring of the changes in the thickness of marine ice floating in the polar oceans and of the variations in the thickness of vast ice sheets [1]. The main payload of CS is a Ku-band pulse-width limited radar altimeter, called SIRAL (Synthetic Interferometric Radar ALtimeter), that is equipped with two antennas for single-pass interferometric capability. SIRAL can operate in three scientific measurement modes: Low Resolution Mode (LRM), Synthetic Aperture Radar (SAR) mode and SAR-Interferometric (SARIn) mode. In SAR/SARIn modes, exploiting the coherence of the emitted pulses, the along-track resolution is improved performing Delay/Doppler processing on-ground [2].

The purpose of the CS interferometer is to determine the across-track location of the received echo. When operating in SARIn mode, SAR processing is combined with across-track interferometry exploiting the echoes received by a second across-track antenna. The complex conjugate cross product of the echoes received by both antennas is formed, and the argument is the phase difference between the two echoes resulting from the different distance traveled to reach the two antennas. Across-track interferometry allows SIRAL to determine the angle to the point of closest approach (POCA) [3]. CS was equipped with this capability to improve the performance of the altimeter over that of pulse limited radars when operating over surfaces with complex topography.

The analysis of CS SARIn acquisitions was exploited to track changes in the elevation and mass of the polar ice sheets [1], which was one of the primary objective of the mission. Additionally, novel scientific applications of SARIn data have been studied, such as inland water monitoring, coastal zone altimetry and swath mode processing [1]. Among them, different studies have shown that a reduced uncertainty in the freeboard heights can be obtained exploiting the interferometric information [4]. Despite the overall improvement on the freeboard accuracy by including the interferometric information in the processing, discontinuous freeboard heights were retrieved at the boundary of the SARIn patches, as discussed in Sect. II. This paper is aimed at analysing the cause of these discontinuities and at demonstrating that the accuracy of the phase difference in CS SARIn L1b products can be increased by improving the current CS SAR/SARIn IPF1, that is the processor in charge of generating the Baseline C L1b products.

II. Freeboard retrieval from CryoSat SARIn acquisitions

Sea ice freeboard is referred to as the height of the sea ice above the local sea surface. For the last 25 years satellite altimetry has proven to be a powerful tool to measure sea ice freeboard and, thus, to estimate sea ice thickness. Freeboard can be measured using satellite altimetry by discriminating between echoes coming from sea ice and those coming from leads [5] – fractures in the sea ice cover caused by diverging ice motion and representing the local sea surface height. The very different roughness of these two surfaces determines the shape of the radar altimetry waveforms. Waveforms generating from leads, quasi-specular surfaces, resemble the impulse response of SIRAL [6], i.e., they are very "peaky" and have a very high power compared to sea ice waveforms, which have a more diffusive look.

One of the challenges when measuring freeboard with satellite altimetry is the accurate estimation of the sea surface height (SSH) in sea ice covered areas. The uncertainty of the SSH throughout the Arctic Ocean highly depends on the amount of leads detected by the satellite as well as by their

A. Di Bella, H. Skourup and R. Forsberg are with DTU Space, National Space Institute, Technical University of Denmark, Elektrovej 327, Kgs. Lyngby, Denmark (email: adia@space.dtu.dk; hsk@space.dtu.dk; rf@space.dtu.dk)

M. Scagliola and L. Maestri are with Aresys, via Privata Flumendosa 16, Milan, Italy (e-mail: michele.scagliola@aresys.it; luca.maestri@aresys.it).

This work was partially supported by the European Space Agency under Contract No. 4000111474/14/I/NB.

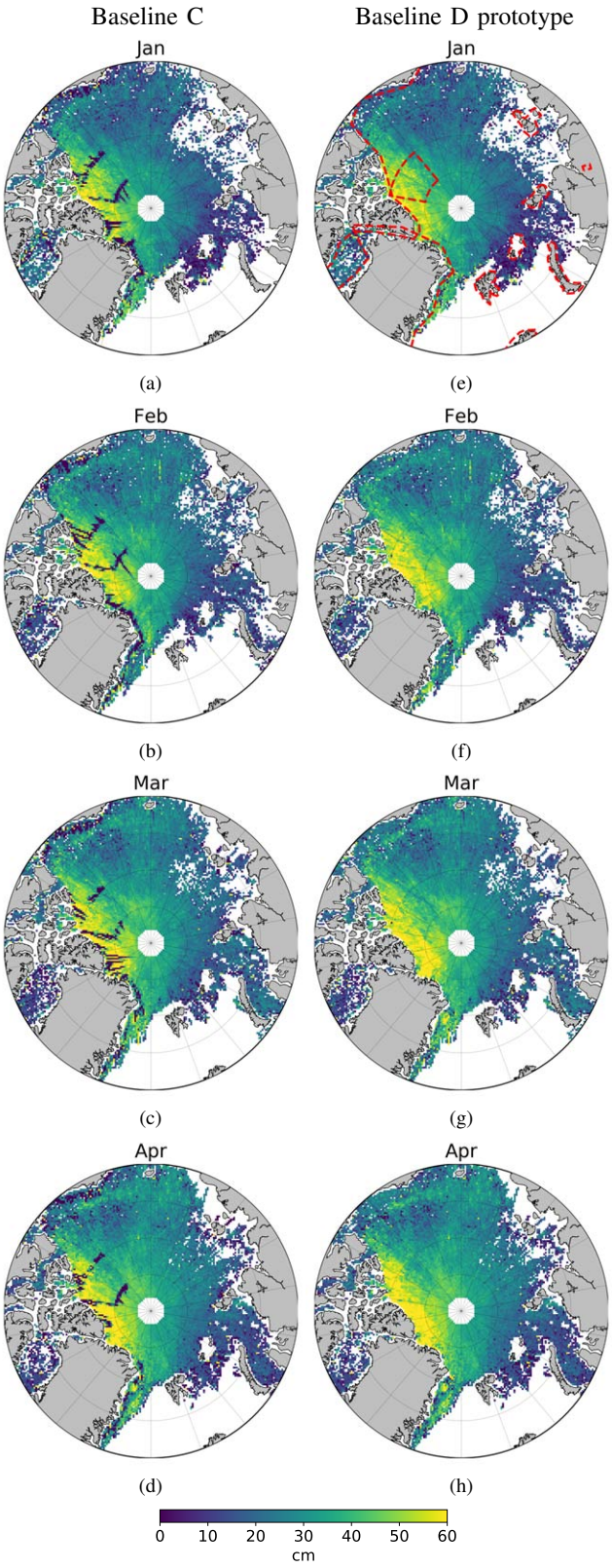

Fig. 1. Gridded monthly freeboard from Baseline C (a-d) and Baseline D prototype (e-h) L1b data for the period January/April 2014. The dashed red line in (e) represents the boundaries of the SARIn acquisition mask

spatial distribution. Echoes generated by off-nadir leads can dominate the satellite waveform [7] ultimately causing, if not accounted for, an underestimation of the SSH, as shown by [8]. The same study additionally shows that the phase information available in the SARIn acquisition mode can be used to estimate the across-track location of leads, correct for the range overestimation and ultimately get a more precise value of the along-track SSH. The higher precision of the SSH enables, in turn, to reduce the uncertainty of the sea ice freeboard retrievals, as shown by [4].

This study uses CS L1b SAR and SARIn waveforms from the latest Baseline C products. While it has been shown by [9] that the maximum power of the waveform is likely the most significant parameter aiding lead detection, surface classification is performed here using the ”pulse peakiness” of the waveform as it enables to separate returns from off-nadir leads, sea ice and leads detected at nadir (purely specular echoes) [8], [4]. All waveforms are retracked using a TFMRA50% threshold retracker based on the one recommended by [10] and the surface heights obtained from SARIn waveforms are corrected applying the off-nadir range correction (ONC) [8], [4]. All elevations are detrended using the DTU15 mean sea surface to improve the accuracy of the interpolated SSH. Finally, freeboard heights are retrieved by subtracting the local sea surface anomaly, obtained by along-track linear interpolation of the lead heights, from the sea ice elevations. A snow range correction accounting for the lower wave propagation speed into snow is applied according to [4], using snow depths and densities from the modified Warren 99 climatology [11], [12] and ice types from the EUMETSAT OSI SAF service. For a more detailed description of the processing steps, the reader is referred to [4].

Fig. 1a-1d show the gridded monthly freeboard in the Arctic Ocean from Baseline C L1b data for the period Jan/Apr 2014. White areas in the plots represent both areas where no sea ice is present – east of Greenland and south of Svalbard – as well as areas where waveforms are discarded by the processor e.g. because of the lack of detected leads or other processing errors. The freeboard spatial distribution shows the similar large-scale patterns that have been observed throughout the years from different satellite sensors, e.g. [5], [13], [12], [14], with the thicker ice growing off the Northern coast of Greenland and Canada thinning when moving towards the central Arctic. The most prominent feature in Fig. 1a-1d, however, is the negative value of freeboard at the boundaries of the SARIn acquisition mask (dashed red line in Fig. 1e). This is attributed to overestimated values of SSH from SARIn data. The fact that the SSH is interpolated and filtered along the satellite track [4] explains the smearing effect of the negative freeboards. As shown in Fig. 2, the negative freeboard values disappear when the ONC is not applied. Further analysis confirmed that the overestimated SSH are indeed caused by large values of ONC used to correct the SARIn range measurements.

Next section further investigates the accuracy of the phase difference between the echoes received at the two antennas, as this indirectly determines the value of ONC [8]. The negative freeboard pattern in Fig. 1a-1d has not been observed before, probably because the majority of the current freeboard

processors treat SARIn waveforms as degraded, i.e. noisier, SAR waveforms, discarding the phase information.

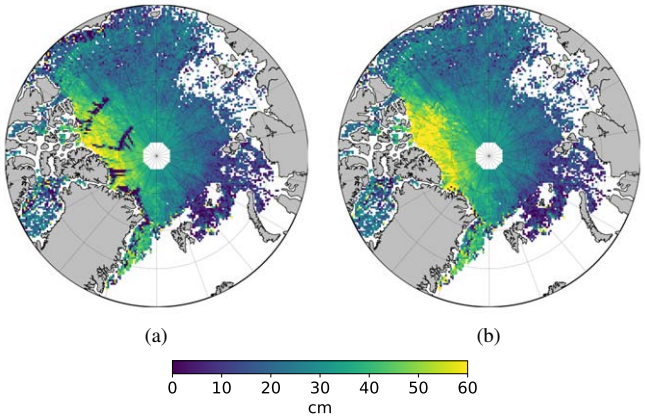

Fig. 2. Gridded freeboard from Baseline C L1b data for January 2014, with (a) and without (b) the ONC applied to the SARIn range measurements

III. Improving phase difference in CryoSat SARIn L1B products

A detailed analysis of CS Baseline C SARIn L1B products was performed, aiming at investigating the behaviour described in Sect. II. Such analysis was focussed on the phase difference and the coherence of the waveforms in correspondence of the retracking point. Fig. 3 shows the phase difference and the coherence at the retracking point for the first 210 waveforms in a Baseline C SARIn L1b product where SIRAL just switched to SARIn mode. Even if the results in Fig. 3 have been obtained identifying the retracking point by an OCOG retracker with threshold 0.8, the phase difference evolution as function of the waveform does not depend on the retracker adopted. There it can be observed that the phase difference of the first waveforms is much higher than in the rest of the product and that the corresponding coherence is low. Those results suggested that the artifacts discussed in Sect. II were likely to be addressed to inaccurate values of phase difference for the first ~ 40 waveforms in Baseline C SARIn L1b products.

Further analysis revealed that the current version of the CS SAR/SARIn IPF1 does not apply the CAL4 correction to the first 19 bursts of each acquisition, since the first CAL4 burst is retrieved about 1 second after the first science burst. It is worth recalling that the CAL4 correction aims to calibrate the phase difference between the two receiving chains [15]. CAL4 calibration is interleaved in the SARIn measurements and it is performed with a repetition frequency of 1 Hz. It has to be underlined that since each science burst contributes to several waveforms, the inaccurate phase difference in the first 19 bursts affects roughly the first 40 waveforms of each SARIn L1b product, as shown in Fig. 3.

A prototype version of the CS SAR/SARIn IPF1 was implemented in order to apply the closest in time CAL4 correction to the first 19 bursts of each acquisition. The obtained improvement on the phase difference and on the coherence at the retracking point can be noticed in Fig. 3. The phase difference of the first waveforms is aligned to the phase difference of the following ones and the corresponding coherence is high. The CS SAR/SARIn IPF1 that will be used to generate the Baseline D L1b products is planned to include this functionality in order to improve the quality of the phase difference information.

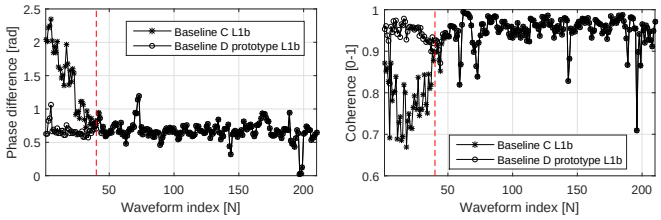

(a) (b)

Fig. 3. Phase difference (a) and coherence (b) at the retracking point for the first 210 waveforms in the product CS_OFFL_SIR_SIN_1B_20180125T012006_20180125T012109_C001.DBL.

IV. Results

In order to assess the impact of the improvement to L1b processing described in Sec. III on the estimated freeboard, the Baseline D prototype L1b processor was used to regenerate the L1b SARIn products for the period Jan/Apr 2014. Fig. 1e-1h show the gridded monthly freeboard from the new data. Comparing these results with those from Baseline C in Fig. 1a-1d, one can observe that the artificial pattern along the boundaries of the SARIn acquisition mask has disappeared, highlighting a continuous freeboard spatial distribution throughout the Arctic.

To get a more quantitative picture of the improvements achieved by the Baseline D prototype, the freeboard distribution within a 12 km area around the northern, eastern and southern boundaries of the Wingham box – the SARIn patch in the Canadian Arctic in Fig. 1e – is computed for January 2014. The distributions for Baseline C and Baseline D prototype are compared in Fig. 4. The western boundary is not included in the histograms since here SIRAL, due to the CS orbit inclination, does not switch from LRM/SAR to SARIn, but only from SARIn to LRM/SAR modes – which is the reason why the western boundary is not affected by the issue in Fig. 1a-1d. The distance of 12 km from the SARIn boundaries is chosen as this is approximately the maximum along-track distance on the ground covered by 40 20Hz CS waveforms (Sect. III). Within the area of interest, the freeboard estimated from Baseline C is largely negative with values down to -8 m (Fig. 4b). In Table I it can be noticed that the amount of negative freeboard estimates is reduced from 17.4% in Baseline C to 0.6% using the developed Baseline D prototype, with the remaining negative freeboard estimates mainly due to measurement noise. The improvement is also noticed on the mean value of freeboard inside the area of interest which increases from -8 cm to 47 cm (Table I), a more reasonable

estimate for regions with predominantly thick multi-year sea ice [6].

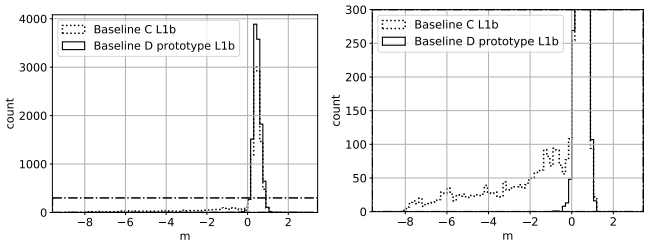

(a) (b)

Fig. 4. Freeboard distribution within the area of interest (Sect. IV) from Baseline C (dotted) and Baseline D prototype (solid) data for January 2014. The rectangle at the bottom of (a) is enlarged in (b). The total number of freeboard retrievals is $\sim$ 12000

TABLE I
BASELINE C VS. BASELINE D PROTOTYPE MEAN FREEBOARD (μ_F) AND PERCENTAGE OF NEGATIVE FREEBOARD ESTIMATES (F_n) INSIDE THE AREA OF INTEREST (SECT. IV) FOR JANUARY 2014

	Baseline C	**Baseline D**
$\mu_{\mathbf{F}}$	-8 cm	47 cm
$\mathbf{F_n}$	17.4%	0.6%

The next Baseline for CS L1b products, i.e. Baseline D, will be corrected for the issues discussed in Sect. II and will deliver accurate values of freeboard also in areas where the instrument switches to SARIn mode. By increasing the amount of usable phase information, it will additionally contribute to reduce the freeboard uncertainty [4].

V. CONCLUSION

CS SARIn data have been used to successfully monitor changes in the elevation of ice sheets, as well as inland water and coastal areas. Recently, it has been shown that the phase information available in this acquisition mode can be used to reduce the uncertainty affecting sea ice freeboard retrievals [4].

Nevertheless, processing pan-Arctic Baseline C SARIn L1b products, exploiting the phase information, has shown large negative freeboard estimates at the boundary of the SARIn acquisition mask (Fig. 1a-1d). This issue, caused by a phase difference calibration not applied to the first 19 bursts of a SARIn acquisition, affects the quality of the phase information of the first $\sim$ 40 SARIn waveforms. By updating the current SAR/SARIn IPF1 to correctly apply such calibration (Sect. III), the quality of the freeboard at the SARIn boundaries improves drastically as the amount of negative retrievals is reduced from 17.4% to 0.6% (Table I). The pattern of negative freeboard observed, using Baseline C products, at the SARIn patch boundaries throughout the Arctic basin consequently disappears (Fig. 1e-1h).

This update will be included in the new SAR/SARIn IPF1 producing the upcoming Baseline D L1b products. Improvements are expected not only for sea ice freeboard retrieval, but for any application that exploits the phase information from SARIn L1b products. According to Sect. III, improvements will be observed in areas up to $\sim$12 km inside the SARIn acquisition mask. The improvement for inland water monitoring applications will be significant especially w.r.t. monitoring small water bodies and narrow rivers, where discarding the first 19 to 40 waveforms might not always be a viable option.

REFERENCES

[1] T. Parrinello, A. Shepherd, J. Bouffard, S. Badessi, T. Casal, M. Davidson, M. Fornari, E. Maestroni, and M. Scagliola, "Cryosat: Esas ice mission eight years in space," *Advances in Space Research*, vol. 62, no. 6, pp. 1178 – 1190, 2018, the CryoSat Satellite Altimetry Mission: Eight Years of Scientific Exploitation.

[2] R. Raney, "The delay/doppler radar altimeter," *Geoscience and Remote Sensing, IEEE Transactions on*, vol. 36, no. 5, pp. 1578–1588, Sep 1998.

[3] D. Wingham, L. Phalippou, C. Mavrocordatos, and D. Wallis, "The mean echo and echo cross product from a beamforming interferometric altimeter and their application to elevation measurement," *Geoscience and Remote Sensing, IEEE Transactions on*, vol. 42, no. 10, pp. 2305–2323, Oct 2004.

[4] A. D. Bella, H. Skourup, J. Bouffard, and T. Parrinello, "Uncertainty reduction of arctic sea ice freeboard from cryosat-2 interferometric mode," *Advances in Space Research*, vol. 62, no. 6, pp. 1251 – 1264, 2018, the CryoSat Satellite Altimetry Mission: Eight Years of Scientific Exploitation.

[5] S. Laxon, N. Peacock, and D. Smith, "High interannual variability of sea ice thickness in the Arctic region," *Nature*, vol. 425, no. 6961, pp. 947–950, 2003.

[6] R. Kwok and G. F. Cunningham, "Variability of Arctic sea ice thickness and volume from CryoSat-2," *Philosophical Transactions of the Royal Society of London A: Mathematical, Physical and Engineering Sciences*, vol. 373, no. 2045, p. 20140157, 2015.

[7] M. R. Drinkwater, "Kuband airborne radar altimeter observations of marginal sea ice during the 1984 Marginal Ice Zone Experiment," *Journal of Geophysical Research*, vol. 96, no. C3, pp. 4555–4572, 1991.

[8] T. W. K. Armitage and M. W. J. Davidson, "Using the Interferometric Capabilities of the ESA CryoSat-2 Mission to Improve the Accuracy of Sea Ice Freeboard Retrievals," *Ieee Transactions on Geoscience and Remote Sensing*, vol. 52, no. 1, pp. 529–536, 2014.

[9] A. Wernecke and L. Kaleschke, "Lead detection in Arctic sea ice from CryoSat-2: Quality assessment, lead area fraction and width distribution," *Cryosphere*, vol. 9, no. 5, pp. 1955–1968, 2015.

[10] R. Ricker, S. Hendricks, V. Helm, H. Skourup, and M. Davidson, "Sensitivity of CryoSat-2 Arctic sea-ice freeboard and thickness on radar-waveform interpretation," *Cryosphere*, vol. 8, no. 4, pp. 1607–1622, 2014.

[11] S. Warren, I. Rigor, N. Untersteiner, V. Radionov, N. Bryazgin, Y. Aleksandrov, and R. Colony, "Snow depth on arctic sea ice," *Journal of Climate*, vol. 12, no. 6, pp. 1814–1829, 1999.

[12] S. W. Laxon, K. A. Giles, A. L. Ridout, D. J. Wingham, R. Willatt, R. Cullen, R. Kwok, A. Schweiger, J. Zhang, C. Haas, S. Hendricks, R. Krishfield, N. Kurtz, S. Farrell, and M. Davidson, "CryoSat-2 estimates of Arctic sea ice thickness and volume," *Geophysical Research Letters*, vol. 40, no. 4, pp. 732–737, 2013.

[13] R. Kwok, G. F. Cunningham, M. Wensnahan, I. Rigor, H. J. Zwally, and D. Yi, "Thinning and volume loss of the arctic ocean sea ice cover: 2003?2008," *Journal of Geophysical Research: Oceans (1978?2012)*, vol. 114, no. C7, 7 2009. [Online]. Available: http:https://doi.org/10.1029/2009JC005312

[14] T. W. K. Armitage and A. L. Ridout, "Arctic sea ice freeboard from AltiKa and comparison with CryoSat-2 and Operation IceBridge," *Geophysical Research Letters*, vol. 42, no. 16, pp. 6724–6731, 2015.

[15] M. Fornari, M. Scagliola, N. Tagliani, T. Parrinello, and A. G. Mondejar, "Cryosat: Siral calibration and performance," in *2014 IEEE Geoscience and Remote Sensing Symposium*, July 2014, pp. 702–705.

Appendix B

Conference posters

B.1 Validation of CryoSat-2 Performance over Arctic Sea Ice

Validation of CryoSat-2 Performance over Arctic Sea Ice

Alessandro Di Bella[1], Henriette Skourup[1], Jerome Bouffard[2], Tommaso Parrinello[2]

[1]DTU Space, National Space Institute, Copenhagen, Denmark, [2]ESA/ESRIN, Frascati, Italy

1. Description

The main objective of this work is to validate CryoSat-2 (CS2) SARIn performance over sea ice by use of airborne laser altimetry data obtained along a CS2 ground track in the Wingham Box during the CryoVEx 2012 campaign. A study by Armitage and Davidson [1] has shown that the extra information from the CS2 SARIn mode increases the number of valid sea surface height estimates which are usually discarded in the SAR mode due to snagging of the radar signal. As the number of valid detected leads increases, the uncertainty of the freeboard heights decreases.

In this study, the snow freeboard heights estimated using data from the airborne laser scanner (ALS) are used to validate the sea ice freeboard obtained by processing CS2 SARIn waveforms. The possible reduction in the random freeboard uncertainty due to the inclusion of the phase information provided by the CS2 SARIn mode is investigated comparing two scenarios. In the first one, a SAR acquisition is emulated by discarding the phase information as well as by processing only purely specular waveforms. In the second one, waveforms generating from off-nadir leads are processed and the phase information is used to correct for the associated range error.

2. Objectives

A. Validate CS2 SARIn performance over sea ice

B. Investigate the possible **reduction** in the random freeboard **uncertainty** using CS2 SARIn data

3. Data

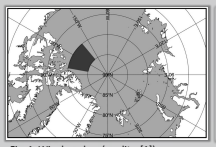

Fig. 1: Wingham box (credits: [1])

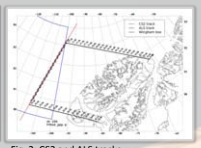

Fig. 2: CS2 and ALS tracks

This study uses data acquired inside the Wingham box (dark grey patch in fig. 1 and blue line in fig. 2) by the SIRAL instrument on board of CS2 on 5/4/2012 (level 1b SARIn, baseline C). The CS2 lead detection capability is evaluated with the aid of Envisat ASAR imagery while the estimated freeboard values are validated using data acquired by the ALS instrument on board of the Norlandair Twin Otter aircraft used in the CryoVEx 2012 campaign. Such data are collected during an underfilght of the CS2 orbit shown in red in fig. 2. Fig. 2 also shows in black the complete route flown by the aircraft on 5/4/2012, partially coinciding with the CS2 orbit inside the Wingham box.

4a. Methods: CS2 SARIn validation

To obtain freeboard heights, the elevation of the sensed surface (h) and the sea surface anomaly (SSA) are estimated (fig. 3).

SIRAL data processing

Level 1b waveforms (WF) are classified according to their pulse peakiness (PP) value. Two scenarios are defined:

- **SIN$_0$**: a SAR-like scenario where only pure specular WF ($PP > 0.25$) are processed and the phase information is discarded
- **SIN**: all WF with $PP > 0.09$ are considered leads and the phase information is used

WF with $PP < 0.045$ are classified as sea ice and those with $0.045 < PP < 0.09$ are discarded. Height values are obtained retracking leads with a Gaussian retracker and sea ice with a TFMRA50%. Additionally, in the SIN scenario the off-nadir range correction (ONC) is applied (fig. 4).

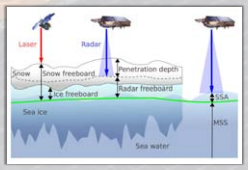

Fig. 3: Instrument-dependent freeboard (credits: [2])

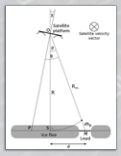

Fig. 4: Geometry for the ONC. Off-nadir leads can cause an overestimation of the range, as $R_{ol} > R$. In the drawing the satellite velocity vector enters the page. (modified from [1])

ALS data processing

Data are relocated taking into account the sea ice drift (due to the time elapsed between aircraft and satellite passes) and averaged to the SIRAL footprint.

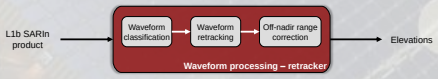

Fig. 5: SIRAL data processing chain

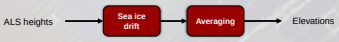

Fig. 6: ALS data processing chain

All heights are then detrended with the UCL13 mean sea surface (MSS). Using the lead elevations, the SSA is estimated for both datasets and the freeboard is computed as

$$F = h - MSS - SSA$$

4b. Methods: freeboard uncertainty

Radar freeboard uncertainty

The total random uncertainty of a single radar freeboard measurement is estimated as the RSS combination of the SIRAL elevation error (σ_{l1b}) and a contribution due to the SSA (σ_{SSA}) dependent on the number of detected leads:

$$\sigma_{F_R}{}^2 = \sigma_{l1b}{}^2 + \sigma_{SSA}{}^2$$

Snow freeboard uncertainty

The random uncertainty of the snow freeboard is estimated as the RSS combination of the ALS vertical accuracy (σ_{ALS}) and a contribution due to the filtering parameters chosen for the lead detection algorithm (σ_{filt}):

$$\sigma_{F_S}{}^2 = \sigma_{ALS}{}^2 + \sigma_{filt}{}^2$$

5. Results

A. Lead detection

By using the phase information provided by the SARIn acquisition mode, CS2 can detect leads (black areas in the ASAR image in fig. 7) up to 1.5 km from nadir. These WF are processed in the SIN scenario while they are discarded in the SIN$_0$ scenario. If, as a test, all WF with $PP > 0.045$ are considered leads, the furthest one is detected at ~ 2.3 km from nadir. However, WF with $0.045 < PP < 0.09$ are mostly ambiguous and difficult to retrack and therefore discarded.

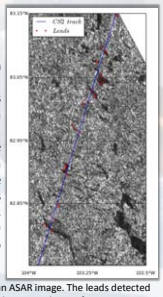

Fig. 7: Segment of CS2 orbit (blue line) on top of an ASAR image. The leads detected by SARAL (red dots) are relocated off-nadir using the SARIn phase information

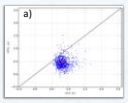

Fig. 10: Direct comparison of snow and radar freeboard in the SIN$_0$ (a) and SIN (b) scenarios. The mean and standard deviation of the data are shown by the red dot and red error bars respectively

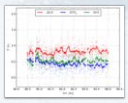

Fig. 11: Along-track snow and radar freeboard. The thick solid lines are the result of a 10-km running mean

A. Elevations and SSAs

Fig. 8 shows how off-nadir leads cause an underestimation of the height estimates (points below -1 m in the top plot) due to the longer range to the satellite measured by SIRAL (fig. 4). The phase information from SARIn enables to correct for this phenomenon by adding the ONC (middle plot) to the height estimates. The largest height underestimations correspond to the largest values of ONC, suggesting the that those low values are indeed caused by off-nadir leads. The bottom plot shows the height estimates corrected with the ONC.

Fig. 9a and 9b show in blue the elevations before and after the ALS measurements are averaged to the SIRAL footprint (ca. 300 x 1600 m). The greater variability of the height estimates before averaging is due to the high spatial resolution of the ALS instrument (ca. 0.7 x 0.7 m). Fig. 9c and 9d show the elevations and SSAs from SIRAL in the SIN$_0$ and SIN scenarios respectively. The SIRAL SSA is smoother in the SIN$_0$ scenario because only 15 leads are detected along the satellite track, compared to the 170 used in the SIN scenario.

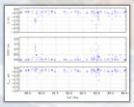

Fig. 8: Heights of the leads detected by SIRAL (top), ONC computed using the SARIn phase information (middle) and lead elevations after correction (bottom)

Scenario	$\mu_F \pm \sigma_F{}^2$ [m]	$\Delta\mu_F$ [m]	$\sigma_{red}{}^2$ [%]
ALS	0.84 ± 0.01	–	–
SIN$_0$	0.45 ± 0.19	0.39	–
SIN	$0.53 \pm \mathbf{0.11}$	0.30	**43.2**

Table 1: Mean freeboard (μ_F) and uncertainty ($\sigma_F{}^2$) of the snow and radar freeboards. $\Delta\mu_F$ is the deviation of the radar freeboard from the snow freeboard and $\sigma_{red}{}^2$ is the reduction of uncertainty comparing the SIN to the SIN$_0$ scenario

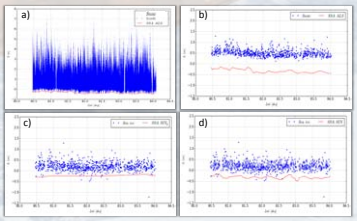

Fig. 9: Elevations (in blue) and SSAs (in red) from ALS (a,b) and SIRAL for the SIN$_0$ (c) and SIN (d) scenarios

A,B. Freeboard comparison and uncertainty

Fig. 10a and 10b compare directly the ALS snow freeboard with the SIRAL radar freeboard estimated for the different scenarios (mean values in table 1). The snow freeboard tends to be larger than the radar freeboard for all cases, as expected. The deviations of the radar freeboard from the snow freeboard ($\Delta\mu_F$ in table 1) are comparable to the ~0.34 m found as a monthly average for March 2011 in the same area in [2].

Figure 11 shows that the snow freeboard (red line) lies on top of the radar freeboard (blue and green lines), as expected. Although the radar freeboard does not have to follow exactly the same features presented by the snow freeboard, this can happen and it is observed that many features are resolved by both datasets, for instance between ~80.5° and 81.25° and around 83.5°.

Table 1 shows that by using the SARIn phase information, the mean freeboard uncertainty is reduced by ~43% in the SIN scenario when compared to the SIN$_0$ scenario.

6. Conclusions

- With SARIn it is possible to include off-nadir leads into the analysis
- Leads are detected up to a distance of 2.3 km from nadir
- Good level of agreement between freeboard heights from ALS and SIRAL
- Including more WF into the analysis (~35%) reduces significantly the random radar freeboard uncertainty (~43%)

7. Additional reading

[1] T. W. K. Armitage and M. W. J. Davidson. Using the Interferometric Capabilities of the ESA CryoSat-2 Mission to Improve the Accuracy of Sea Ice Freeboard Retrievals. *Ieee Transactions on Geoscience and Remote Sensing*, 52(1):529–536, 2014.

[2] R. Ricker, S. Hendricks, V. Helm, H. Skourup, and M. Davidson. Sensitivity of CryoSat-2 Arctic sea-ice freeboard and thickness on radar-waveform interpretation. *Cryosphere*, 8(4):1607–1622, 2014.

Living Planet Symposium 2016, Prague, Czech Republic, 9 – 13 May 2016

Correspondence to: adia@space.dtu.dk

B.2 Greenlandic coastal sea ice freeboard and thickness from CryoSat-2 SARIn data

Greenlandic coastal sea ice freeboard from CryoSat-2 SARIn data

A. Di Bella[1,2], R. Kwok[2], T. Armitage[2], H. Skourup[1], R. Forsberg[1]
[1]DTU Space, National Space Institute, Copenhagen, Denmark, [2]NASA/JPL, Pasadena, CA, USA

1. Abstract

Coastal altimetry is becoming increasingly important and relevant to society in connection to sea level rise, fishery, shipping and other off-shore activities [6]. On the other hand, altimetry in coastal areas has proven to be more challenging than over open ocean due to e.g. land footprint contamination and degradation of geophysical corrections [3,5].
In the last 8 years, ESA's CryoSat-2 (CS2) radar altimetry mission has made a big contribution to coastal altimetry. In fact, it enabled to measure sea surface height closer to the coast than conventional altimeters previously did, using SAR and SAR Interferometric (SARIn) acquisition modes to reduce footprint contamination.
This study builds on previous work by [1] and [4] and attempts to estimate sea ice freeboard using level 1b SARIn data acquired by CS2 along the northern coasts of Greenland. The challenges and limitations of SARIn altimetry in coastal areas will be identified with the support of airborne validation data from the NASA Operation IceBridge campaign.

2. Background and methods

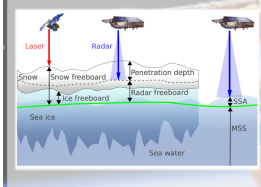

Fig 2a. Instrument-dependent freeboard. While laser altimeters like the OIB Airborne Topographic Mapper (ATM) sense the snow surface, the CryoSat-2 Ku-band radar altimeter (SIRAL) penetrates the snowpack, with a penetration depth dependent on snow properties. Credits: [7]

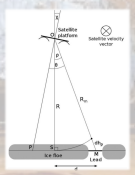

Fig 2b. Off-nadir range correction (ONC). Off-nadir leads can cause an overestimation of the range, as $R_m > R$. The phase information available in the CryoSat-2 SARIn mode enables to compute the ONC (dh_p in the figure) and to correct for the range overestimation. Modified from [2]

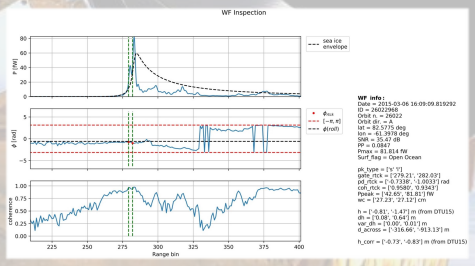

Fig 2c. Example of multi-peak retracking. In sea ice covered areas, high-coherence peaks occurring after the first one might be the result of strong reflections from off-nadir leads. The peaks having power larger than the sea ice power envelope (computed by aligning and averaging sea ice waveforms in the Wingham Box in the period Oct-Mar) are retracked. The corresponding heights are then compared to a reference SSA to increase the confidence of those reflections being actually generated by leads. The green dashed lines show the retracking gate for the selected peaks.

3. Challenges

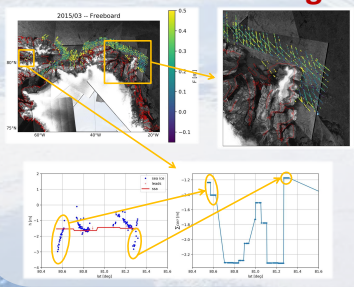

Fig 3. Challenges in coastal altimetry. The top left plot shows freeboard estimates from CS2 data in March 2015. Some of the challenges encountered in northern Greenland include the discrepancy, in this area, between the GSHHG and the real coastline (top right) as well as the quality of the geophysical corrections close to the coast and in between fjords (bottom, largest contribution from inverse barometric and dry troposphere)

4. Validation

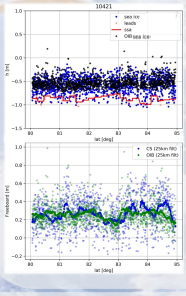

h	Mean ± STD [m]
H_{OIB}	-0.52± 0.12
H_{CS}	-0.57 ± 0.17
SSA	-0.87 ± 0.06 (54 leads)
F_{CS}	0.27 ± 0.17
F_{OIB}	0.26 ± 0.12
OIB SD	0.23

Fig 4a. Along-track assessment. Comparison of elevations (top) and freeboard (bottom) from an OIB underflight of CS2 orbit #10421 inside the Wingham Box on 26/03/2012

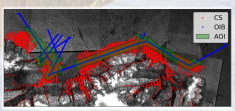

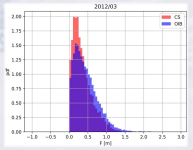

Fig 4b. Areal analysis. OIB freeboard heights from the 2012 campaign are compared to the CS2 freeboard estimates, using only measurements inside the area of interest (AOI, top). While OIB results point to a slightly larger amount of thicker ice, a good agreement is found between the mode of both CS2 and OIB freeboard estimates (bottom).
N. of measurements: 6688 (CS2) vs. 30000 (OIB)

5. Monthly freeboard

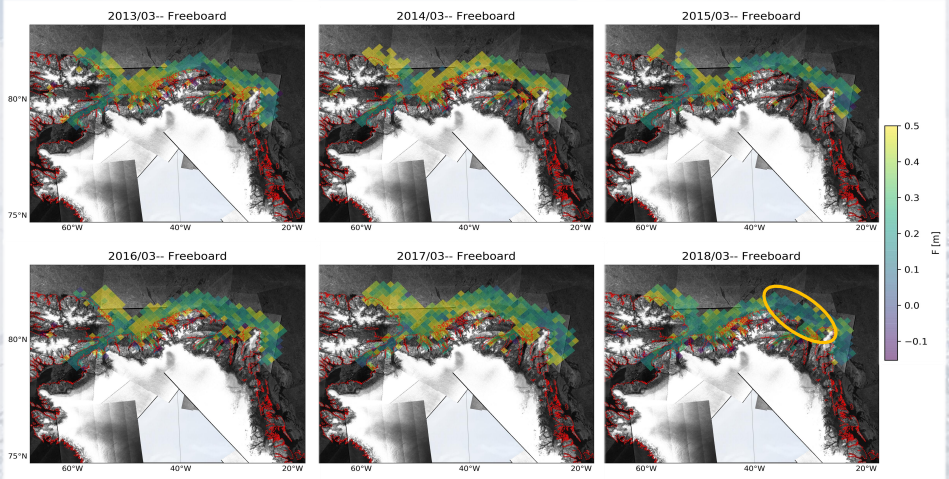

Fig 5. Gridded March freeboard from 2013 to 2018. Freeboard estimates are averaged to a 25-km grid and cover the majority of the northern coast of Greenland. The yellow circle in March 2018 shows unusually low values of freeboard for NE Greenland. This is likely related to the opening and refreezing events caused by the anomalous warm temperatures registered in the same area in February 2018 (Sentinel-1 video of the opening and refreezing available at http://www.seaice.dk/movies/S1AB-Arctic18/s1ab-arctic18-450-h264.mp4)

References

[1] Abulaitijiang, A., Andersen, O. B., & Stenseng, L. (2015). Coastal sea level from inland CryoSat-2 interferometric SAR altimetry. Geophysical Research Letters, 42(6), 1841–1847. https://doi.org/10.1002/2015GL063131

[2] Armitage, T. W. K., & Davidson, M. W. J. (2014). Using the Interferometric Capabilities of the ESA CryoSat-2 Mission to Improve the Accuracy of Sea Ice Freeboard Retrievals. Ieee Transactions on Geoscience and Remote Sensing, 52(1), 529–536. https://doi.org/10.1109/TGRS.2013.2242082

[3] Cipollini, P., et al. (2010), The role of altimetry in coastal observing systems, in Proceedings of OceanObs'09: Sustained Ocean Observations and Information for Society, Venice, Italy, 21–25 Sept. 2009, vol. 2, edited by J. Hall, D. E. Harrison, and D. Stammer, pp. 181–191, ESA Publ., Noordwijk, Netherlands.

[4] Di Bella, A., Skourup, H., Bouffard, J., & Parrinello, T. (2018). Uncertainty Reduction of Arctic Sea Ice Freeboard from CryoSat-2 Interferometric Mode. Advances in Space Research, 62(6), 1251–1264. https://doi.org/10.1016/j.asr.2018.03.018

[5] Gomez-Enri, J., Vignudelli, S., Quartly, G. D., Gommenginger, C. P., Cipollini, P., Challenor, P. G., & Benveniste, J. (2010). Modeling Envisat RA-2 Waveforms in the Coastal Zone: Case Study of Calm Water Contamination. Ieee Geoscience and Remote Sensing Letters, 7(3), 474–478. https://doi.org/10.1109/LGRS.2009.2039193

[6] Pugh, D., & Woodworth, P. (2012). Sea-level science: Understanding tides, surges, tsunamis and mean sea-level changes. Sea-Level Science: Understanding Tides, Surges, Tsunamis and Mean Sea-Level Changes, 1–395. https://doi.org/10.1017/CBO9781139235778

[7] Ricker, R., Hendricks, S., Helm, V., Skourup, H., & Davidson, M. (2014). Sensitivity of CryoSat-2 Arctic sea-ice freeboard and thickness on radar-waveform interpretation. Cryosphere, 8(4), 1607–1622. https://doi.org/10.5194/tc-8-1607-2014

25 years of progress in radar altimetry, Ponta Delgada, Azores, 24 – 29 September 2018
Correspondence to Alessandro Di Bella: adia@space.dtu.dk

Appendix C

Statistics and gridding

C.1 Gaussian propagation of the uncertainty

If the variables $x, \ldots, z$, with respective independent and random uncertainties $\sigma_x, \ldots, \sigma_z$, are used to compute the function $f(x, \ldots, z)$, then the uncertainty in f is [Taylor, 1997]

$$\sigma_f = \sqrt{\left(\frac{\partial f}{\partial x}\sigma_x\right)^2 + \cdots + \left(\frac{\partial f}{\partial z}\sigma_z\right)^2} \tag{C.1}$$

In any case, it is never larger than the ordinary sum

$$\sigma_f \leq \left|\frac{\partial f}{\partial x}\right|\sigma_x + \cdots + \left|\frac{\partial f}{\partial z}\right|\sigma_z \tag{C.2}$$

C.2 Gridding

In this work, whenever a parameter is gridded, it is gridded to the 25-km EASE-Grid 2.0 [Brodzik et al., 2012] which, for the Northern Hemisphere, uses a polar aspect Lambert azimuthal equal-area projection. For more details about this grid, the reader is referred to [Brodzik et al., 2012].
For N measurements of a variable x, the representative value in each grid cell, i.e. the average $\overline{x}$, is computed using a weighted average

$$\overline{x} = \frac{\sum_{i=0}^{N} w_i x_i}{\sum_{i=0}^{N} w_i} \tag{C.3}$$

where w_i is the weight of each measurement, defined as the inverse of the squared point uncertainty σ_{x_i}

$$w_i = \frac{1}{\sigma_{x_i}^2} \tag{C.4}$$

Because the weighted average $\overline{x}$ is a function of the original measured values $x_1, x_2, \ldots, x_N$, the uncertainty in $\overline{x}$ can be calculated using error propagation [Taylor, 1997]

$$\sigma_{\overline{x}} = \frac{1}{\sqrt{\sum_{i=0}^{N} w_i}} \tag{C.5}$$

Appendix D

ASIP SARIn Arctic maps

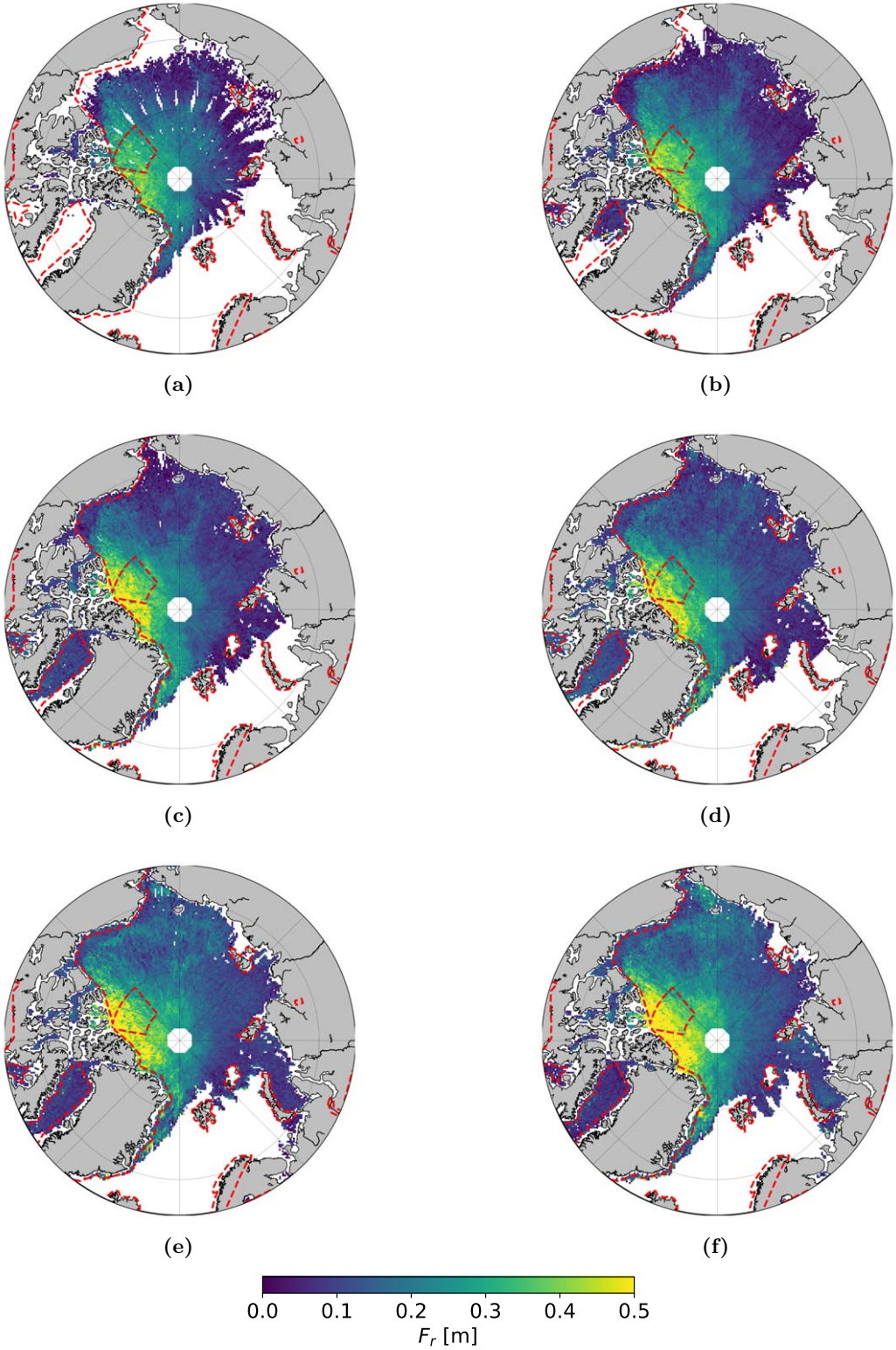

Figure D.1: Arctic sea ice freeboard maps for October 2013 (a), November 2013 (b), December 2013 (c), January 2014 (d), February 2014 (e) and March 2014 (f) from the ASIP SARIn processor

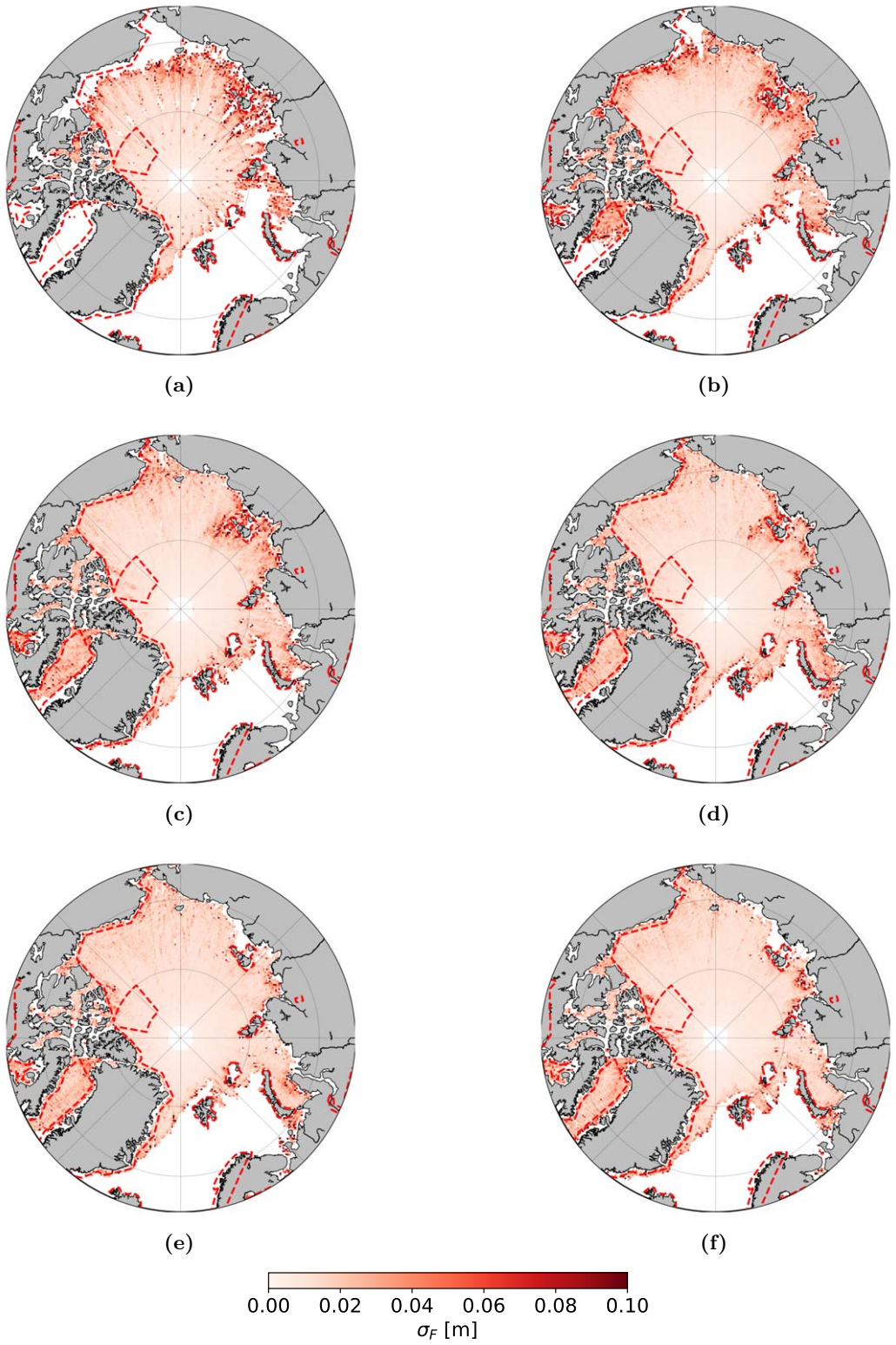

Figure D.2: Arctic sea ice random freeboard uncertainty maps for October 2013 (a), November 2013 (b), December 2013 (c), January 2014 (d), February 2014 (e) and March 2014 (f) from the ASIP SARIn processor

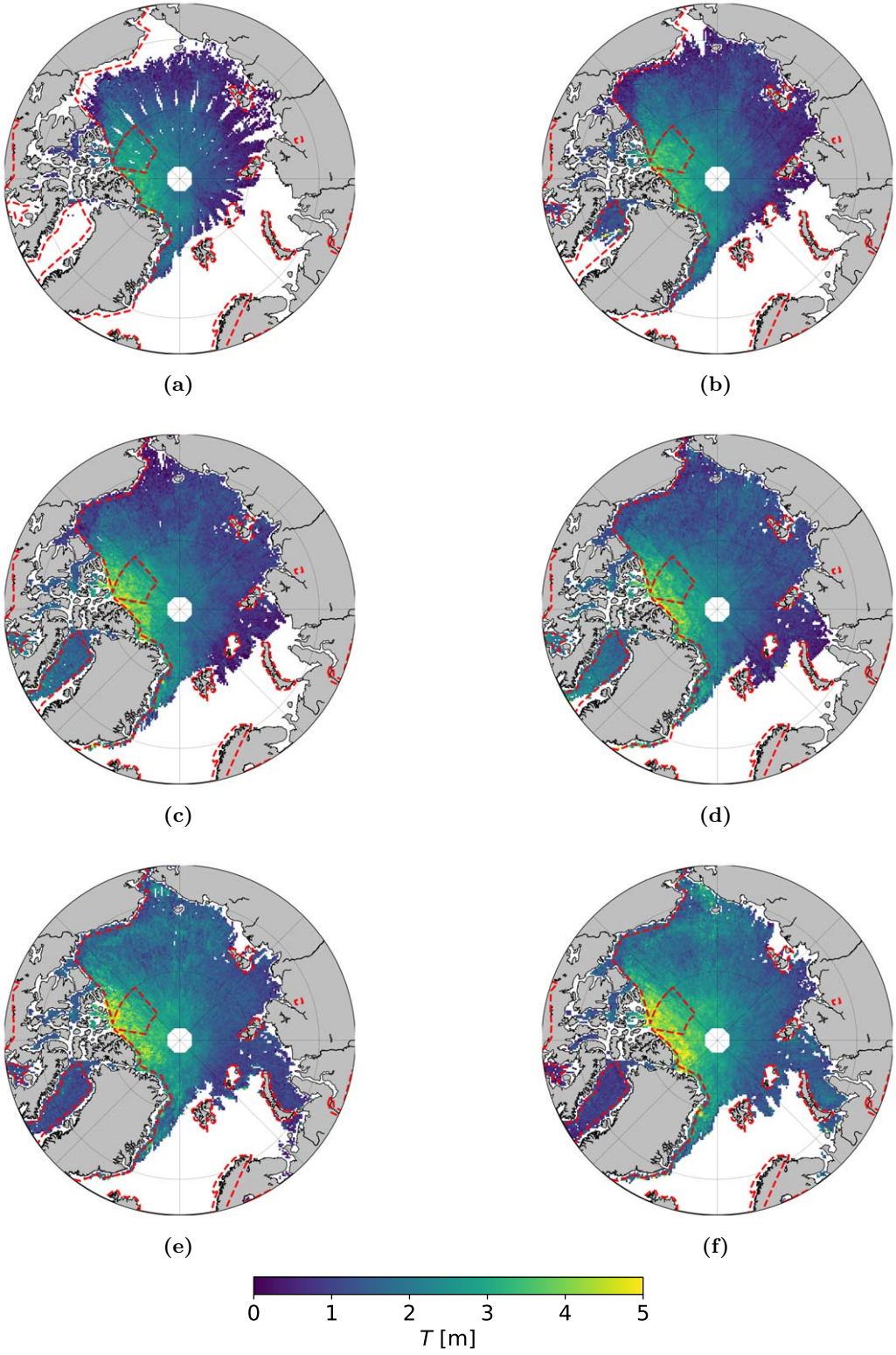

Figure D.3: Arctic sea ice thickness maps for October 2013 (a), November 2013 (b), December 2013 (c), January 2014 (d), February 2014 (e) and March 2014 (f) from the ASIP SARIn processor

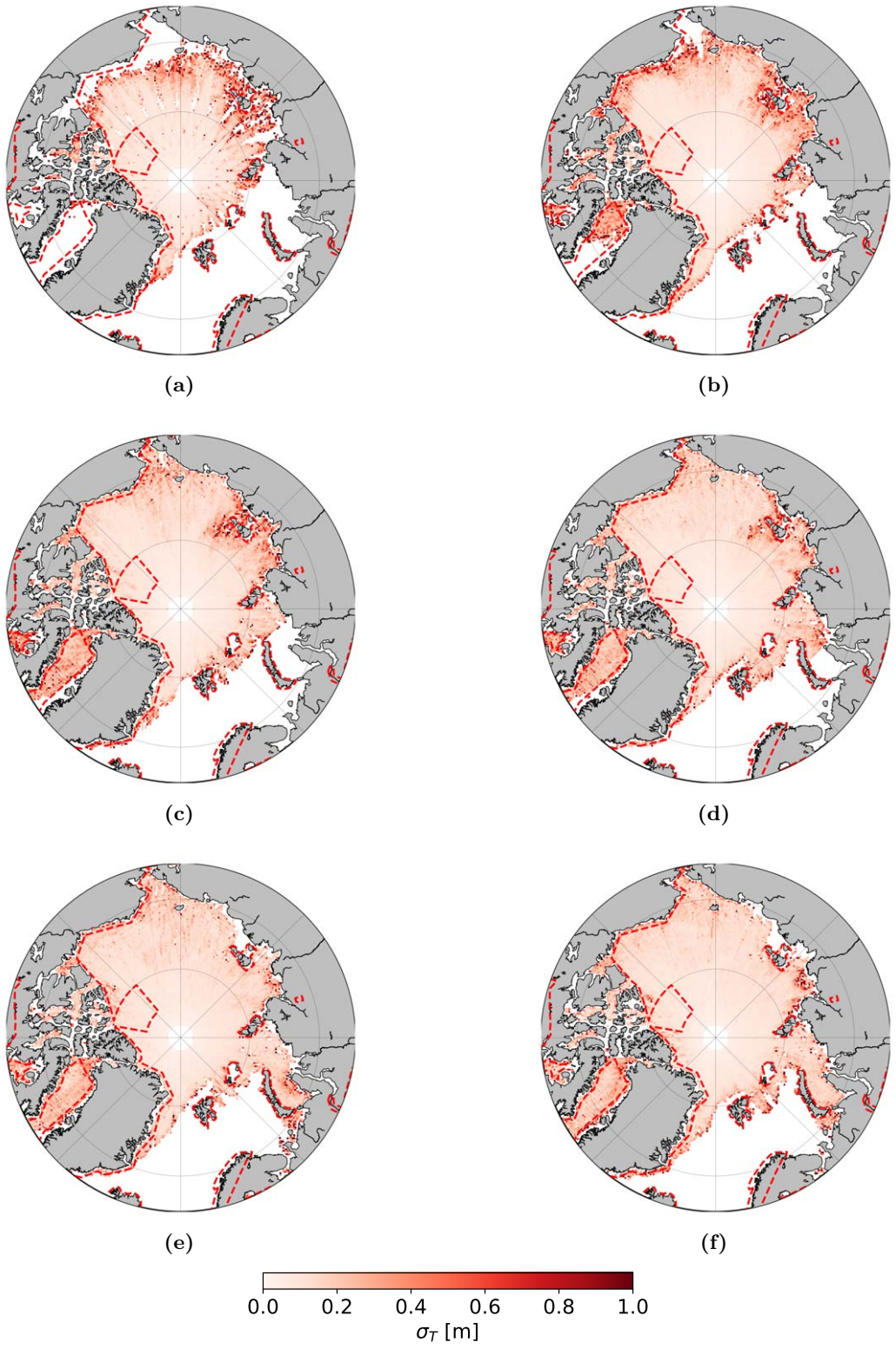

Figure D.4: Arctic sea ice random thickness uncertainty maps for October 2013 (a), November 2013 (b), December 2013 (c), January 2014 (d), February 2014 (e) and March 2014 (f) from the ASIP SARIn processor

Appendix E

MPASIP Arctic maps

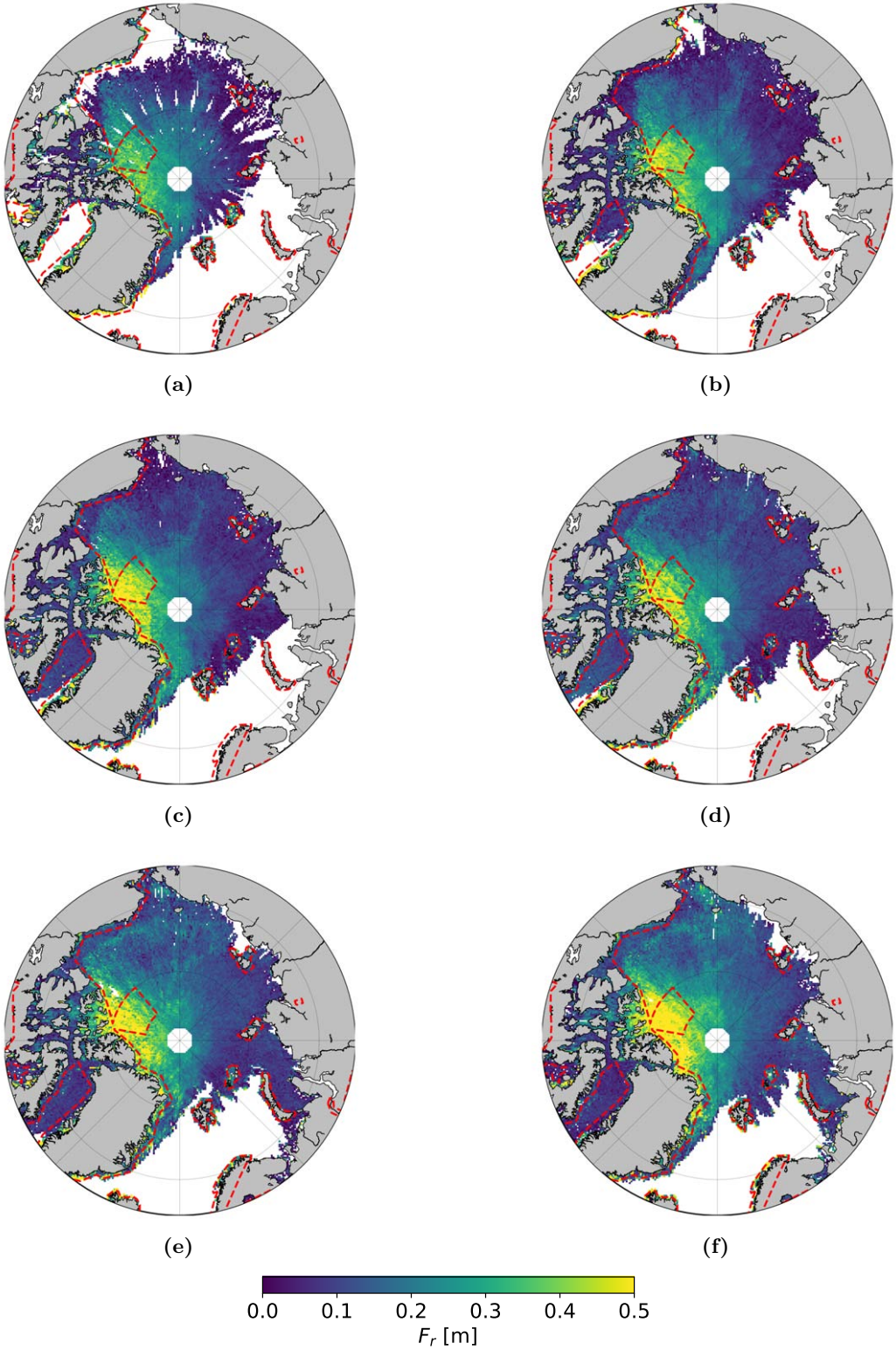

Figure E.1: Arctic sea ice freeboard maps for October 2013 (a), November 2013 (b), December 2013 (c), January 2014 (d), February 2014 (e) and March 2014 (f) from the MPASIP processor

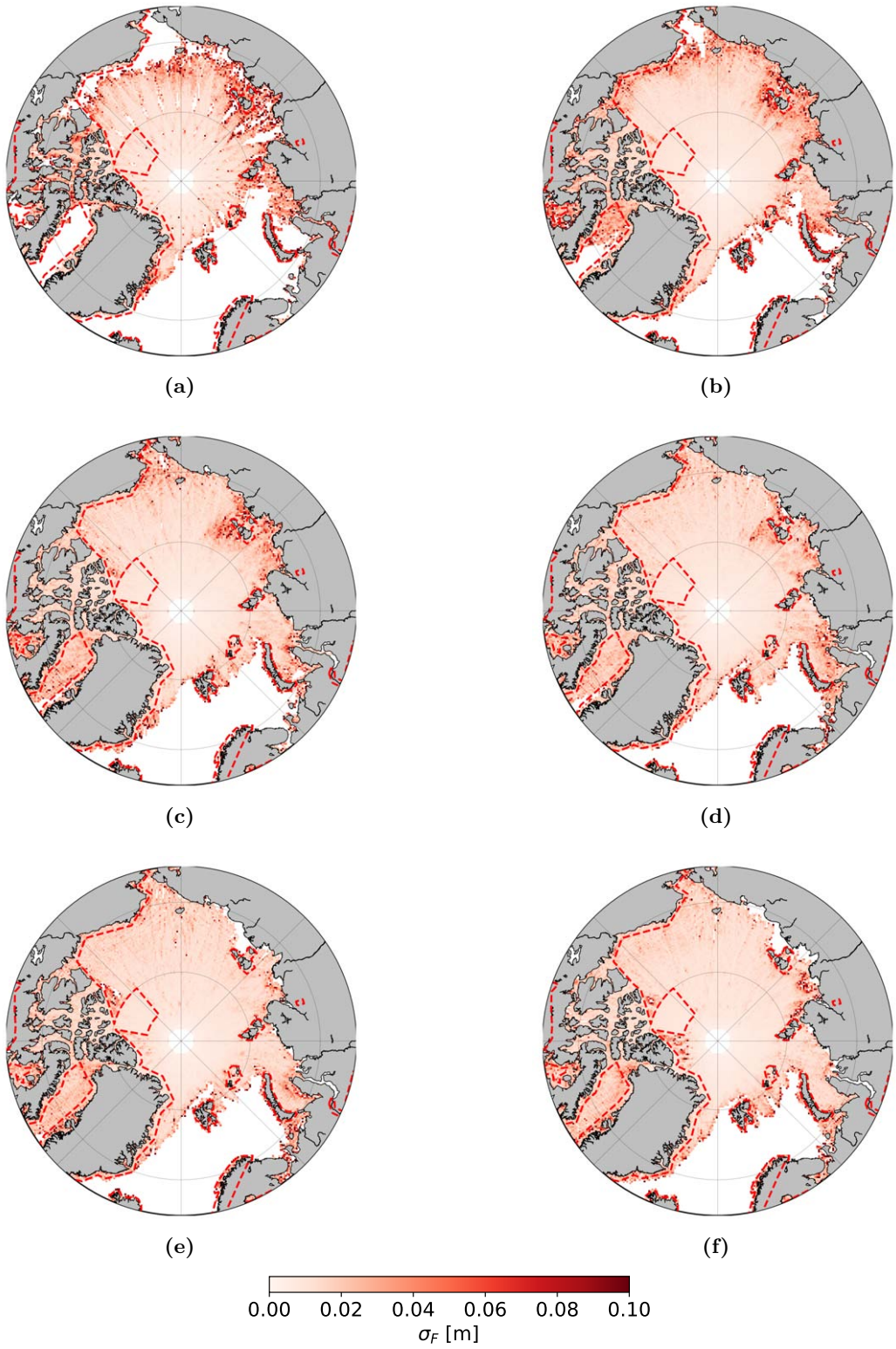

Figure E.2: Arctic sea ice random freeboard uncertainty maps for October 2013 (a), November 2013 (b), December 2013 (c), January 2014 (d), February 2014 (e) and March 2014 (f) from the MPASIP processor

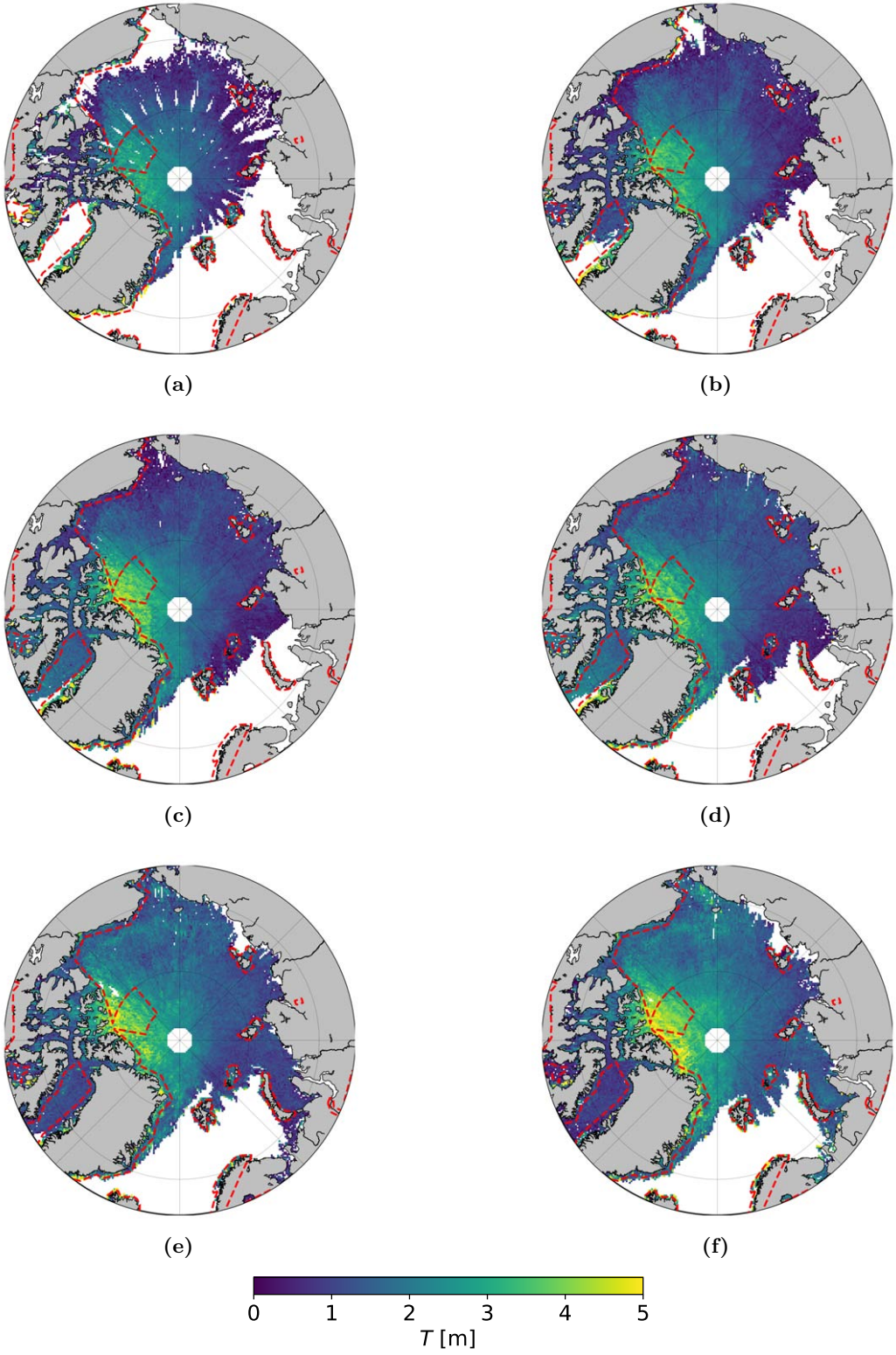

Figure E.3: Arctic sea ice thickness maps for October 2013 (a), November 2013 (b), December 2013 (c), January 2014 (d), February 2014 (e) and March 2014 (f) from the MPASIP processor

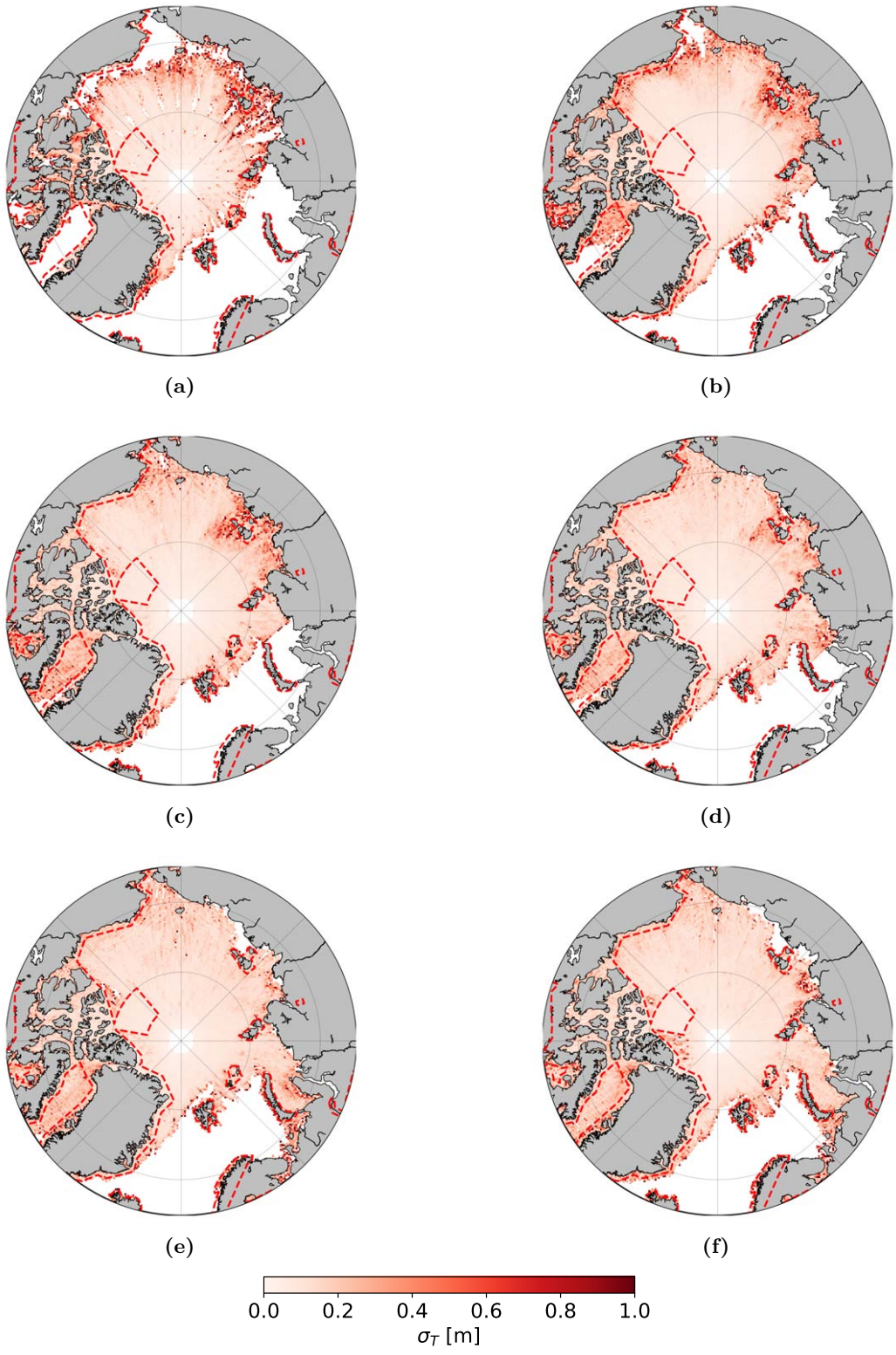

Figure E.4: Arctic sea ice random thickness uncertainty maps for October 2013 (a), November 2013 (b), December 2013 (c), January 2014 (d), February 2014 (e) and March 2014 (f) from the MPASIP processor

DTU Space
National Space Institute
Technical University of Denmark

Elektrovej, building 327+328 + 371 and
Ørsteds Plads, building 348
DK-2800 Kgs. Lyngby
Tel: +45 4525 9500

www.space.dtu.dk